Fault-Tolerant Flight Control for a Fixed-Wing Unmanned Aerial Vehicle with Partial Horizontal and Vertical Stabiliser Losses

by

Ryan Lee Maggott

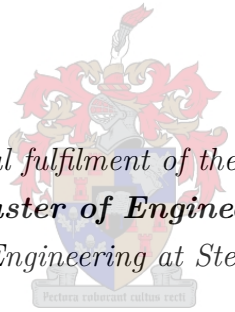

Thesis presented in partial fulfilment of the requirements for the degree
Master of Engineering
in the Faculty of Engineering at Stellenbosch University.

Supervisor:
Mr J.A.A. Engelbrecht

Department of Electrical and Electronic Engineering

December 2016

Declaration

By submitting this thesis electronically, I declare that the entirety of the work contained therein is my own, original work, that I am the sole author thereof (save to the extent explicitly otherwise stated), that reproduction and publication thereof by Stellenbosch University will not infringe any third party rights and that I have not previously in its entirety or in part submitted it for obtaining any qualification.

December 2016

Acknowledgements

I would like to thank the following people for their assistance in completing this project:

- God for His continued guidance and support.
- Mr Japie Engelbrecht, for all your input, help and guidance as my supervisor.
- My family for constantly supporting and motivating me. My father (Shaun) for his help with the hardware manufacturing. My mother (Lindy) for her continued care, support and concern. My sister (Stacey) for always being interested and willing to help.
- Michael Basson for all the aircraft related advice and for being a great safety pilot.
- Wiaan Beeton, Nico Alberts, Cornelus Le Roux and Chris Fourie as ESL lab engineers for assistance in the lab and flight test preparation.
- Andrew de Bruyn, Gideon Hugo and Piero Ioppo for their willing nature to help at flight tests.
- All the friends that I have made at the ESL throughout my studies.

Declaration

By submitting this thesis electronically, I declare that the entirety of the work contained herein is my own, original work, that I am the sole author thereof (save to the extent explicitly otherwise stated), that reproduction and publication thereof by Stellenbosch University will not infringe any third-party rights and that I have not previously in its entirety or in part submitted it for obtaining any qualification.

December 2016

Abstract

In the study reported here, a fault-tolerant flight control system for a fixed-wing unmanned aerial vehicle with partial stabiliser loss is designed, analysed, implemented and verified. The partial stabiliser damage changes the natural dynamics of the aircraft and causes asymmetry.

The control system must maintain aircraft stability and transition from the healthy to the damaged configuration without depending on in-flight knowledge of the change in dynamics. The control system must also provide satisfactory transient performance for both the healthy and the damaged configuration.

Using existing reference frames and conventions, a six-degrees-of-freedom equations of motion model of the aircraft is derived that can model the effects of the partial horizontal and vertical stabiliser loss on the aircraft dynamics. This model considers the changes in the mass, moment of inertia, aerodynamic model, control authority of the aerodynamic control surfaces, as well as the shift in the centre of gravity. The altered aerodynamic coefficients are calculated using vortex lattice techniques for the different damage configurations. In order to determine the trim states and inputs of the aircraft as a function of the partial horizontal and vertical stabiliser loss, a multivariate Newton–Raphson technique is applied to the equations of motion. The required trim actuator deflections are compared to the physical actuator limitations to establish the feasibility of maintaining trim flight for each damage case. Assuming feasible trim states and inputs, the system is linearised and the open-loop dynamics of the aircraft are investigated as a function of partial stabiliser loss.

A combination of classical and acceleration-based control architectures are designed and implemented. The stability, performance and robustness of the flight control system are verified in simulation for damage cases up to 70% left horizontal stabiliser loss and 20% vertical stabiliser loss.

The fault-tolerant flight control system is verified with flight tests. A release mechanism is designed and manufactured to allow 70% of the left horizontal stabiliser and 20% of the vertical stabiliser to be jettisoned in flight. The flight control system is implemented on a practical unmanned aerial vehicle and successful reference tracking is demonstrated. Practical flight tests showed that the flight control was stable for both the healthy and the damaged aircraft configurations, and able to handle the transition following an in-flight partial stabiliser loss event.

Opsomming

Hierdie tesis beskryf die ontwerp, analise, implementasie en verifikasie van ‘n fout-tolerante vlugbeheerstelsel vir ‘n vastevlerk onbemande vliegtuig met gedeeltelike stabiliseerder verlies. Hierdie verlies veroorsaak ‘n verandering in die natuurlike dinamika van die vliegtuig en veroorsaak asimmetrie.

Die beheerstelsel moet in staat wees om stabiliteit te handhaaf en die oorgang van die gesonde na die beskadigde konfigurasies te hanteer, en moet nie staatmaak op in-vlug kennis van die verandering in die dinamika nie. Die beheerstelsel moet ook bevredigende oorgangsgedrag vertoon vir beide die gesonde en die beskadigde konfigurasies.

Bestaande verwysingsraamwerke en konvensies is gebruik om ‘n ses-grade-van-vryheid bewegingsvergelykingsmodel vir die vliegtuig af te lei wat die effekte van die gedeeltelike horisontale en vertikale stabiliseerder verlies op die vlugdinamika modelleer. Hierdie model neem die veranderinge in die massa, traagheidsmoment, aerodinamiese model, beheergesag van die aerodinamiese oppervlakkeverskuiwing en massamiddelpunt in ag. Die veranderinge in die aerodinamiese koëffisiënte word bereken met draaikolk rooster tegnieke vir die verskillende beskadigde konfigurasies. ‘n Meerveranderlike Newton–Raphson tegniek word gebruik om die bewegingsvergelykings op te los om die ekwilibrium toestande en intrees van die vliegtuig te bereken as ‘n funksie van persentasies gedeeltelike horisontale en vertikale stabiliseerder verlies. Die benodigde aktueerder defleksies vir ekwilibrium vlug word vergelyk met die fisiese aktueerder limiete om te bepaal of dit haalbaar is vir die spesifieke hoeveelheid skade. Gegee haalbare ekwilibrium toestande en intrees, word die stelsel gelineariseer en die ooplusdinamika van die vliegtuig ondersoek as ‘n funksie van gedeeltelike stabiliseerder verlies.

‘n Kombinasie van klassieke en versnellingsgebaseerde beheerargitekture is ontwerp en implementeer. Die stabiliteit, prestasie en robuustheid van die vlugbeheerstelsel word verifieer in simulasie vir skade tot by verlies van 70% van die linkerkantste horisontale stabiliseerder en 20% van die vertikale stabiliseerder.

Die fout-tolerante vlugbeheerstelsel is ook verifieer met praktiese vlugtoetse. ‘n Loslaatmeganisme is ontwerp en vervaardig om 70% van die linker horisontale stabiliseerder en 20% van die vertikale stabiliseerder in vlug af te gooi. Die vlugbeheerstelsel is implementeer op ‘n praktiese onbemande vliegtuig en suksesvolle verwysingsvolging is gedemonstreer. Die praktiese vlugtoetsresultate wys dat die vlugbeheer stabiel is vir beide die gesonde en die beskadigde vliegtuig konfigurasies, en dat dit in staat is om die oorgang te hanteer na in-vlug gedeeltelike stabiliseerder verlies.

Table of Contents

List of Figures

List of Tables

Nomenclature

Acronyms

6DoF	six degrees of freedom
AEoM	asymmetric equations of motion
AP	autopilot
AVL	Athena Vortex Lattice
CAD	computer-aided design
CAN	controller area network
CG	centre of gravity
CM	centre of mass
DCM	direct cosine matrix
EoM	equations of motion
ESL	Electronic Systems Laboratory
FDI	fault detection and isolation
FTC	fault-tolerant control
GCS	ground station control software
GPS	global positioning system
HIL	hardware in the loop
IMU	inertial measurement unit
LSA	lateral specific acceleration
MEMS	microelectromechanical systems
MoI	moment of inertia

NED	north, east and down
NSA	normal specific acceleration
OBC	on-board computer
PI	proportional integral
PID	proportional integral derivative
PWM	pulse width modulation
RC	remote control
RF	radio frequency
UAV	unmanned aerial vehicle

Lowercase Letters

$\overline{c}$	mean aerodynamic chord
b	wing span
e	oswald efficiency factor

Greek Symbols

α	angle of attack
β	angle of sideslip
δ	control surface deflection
δ_A	aileron deflection
δ_E	elevator deflection
δ_R	rudder deflection
$\overline{q}$	dynamic pressure
$\overline{V}$	airspeed
ϕ	roll angle
π	pi
ψ	yaw angle
ρ	air density
τ	time constant

θ	pitch angle

Uppercase Letters

A	wing aspect ratio
$C_{(\cdot)_{(\cdot)}}$	non-dimensional aerodynamic coefficient
$C_{(\cdot)}$	cosine of $(\cdot)$
S	wing area
$S_{(\cdot)}$	sine of $(\cdot)$
D	down
E	east
N	north
P	roll rate
Q	pitch rate
R	yaw rate
T	thrust
U	X-velocity
V	Y-velocity
W	Z-velocity

Subscripts

A	aerodynamic
B	body
D	down
E	east
G	gravitational
N	north
O	inertial
T	trim or thrust
W	wind

§ 1

Introduction

1.1 Background

There is an increasing number of commercial opportunities for unmanned aerial vehicles (UAVs) in business (aerial photography, speed courier services in cities), agriculture (surveying, crop inspection, crop dusting, farm security), industry and mining (power line inspection, prospecting), the emergency services (disaster monitoring, delivery of emergency supplies, fire-fighting) and in security services (surveillance, policing).

However, a major barrier to the commercialisation of unmanned aircraft, is the certification process. Before UAVs can be operated in civil airspace, they must first pass a rigorous certification process to prove that they will operate safely.

A key enabling technology required for certification and eventually integration of autonomous unmanned aircraft into commercial airspace is fault-tolerant flight control. Fault-tolerant flight control represents the ability of an aircraft to accommodate sensor and actuator faults, as well as changes in the aircraft dynamics due to airframe damage. Certification of conventional manned aircraft assumes that a human pilot provides these functions, while certification of unmanned aircraft requires that these same functions be performed by the autonomous flight control system. To enable the commercialisation of autonomous UAVs, fault-tolerant control must therefore first be developed and established.

1.2 Previous Work

This section provides a brief overview of the existing work in the field of modelling and control of damaged or asymmetric aircraft. There are two subsections presented. The first focuses on work done in the Electronic Systems Laboratory (ESL) at the University of Stellenbosch. The second section focuses on external work. Investigating previous research allows the identification of a research gap and provides insight into the required modelling of the asymmetric aircraft, techniques of determining trim, and possible robust control systems that can be implemented.

1.2.1 Internal Research

In 2005, Peddle developed a method of autonomous flight of a model aircraft using classical control architectures [1]. The robustness of these techniques were briefly discussed but not thoroughly tested for differences in the airframe. In 2008, Peddle went on to investigate acceleration-based control. This technique used the axial, normal and lateral accelerations to control the aircraft. The acceleration-based control is used as the innermost controllers on the aircraft. Acceleration-based control ensures robustness through designing high-bandwidth controllers to help suppress any uncertainties in the aircraft model, and in this case, changes in the aircraft model due to damage.

Blaauw designed a flight control system with gain-scheduling for a variable stability UAV [2]. The flight controller scheduled the necessary gains through explicit knowledge of the centre of gravity (CG) location to ensure that the aircraft was statically stable for all CG locations.

Pietersen investigated techniques for system identification on a modular UAV [3]. He developed the necessary equations for system identification, which would allow for the accommodation of sudden changes in the parameters in the event of a fault.

Basson investigated the use of an adaptive control technique using Lyapunov stability theory for the inner-most loop for a pitch rate damper on a variable-stability UAV [4]. Basson focussed on designing an adaptive controller to accommodate a longitudinal shift in CG and to reconfigure the inner loop controller to provide a desired model reference response that would remain consistent from the perspective of the outer loop controllers. This would allow the outer-loop controllers to perform as usual with the inner-loop controller providing the desired or expected response.

Basson developed a control allocation algorithm that would optimise the performance of the virtual actuators of an aircraft [5]. A range of failure categories and two different aircraft were used to test the re-allocation algorithm. Sequential quadratic programming techniques were used for the control allocation. Basson's research showed that this allocation algorithm is capable of handling both single and multiple actuator failures, and also highlighted the importance of having redundant actuators on the aircraft.

Odendaal investigated two fault detection and isolation methods for actuator failure. The first method is a multiple model adaptive estimator which uses a bank of extended Kalman filters. Each filter in the bank produces a residual vector and covariance matrix, which is then parsed to a Bayes classifier to determine the fault scenario. The second method uses a parity space approach. This consists of the parity relations that quantify the redundancies between the outputs of the available sensors. Actuator failure causes the variance to increase indicating failure [6]. This form of identification could be used to determine damage to the model should a gain-scheduling control approach be needed.

Beeton investigated the autonomous flight control of a fixed-wing UAV with partial loss of its primary lifting surface [7]. A combination of classical and acceleration-based control was used for this project. It was found that damage to the lifting surface greatly affects the trim settings of the aircraft while having a small effect on the stability and dynamics of the aircraft.

This agrees with the findings of Shah, which are discussed later in this chapter (see 1.2.2) [8].

The information presented in this subsection reveals a research gap in the fault detection and control research performed at the ESL. Some research has been done in fault detection and isolation as well as on the system identification of an aircraft to determine whether a fault exists. Gain-scheduling and adaptive control techniques were investigated for shifts in CG on a variable stability UAV. A control system for a fixed-wing UAV with partial loss of its primary lifting surface was also designed. This project is therefore the next logical progression of the damage-tolerant flight control research in the ESL.

1.2.2 External Research

This section provides a brief survey of relevant external research on fault-tolerant control and the dynamics of aircraft under the influence of damage. Following this, a brief summary discussing the literature study is provided.

Bacon and Gregory provide a set of general equations of motion (EoM) for an asymmetric aircraft [9]. Their technique sets up the EoM around an arbitrary point on the aircraft or body, where the arbitrary point does not have to coincide with the centre of mass. This allows the effect of a large instantaneous centre of mass shift to be modelled. Use of these new equations allows the aerodynamic forces and moments acting on the aircraft to still be referenced around the original centre of mass still and not around the new one.

Shah performed a wind tunnel investigation to measure the aerodynamic effects of damage to the primary lifting surface, the stabilisers or the control surfaces in a commercial transport aircraft configuration [8]. It was found that the primary effect of damage to the tail surfaces is on the stability characteristics of the aircraft while damage/area loss to the wing results in lift and lateral control limitations. The study also showed that it is important to model all mass properties and aerodynamic changes resulting from the asymmetry.

Ahn et al. investigated the stability of a wing-damaged UAV [10]. Wind tunnel tests were conducted to identify the changes in the aerodynamic coefficients and took the shift in CG and moment of inertia (MoI) into account. The longitudinal and lateral flight mode poles were studied to evaluate the changes in flight dynamics due to the damage. The wing damage resulted in the short period mode increasing in frequency and the roll mode slowing down. The aircraft used was a wing body aircraft and therefore did not consider the effects of damage to a horizontal stabiliser.

Cheng et al. looked at an approach to determine the trim settings for a wing-damaged asymmetric aircraft [11]. They made use of the CM-centric approach from B. Bacon [9] to determine the EoM of their aircraft. Cheng et al. looked at the multidimensional Newton iteration as a technique to find an equilibrium, and then investigated the global convergence of this technique in their application.

Jourdan et al. designed a damage-tolerant control technology for Rockwell Collins [12]. This system was verified on practical flight tests using a sub-scale F-18 UAV. A model reference adaptive control, an automatic supervisory adaptive control and an emergency mission

management system were used and had shown to provide satisfactory robustness in cases of primary control surface damage, airframe damage and complete engine failure.

This subsection shows that there has been investigation into aircraft that have suffered damage. Wind tunnel tests have been conducted on a scale size general transport model aircraft to investigate the effects of different damage configuration on the aircraft. Adaptive control techniques have also been designed to accommodate control surface damage, airframe damage and engine failure.

This project will therefore focus on the design of a fixed-gain non-adaptive fault-tolerant flight control system that is able to accommodate partial loss of the horizontal and/or vertical stabilisers. This damage case is chosen because partial loss of the stabilisers result in significant changes in the stability and dynamics of the aircraft.

1.3 Research Objective

The present project aimed to investigate, design, implement and verify damage-tolerant flight control laws for a fixed-wing UAV that had suffered partial loss of its horizontal and vertical stabilisers. An asymmetric flight dynamics model was derived that models the effects of the partial stabiliser losses. The maximum percentages of partial horizontal and vertical stabiliser losses that can realistically be accommodated were determined through a trim analysis. The aircraft model was then linearised and the stability of the natural dynamics was analysed as a function of the percentage losses. A robust, non-adaptive flight control system was then designed to provide acceptable closed-loop dynamics over all feasible damage cases. The flight control system was verified through simulation and practical flight testing.

1.4 Contributions

The following contributions were made in the execution of this masters research project:

- Derivation of an adapted aircraft model taking into account changes resulting from partial stabiliser loss.
- Implementation of a multivariate Newton–Raphson solver to determine the trim conditions for the different amounts of partial stabiliser loss.
- Stability analysis of a fixed-wing UAV with partial stabiliser loss.
- Fault-tolerant control system design, implementation and verification for a fixed-wing UAV with partial stabiliser loss.
- Simulation and practical flight test results for a non-adaptive fixed-gain flight control system for a fixed-wing UAV with partial stabiliser loss.
  - Step response results for the healthy and damaged aircraft configuration.

Figure 1.1: Trainer 60 RC aircraft

– Telemetry data of full autonomous control during a healthy to damaged aircraft configuration transition flight test.

1.5 Research Vehicle

The research vehicle used in this project built upon the previous UAV projects done in the ESL at the University of Stellenbosch. This section reports on the vehicle, the components used and the basic structure of how it all fitted together.

A modified Trainer 60 remote control (RC) aircraft, as shown in Figure 1.1, was used for the practical flight testing.

The avionics package used in the UAV is an in-house system developed by the ESL. A system diagram of the avionics package is shown in Figure 1.2. Its central component is the on-board computer (OBC). The OBC receives and processes the data from the sensors, provides telemetry to the ground station operator, provides commands to the actuators and runs the automatic flight control when active. A servo board is used to interpret the input received from the RC transmitter operated by the manual safety pilot and send it to the OBC. The OBC in turn sends the necessary pulse width modulation (PWM) signals to the servo board (either from the autopilot or the RC), which then provides the relevant actuator with the command. The OBC provides telemetry data to the ground station control software (GCS) which allows the operator to monitor the aircraft states and upload commands to the autopilot system. A radio frequency (RF) link is used to communicate between the GCS and OBC to provide telemetry to the operator, or commands to the aircraft.

The sensors on board the aircraft consist of:

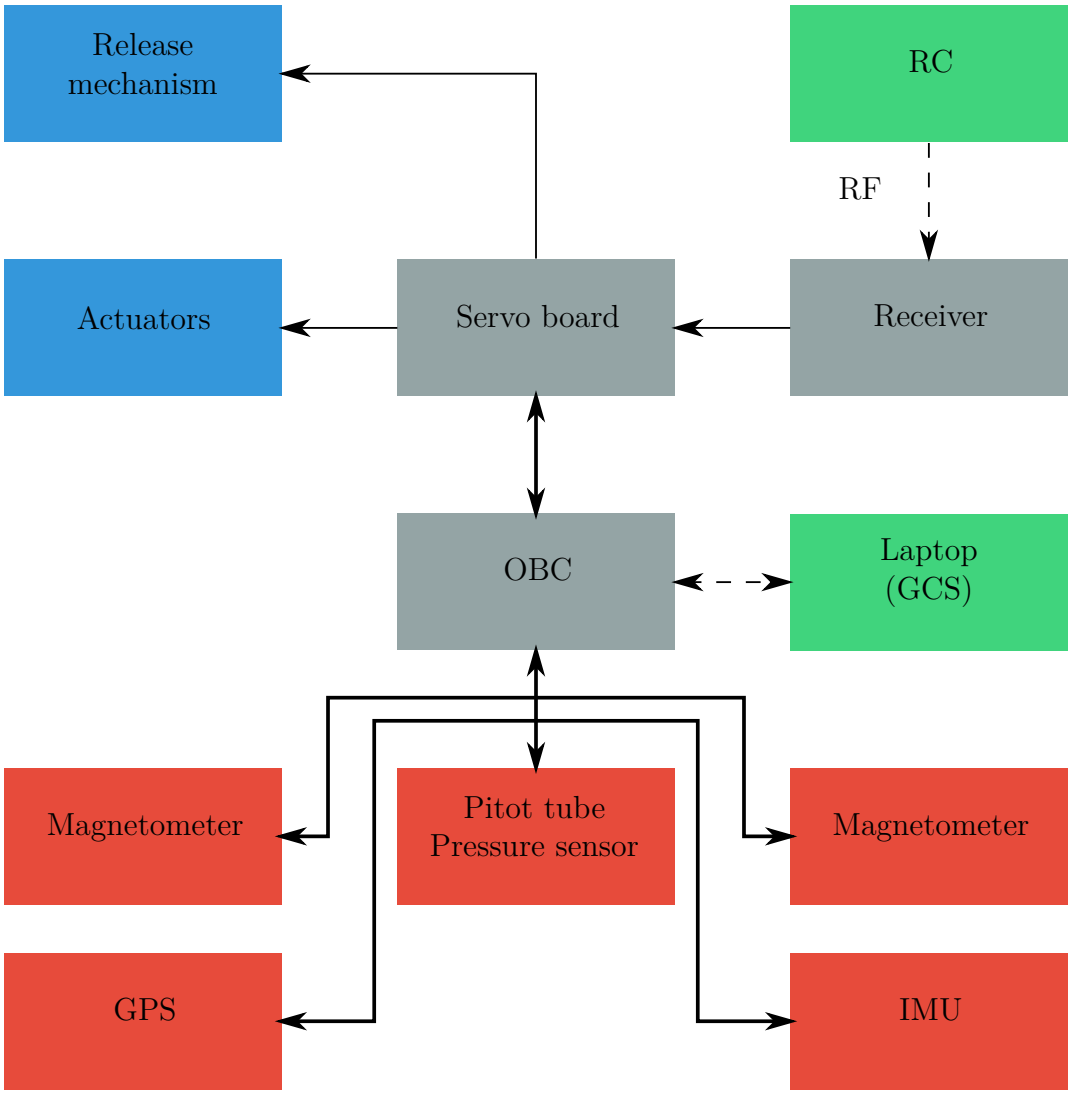

Figure 1.2: Hardware overview

magnetometer - Measures the magnetic field to provide heading and attitude angles;

pressure sensor - Measures the air pressure to provide airspeed, climb rate and altitude;

global positioning system (GPS) - Uses satellites to provide positioning and absolute velocities; and

inertial measurement unit (IMU) - Uses microelectromechanical systems (MEMS) to provide acceleration and angular velocity measurements.

These sensors are all connected to the OBC via a controller area network (CAN) bus. The sensor measurements are used by the on-board state estimator to provide estimates of the attitude, velocity and position of the aircraft for the feedback control laws of the flight control system. The vehicle was modified for this study to enable in-flight release of the partial left horizontal and vertical stabiliser portions.

1.6 Project Overview

This section presents an overview of the main stages of this project by providing a chronological order of events that were executed to achieve the goal of the project.

Firstly, the six degrees of freedom (6DoF) model for the symmetric aircraft model was defined. This covered the kinetic and kinematic equations, the attitude and position dynamics as well as the force and moment equations of the aircraft. The force and moment equations cover the aerodynamic, gravitational and thrust forces that act on the aircraft. The symmetric 6DoF model was necessary to provide a baseline that was used to provide the extended mechanics to include the effects of partial tail loss. The extended flight mechanics model built on the general one used for the symmetric model. The force and moment equations were adapted as discussed by Bacon [9]. This method provided new force and moment equations based on the shift in CG and MoI. The gravitational forces acting on the aircraft were also adapted using this technique while the thrust force was not affected by the damage. The change in aerodynamic coefficients was among the most significant. These coefficients were recalculated using Athena Vortex Lattice (AVL) for the specific aircraft dimensions based on the damage percentage.

With the model defined, the trim could be calculated. The trim of the aircraft is a set of actuator settings that allows the aircraft to fly in equilibrium (straight, straight and level, or constant bank, all while maintaining altitude). This is important as it will indicate mean actuator settings around which the control system will eventually command the actuators. An analytic trim calculation was used to determine the trim of the symmetric aircraft. This provided a benchmark to assess how much the trim of the aircraft changed due to the amount of damage present on the aircraft. The trim settings also provided information regarding the required range of the actuator to achieve straight and level flight. If these settings were outside or near the limits of the actuators, controlling the aircraft at those damage cases would not have been possible. This provided the first indication of the damage conditions that could not be realistically accommodated. The trim results for the damage cases of the independent surfaces had trims well within the range of the actuators, while certain combined cases had large trim settings, which were not practically viable.

The trim conditions were then used for the linearisation of the model which allowed an open-loop stability analysis. The different modes of the aircraft could be investigated using the linearised model, and the affect of the damage on these different modes could be assessed. It was assumed that there is no cross-coupling present between the longitudinal and lateral dynamics. The aircraft model could then be decoupled into its longitudinal and lateral states to simplify the analyses of the flight dynamics. Further testing indicated that this assumption was valid as the combined stability analysis is almost a superimposition of the lateral and longitudinal states as shown in Figure 4.3. The partial horizontal stabiliser had a large effect on the short period mode of the aircraft where it reduced the frequency and the damping ratio of the mode. While the change seems large, the mode was still relatively quick and did not affect the performance of the aircraft drastically. The partial vertical stabiliser affected the

dutch roll mode of the aircraft. This mode was rather slow in the healthy case and became slower and less damped as more of the vertical stabiliser was removed.. The roll mode of the aircraft was hardly affected. It is common for the spiral mode of this type of aircraft to be unstable, but it was very slow and easily stabilised through roll angle control. In all the damage cases, the aircraft remained stable in its open-loop analysis. The aircraft did however become slower to respond and some of the resultant poles were very close to crossing into the right-hand plane, indicating an unstable mode.

With the open-loop poles of the aircraft analysed, the control design architecture was chosen and the controller gains were designed and tested. A combination of classic and acceleration-based control was used as the architecture of the control system. The aircraft model that the control system was designed for was assumed to be symmetric and that the deviations from trim are small allowing the linearised aircraft model to be decoupled. The control system was designed for the healthy aircraft with robustness included to accommodate the changes in the aircraft model due to the partial stabiliser loss. The controllers were verified through linear simulation to ensure that the responses met the specifications for which they were designed. The linear simulations were then run to observe the difference between the healthy and damaged aircraft configuration under control. While there were some noticeable differences between the two configurations, the control system remained stable and still provided acceptable transient characteristics in the damaged case. The closed-loop pole plots and step responses indicated that the control systems remained stable.

The control systems were implemented on the hardware to allow hardware in the loop (HIL) simulations. These simulations allowed the full nonlinear aircraft model to be tested with the control system running on the OBC. The results from the HIL simulations agreed with the linear responses with a few minor differences that arose due to the cross-coupling between the longitudinal and the lateral dynamics that increased due to the aircraft asymmetry resulting from the damage. These minor differences did not affect the overall response significantly. The successful HIL simulations allowed the practical implementation to take place and for the practical flight tests to be carried out.

The hardware used for this project was a previously used Trainer 60 RC aircraft that had been modified to accommodate the OBC and sensors that make up the avionics package in the ESL. The initial flight tests were used to determine whether the aircraft can be flown in the damage configuration, and whether the safety pilot was comfortable to manually control the aircraft in the damaged configuration, if the need arises. Different controller responses were then tested in practical flight through the execution of reference steps to see the responses of the specific controller. These step responses were then used to investigate how the aircraft response changed due to the damage, and ultimately indicated whether the control system was capable of accommodating the damage while maintaining flight stability and acceptable dynamic response. The control systems performed similarly to what was expected from the linear and HIL simulations in both the healthy and damaged aircraft case. A transition from the healthy to damaged aircraft configuration was also tested while the full guidance control system

was active, and the results showed that the control system handled the transition successfully.

1.7 Thesis Outline

This section presents the flow of the thesis. A brief overview of the contents of each chapter is given.

Chapter 2 presents the mathematical model used in this thesis. The reference frames and conventions used in this thesis are defined in this chapter. The flight dynamics are then presented and extended to represent the different damage configurations of the aircraft. The aerodynamic effects due to the different damage configurations are also presented.

The trim calculations and analyses is presented in chapter 3. This provides the different trim solving techniques and discusses the results that are determined by these trim techniques. Simulation results of the flight paths resulting from these trim settings are also presented in this chapter.

The aircraft model is then linearised about its trim conditions in chapter 4. The flight dynamics of the aircraft as a function of percentage stabiliser loss is presented, which shows how the different modes of the aircraft change as the aircraft model is changed as a function of percentage stabiliser loss.

Chapter 5 presents the control architecture and controller design process for this project. The control architecture is discussed and the desired controller responses and design process is presented. Linear simulation results for the controllers and their performance on the different aircraft configurations are presented at the end of this chapter.

The nonlinear simulation process and results are presented in chapter 6. This section presents the HIL nonlinear simulation environment and the testing of the flight controllers in a nonlinear simulation environment. The simulation results are compared to the linear results from chapter 5 to determine any inconsistencies.

The practical flight tests are presented in chapter 7. This chapter presents the vehicle modifications necessary for the completion of this project. The flight test overview motivates the different practical tests that were executed and the contribution they make. The practical flight test results are then presented and compared to the nonlinear simulation results from chapter 6.

Finally, the conclusion is presented in chapter 8. This provides a summary of this study and highlights the observations made as well as identifies future work and improvements that could be made.

§ 2

Modelling

This chapter presents the modelling of the aircraft in both its healthy and damaged configurations. This model is used for analysis and simulation, and will also serve as the basis for the design of the flight control system.

First, the reference frames and conventions that were used in the aircraft model are established. The different axis systems are discussed and the equations used to convert from one reference frame to another are presented. A notation is introduced to distinguish between the different categories of forces or moments acting on the aircraft. The actuator conventions and their effects on the aircraft are then described.

Next, the six-degrees-of-freedom equations of motion (6DoF EoM) are presented for the healthy, symmetric aircraft. These EoM model the forces and moments acting on the aircraft, as well as the attitude and position dynamics of the aircraft. The different categories of forces and moments are identified and modelled. The healthy, symmetric aircraft model was subsequently extended to include the effects of partial horizontal and vertical stabiliser loss. The partial stabiliser losses result in a shift in the centre of gravity (CG), change in the mass and moment of inertial (MoI), and changes in the aerodynamic coefficients.

Finally, the method used to determine the changes in the aerodynamic coefficients is described, and the effects of the partial stabiliser losses on the aerodynamic coefficients are discussed.

2.1 Reference Frames and Conventions

This section presents a discussion on the reference frames that were used in this study. The reference frames that were used were the inertial, body axis and wind reference frames. The conventions that are described are those that defined the attitude, angular rates, position, velocity and forces and moments of the UAV. The conventions defining the actuator operations are also described in this section.

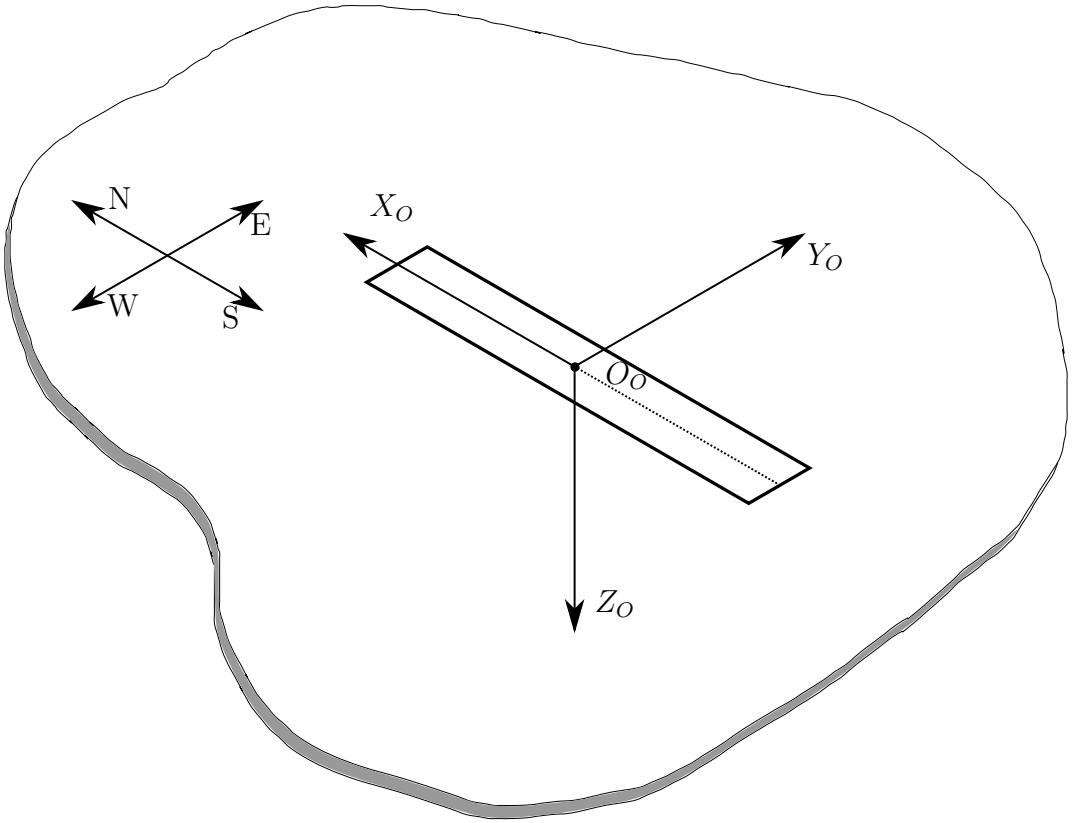

Figure 2.1: Inertial reference frame

2.1.1 Inertial, Body and Wind Reference Frames

The convention followed throughout this study regarding the reference frames is taken from that defined in the "Introduction to the aerodynamics of flight" by NASA [13].

2.1.1.1 Inertial Axes

Figure 2.1 shows the definition of the inertial axis system. The inertial axis system $F_O(O_O, X_O, Y_O, Z_O)$ was chosen as an earth-fixed axis system with the origin at a convenient point on the earth's surface (O_O). The origin is often chosen to coincide with the point on the runway below the aircraft's CG at the start of the motion under study. The inertial axis system is right-handed with the positive Z_O-axis pointing down perpendicular to the local horizontal plane. The X_O-axis is positive to the north and perpendicular to the Z_O-axis. The Y_O-axis is positive to the east and is perpendicular to the X_OZ_O-plane. This axis system is also referred to as the north, east and down (NED) axis system.

In order to simplify the EoM and 6DoF model of the aircraft, the earth was considered to be flat and non-rotating (these are essential qualities of an inertial axis system.). These assumptions were reasonable as the ranges flown in the present study were small in comparison with the radius of the earth and the typical angular rotations of the aircraft were much greater than the angular rotation rate of the earth.

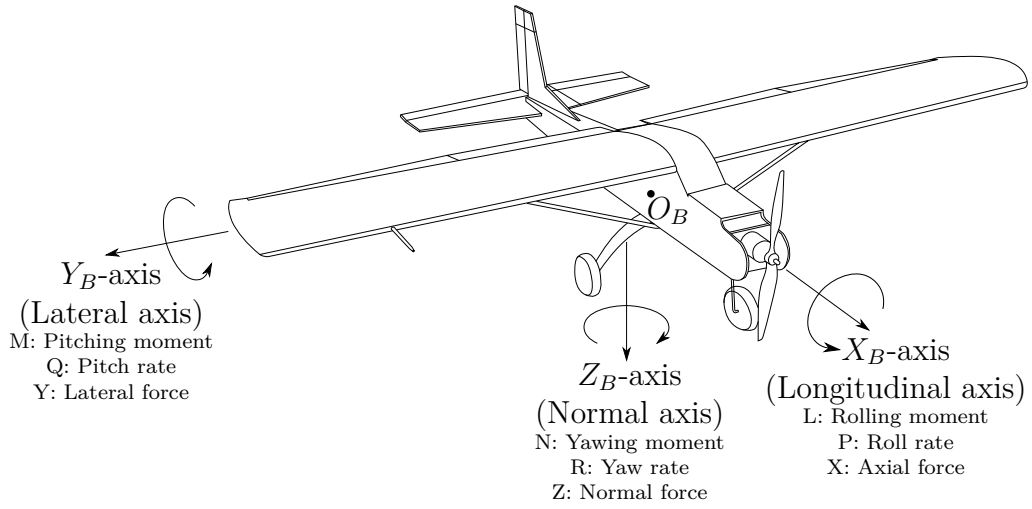

Figure 2.2: Body reference frame

2.1.1.2 Body Axes

The body axis system is vital to define a concise set of aircraft dynamic equations, which will become clearer as the aircraft model is developed further.

Figure 2.2 shows the body axis system that was used in this study. The body axis system $F_B(O_B, X_B, Y_B, Z_O)$ used was a right-handed axis system and is chosen as a body-fixed axis system with the origin (O_B) located at the CG of the aircraft. The X_B-axis is in the plane of symmetry of the aircraft and is positive in the forward direction. The exact forward direction is determined by the specific body axis system used. The Z_B-axis is also in the axis of symmetry of the aircraft and perpendicular to the X_B-axis with positive in the downward direction. The Y_B-axis is perpendicular to the X_BZ_B-plane and is positive to the right. The aircraft is said to roll about the X_B-axis, pitch about the Y_B-axis and yaw around the Z_B-axis. The positive directions are indicated in Figure 2.2 and adhere to the right-hand convention.

2.1.1.3 Wind Axes

Figure 2.3 shows the wind axis system used in this study. The wind axes system $F_W(O_B, X_W, Y_W, Z_W)$ is a rectangular Cartesian axis system with its origin at the CG of the aircraft (the same as the body axis centre). The X_W-axis points in the direction of the oncoming wind velocity vector. The Z_W-axis lies in the plane of symmetry of the aircraft, is perpendicular to the X_W-axis and is directed generally downwards. The Y_W-axis is both perpendicular to the X_W- and Z_W-axes and generally points out of the right wing of the aircraft. This system also follows the right-handed axis system convention.

2.1.2 Standard Notation and Conventions

With the reference frames provided in section 2.1.1, the notations and conventions that were used to describe the attitude of the aircraft can be defined.

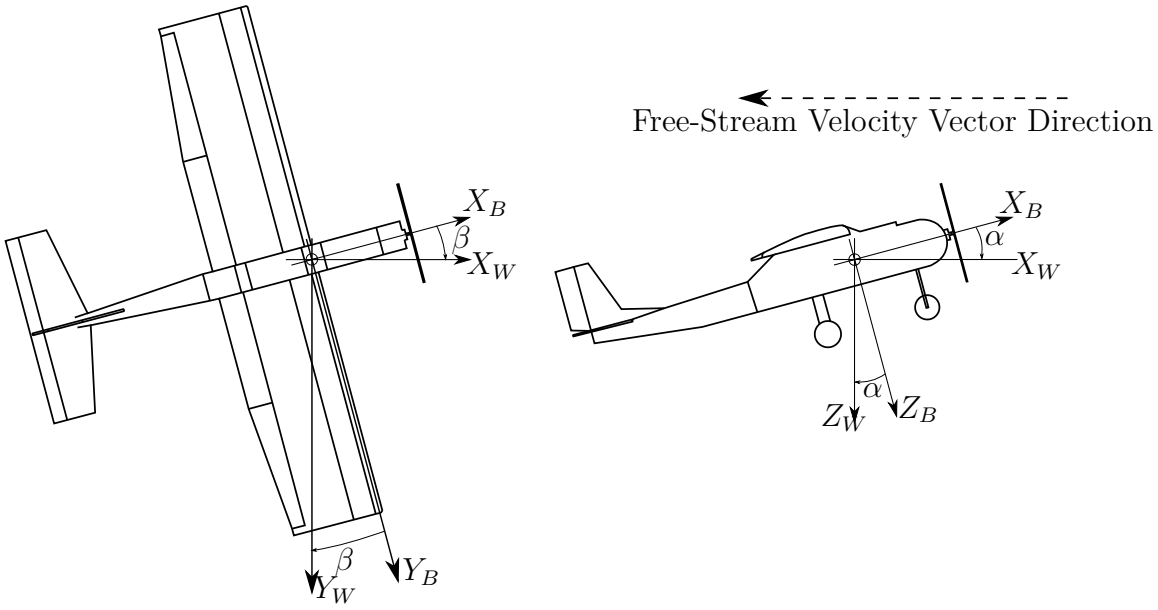

Figure 2.3: Wind reference frame

2.1.2.1 General Conventions

The conventions concerning the forces and moments acting on the UAV are discussed first. There are three categories of forces and moments namely, aerodynamic, gravitational and thrust. These forces and moments comprise components in the x-, y-, and z-axes. The forces are denoted by $X_{(.)}$, $Y_{(.)}$ and $Z_{(.)}$, according to their axes and the category to which they belong. The first category is the forces that result from the aerodynamics of the aircraft. These forces are usually modelled in the wind reference frame, and are introduced using non-dimensional aerodynamic coefficients. The aerodynamic forces are subscripted with an A (e.g. X_A). The second category of force on the aircraft is that due to the thrust generated by the engine of the aircraft. The engine on this particular UAV was aligned with the body reference frame x-axis. It was assumed that the force generated by the engine acts in line with the CG of the aircraft, and no moment is introduced by it. The thrust forces are subscripted with a T (e.g. X_T). The final force acting on the aircraft originates from gravity and is modelled in the inertial frame. Gravity acts through the aircraft's CG and it is assumed that no moments are caused due to gravity acting on the aircraft. The gravitational forces are subscripted with a G (e.g. X_G).

The moments acting on the aircraft are defined in the body reference axes. This convention is used due to the UAV rotating around its CG. The moments of the aircraft are represented by $L_{(.)}$, $M_{(.)}$ and $N_{(.)}$ respectively for the x-, y- and z-axes. The subscripts are the same as those defined for the forces (aerodynamic, thrust and gravitational). The rotational rates of the UAV are also defined in the body reference axes. The components of the angular rates are represented by P, Q and R. The right-hand rule is used to define the positive direction of both the moments and rotational rates around the axis within which they are defined.

The attitude of the aircraft is represented using Euler angles, and ϕ, θ and ψ are used to represent the bank, pitch and heading angles of the aircraft. An Euler 3-2-1 rotation was used to represent the orientation of the body axis system relative to the inertial axis system. The

Euler 3-2-1 rotation consists of first rotating through the heading angle (ψ), then through the pitch angle (θ) and finally through the bank angle (ϕ). The results of this rotation can be used to define a direct cosine matrix (DCM). Equation 2.1.1 represents the DCM for the rotation from the inertial axis system to the body axis system. The transpose of equation 2.1.1 enables the rotation from the body axis system to the inertial axis system. The full derivation of this equation can be found in section 2.2.1.4.

$$DCM_{I\to B} = \begin{bmatrix} C_\Psi C_\Theta & S_\Psi C_\Theta & -S_\Theta \\ C_\Psi S_\Theta S_\Phi - S_\Psi C_\Phi & S_\Psi S_\Theta S_\Phi + C_\Psi C_\Phi & C_\Theta S_\Phi \\ C_\Psi S_\Theta C_\Phi + S_\Psi S_\Phi & S_\Psi S_\Theta C_\Phi + C_\Psi C_\Phi & C_\Theta C_\Phi \end{bmatrix} \quad \text{where } C_{(\cdot)} = \cos(\cdot), S_{(\cdot)} = \sin(\cdot) \tag{2.1.1}$$

The position of the UAV is described in the inertial reference frame (see 2.1.1.1). In order to simplify the system it was assumed that, for this particular project, the earth is flat as the distances taken into consideration were much smaller than the radius of the earth. The velocity of the aircraft can be expressed either in terms of the rectangular coordinates U_B, V_B and W_B, or in terms of spherical coordinates $\overline{V}$, α and β. $\overline{V}$ is the magnitude of the velocity vector, α is the angle of attack and β is the angle of sideslip. The airspeed of the aircraft is the speed of the aircraft relative to the air, and the ground-speed is the speed of the aircraft relative to the ground.

$$\overline{V} = \sqrt{U_B^2 + V_B^2 + W_B^2} \tag{2.1.2}$$

$$\alpha = \arctan\left(\frac{W_B}{U_B}\right) \tag{2.1.3}$$

$$\beta = \arcsin\left(\frac{V_B}{\overline{V}}\right) \tag{2.1.4}$$

The α and β values can be used to define a transformation from the wind- to body-axis system and vice versa. Equation 2.1.5 shows the transformation from the wind- to body-axis systems. The body to wind axis transformation is simply the transpose of equation 2.1.5

$$DCM_{W\to B} = \begin{bmatrix} C_\alpha C_\beta & -C_\alpha S_\beta & -S_\alpha \\ S_\beta & C_\beta & 0 \\ S_\alpha C_\beta & -S_\alpha S_\beta & C_\alpha \end{bmatrix}, \text{ where } C_{(\cdot)} = \cos(\cdot), S_{(\cdot)} = \sin(\cdot) \tag{2.1.5}$$

The components of the velocity coordinated in the inertial axis system are represented by V_N, V_E and V_D.

2.1.2.2 Actuator Conventions

The actuator convention that was used is one where a positive actuator deflection causes a negative moment on the UAV. Figure 2.4 shows the actuator deflections and the resultant moment on the UAV.

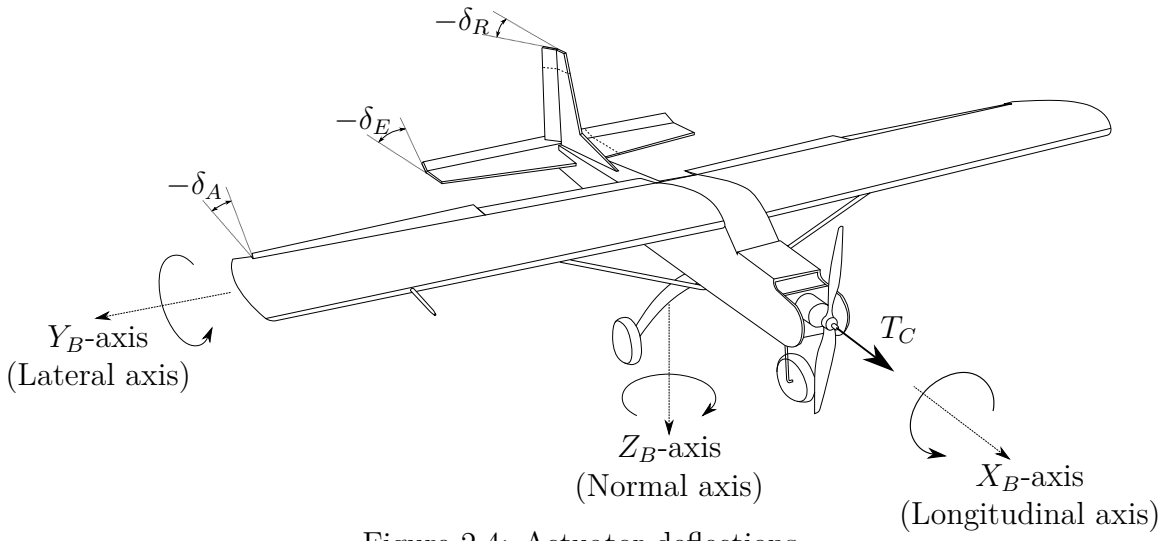

Figure 2.4: Actuator deflections

The aileron deflections, represented by δ_A, are deflected in a differential manner in order to generate a moment around the body x-axis. This moment is called the rolling moment. Negative differential aileron deflections, as shown in Figure 2.4, cause the UAV to experience a rolling moment in the positive y-axis direction (positive rolling moment).

The elevator deflections, represented by δ_E, cause a moment around the body y-axis of the UAV. This moment is called the pitching moment. A negative deflection of the elevator, shown in Figure 2.4, causes a nose-up moment in the positive z-axis direction (positive pitching moment).

The rudder deflections, represented by δ_R, cause a moment around the body z-axis of the UAV. This moment is called the yawing moment. A negative deflection of the rudder, shown in Figure 2.4, causes a positive yawing moment in the positive z-axis direction.

A brief summary regarding the defined notation is listed below:

- P, Q, R: x-, y- and z-body-referenced angular rates.
- U, V, W: x-, y- and z-body-referenced velocities.
- V_N, V_E, V_D: x-, y- and z-inertial-referenced velocities.
- $(\cdot)_N$, $(\cdot)_E$, $(\cdot)_D$: north, east or down inertial frame identifiers.
- $(\cdot)_O$, $(\cdot)_W$, $(\cdot)_B$: inertial-, wind- or body-reference frame identifier.
- δ_A, δ_E, δ_R: actuator surface deflections.
- $\overline{V}$, α, β: airspeed, angle of attack and angle of sideslip

The motion of the aircraft was described using the reference frames and conventions established in this section. Figure 2.5 shows a system overview of the aircraft model and highlights the main components that describe the aircraft mechanics including those that model the effects of the partial tail damage. The five main components of the aircraft model are identified as:

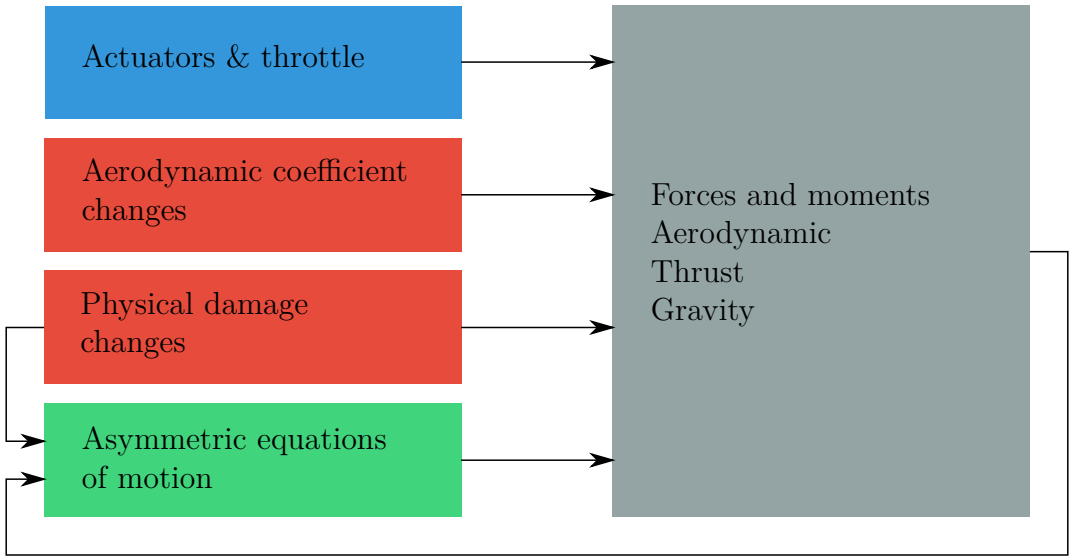

Figure 2.5: System overview

- Inputs: The actuators and throttle were used by the safety pilot and the control system to influence the system (inducing moments and forces). Section 2.1.2.2 describes the associated conventions and effects of the aileron, elevator and rudder on the UAV.
- Aerodynamic coefficient changes: As the aircraft model was changed due to the damage being introduced, the aerodynamic coefficients of the aircraft changed as well. The coefficient changes are discussed in Section 2.4. Discrete damage cases were investigated and interpolation was used for the cases in between. These values are fed into the extended force and moment equations of the aircraft.
- Physical changes: The mass, CG and MoI of the aircraft changed as portions of the tail were removed. Section 2.3.1 discusses how these changes as well as their overall effect on the aircraft and its dynamics were taken into account.
- Asymmetric equations of motion: The EoM of the aircraft needed to be adapted to model the affect of the asymmetry in the aircraft body resulting from the partial tail loss. Section 2.3 discusses these changes and their implementation.
- Forces and moments: These are all the forces and moments acting on the body of the aircraft.

The points above model the effects of the partial stabiliser loss on the dynamics of the aircraft. In general, an aircraft is not designed in an asymmetric configuration. As a result, the symmetric aircraft model is discussed first and then extended for the asymmetric aircraft model to represent the effects of the tail damage. The extended asymmetric aircraft model takes the shift in CG, change in aerodynamic coefficients and the change in mass and MoI due to the partial stabiliser loss into account.

2.2 Symmetric Flight Dynamics

This section covers the flight dynamics of the healthy symmetric aircraft. The EoM and force and moment equations are discussed in this section. This provides the basis from which the extended flight dynamics of the asymmetric aircraft model will be derived.

2.2.1 Standard Six Degrees of Freedom (6DoF)

An aircraft can be well modelled as a 6DoF rigid body. The six degrees of freedom refer to the three translational and three rotational degrees of freedom. A rigid body means that each mass position of the aircraft remains fixed relative to the body axis at all times. Large aircraft typically display structural flexibility, but these modes of motion are often not in the bandwidth of conventional controllers. In the case of this project, the airspeed was low enough that the structural flexibility can be neglected. The 6DoF model will be used as the basis for the control system design.

2.2.1.1 Kinetics

The kinetics of aircraft is a branch of the mechanics that relate the forces and moments acting on an object to its kinematic state (i.e. position, velocity and acceleration). This relationship can be modelled using Newton's laws of motion for a 6DoF rigid body. The form of the kinetic equations depends on the axis system in which they are used. The equations of motion where all the vectors are coordinated in body axes are used as

$$X = m(\dot{U} - VR + WQ) \tag{2.2.1}$$
$$Y = m(\dot{V} + UR - WP) \tag{2.2.2}$$
$$Z = m(\dot{W} - UQ + VP) \tag{2.2.3}$$
$$L = \dot{P}I_{xx} + QR(I_{zz} - I_{yy}) \tag{2.2.4}$$
$$M = \dot{Q}I_{yy} + PR(I_{xx} - I_{zz}) \tag{2.2.5}$$
$$N = \dot{R}I_{zz} + PQ(I_{yy} - I_{zz}) \tag{2.2.6}$$

where m is the aircraft mass and I_{xx}, I_{yy} and I_{zz} are the principle MoI about the respective body axes. A full derivation of equations 2.2.1 to 2.2.6 can be found in Chapter 1 of *Automatic control of aircraft and missiles* [14]. These equations however make use of the following two assumptions to simplify the calculation:

- the aircraft is symmetric about its xz-plane, which implies that the moments of inertia I_{xy} and I_{yz} are exactly zero; and
- the inertia I_{xz} is negligibly small (which is often the case in conventional aircraft).

These assumptions are valid for most conventional aircraft, and are also valid for the UAV used in this project.

The kinetic equations relate the forces and moments acting on an aircraft to the time rate of change of the velocity and angular rates, and allow the translational and angular velocities to be propagated over time.

2.2.1.2 Kinematics

The kinematics equations describe the relationship between the various motion variables (translational velocity, angular velocity and attitude) without being concerned with the forces and moments that cause the motion. Some of these relationships were discussed in Section 2.1.2.1 and are expanded upon for clarity in this section.

N, E and D are the coordinates of the position vector in the inertial axis system. ϕ, θ and ψ are the Euler 3-2-1 attitude parameters that describe the attitude of the body axis system relative to the inertial axis system.

Euler 3-2-1

Euler angles are used to parametrise the attitude of an aircraft due to their simplicity and the fact that they are intuitive to work with. One disadvantage of Euler angles is that they always contain a singularity in the equations for the attitude dynamics. This singularity in the Euler 3-2-1 convention occurs at $\theta = \pm 90°$. During conventional flight the aircraft pitch angle is significantly smaller than this limitation. This project does not require extreme pitch angles which validates the use of the Euler 3-2-1 convention.

The Euler 3-2-1 convention uses three angles and a predefined order of rotation to describe the attitude of the body axis system with respect to the inertial axis system. As can be seen in Figure 2.6, this rotation starts with both the axis systems aligned, and then moves the body axis through the following set of rotations:

- yaw the body axis system positively through the heading angle ψ;
- pitch the body axis system positively through the pitch angle θ; and
- roll the body axis system positively through the roll angle ϕ.

2.2.1.3 Attitude Dynamics

Now that the Euler attitude parameters have been defined, the time rate of change of these parameters can be considered. The rates of change of the Euler angles are related to the body angular rates (P, Q, R) as:

$$\begin{bmatrix} \dot{\phi} \\ \dot{\theta} \\ \dot{\psi} \end{bmatrix} = \begin{bmatrix} 1 & \sin\phi\tan\theta & \cos\phi\tan\theta \\ 0 & \cos\phi & -\sin\theta \\ 0 & \sin\phi\sec\theta & \cos\phi\sec\theta \end{bmatrix} \begin{bmatrix} P \\ Q \\ R \end{bmatrix} \qquad where|\theta| \neq \frac{\pi}{2} \tag{2.2.7}$$

The full derivation of this equation can be found in [15].

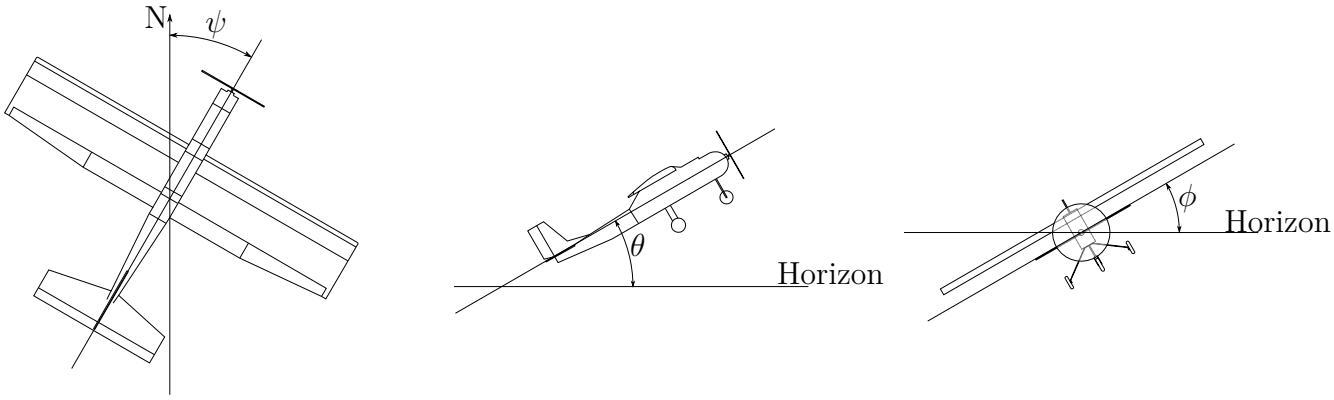

(a) Pitch angle (b) Roll angle (c) Yaw angle

Figure 2.6: Basic illustration of attitude angles

The Euler rates are a function of both the current Euler attitude and the body angular rates. This equation shows the singularity that occurs when the pitch angle is $\pm 90°$. At that angle, there is ambiguity between the roll and pitch angles, resulting in a mathematical singularity. This is not a concern as, during conventional flight, the pitch angle is far from $\pm 90°$ at all times. While the damaged aircraft configuration itself is unconventional, the flight behaviour will still be that of straight and level flight, with turns for waypoint navigation. This prevents the pitch angle of the aircraft reaching $\pm 90°$.

2.2.1.4 Position Dynamics

The next step is to define the position dynamics of the aircraft, i.e. how the north, east and down states change over time as a result of the velocity of the aircraft. The kinematic relationship between position and velocity, with both vectors coordinated in the inertial axis system is represented by the following equation

$$\begin{bmatrix} \dot{N} \\ \dot{E} \\ \dot{D} \end{bmatrix} = \begin{bmatrix} V_N \\ V_E \\ V_D \end{bmatrix} \tag{2.2.8}$$

where V_N, V_E and V_D are the north, east and down velocities respectively. The kinetics equations have been expressed in terms of the body axis velocity vectors (U, V, W). It is therefore necessary to relate the coordinates of a vector expressed in the body axis system to the coordinates of the same vector in the inertial axis system. The transformation matrix that performs this transformation shown in equation 2.2.15. Figure 2.7 shows a single-axis rotation that was used as the basis for these equations.

Vector $\boldsymbol{V}$ is given in the original axis system.

$$\boldsymbol{V}_0 = \begin{bmatrix} x_0 \\ y_0 \\ z_0 \end{bmatrix} \tag{2.2.9}$$

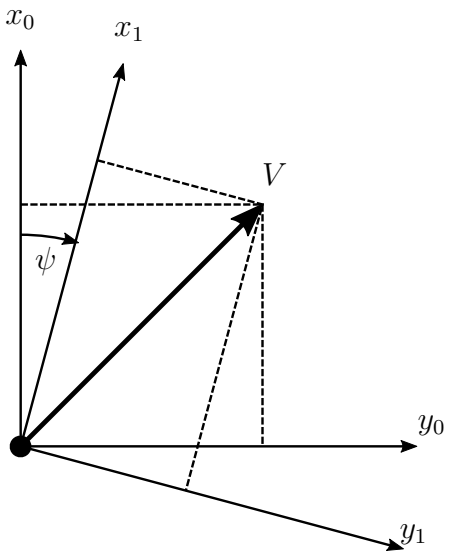

Figure 2.7: Single axis rotation

$\boldsymbol{V}$ is first rotated through the yaw angle:

$$\begin{bmatrix} x_1 \\ y_1 \\ z_1 \end{bmatrix} = \begin{bmatrix} \cos\psi & \sin\psi & 0 \\ -\sin\psi & \cos\psi & 0 \\ 0 & 0 & 1 \end{bmatrix} \begin{bmatrix} x_0 \\ y_0 \\ z_0 \end{bmatrix} \tag{2.2.10}$$

The resultant vector is then rotated through the pitch angle:

$$\begin{bmatrix} x_2 \\ y_2 \\ z_2 \end{bmatrix} = \begin{bmatrix} \cos\theta & 0 & -\sin\theta \\ 0 & 1 & 0 \\ \sin\theta & 0 & \cos\theta \end{bmatrix} \begin{bmatrix} x_1 \\ y_1 \\ z_1 \end{bmatrix} \tag{2.2.11}$$

Finally the resultant vector is rotated once more around the roll angle to provide the final transformation matrix:

$$\begin{bmatrix} x_3 \\ y_3 \\ z_3 \end{bmatrix} = \begin{bmatrix} 1 & 0 & 0 \\ 0 & \cos\phi & \sin\phi \\ 0 & -\sin\phi & \cos\phi \end{bmatrix} \begin{bmatrix} x_2 \\ y_2 \\ z_2 \end{bmatrix} \tag{2.2.12}$$

These equations can be substituted into one another to relate the coordinates of vector $\boldsymbol{V}$ in the original axis system to the coordinates of the same vector in the system that has been yawed, pitched and rolled. The resulting equation is:

$$\begin{bmatrix} x_3 \\ y_3 \\ z_3 \end{bmatrix} = \begin{bmatrix} 1 & 0 & 0 \\ 0 & \cos\phi & \sin\phi \\ 0 & -\sin\phi & \cos\phi \end{bmatrix} \begin{bmatrix} \cos\theta & 0 & -\sin\theta \\ 0 & 1 & 0 \\ \sin\theta & 0 & \cos\theta \end{bmatrix} \begin{bmatrix} \cos\psi & \sin\psi & 0 \\ -\sin\psi & \cos\psi & 0 \\ 0 & 0 & 1 \end{bmatrix} \begin{bmatrix} x_0 \\ y_0 \\ z_0 \end{bmatrix} \tag{2.2.13}$$

Equation 2.2.13 can now be used to convert from inertial coordinates to body coordinates. The transformation matrix shown in equation 2.2.13 performs this conversion and is referred to as

the DCM as shown in equation 2.1.1.

For the position dynamics, a transformation is needed that allows the conversion of the body coordinates of a velocity vector to the inertial coordinate system. The inverse of the DCM in equation 2.1.1 can be used to achieve this transformation. It can be shown that the DCM is orthogonal, so the inverse is simply the transpose of the DCM matrix.

$$DCM_{B\to I} = \begin{bmatrix} C_\psi C_\theta & C_\psi S_\theta S_\phi - S_\psi C_\phi & C_\psi S_\theta C_\phi + S_\psi S_\phi \\ S_\psi C_\theta & S_\psi S_\theta S_\phi + C_\psi C_\phi & S_\psi S_\theta C_\phi + C_\psi C_\phi \\ -S_\theta & C_\theta S_\phi & C_\theta C_\phi \end{bmatrix} \tag{2.2.14}$$

$$\text{where } C_{(\cdot)} = \cos(\cdot), S_{(\cdot)} = \sin(\cdot) \tag{2.2.15}$$

2.2.2 Forces and Moments

Now that the 6DoF EoM have been defined, the forces and moments that acted on the aircraft as a function of the current state could be determined. Three categories of forces and moments are identified: aerodynamic, thrust and gravitational.

The force and moment coordinates defined in section 2.2.1.1 can be expanded as:

$$X = X_A + X_T + X_G \tag{2.2.16}$$

$$Y = Y_A + Y_T + Y_G \tag{2.2.17}$$

$$Z = Z_A + Z_T + Z_G \tag{2.2.18}$$

$$L = L_A + L_T + L_G \tag{2.2.19}$$

$$M = M_A + M_T + M_G \tag{2.2.20}$$

$$N = N_A + N_T + N_G \tag{2.2.21}$$

The subscripts A, T and G denote abbreviations for aerodynamic, thrust and gravitational components respectively. The subsections below will provide discussions of each of the categories in detail.

2.2.2.1 Aerodynamic

Aerodynamic forces and moments are the most complex to model, and introduce most of the uncertainty to the aircraft model. The Bernoulli equation and the continuity principle for incompressible fluids can be used to show (i.e. subsonic flight) that aerodynamic forces and moments are proportional to the dynamic pressure experienced by the aircraft [16]. This dynamic pressure is annotated as $\overline{q}$ and is defined as:

$$\overline{q} = \frac{1}{2}\rho \overline{V}^2, \tag{2.2.22}$$

where ρ is the air density.

The aerodynamic force and moment equations can be expanded as

$$X_A = \overline{q}SC_X \tag{2.2.23}$$
$$Y_A = \overline{q}SC_Y \tag{2.2.24}$$
$$Z_A = \overline{q}SC_Z \tag{2.2.25}$$
$$L_A = \overline{q}SbC_l \tag{2.2.26}$$
$$M_A = \overline{q}S\overline{c}C_m \tag{2.2.27}$$
$$N_A = \overline{q}SbC_n \tag{2.2.28}$$

where S is the wing area, b is the wing span, $\overline{c}$ is the mean aerodynamic chord and $C_{(\cdot)}$ refers to the non-dimensional aerodynamic force and moment coefficients. These non-dimensional coefficients describe the aerodynamic properties of the aircraft under certain operating conditions and are largely independent of the scale and flying speed of the aircraft (these are taken into account in the dynamic pressure). These coefficients are normally modelled in the wind axis system and it is assumed that the sideslip angle is zero. The axial and normal forces can be expanded to get

$$C_X = -C_D \cos\alpha + C_L \sin\alpha \tag{2.2.29}$$
$$C_Z = -C_L \cos\alpha - C_D \sin\alpha, \tag{2.2.30}$$

where C_D and C_L are the drag and lift coefficients respectively. The remaining coefficients could be transformed in a similar manner; however, the angle of attack is typically very small, so it was assumed that the wind and body axis systems coincided, and the transformation would have added an unnecessary complication. Expanding the non-dimensional coefficients results in the following equations:

$$C_D = C_{D_0} + \frac{C_L^2}{\pi A e} \tag{2.2.31}$$
$$C_L = C_{L_0} + C_{L_\alpha}\alpha + \frac{\overline{c}}{2\overline{V}}C_{L_Q}Q + C_{L_{\delta_E}}\delta_E \tag{2.2.32}$$
$$C_Y = C_{Y_\beta}\beta + \frac{b}{2\overline{V}}C_{Y_P}P + \frac{b}{2\overline{V}}C_{Y_R}R + C_{Y_{\delta_A}}\delta_A + C_{Y_{\delta_R}}\delta_R \tag{2.2.33}$$
$$C_l = C_{l_\beta}\beta + \frac{b}{2\overline{V}}C_{l_P}P + \frac{b}{2\overline{V}}C_{l_R}R + C_{l_{\delta_A}}\delta_A + C_{l_{\delta_R}}\delta_R \tag{2.2.34}$$
$$C_m = C_{m_0} + C_{m_\alpha}\alpha + \frac{\overline{c}}{2\overline{V}}C_{m_Q}Q + C_{m_{\delta_E}}\delta_E \tag{2.2.35}$$
$$C_n = C_{n_\beta}\beta + \frac{b}{2\overline{V}}C_{n_P}P + \frac{b}{2\overline{V}}C_{n_R}R + C_{n_{\delta_A}}\delta_A + C_{n_{\delta_R}}\delta_R \tag{2.2.36}$$

In these equations, C_{D_0}, C_{L_0} and C_{m_0} are the parasitic drag coefficient, static lift and pitching moments coefficients respectively. A is the aspect ratio of the wing, and e is the Oswald efficiency factor. The aerodynamic coefficients are in their non-dimensional form and referenced

in the wind axis system. As an example

$$C_{L_\alpha} = \frac{\partial C_L}{\partial \alpha'} \qquad (\ \alpha' = n\alpha \text{ where } n \text{ is the normalising coefficient of } \alpha) \tag{2.2.37}$$

is the non-dimensional stability derivative that describes the lift force due to the angle of attack of the aircraft. The normalising coefficients for the incidence angles and the control deflections angles is 1, while for the pitch rate it is $\overline{c}/2\overline{V}$ and for the roll and yaw rates it is $b/2\overline{V}$.

Determining aerodynamic coefficients

Various analytical and empirical techniques are used to calculate these coefficients (finite element modelling, vortex lattice techniques, mathematical modelling etc.). The analytic techniques are usually not very accurate but provide insight into how the physical structure and changes affect the coefficients. The empirical techniques make use of experimental results to determine the coefficient values. The empirical techniques can be very accurate, but are very specific to the airframe used in the experiment. Empirical techniques also provides less insight into the effects of the physical structure of the aircraft.

In practice, the experimental technique is often used for the calculation of the aerodynamic coefficients of the aircraft. The experimental techniques often require a wind tunnel and/or practical flight tests to determine these coefficients. This process is however a lengthy and costly one, making it unattractive.

Software packages are available that allow the user to implement numeric methods to calculate the aerodynamic coefficients. These numerical methods include vortex lattice codes, computational fluid dynamics, etc. The program that was used to determine the coefficients for this project was Athena Vortex Lattice (AVL). The coefficient notation consists of a double subscript. The first subscript is the moment or force represented by this coefficient, the second subscript indicates the cause of this force or moment as described in equation 2.2.37.

2.2.2.2 Thrust

There are various complex propulsion models available for the different types of aircraft engines. The UAV used in this project had an electric motor that could be represented with a first-order lag model. This model adequately captures the significantly band-limited nature of most propulsion sources

$$\dot{T} = -\frac{1}{\tau}T + \frac{1}{\tau}T_c, \tag{2.2.38}$$

where T is the thrust magnitude, T_c the thrust command, and τ the engine lag time constant. It was assumed that the thrust vector of the aircraft acted in the body x-axis, which resulted

in the following thrust model:

$$X_T = T \tag{2.2.39}$$
$$Y_T = Z_T = 0 \tag{2.2.40}$$
$$L_T = M_T = N_T = 0 \tag{2.2.41}$$

2.2.2.3 Gravitational

As discussed in Section 2.1.1, it was assumed that a flat earth NED axis system was used. The gravitational force vector was modelled as a force proportional to the mass of the aircraft pointing in the down direction. In the inertial axis system, the gravitational force vector was expressed as:

$$\mathbf{F_{G_I}} = \begin{bmatrix} 0 \\ 0 \\ mg \end{bmatrix} \tag{2.2.42}$$

This coordinate vector could be transformed to the body axis system using the DCM from equation 2.1.1. The result of this transformation is:

$$\begin{bmatrix} X_G \\ Y_G \\ Z_G \end{bmatrix} = \begin{bmatrix} -\sin\Theta \\ \cos\Theta\sin\Phi \\ \cos\Theta\cos\Phi \end{bmatrix} mg \tag{2.2.43}$$

Finally, the uniform gravitational field resulted in the CG and centre of mass coinciding. As a result, the gravitational force produced no moments on the aircraft.

$$L_G = M_G = N_G = 0 \tag{2.2.44}$$

A block diagram representation of the flight mechanics model for the healthy, symmetric aircraft is shown in Figure 2.8.

Now that the 6DoF EoM and forces and moment equations for the healthy symmetric aircraft have been defined, the extended equations for the damaged asymmetric aircraft model can be discussed.

2.3 Extended Aircraft Flight Mechanics Model

The previous section presented the flight mechanics modelling based on the standard symmetric aircraft assumption. However, for this project a flight mechanics model for an aircraft with partial horizontal and vertical stabiliser loss was required. The partial horizontal stabiliser resulted in the symmetric aircraft model assumption being invalid and required that the flight dynamics be extended to account for asymmetry. The partial vertical stabiliser had no influence

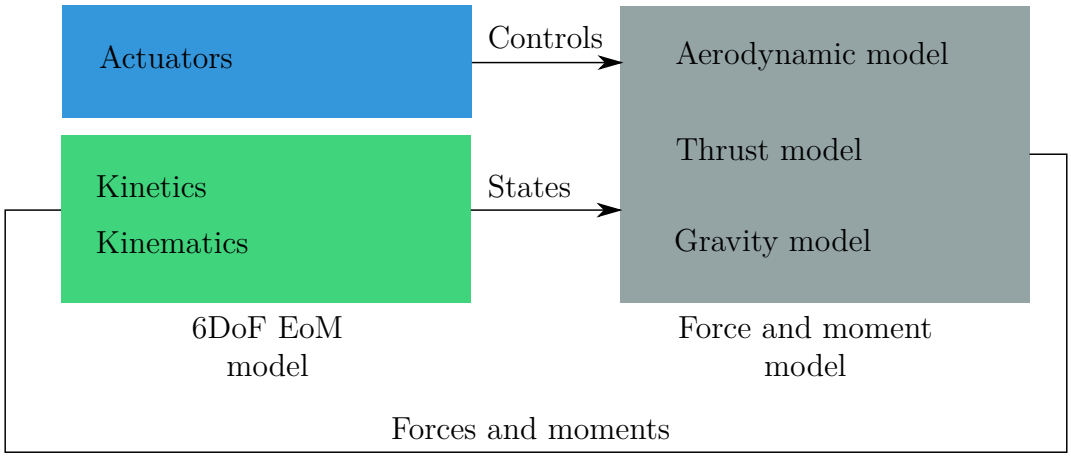

Figure 2.8: Standard aircraft model

on the symmetry of the aircraft. Both partial horizontal and vertical stabiliser loss affected the mass, the CG location, the MoI of the aircraft and most importantly, it affected the aerodynamic stability and control derivatives.

This section looks at the derivation of the 6DoF model from basic principles, without the assumption of aircraft symmetry. This section also reflects how the model was extended to accommodate an instantaneous CG and MoI change. The effects of the partial stabiliser loss were examined in terms of their effect on the aerodynamic coefficients, mass, MoI and CG location.

2.3.1 Effect of Partial Stabiliser Loss

This section reports on the technique of Bacon to take into account the effects of an instantaneous shift in CG and get the resultant change of MoI [9]. When a portion of the tail is lost, a portion of the mass of the UAV is lost along with it. The loss of mass also affects the CG and MoI of the UAV. This section discusses how to represent this change. Before the loss of mass, change in the CG and change in the moment of inertia can be described, it is important to discuss the mathematics of the implementation of this change.

2.3.2 Asymmetric Six Degrees of Freedom Model

It was stated in Section 2.2 that a 6DoF model comprises kinetics and kinematics. The kinetics can be described using Newton's second law. The linear and rotational movement is presented in Sections 2.3.2.1 and 2.3.2.2. The kinematics of the aircraft did not change from the symmetric model, so the asymmetric kinematics part will be combined with the existing kinematics model in Section 2.2.1.2.

This section refers to Figure 2.9, which shows a rigid body and a fixed inertial reference frame. The X-Y-Z reference frame is fixed inertially at point O and the x-y-z reference frame is attached to the body at an arbitrary point A. The body is free to move, and has an instantaneous angular rate of $\boldsymbol{\omega}$ with respect to X-Y-Z. The particle of mass of the body is

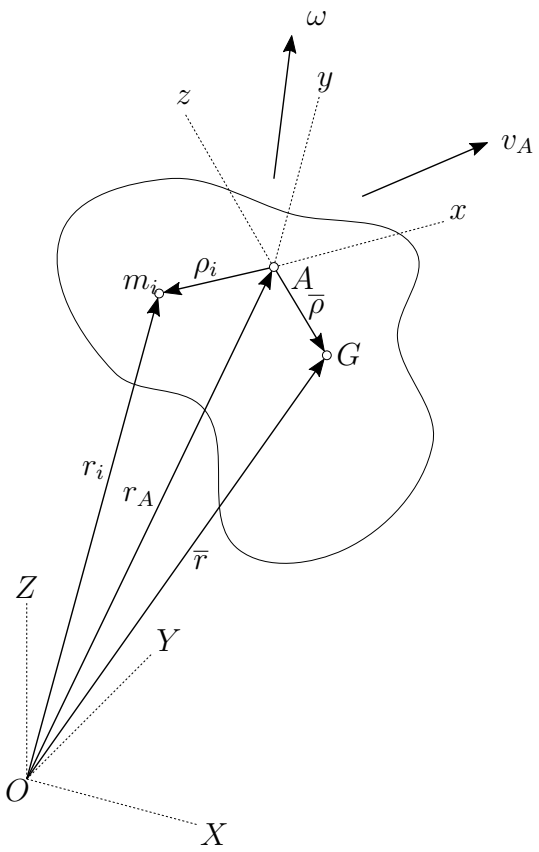

Figure 2.9: Arbitrary body referenced in inertial and body-centric frames

denoted as m_i and fixed in the inertial reference frame as

$$\boldsymbol{r}_i = \boldsymbol{r}_A + \boldsymbol{\rho}_i \tag{2.3.1}$$

where $\boldsymbol{r}_A$ is the position of point A with respect to O, and $\boldsymbol{\rho}_i$ is the position of m_i with respect to A. G is defined as the CG located at $\overline{\boldsymbol{\rho}}$ from A and $\boldsymbol{r}$ from O.

The full derivation for the asymmetric force and moment equations can be found in appendix A. The resultant equations and their implementation is briefly presented in the following subsections.

2.3.2.1 Force Equations

From Appendix A the force equations for the asymmetric aircraft model are defined as

$$\sum \boldsymbol{F}_x = m(\dot{U}_A + QW_A - RV_A - (Q^2 + R^2)\Delta x + (QP - \dot{R})\Delta y + (RP + \dot{Q})\Delta z \tag{2.3.2}$$

$$\sum \boldsymbol{F}_y = m(\dot{V}_A + RU_A - PW_A + (PQ + \dot{R})\Delta x - (P^2 + R^2)\Delta y + (QR - \dot{P})\Delta z \tag{2.3.3}$$

$$\sum \boldsymbol{F}_z = m(\dot{W}_A + PV_A - QU_A + (PR - \dot{Q})\Delta x + (QR + \dot{P})\Delta y + (P^2 + Q^2)\Delta z \tag{2.3.4}$$

Equations 2.3.2 to 2.3.4 allow the CG location to be moved from its original location. It is also possible to apply the assumed CG of the healthy aircraft at point A (i.e. $\overline{\boldsymbol{\rho}} = 0$) to equations 2.3.2 to 2.3.4 which are then reduced to those defined for the symmetric case in equations 2.2.1 to 2.2.3. The resulting forces of the extended equations still allow for the simulation of the

aircraft in its normal symmetric configuration as well as the partial stabiliser configuration.

2.3.2.2 Moment Equations

From Appendix A the moment equations for the asymmetric aircraft model are defined as

$$\begin{aligned}\sum \boldsymbol{L} =& I_{xx}\dot{P} - I_{xy}\dot{Q} - I_{xz}\dot{R} + I_{xy}PR - I_{xz}PQ + (I_{zz} - I_{yy})QR + (R^2 - Q^2)I_{yz} \\ &+ m((PV_A - QU_A + \dot{W}_A)\Delta y + (PW_A - RU_A - \dot{(V)}_A)\Delta z) \qquad (2.3.5)\\ \sum \boldsymbol{M} =& - I_{xy}\dot{P} + I_{yy}\dot{Q} - I_{yz}\dot{R} + I_{yz}PQ - I_{xy}QR + (I_{xx} - I_{zz})PR + (P^2 - R^2)I_{xz} \\ &+ m((QU_A - PV_A - \dot{W}_A)\Delta x + QW_A - RV_A + \dot{U}_A)\Delta z) \qquad (2.3.6)\\ \sum \boldsymbol{N} =& - I_{xz}\dot{P} + I_{yz}\dot{Q} + I_{zz}\dot{R} + I_{xz}QR - I_{yz}PR + (I_{yy} - I_{xx})PQ + (Q^2 - P^2)I_{xy} \\ &+ m((RU_A - PW_A + \dot{V}_A)\Delta x + (RV_A - QW_A - \dot{U}_A)\Delta y) \qquad (2.3.7)\end{aligned}$$

These equations contain the coupling of both angular and translational acceleration due to the offset of the centre of mass. Additionally if it is assumed that the CG has not shifted and the body is still symmetric in its xz-axis of the body reference frame, the non-diagonal MoI terms all equal zero (i.e. $I_{xy} = I_{xz} = Y_{yz} = 0$) and can be removed. This reduces equations 2.3.5 to 2.3.7 to equations 2.2.4 to 2.2.6. This allows the use of the extended equations for the healthy symmetric state, as well as the partial loss and CG shifted state of the aircraft.

2.3.2.3 Implementation

In the previous sections, the equations of motion were developed with reference to an arbitrary fixed point on a rigid body with the centre of mass fixed relative to this point. These equations of motion can be used to model the effect of the centre of mass shifting instantaneously to another location. In this project, the centre of mass shifts due to the partial losses of the horizontal and vertical stabilisers. Bacon discussed two possible approaches implementing the centre of mass shift, namely a CM-Centric approach and a non-CM approach [9]. The non-CM approach was used in this project, and is briefly discussed in the rest of this section.

Non-CM Approach

For the use of the equations of motion, the location of the centre of mass with respect to A ($\overline{\boldsymbol{\rho}}$) is required. From [9], equations 2.3.2 to 2.3.4 and 2.3.5 to 2.3.7 were used and can be expressed as

$$\begin{bmatrix}\dot{\boldsymbol{v}}_A \\ \dot{\boldsymbol{\omega}}\end{bmatrix} = \begin{bmatrix}m\boldsymbol{I}_3 & -\boldsymbol{D}_x \\ \boldsymbol{D}_x & \boldsymbol{I}\end{bmatrix}^{-1} \left[\begin{bmatrix}\sum \boldsymbol{F} \\ \sum \boldsymbol{M}_A\end{bmatrix} - \begin{bmatrix}m\boldsymbol{\Omega}_x & -\boldsymbol{\Omega}_x\boldsymbol{D}_x \\ \boldsymbol{\Omega}_x\boldsymbol{D}_x & \boldsymbol{\Omega}_x\boldsymbol{I} - \boldsymbol{V}_x\boldsymbol{D}_x\end{bmatrix}\begin{bmatrix}\boldsymbol{v}_A \\ \boldsymbol{\omega}\end{bmatrix}\right] \qquad (2.3.8)$$

where

$$\boldsymbol{D}_x = \begin{bmatrix} 0 & -m\Delta z & m\Delta y \\ m\Delta z & 0 & -m\Delta x \\ -m\Delta y & m\Delta x & 0 \end{bmatrix}, \boldsymbol{\Omega}_x = \begin{bmatrix} 0 & -R & Q \\ R & 0 & -P \\ -Q & P & 0 \end{bmatrix}$$
$$\boldsymbol{V}_x = \begin{bmatrix} 0 & -W_A & V_A \\ W_A & 0 & -U_A \\ -V_A & U_A & 0 \end{bmatrix}, \boldsymbol{I} = \begin{bmatrix} I_{xx} & -I_{xy} & -I_{xz} \\ -I_{xy} & I_{yy} & -I_{yz} \\ -I_{xz} & -I_{yz} & I_{zz} \end{bmatrix} \quad (2.3.9)$$

These equations were used directly to calculate the forces and moments acting on either the healthy or the damaged aircraft. One issue with the non-CM approach is that of inverting a 6x6 matrix. For this application, it was not a problem as it was only used for modelling and simulation where real-time processing was not vital.

This implementation concludes the kinetic branch of the 6DoF model. This model is highly complicated for the case of a symmetric aircraft, but it allows the simulation of an asymmetric aircraft without invalidating the model due to simplification assumptions. An important aspect of this implementation was that all the forces and moments are still calculated around the original CG of the aircraft. The extra calculations that were required were those of the moment of the shifted CG around point A. The mass displacement matrix (D_x) and inertia matrix (I) accounted for the shift in CG, mass and MoI.

In order to determine the new force and moment equations it was important to determine the new mass, CG and MoI of the damaged aircraft first. The parallel theorem was used and the inertia matrix was adapted by using the mass, CG and MoI of the broken portion. Equations 2.3.10 to 2.3.14 were used to adapt the mass, CG and MoI of the UAV

$$m \rightarrow m_{dac} = m - m_{tip} \quad (2.3.10)$$
$$\overline{\boldsymbol{\rho}} \rightarrow \overline{\boldsymbol{\rho}}_{dac} = (m\overline{\boldsymbol{\rho}} - m_{tip}\overline{\boldsymbol{\rho}}_{tip})/m_{dac} \quad (2.3.11)$$
$$\mathrm{I}_{ij} \rightarrow \mathrm{I}_{ij,dac} = \mathrm{I}_{ij} - \mathrm{I}_{ij,tip} \qquad i,j = x,y,z \quad (2.3.12)$$
$$\mathrm{I}_{ii,tip} = \mathrm{I}_{ii,tip,cm} + m_{tip}(\Delta j_{tip}^2 + \Delta k_{tip}^2) \qquad i,j,k = x,y,z \| i \neq j \& i \neq k \quad (2.3.13)$$
$$\mathrm{I}_{ij,tip} = \mathrm{I}_{ij,tip,cm} + m_{tip}\Delta i_{tip}\Delta j_{tip} \qquad i,j = x,y,z \| i \neq j \quad (2.3.14)$$

where the subscripts *dac* is for the damaged aircraft configuration and *tip* is for the portion of the aircraft that is removed. The subscripts ij correspond to the elements of the moment of inertia matrix.

Equations 2.3.10 to 2.3.14 can take multiple mass, CG and MoI shifts into account by simply repeating the set of equations, or by adding the components of all the removed portions to these equations.

With these equations, it was only necessary to determine the mass, CG and MoI of the tail portions that had been removed. These could be calculated either by using applied mathematics equations or by using a computer-aided design (CAD) program that determines these values based on the material density and the structure of the model.

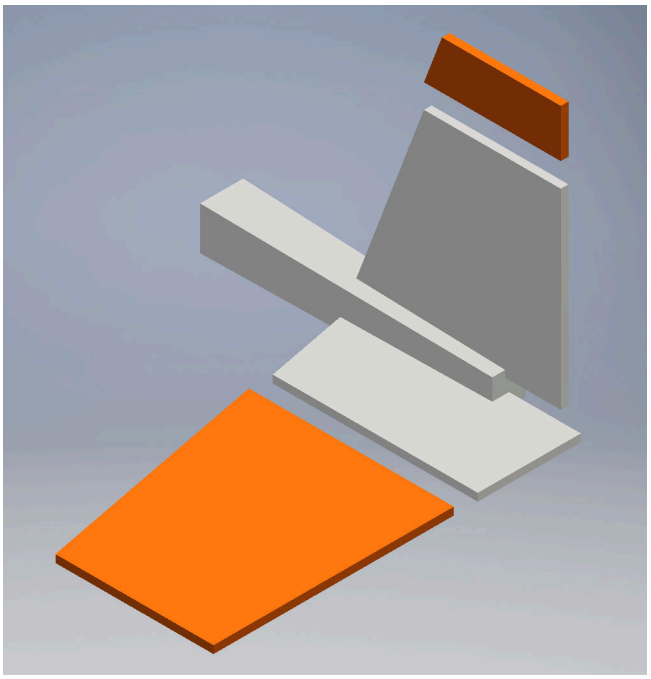

Figure 2.10: Exploded view of stabiliser

For simplicity, the second method was used. The Autodesk Inventor software package was used for this model. This allowed the properties to be changed relatively quickly and determining the new properties automatically. The technique used to determine the mass, CG and MoI was as follows:

- construct the horizontal and vertical stabiliser according to the physical measurements of the aircraft;
- place the necessary surface the exact distance away from the CG location of the UAV in the reference frame;
- section off increments of the surface from the tip towards the body of the aircraft in 10% sections, starting at 90%, which represents 10% span loss of the surface;
- calculate the removed surface CG location to the reference axis;
- calculate the MoI of the tip around its principle axis; and
- calculate the mass of the tip.

Using the technique described above, the full mass, CG and MoI of the removed surfaces could be calculated for the implementation of the instantaneous CG shift. Figure 2.10 shows the CAD model of the stabiliser. The orange sections are the pieces that were removed and modelled separately to allow the implementation of the method discussed above using the nominal cases of 70% horizontal and 20% vertical partial stabiliser. The resultant mass, CG and MoI are shown in Table 2.1.

Table 2.1: Mass, CG and MoI for nominal damage case.

	Mass (kg)	Δ_x (m)	Δ_y (m)	Δ_z (m)	I_{xx} (kgm^2)	I_{xy} (kgm^2)	I_{xz} (kgm^2)	I_{yy} (kgm^2)	I_{yz} (kgm^2)	I_{zz} (kgm^2)
Healthy	7.100	0	0	0	0.7212	0	0	0.5139	0	0.9239
Damaged	6.949	0.0185	0.0035	0.0008	0.7114	−0.0211	−0.0073	0.400	0.0015	0.8075

2.3.3 Gravity

In Section 2.2.2.3, the force and moments due to gravity were discussed. The force equation remained the same for the partial stabiliser case. There was however an introduction of an additional moment equation due to the CG shift. The CG location was defined as $\begin{bmatrix}\Delta x & \Delta y & \Delta z\end{bmatrix}^T$ as the distance away from the origin of the body reference frame point at A. Using this information, the cross product of the CG location vector, together with the gravitational force acting on the body, provided the moment generated by gravity on the UAV. The result of this cross product is:

$$M_{G_B} = \begin{bmatrix} L_G \\ M_G \\ N_G \end{bmatrix} = \begin{bmatrix} \Delta x \\ \Delta y \\ \Delta z \end{bmatrix} \times \begin{bmatrix} -S_\theta mg \\ C_\theta S_\phi mg \\ C_\theta C_\phi mg \end{bmatrix} = \begin{bmatrix} \Delta y C_\theta C_\phi mg - \Delta z C_\theta S_\phi mg \\ -\Delta x C_\theta C_\phi mg - \Delta z S_\theta mg \\ \Delta x C_\theta S_\phi mg + \Delta y S_\theta mg \end{bmatrix} \tag{2.3.15}$$

2.4 The Effects of Partial Stabiliser Loss on Aerodynamic Coefficients

This section focuses on the modelling of the effects of partial stabiliser loss on the aerodynamic forces and moments acting on the UAV. AVL was used for the calculation of the coefficients and a discussion of the results is included in this section.

The following effects are expected due to the partial stabiliser loss.

- the amount of drag should be slightly reduced because of the reduced surface area to make contact with the air;
- very little influence on the side force as the aircraft body is significantly larger than the change in size of the vertical stabiliser;
- slight bias in rolling moment due to the change in centre of gravity location and a slight differential lift on the horizontal stabiliser;
- the pitching moment should decrease due to the shift in centre of gravity as a result of the mass being removed from the tail of the aircraft;
- the effectiveness of the elevator to pitch the UAV should decrease due to the smaller surface area of the horizontal stabiliser and elevator; and

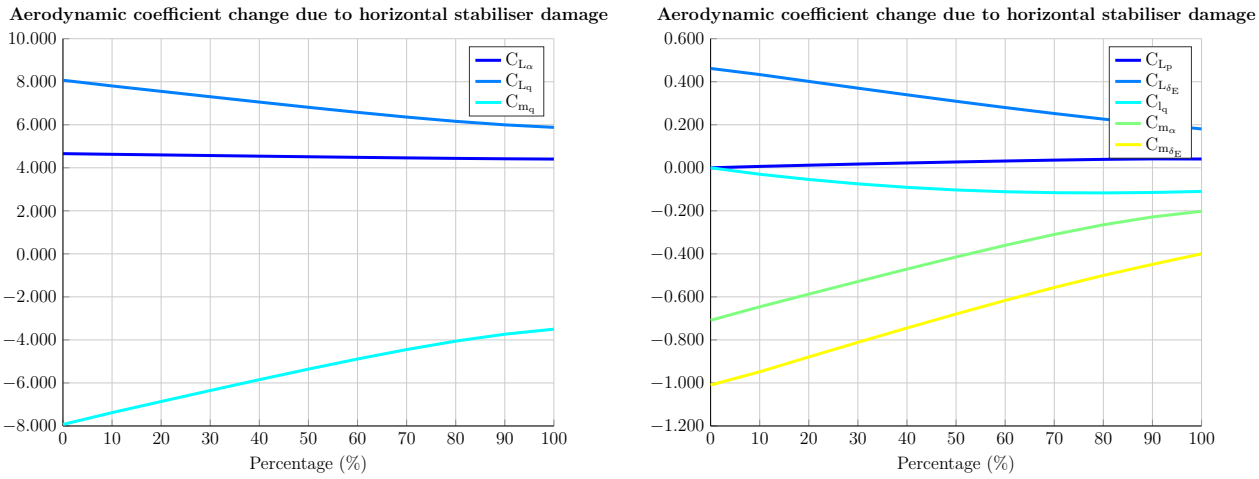

(a) (b)

Figure 2.11: Aerodynamic coefficient change due to partial horizontal stabiliser damage

- the effectiveness of the rudder to yaw the UAV should decrease due to the smaller surface area of the vertical stabiliser and rudder.

2.4.1 Numerical Calculation

This section reports on the use of a software package, AVL, to calculate the effect of the partial stabiliser loss on the aerodynamic coefficients numerically.

AVL provides a platform to investigate the aerodynamics and flight dynamics of rigid aircraft of arbitrary configuration [17]. An extended vortex model is used for the lifting surfaces, and a slender-body model is used for the fuselage. For the flight dynamics analysis, a full linearisation of the aerodynamic model about any defined flight state, along with the specified mass information, was used.

AVL allows the simulation of the fuselage as a slender body, but warns users that this might not be accurate. AVL models the fuselage with a circular circumference. Any other shape should be estimated with a circular area. Including the fuselage in the model introduced complications and inconsistencies in the results of the aerodynamic coefficients and the fuselage was therefore omitted from the model. Previous research by Beeton found that the calculated coefficients showed no major difference whether the fuselage was included or not [7].

The wing, horizontal and vertical stabilisers were modelled in AVL using the physical measurements taken from the dimensions of the UAV. The UAV had been used previously in the ESL with known coefficients. The calculated coefficients compare well to those previously used in the ESL. The percentage stabiliser loss was incremented with fixed intervals and one stabiliser at a time and then combinations of vertical and horizontal stabiliser losses to observe the changes in the coefficients. This also provided insight into the cross-coupling of the partial stabilisers.

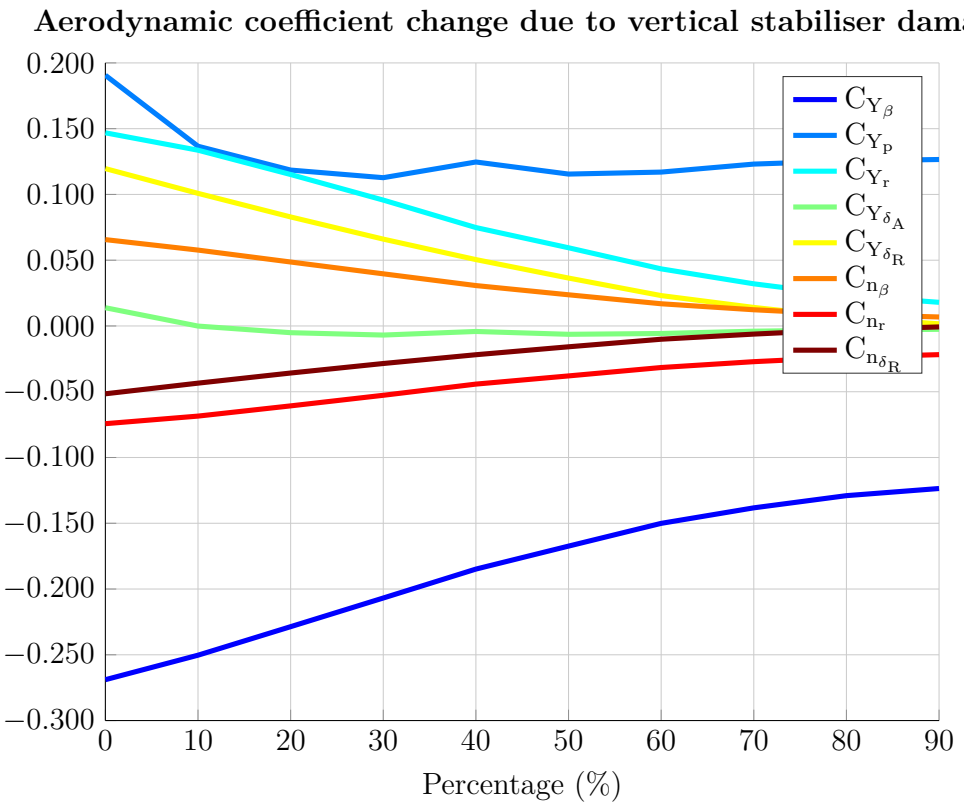

Figure 2.12: Aerodynamic coefficient change due to partial vertical stabiliser damage

2.4.2 Discussion

This section reports on the aerodynamic coefficients and the effects of the partial stabilisers on the UAV. A comparison to the existing coefficients is made and then the effects of the partial losses are discussed. The significant changes are highlighted and investigated in more detail to see whether they agree with the expectation. The coefficients are represented in their non-dimensional form. While this makes it more difficult to interpret, it should be possible to see the effects due to the partial stabiliser loss. Figures 2.11 and 2.12 show the significant coefficient changes due to the inflicted damage.

As portions of the horizontal stabiliser were removed, the lift aerodynamic coefficients as well as the coefficients that affected the pitching behaviour of the aircraft were affected most. There was also a slight effect on the rolling moment coefficient of the aircraft. The reduced effectiveness of the pitching components was expected as there was less horizontal stabiliser surface to induce the necessary moment ($C_{m_{(\cdot)}}$). The horizontal stabiliser also generates lift on the aircraft and as portions of the horizontal stabiliser were removed, the lift generated was also reduced ($C_{L_{(\cdot)}}$). The change in the rolling moment coefficient was due to the fact that there was differential lift on the horizontal stabiliser as well as a lateral shift in CG, which would induce some rolling moment (C_{l_q}). This rolling moment was not significant as the surface area of the missing elevator was small and not designed for lift in comparison to the surface area of the wings of the aircraft, which were designed to generate lift and induce a rolling moment.

As portions of the vertical stabiliser were removed, the side force and yawing aerodynamic

coefficients were affected most. The reduction in the side force coefficients was expected as the surface area of the vertical stabiliser was being reduced, which in effect reduced the surface area on which a side wind could act ($C_{Y_{(\cdot)}}$). The vertical stabiliser is designed to keep the aircraft in line with the oncoming wind. As there was less surface area on the vertical stabiliser, the yawing moment was reduced due to less wind coming into contact with the vertical stabiliser reducing the generated yawing moment ($C_{n_{(\cdot)}}$).

§ 3

Trim

This section presents the trim calculation and analysis of the aircraft in its different damage configurations. The trim condition requires that the aircraft fly in equilibrium (zero force, moment and acceleration values). The aircraft can be trimmed in a number of different equilibrium conditions, for example straight and level flight, constant coordinated turning, etc. The trim conditions provide a working point around which the aircraft dynamics are linearised allowing a stability analysis to be performed and control laws to be designed using linear control theory. It is important to note that, even if a trim setting is found, there might not be sufficient actuator travel available to allow that setting. This allowed a maximum damage case to be determined for this study.

Firstly, the conventions used to define trim for this study are discussed. The fact that the aircraft was asymmetric necessitated that conventions be defined to describe the trim of the aircraft.

Secondly, an analytic trim solution is presented. This technique makes certain approximations about aircraft flight in equilibrium, and calculates the required trim settings to meet these conditions. This analytic trim calculation is performed on both the healthy and damaged aircraft configurations to provide a baseline. The analytic trim technique is expanded for the asymmetric case so that the trim can be more accurately calculated.

Thirdly, a multivariate Newton–Raphson technique was implemented to solve the full asymmetric equations of motion of the aircraft in the different configurations simultaneously. This took the full aerodynamic change, shift in centre of gravity (CG) and change in mass and moment of inertia (MoI) into account and provided a more accurate trim and a point around which the aircraft could be linearised for all the different damage configurations.

3.1 Trim Conventions

A common trim trajectory for an aircraft is that of straight and level flight. For a healthy, symmetric aircraft only the forces and moments in the longitudinal direction are trimmed to produce this trajectory. In the present study, this simplification could be made due to the

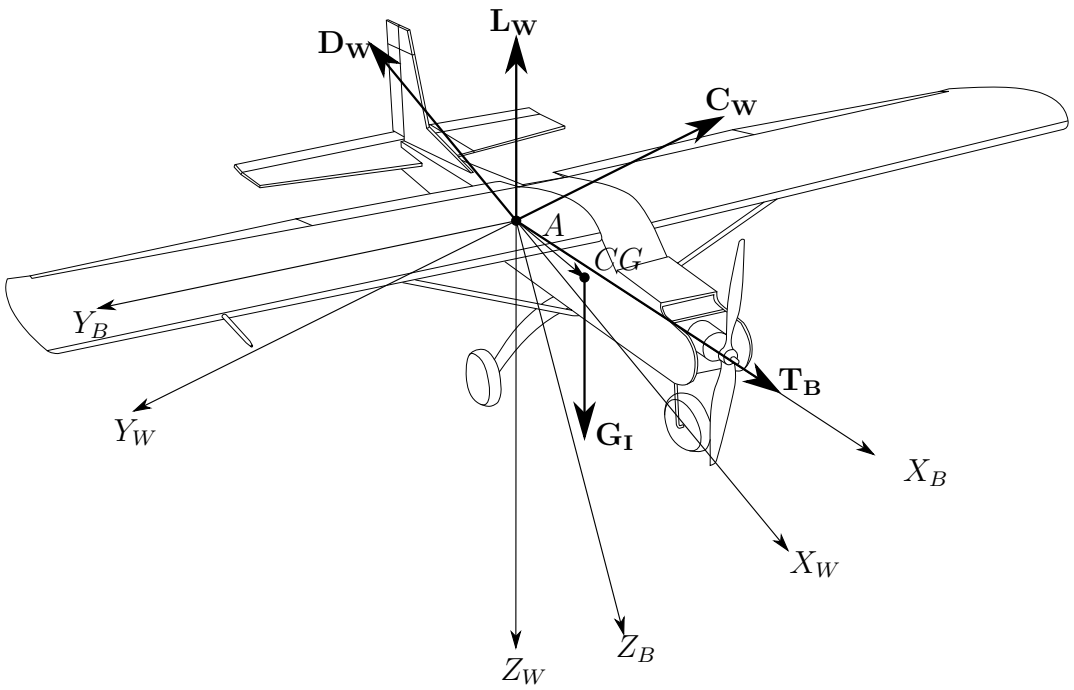

Figure 3.1: Free body diagram of the UAV

assumed symmetry of the aircraft about its xz-plane. In the case of a damaged, asymmetric aircraft the forces and moments have to be trimmed in both the longitudinal and lateral directions. Two approaches to trimming the asymmetric aircraft for straight and level flight are considered

- trimming with a zero sideslip angle and a nonzero roll angle; or
- trimming with a zero roll angle and a nonzero sideslip angle.

For an aircraft in straight flight, the trim condition also requires zero angular rates and a constant airspeed and altitude.

The trim conditions are defined for the forces and moments acting through the CG of the aircraft. When the aircraft is asymmetric due to the partial stabiliser loss, the CG of the aircraft shifts. If this location is still used to determine the trim of the system, both the aerodynamic and thrust forces will induce moments on the aircraft. If point A, specified in section 2.3.2, is used, only gravity will cause an additional moment as discussed in section 2.3.3. Figure 3.1 shows the free body diagram of the aircraft. This figure shows that only $\boldsymbol{G}$ does not act directly on point A and will generate a moment around it.

The trim variables are denoted with a subscript T, e.g. α_T is the angle of attack of the aircraft at trim flight.

An airspeed of $18m.s^{-1}$ and an altitude of $30m$ was used for all the trim calculations.

3.2 Symmetric Trim

To calculate the trim for a symmetric aircraft, straight and level flight is used. This trim state means that the aircraft will stay at a constant altitude and remain at wings level with the

horizon. In the healthy configuration, the aircraft was symmetric about its xz-plane, allowing the assumption that the sum of all the lateral forces and moments acting on the aircraft was zero, allowing these forces and moments to be omitted from the trim calculations. It is common to trim the aircraft at a certain airspeed and at a given altitude. Through specifying the airspeed and altitude of the aircraft in trim flight, the air pressure was fixed. The trim angle of attack was assumed to be the same as the pitch angle (i.e. $\alpha_T = \theta_T$). The dynamic pressure at trim was defined as

$$\overline{q}_T = \frac{1}{2}\rho \overline{V}_T^2 \tag{3.2.1}$$

for the specified trim constraints.

Through setting the airspeed and altitude of the aircraft, the number of unknown longitudinal variables was reduced. For straight and level flight, the pitch rate had to be zero, further reducing the trim problem to that of calculating angle of attack, elevator deflection and thrust $(\alpha, \delta_E, T)_T$. These variables could be solved by using the three trim equations obtained by balancing the forces along the x- and z-axes and the pitching moment around the CG.

Using equations 2.2.16, 2.2.18 and 2.2.20 with the appropriate substitutions and setting the constraints results in the following three equations:

$$(-\overline{q}_T S C_{D_T} \cos\alpha_T + \overline{q}_T S C_{L_T} \sin\alpha_T) + T_T - mg\sin\theta_T = 0 \tag{3.2.2}$$

$$(-\overline{q}_T S C_{L_T} \cos\alpha_T - \overline{q}_T S C_{D_T} \sin\alpha_T) + mg\cos\theta_T = 0 \tag{3.2.3}$$

$$\overline{q}_T S \overline{c} C_{m_T} = 0, \tag{3.2.4}$$

It was possible to make simplifying assumptions to solve the above equations without the use of iterative numerical methods. The two assumptions that were made hold well for trim flight of the aircraft. These assumptions were:

- the trim angle of attack ($\alpha_T = \theta_T$) is small; and
- the lift is an order of magnitude greater than the drag at trim.

This allowed equations 3.2.3 and 3.2.4 to be simplified to:

$$-\overline{q}_T S C_{L_T} + mg = 0 \tag{3.2.5}$$

$$\overline{q}_T S \overline{c} C_{m_T} = 0 \tag{3.2.6}$$

Substituting the pitching moment and lift coefficients from the aerodynamic equations in 2.2.32 and 2.2.35 and rearranging these equations yielded:

$$\begin{bmatrix} C_{L_0} \\ C_{m_0} \end{bmatrix} + \begin{bmatrix} C_{L_\alpha} & C_{L_{\delta_E}} \\ C_{m_\alpha} & C_{m_{\delta_E}} \end{bmatrix} \begin{bmatrix} \alpha_T \\ \delta_{E_T} \end{bmatrix} = \begin{bmatrix} \frac{mg}{\overline{q}_T S} \\ 0 \end{bmatrix} \tag{3.2.7}$$

The subject of equation 3.2.7 was then changed to allow the trim angle of attack and elevator

Table 3.1: Analytic trim calculation — Partial horizontal stabiliser

Hor (Perc)	Thrust (N)	α (°)	δ_E (°)
0%	13.039	6.707	−4.707
10%	13.020	6.709	−4.572
20%	13.016	6.712	−4.482
30%	13.013	6.715	−4.374
40%	13.009	6.718	−4.247
50%	13.004	6.721	−4.098
60%	12.999	6.724	−3.930
70%	12.994	6.728	−3.746
80%	12.987	6.732	−3.565
90%	12.980	6.735	−3.426
100%	12.968	6.737	−3.407

Table 3.2: Analytic trim calculation — Partial vertical stabiliser

Ver (Perc)	Thrust (N)	α (°)	δ_E (°)
0% − 90%	13.039	6.707	−4.707

settings to be solved as:

$$\begin{bmatrix} \alpha_T \\ \delta_{E_T} \end{bmatrix} = \begin{bmatrix} C_{L_\alpha} & C_{L_{\delta_E}} \\ C_{m_\alpha} & C_{m_{\delta_E}} \end{bmatrix}^{-1} \begin{bmatrix} \frac{mg}{\bar{q}_T S} - C_{L_0} \\ -C_{m_0} \end{bmatrix} \tag{3.2.8}$$

The solutions to equation 3.2.8 were then used to allow the trim thrust to be calculated using

$$T_T = \bar{q}_T S C_{D_T} \cos\alpha_T - \bar{q}_T S C_{L_T} \sin\alpha_T + mg \sin\alpha_T \tag{3.2.9}$$

where

$$C_{D_T} = C_{D_0} + \frac{C_{L_T}^2}{\pi A e} \tag{3.2.10}$$

Equations 3.2.8 and 3.2.9 were then used to determine the trim setting for the different damage cases of the UAV.

Tables 3.1 and 3.2 show the trim settings for the different amounts of partial horizontal and vertical stabiliser loss respectively. For the partial horizontal stabiliser loss, the largest change was that of the elevator deflection angle. This larger deflection angle was due to the reduced horizontal stabiliser and elevator size. The larger deflection angle was necessary to provide the required angle of attack to maintain straight and level flight. The trim results for the partial vertical stabiliser did not change as the aircraft remained symmetric and the shift in CG was not taken into account. Tables 3.3 to 3.5 show the residual forces and moments acting on the aircraft for the respective trim conditions. For the healthy aircraft configuration, the only nonzero force acting on the aircraft was in the z-axis. The other forces and moments were

Table 3.3: Analytic trim residual forces and moments — Partial horizontal stabiliser

Hor (Perc)	X (N)	Y (N)	Z (N)	L (Nm)	M (Nm)	N (Nm)
0%	−0.000	0.000	−1.533	−0.000	0.000	0.000
10%	0.048	0.004	−1.943	0.104	−0.353	0.017
20%	0.060	0.009	−2.041	0.107	−0.437	0.020
30%	0.071	0.015	−2.139	0.106	−0.520	0.020
40%	0.084	0.024	−2.247	0.105	−0.610	0.017
50%	0.096	0.037	−2.355	0.100	−0.701	0.009
60%	0.110	0.053	−2.473	0.096	−0.799	−0.002
70%	0.124	0.072	−2.591	0.089	−0.897	−0.017
80%	0.139	0.088	−2.718	0.085	−1.003	−0.032
90%	0.153	0.091	−2.836	0.079	−1.100	−0.037
100%	0.169	0.032	−2.973	0.081	−1.213	0.004

Table 3.4: Analytic trim residual forces and moments — Partial vertical stabiliser

Ver (Perc)	X (N)	Y (N)	Z (N)	L (Nm)	M (Nm)	N (Nm)
0%	−0.000	0.000	−1.533	−0.000	0.000	0.000
10%	0.042	0.000	−1.894	−0.000	−0.150	0.000
20%	0.049	0.000	−1.952	−0.000	−0.364	0.000
30%	0.056	0.000	−2.011	−0.000	−0.413	0.000
40%	0.063	0.000	−2.069	−0.000	−0.461	0.000
50%	0.071	0.000	−2.137	−0.000	−0.517	0.000
60%	0.079	0.000	−2.206	−0.000	−0.573	0.000
70%	0.087	0.000	−2.274	−0.000	−0.628	0.000
80%	0.096	0.000	−2.352	−0.000	−0.690	0.000
90%	0.105	0.000	−2.430	−0.000	−0.752	0.000

zero, indicating that the aircraft would lose altitude, but still fly straight. The damage cases for the partial horizontal stabiliser loss had nonzero forces and moments in all directions, which resulted in the aircraft not maintaining straight and level flight. The partial vertical stabiliser loss case had nonzero longitudinal and zero lateral forces and moments. This indicated straight flight for the partial vertical stabiliser damage cases, but the aircraft was not able to maintain altitude. The nominal damage configuration has forces and moments in all directions resulting in the aircraft not maintaining straight and lever flight.

Figure 3.2 shows the flight paths for the different damage cases reinforcing the observations made from the residual force and moment results. This shows that the aircraft started losing

Table 3.5: Analytic trim residual forces and moments — Nominal damage case

Hor-Ver (Perc)	X (N)	Y (N)	Z (N)	L (Nm)	M (Nm)	N (Nm)
0% − 0%	−0.000	0.000	−1.533	−0.000	0.000	0.000
70% − 20%	0.174	0.044	−3.010	0.088	−1.261	0.005

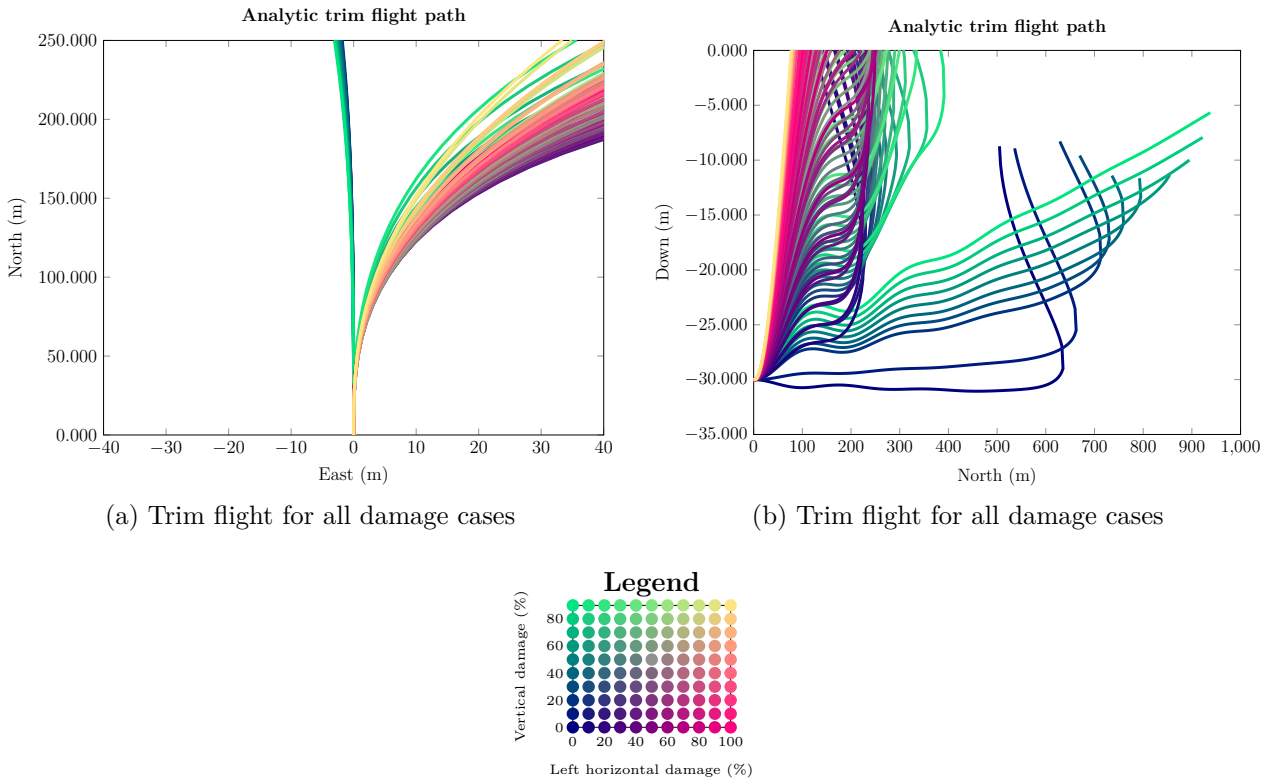

(a) Trim flight for all damage cases

(b) Trim flight for all damage cases

Figure 3.2: Analytic trim flight path

altitude almost immediately for the partial horizontal stabiliser and most of the partial vertical stabiliser scenarios. The trim results for the healthy aircraft configuration is usable. The analytic trim for the different damage configurations had significant residual forces and moments resulting in the aircraft becoming unstable quickly. Consequently, alternative trim techniques were investigated for the asymmetric aircraft configurations and are discussed in the next section.

3.3 Asymmetric Trim

The results in the previous section showed that assuming symmetry for the trim calculation of the asymmetric UAV model resulted in the aircraft not maintaining straight and level flight. This section presents an approach for calculating the trim for the asymmetric aircraft that explicitly takes the asymmetry into account to determine a trim that would allow straight and level flight. First, the analytic trim technique was adapted to take the asymmetry into account, but still contained solutions that resulted in significant residual forces on the aircraft. Next, an iterative Newton–Raphson technique is implemented to iteratively solve the full nonlinear system of equations.

3.3.1 Analytic Trim

The analytic trim calculation for the asymmetric aircraft model accounts for the shift in CG and change in mass and MoI. Certain assumptions were still made to simplify the trim calculation.

The assumption that the drag was an order of magnitude less than the lift was made. The small angle assumption was also used on the attitude angles of the aircraft. The full derivation and trim calculation with their results can be found in Appendix B.

The residual forces and moments for the calculated trims of the damaged aircraft models were significant, and resulted in the aircraft becoming unstable quickly in uncontrolled flight simulations. The Newton–Raphson technique discussed in the next section provides an iterative trim calculating technique that provided a more accurate and usable trim condition.

3.3.2 Newton–Raphson

It was clear from the results of the analytic calculations and simulations (reported on in Appendix B) that the trim settings did not maintain equilibrium flight. To address this problem, an iterative trim-solving technique was used. A multivariate Newton–Raphson method was implemented to determine trim conditions for straight and level flight of the aircraft in both healthy and damaged states.

The Newton–Raphson method uses linearisation to iteratively determine better approximations for the roots of nonlinear real-valued functions.

The method is initialised with an initial guess of the solution (in this case, the trim of the healthy aircraft). The nonlinear function is then approximated by its tangent line and the x-intercept of this tangent line. Ideally this x-intercept will be closer to the actual roots of the function than the initial or previous guess. There is a possibility that the Newton–Raphson technique diverges and a solution cannot be found. In such a case, a different initial guess is used. This technique can be iterated until a certain number of iterations have run (if there is no exact solution), or a specified tolerance has been achieved.

Equations 2.2.16 to 2.2.21 were solved to determine the trim of the aircraft in this manner. In these six equations, there were eight unknowns (i.e. $U = \begin{bmatrix} \overline{V} & \alpha & \beta & \phi & \delta_A & \delta_E & \delta_R & T \end{bmatrix}$). Some of these variables could be constrained based on the chosen approach to trimming the aircraft. Two trim cases were considered in this project, one with zero roll angle and nonzero sideslip angle, and another with zero sideslip angle and a nonzero roll angle. These constraints, along with a fixed airspeed, reduced the number of unknowns from eight to six (U_{red}), allowing the solution of the system of equations to be found. The Newton–Raphson technique was implemented as follows:

A multivariate function for the forces and moments of the aircraft in trim flight is defined as:

$$F = \begin{bmatrix} X & Y & Z & L & M & N \end{bmatrix} = 0 \tag{3.3.1}$$

The derivative of this function is defined as:

$$F' = J = \frac{\partial F}{\partial U_{red}} \tag{3.3.2}$$

An initial guess, X_0, for the root of function F is chosen as the trim of the healthy, symmetric

Table 3.6: Newton–Raphson trim calculation — Partial left horizontal stabiliser

Hor (Perc)	Thrust (N)	α (°)	β (°)	ϕ (°)	δ_A (°)	δ_E (°)	δ_R (°)
0%	13.123	6.563	0.000	−0.000	0.000	−4.606	0.001
10%	13.099	6.568	0.000	−0.012	0.089	−4.906	0.027
20%	13.093	6.571	0.000	−0.019	0.101	−4.962	0.044
30%	13.088	6.575	0.000	−0.024	0.112	−5.023	0.052
40%	13.082	6.578	0.000	−0.029	0.125	−5.107	0.052
50%	13.076	6.582	0.000	−0.033	0.138	−5.207	0.043
60%	13.069	6.586	0.000	−0.036	0.155	−5.349	0.028
70%	13.063	6.589	0.000	−0.038	0.172	−5.534	0.010
80%	13.055	6.593	0.000	−0.038	0.193	−5.811	0.001
90%	13.049	6.597	0.000	−0.037	0.215	−6.197	0.030
100%	13.041	6.599	0.000	−0.032	0.252	−6.882	0.198

aircraft. If the initial guess is close to a solution, a better approximation is determined by:

$$X_1 = X_0 - J^{-1}F \tag{3.3.3}$$

This process is then repeated as

$$X_{n+1} = X_n - J^{-1}F \tag{3.3.4}$$

until a predefined number of iterations have passed, or a sufficiently accurate value is obtained. If the initial guess is not close to a solution, the algorithm will diverge and an incorrect root will be determined.

3.3.2.1 Results

The aircraft trim was calculated for both trim conditions (zero sideslip and nonzero roll angle, and zero roll angle and nonzero sideslip). For the trim results where the sideslip was constrained to zero, there was a very small roll angle. Similarly, the trim results where the roll angle was constrained to zero, there was a very small sideslip angle. As a result, there was no significant difference in the actuator settings for the different trim constraints. The largest difference was a rudder deflection of 0.8° for a damage condition of 100% left horizontal stabiliser and 90% vertical stabiliser loss. The rest of this study used the trim settings for zero sideslip and a nonzero bank angle.

Tables 3.6 to 3.8 show the trim settings for the different damage configuration as well as the nominal damage configuration. These trim conditions are all within the operable range of the actuators.

Table 3.9 shows the residual force and moments of the aircraft, in the healthy and nominal damage configurations, for their respective trim calculations. All the forces and moments acting on the aircraft in the different damage configurations were less than 10^{-14}. This indicated that the trim conditions for the different damage cases were accurate and would provide straight

Table 3.7: Newton–Raphson trim calculation — Partial vertical stabiliser

Ver (Perc)	Thrust (N)	α (°)	β (°)	ϕ (°)	δ_A (°)	δ_E (°)	δ_R (°)
0%	13.123	6.563	0.000	−0.000	0.000	−4.606	0.001
10%	13.101	6.547	0.000	−0.000	0.000	−4.767	0.002
20%	13.098	6.567	0.000	−0.000	0.000	−5.024	0.002
30%	13.095	6.567	0.000	−0.000	0.000	−5.080	0.003
40%	13.091	6.567	0.000	−0.000	−0.000	−5.136	0.003
50%	13.087	6.567	0.000	−0.000	−0.000	−5.200	0.005
60%	13.083	6.568	0.000	−0.000	−0.000	−5.263	0.006
70%	13.079	6.568	0.000	−0.000	−0.000	−5.326	0.012
80%	13.074	6.568	0.000	−0.000	−0.000	−5.398	0.023
90%	13.069	6.568	0.000	−0.000	−0.000	−5.468	0.098

Table 3.8: Newton–Raphson trim calculation — Nominal damage case

Hor - Ver (Perc)	Thrust (N)	α (°)	β (°)	ϕ (°)	δ_A (°)	δ_E (°)	δ_R (°)
0%	13.123	6.563	0.000	−0.000	0.000	−4.606	0.001
70% − 20%	13.038	6.593	0.000	−0.0389	0.215	−6.297	0.181

and level flight.

Figure 3.3 shows the flight path of the aircraft under all the different damage configurations. The aircraft flew very straight and lost negligible amounts of altitude. This corresponds with the residual forces and moments for the different damage configurations. The trim results from the Newton–Raphson resulted in a straighter flight path than the analytic techniques.

Certain trim conditions were found to have rather large actuator deflections. The damage configurations that required more than half the actuator deflection (±7.5°) are listed in Table 3.10. These damage conditions were not feasible for investigation as their trim settings would not allow sufficient actuation range on the control surfaces to execute manoeuvres.

Initially the damage configuration of 70% left horizontal stabiliser and 40% vertical stabiliser loss was chosen for the nominal case. The safety pilot was uncomfortable during the practical flight of this damage configuration (see 7.2.2.1). The nominal case was then chosen as 70% left horizontal stabiliser and 20% vertical stabiliser loss.

The trim results from the Newton–Raphson are used in the next section when reporting on the linearisation and stability analysis of the aircraft. This simplified the aircraft model about the trim settings and allowed for the control systems to be designed by only considering the linear model of the aircraft around this point.

Table 3.9: Newton–Raphson trim residual forces and moments — Nominal damage case

Hor - Ver (Perc)	X (N)	Y (N)	Z (N)	L (Nm)	M (Nm)	N (Nm)
0% − 0%	−8.9E−16	5.4E−20	1.4E−14	5.3E−22	−6.9E−16	−4.2E−21
70% − 20%	−8.9E−16	−1.4E−17	1.4E−14	2.8E−17	2.2E−16	6.9E−18

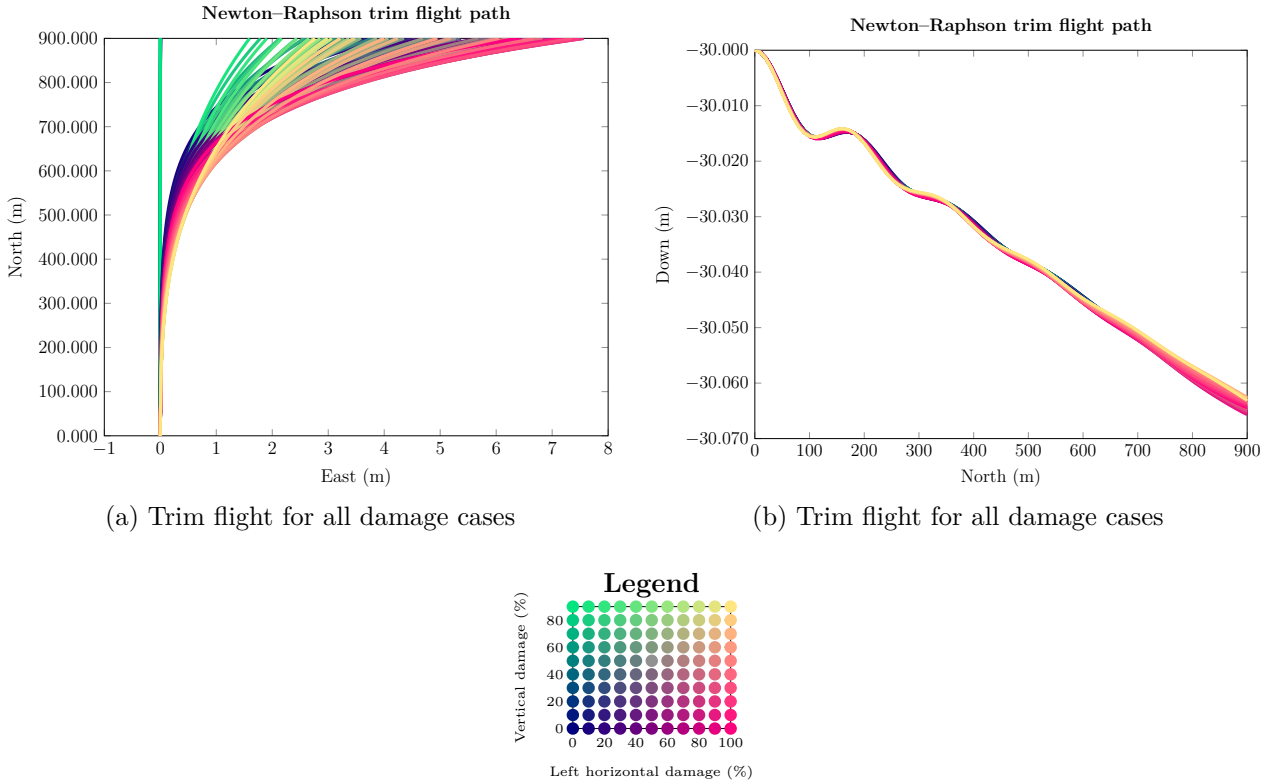

(a) Trim flight for all damage cases

(b) Trim flight for all damage cases

Figure 3.3: Newton–Raphson trim flight path

Table 3.10: Borderline trim conditions

Hor - Ver (Perc)	Thrust (N)	α (°)	β (°)	ϕ (°)	δ_A (°)	δ_E (°)	δ_R (°)
30% – 90%	13.035	6.580	0.000	−0.024	0.147	−6.091	**9.229**
40% – 90%	13.029	6.583	0.000	−0.029	0.173	−6.269	**11.342**
50% – 90%	13.023	6.586	0.000	−0.033	0.200	−6.481	**13.185**
60% – 90%	13.016	6.590	0.000	−0.036	0.231	−6.756	**14.776**
70% – 90%	13.010	6.594	0.000	−0.037	0.262	−7.103	**16.058**
80% – 90%	13.003	6.597	0.000	−0.037	0.298	**−7.575**	**17.102**
90% – 50%	13.013	6.600	0.000	−0.038	0.295	**−7.567**	0.794
90% – 60%	13.009	6.600	0.000	−0.037	0.305	**−7.719**	1.325
90% – 70%	13.005	6.601	0.000	−0.036	0.314	**−7.869**	2.198
90% – 80%	13.001	6.601	0.000	−0.035	0.325	**−8.039**	4.773
90% – 90%	12.996	6.601	0.000	−0.034	0.334	**−8.202**	**18.108**
100% – 20%	13.016	6.602	0.000	−0.034	0.310	**−7.956**	0.463
100% – 30%	13.013	6.602	0.000	−0.034	0.318	**−8.106**	0.612
100% – 40%	13.009	6.602	0.000	−0.034	0.327	**−8.255**	0.806
100% – 50%	13.005	6.603	0.000	−0.033	0.337	**−8.429**	1.155
100% – 60%	13.001	6.603	0.000	−0.032	0.347	**−8.605**	1.819
100% – 70%	12.997	6.603	0.000	−0.032	0.357	**−8.778**	2.901
100% – 80%	12.993	6.603	0.000	−0.031	0.368	**−8.979**	6.069
100% – 90%	12.988	6.603	0.000	−0.030	0.380	**−9.180**	**22.152**

§ 4

Stability Analysis

In this chapter, the aircraft model is linearised about a trim condition and the stability of the natural dynamics is analysed as a function of percentage horizontal and vertical stabiliser losses.

First, the aircraft model is linearised about the trims presented in Chapter 3. This provides a state space model of the aircraft which can be used to investigate the open-loop dynamics of the aircraft.

Next, the open-loop pole plot was determined using the eigenvalues of the linearised state space model allowing the change in modes of the aircraft as a function of the different stabiliser damage percentages to be discussed.

4.1 Linearisation of Aircraft Dynamics

The nonlinear aircraft dynamics are linearised about the trim points calculated in the previous chapter (see 3). The linearised model will allow linear control systems theory to be applied in order to perform a stability analysis of the aircraft open-loop dynamics, and to perform the control system design. The fundamental nonlinear dynamics of the aircraft are obtained from the asymmetric equations of motion (equation 2.3.8) and the attitude kinematics (equation 2.2.7) as shown below. Equation 2.3.8 is restated below for convenience:

$$\begin{bmatrix} \dot{\boldsymbol{v}}_A \\ \dot{\boldsymbol{\omega}} \end{bmatrix} = \begin{bmatrix} m\boldsymbol{I}_3 & -\boldsymbol{D}_x \\ \boldsymbol{D}_x & \boldsymbol{I} \end{bmatrix}^{-1} \left[\begin{bmatrix} \sum \boldsymbol{F} \\ \sum \boldsymbol{M}_A \end{bmatrix} - \begin{bmatrix} m\boldsymbol{\Omega}_x & -\boldsymbol{\Omega}_x \boldsymbol{D}_x \\ \boldsymbol{\Omega}_x \boldsymbol{D}_x & \boldsymbol{\Omega}_x \boldsymbol{I} - \boldsymbol{V}_x \boldsymbol{D}_x \end{bmatrix} \begin{bmatrix} \boldsymbol{v}_A \\ \boldsymbol{\omega} \end{bmatrix} \right]$$

$$\dot{\phi} = P + Q \sin\phi \tan\theta + R \cos\phi \tan\theta \tag{4.1.1}$$

$$\dot{\theta} = Q \cos\phi - R \sin\theta \tag{4.1.2}$$

The dynamics governing the heading and position states ψ, N, E and D were omitted for the linearisation process because they do not couple back into the dynamics and therefore do not form part of the fundamental aircraft dynamics. They are simply the kinematic results of the primary aircraft dynamics. The nonlinear aircraft dynamics equations could be written in a

nonlinear state space form as

$$\dot{\boldsymbol{x}} = f(\boldsymbol{x}, \boldsymbol{u}) \tag{4.1.3}$$

with

$$\boldsymbol{x} = \begin{bmatrix} U & V & W & P & Q & R & \Phi & \Theta \end{bmatrix}^T \tag{4.1.4}$$

$$\boldsymbol{u} = \begin{bmatrix} \delta_A & \delta_E & \delta_R & T \end{bmatrix}^T \tag{4.1.5}$$

Small disturbance theory could be used if the aircraft is subjected to small perturbations and external disturbances [18]. When calculating the trim for the combined damage cases of partial stabiliser loss, there were certain damage cases where an equilibrium was found, but they were beyond the capabilities of or near the actuation limits of the control surfaces. These damage configurations were still considered in the stability analysis assuming the trim was achievable. These conditions were not considered for the simulation or practical assessment of this study.

Each of the states and control inputs could be written as the sum of a trim value and some small perturbation about the trim, as

$$\boldsymbol{x} = \boldsymbol{x}_T + \Delta\boldsymbol{x} \tag{4.1.6}$$

$$\boldsymbol{u} = \boldsymbol{u}_T + \Delta\boldsymbol{u} \tag{4.1.7}$$

where

$$\Delta\boldsymbol{x} = \begin{bmatrix} u & v & w & p & q & r & \phi & \theta \end{bmatrix}^T \tag{4.1.8}$$

$$\Delta\boldsymbol{u} = \begin{bmatrix} \delta_a & \delta_e & \delta_r & \Delta T \end{bmatrix}^T \tag{4.1.9}$$

The nonlinear state space equation could be expanded in a Taylor series around the trim conditions as:

$$\dot{\boldsymbol{x}}_T + \Delta\dot{\boldsymbol{x}} = \boldsymbol{f}(\boldsymbol{x}_T + \Delta\boldsymbol{x}, \boldsymbol{u}_T + \Delta\boldsymbol{u}) = \boldsymbol{f}(\boldsymbol{x}_T, \boldsymbol{u}_T) + \left.\frac{\partial \boldsymbol{f}}{\partial \boldsymbol{x}}\right|_T \Delta x + \left.\frac{\partial \boldsymbol{f}}{\partial \boldsymbol{x}}\right|_T \Delta\boldsymbol{u} + \underset{\textit{higher-order terms}}{} \tag{4.1.10}$$

Assuming that the deviations from trim were small, the higher-order terms were ignored. This allowed the state space equation to be linearised as

$$\Delta\dot{\boldsymbol{x}} \approx \boldsymbol{A}_T\Delta\boldsymbol{x} + \boldsymbol{B}_T\Delta\boldsymbol{u} \tag{4.1.11}$$

where

$$\boldsymbol{A}_T = \left.\frac{\partial f}{\partial x}\right|_T \tag{4.1.12}$$

$$\boldsymbol{B}_T = \left.\frac{\partial f}{\partial u}\right|_T \tag{4.1.13}$$

and given that at the trim (equilibrium) condition, the rate of change of the state vector is zero

$$\dot{\boldsymbol{x}}_T = \boldsymbol{f}(\boldsymbol{x}_T, \boldsymbol{u}_T) = 0 \tag{4.1.14}$$

Normally, the next step of the linearisation process would be to decouple the longitudinal and lateral dynamics of the aircraft. For a symmetric aircraft, the longitudinal dynamics do not couple into the lateral dynamics, and the coupling of the lateral dynamics into the longitudinal dynamics is small enough to be neglected. However, when partial horizontal stabiliser loss occurs, the aircraft becomes asymmetric and the cross-coupling between the longitudinal and lateral dynamics may no longer be a good approximation. The cross-coupling effects therefore needed to be investigated first before deciding whether decoupling between the longitudinal and lateral dynamics may be assumed.

The linear state space representation of the full aircraft model with coupled longitudinal and lateral dynamics is written as:

$$\begin{bmatrix} \dot{u} \\ \dot{v} \\ \dot{w} \\ \dot{p} \\ \dot{q} \\ \dot{r} \\ \dot{\theta} \\ \dot{\phi} \end{bmatrix} = \begin{bmatrix} \frac{\partial \dot{U}}{\partial U} & \frac{\partial \dot{U}}{\partial V} & \frac{\partial \dot{U}}{\partial W} & \frac{\partial \dot{U}}{\partial P} & \frac{\partial \dot{U}}{\partial Q} & \frac{\partial \dot{U}}{\partial R} & \frac{\partial \dot{U}}{\partial \theta} & \frac{\partial \dot{U}}{\partial \phi} \\ \frac{\partial \dot{V}}{\partial U} & \frac{\partial \dot{V}}{\partial V} & \frac{\partial \dot{V}}{\partial W} & \frac{\partial \dot{V}}{\partial P} & \frac{\partial \dot{V}}{\partial Q} & \frac{\partial \dot{V}}{\partial R} & \frac{\partial \dot{V}}{\partial \theta} & \frac{\partial \dot{V}}{\partial \phi} \\ \frac{\partial \dot{W}}{\partial U} & \frac{\partial \dot{W}}{\partial V} & \frac{\partial \dot{W}}{\partial W} & \frac{\partial \dot{W}}{\partial P} & \frac{\partial \dot{W}}{\partial Q} & \frac{\partial \dot{W}}{\partial R} & \frac{\partial \dot{W}}{\partial \theta} & \frac{\partial \dot{W}}{\partial \phi} \\ \frac{\partial \dot{P}}{\partial U} & \frac{\partial \dot{P}}{\partial V} & \frac{\partial \dot{P}}{\partial W} & \frac{\partial \dot{P}}{\partial P} & \frac{\partial \dot{P}}{\partial Q} & \frac{\partial \dot{P}}{\partial R} & \frac{\partial \dot{P}}{\partial \theta} & \frac{\partial \dot{P}}{\partial \phi} \\ \frac{\partial \dot{Q}}{\partial U} & \frac{\partial \dot{Q}}{\partial V} & \frac{\partial \dot{Q}}{\partial W} & \frac{\partial \dot{Q}}{\partial P} & \frac{\partial \dot{Q}}{\partial Q} & \frac{\partial \dot{Q}}{\partial R} & \frac{\partial \dot{Q}}{\partial \theta} & \frac{\partial \dot{Q}}{\partial \phi} \\ \frac{\partial \dot{R}}{\partial U} & \frac{\partial \dot{R}}{\partial V} & \frac{\partial \dot{R}}{\partial W} & \frac{\partial \dot{R}}{\partial P} & \frac{\partial \dot{R}}{\partial Q} & \frac{\partial \dot{R}}{\partial R} & \frac{\partial \dot{R}}{\partial \theta} & \frac{\partial \dot{R}}{\partial \phi} \\ \frac{\partial \dot{\theta}}{\partial U} & \frac{\partial \dot{\theta}}{\partial V} & \frac{\partial \dot{\theta}}{\partial W} & \frac{\partial \dot{\theta}}{\partial P} & \frac{\partial \dot{\theta}}{\partial Q} & \frac{\partial \dot{\theta}}{\partial R} & \frac{\partial \dot{\theta}}{\partial \theta} & \frac{\partial \dot{\theta}}{\partial \phi} \\ \frac{\partial \dot{\phi}}{\partial U} & \frac{\partial \dot{\phi}}{\partial V} & \frac{\partial \dot{\phi}}{\partial W} & \frac{\partial \dot{\phi}}{\partial P} & \frac{\partial \dot{\phi}}{\partial Q} & \frac{\partial \dot{\phi}}{\partial R} & \frac{\partial \dot{\phi}}{\partial \theta} & \frac{\partial \dot{\phi}}{\partial \phi} \end{bmatrix} \begin{bmatrix} u \\ v \\ w \\ p \\ q \\ r \\ \theta \\ \phi \end{bmatrix} + \begin{bmatrix} \frac{\partial \dot{U}}{\partial \delta_A} & \frac{\partial \dot{U}}{\partial \delta_E} & \frac{\partial \dot{U}}{\partial \delta_R} & \frac{\partial \dot{U}}{\partial \Delta T} \\ \frac{\partial \dot{V}}{\partial \delta_A} & \frac{\partial \dot{V}}{\partial \delta_E} & \frac{\partial \dot{V}}{\partial \delta_R} & \frac{\partial \dot{V}}{\partial \Delta T} \\ \frac{\partial \dot{W}}{\partial \delta_A} & \frac{\partial \dot{W}}{\partial \delta_E} & \frac{\partial \dot{W}}{\partial \delta_R} & \frac{\partial \dot{W}}{\partial \Delta T} \\ \frac{\partial \dot{P}}{\partial \delta_A} & \frac{\partial \dot{P}}{\partial \delta_E} & \frac{\partial \dot{P}}{\partial \delta_R} & \frac{\partial \dot{P}}{\partial \Delta T} \\ \frac{\partial \dot{Q}}{\partial \delta_A} & \frac{\partial \dot{Q}}{\partial \delta_E} & \frac{\partial \dot{Q}}{\partial \delta_R} & \frac{\partial \dot{Q}}{\partial \Delta T} \\ \frac{\partial \dot{R}}{\partial \delta_A} & \frac{\partial \dot{R}}{\partial \delta_E} & \frac{\partial \dot{R}}{\partial \delta_R} & \frac{\partial \dot{R}}{\partial \Delta T} \\ \frac{\partial \dot{\theta}}{\partial \delta_A} & \frac{\partial \dot{\theta}}{\partial \delta_E} & \frac{\partial \dot{\theta}}{\partial \delta_R} & \frac{\partial \dot{\theta}}{\partial \Delta T} \\ \frac{\partial \dot{\phi}}{\partial \delta_A} & \frac{\partial \dot{\phi}}{\partial \delta_E} & \frac{\partial \dot{\phi}}{\partial \delta_R} & \frac{\partial \dot{\phi}}{\partial \Delta T} \end{bmatrix} \begin{bmatrix} \delta_a \\ \delta_e \\ \delta_r \\ \Delta T \end{bmatrix} \tag{4.1.15}$$

To perform the linearisation, the partial derivatives of 2.3.8 had to be determined. The asymmetric equations of motion contained a 6x6 inverse matrix which made it difficult to calculate the partial derivatives by hand. The `Matlab Symbolic Toolbox` was therefore used to obtain the partial derivatives in symbolic form. Using this procedure, the linearisation could be performed for the healthy configuration as well as for the damaged aircraft configurations for any combination of partial horizontal and vertical stabiliser losses. The full system of equations was considered for this section for completeness and improved accuracy.

It is common to work with the velocity magnitude, angle of attack and sideslip angle $(\overline{v}, \alpha, \beta)$ perturbations in the state vector instead of the axial, lateral and normal velocity perturbations (u, v, w). The following approximations could be made for the straight and level trim flight

condition, assuming both the angle of attack and sideslip angle are small angles:

$$\overline{v} = \sqrt{u^2 + v^2 + w^2} \approx u \tag{4.1.16}$$

$$w = \overline{v}\sin\alpha\cos\beta \approx \overline{v}\alpha = (\overline{V}_T + \overline{v})\alpha \approx \overline{V}_T\alpha \tag{4.1.17}$$

$$v = \overline{v}\sin\beta \approx \overline{v}\beta = (\overline{V}_T + \overline{v})\beta \approx \overline{V}_T\beta \tag{4.1.18}$$

thus

$$\dot{\overline{v}} \approx \dot{u} \tag{4.1.19}$$

$$\dot{w} \approx V_T\dot{\alpha} \tag{4.1.20}$$

$$\dot{v} \approx V_T\dot{\beta} \tag{4.1.21}$$

These assumptions allowed equation 4.1.15 to be rewritten as:

$$\begin{bmatrix} \dot{\overline{v}} \\ \overline{V}_T\dot{\beta} \\ \overline{V}_T\dot{\alpha} \\ \dot{p} \\ \dot{q} \\ \dot{r} \\ \dot{\theta} \\ \dot{\phi} \end{bmatrix} = \begin{bmatrix} \frac{\partial\dot{U}}{\partial U} & \frac{\partial\dot{U}}{\partial V} & \frac{\partial\dot{U}}{\partial W} & \frac{\partial\dot{U}}{\partial P} & \frac{\partial\dot{U}}{\partial Q} & \frac{\partial\dot{U}}{\partial R} & \frac{\partial\dot{U}}{\partial\theta} & \frac{\partial\dot{U}}{\partial\phi} \\ \frac{\partial\dot{V}}{\partial U} & \frac{\partial\dot{V}}{\partial V} & \frac{\partial\dot{V}}{\partial W} & \frac{\partial\dot{V}}{\partial P} & \frac{\partial\dot{V}}{\partial Q} & \frac{\partial\dot{V}}{\partial R} & \frac{\partial\dot{V}}{\partial\theta} & \frac{\partial\dot{V}}{\partial\phi} \\ \frac{\partial\dot{W}}{\partial U} & \frac{\partial\dot{W}}{\partial V} & \frac{\partial\dot{W}}{\partial W} & \frac{\partial\dot{W}}{\partial P} & \frac{\partial\dot{W}}{\partial Q} & \frac{\partial\dot{W}}{\partial R} & \frac{\partial\dot{W}}{\partial\theta} & \frac{\partial\dot{W}}{\partial\phi} \\ \frac{\partial\dot{P}}{\partial U} & \frac{\partial\dot{P}}{\partial V} & \frac{\partial\dot{P}}{\partial W} & \frac{\partial\dot{P}}{\partial P} & \frac{\partial\dot{P}}{\partial Q} & \frac{\partial\dot{P}}{\partial R} & \frac{\partial\dot{P}}{\partial\theta} & \frac{\partial\dot{P}}{\partial\phi} \\ \frac{\partial\dot{Q}}{\partial U} & \frac{\partial\dot{Q}}{\partial V} & \frac{\partial\dot{Q}}{\partial W} & \frac{\partial\dot{Q}}{\partial P} & \frac{\partial\dot{Q}}{\partial Q} & \frac{\partial\dot{Q}}{\partial R} & \frac{\partial\dot{Q}}{\partial\theta} & \frac{\partial\dot{Q}}{\partial\phi} \\ \frac{\partial\dot{R}}{\partial U} & \frac{\partial\dot{R}}{\partial V} & \frac{\partial\dot{R}}{\partial W} & \frac{\partial\dot{R}}{\partial P} & \frac{\partial\dot{R}}{\partial Q} & \frac{\partial\dot{R}}{\partial R} & \frac{\partial\dot{R}}{\partial\theta} & \frac{\partial\dot{R}}{\partial\phi} \\ \frac{\partial\dot{\theta}}{\partial U} & \frac{\partial\dot{\theta}}{\partial V} & \frac{\partial\dot{\theta}}{\partial W} & \frac{\partial\dot{\theta}}{\partial P} & \frac{\partial\dot{\theta}}{\partial Q} & \frac{\partial\dot{\theta}}{\partial R} & \frac{\partial\dot{\theta}}{\partial\theta} & \frac{\partial\dot{\theta}}{\partial\phi} \\ \frac{\partial\dot{\phi}}{\partial U} & \frac{\partial\dot{\phi}}{\partial V} & \frac{\partial\dot{\phi}}{\partial W} & \frac{\partial\dot{\phi}}{\partial P} & \frac{\partial\dot{\phi}}{\partial Q} & \frac{\partial\dot{\phi}}{\partial R} & \frac{\partial\dot{\phi}}{\partial\theta} & \frac{\partial\dot{\phi}}{\partial\phi} \end{bmatrix} \begin{bmatrix} \overline{v} \\ \overline{V}_T\beta \\ \overline{V}_T\alpha \\ p \\ q \\ r \\ \theta \\ \phi \end{bmatrix} + \begin{bmatrix} \frac{\partial\dot{U}}{\partial\delta_A} & \frac{\partial\dot{U}}{\partial\delta_E} & \frac{\partial\dot{U}}{\partial\delta_R} & \frac{\partial\dot{U}}{\partial\Delta T} \\ \frac{\partial\dot{V}}{\partial\delta_A} & \frac{\partial\dot{V}}{\partial\delta_E} & \frac{\partial\dot{V}}{\partial\delta_R} & \frac{\partial\dot{V}}{\partial\Delta T} \\ \frac{\partial\dot{W}}{\partial\delta_A} & \frac{\partial\dot{W}}{\partial\delta_E} & \frac{\partial\dot{W}}{\partial\delta_R} & \frac{\partial\dot{W}}{\partial\Delta T} \\ \frac{\partial\dot{P}}{\partial\delta_A} & \frac{\partial\dot{P}}{\partial\delta_E} & \frac{\partial\dot{P}}{\partial\delta_R} & \frac{\partial\dot{P}}{\partial\Delta T} \\ \frac{\partial\dot{Q}}{\partial\delta_A} & \frac{\partial\dot{Q}}{\partial\delta_E} & \frac{\partial\dot{Q}}{\partial\delta_R} & \frac{\partial\dot{Q}}{\partial\Delta T} \\ \frac{\partial\dot{R}}{\partial\delta_A} & \frac{\partial\dot{R}}{\partial\delta_E} & \frac{\partial\dot{R}}{\partial\delta_R} & \frac{\partial\dot{R}}{\partial\Delta T} \\ \frac{\partial\dot{\theta}}{\partial\delta_A} & \frac{\partial\dot{\theta}}{\partial\delta_E} & \frac{\partial\dot{\theta}}{\partial\delta_R} & \frac{\partial\dot{\theta}}{\partial\Delta T} \\ \frac{\partial\dot{\phi}}{\partial\delta_A} & \frac{\partial\dot{\phi}}{\partial\delta_E} & \frac{\partial\dot{\phi}}{\partial\delta_R} & \frac{\partial\dot{\phi}}{\partial\Delta T} \end{bmatrix} \begin{bmatrix} \delta_a \\ \delta_e \\ \delta_r \\ \Delta T \end{bmatrix} \tag{4.1.22}$$

Reworking equation 4.1.22 gives

$$\begin{bmatrix} \dot{\overline{v}} \\ \dot{\alpha} \\ \dot{q} \\ \dot{\theta} \\ \dot{\beta} \\ \dot{p} \\ \dot{r} \\ \dot{\phi} \end{bmatrix} = \begin{bmatrix} \frac{\partial \dot{U}}{\partial U} & \frac{\partial \dot{U}}{\partial W}\overline{V} & \frac{\partial \dot{U}}{\partial Q} & \frac{\partial \dot{U}}{\partial \theta} & \frac{\partial \dot{U}}{\partial V}\overline{V} & \frac{\partial \dot{U}}{\partial P} & \frac{\partial \dot{U}}{\partial R} & \frac{\partial \dot{U}}{\partial \phi} \\ \frac{\partial \dot{W}}{\partial U}\frac{1}{\overline{V}} & \frac{\partial \dot{W}}{\partial W} & \frac{\partial \dot{W}}{\partial Q}\frac{1}{\overline{V}} & \frac{\partial \dot{W}}{\partial \theta}\frac{1}{\overline{V}} & \frac{\partial \dot{W}}{\partial V} & \frac{\partial \dot{W}}{\partial P}\frac{1}{\overline{V}} & \frac{\partial \dot{W}}{\partial R}\frac{1}{\overline{V}} & \frac{\partial \dot{W}}{\partial \phi}\frac{1}{\overline{V}} \\ \frac{\partial \dot{Q}}{\partial U} & \frac{\partial \dot{Q}}{\partial W}\overline{V} & \frac{\partial \dot{Q}}{\partial Q} & \frac{\partial \dot{Q}}{\partial \theta} & \frac{\partial \dot{Q}}{\partial V}\overline{V} & \frac{\partial \dot{Q}}{\partial P} & \frac{\partial \dot{Q}}{\partial R} & \frac{\partial \dot{Q}}{\partial \phi} \\ \frac{\partial \dot{\theta}}{\partial U} & \frac{\partial \dot{\theta}}{\partial W}\overline{V} & \frac{\partial \dot{\theta}}{\partial Q} & \frac{\partial \dot{\theta}}{\partial \theta} & \frac{\partial \dot{\theta}}{\partial V}\overline{V} & \frac{\partial \dot{\theta}}{\partial P} & \frac{\partial \dot{\theta}}{\partial R} & \frac{\partial \dot{\theta}}{\partial \phi} \\ \frac{\partial \dot{V}}{\partial U}\frac{1}{\overline{V}} & \frac{\partial \dot{V}}{\partial W} & \frac{\partial \dot{V}}{\partial Q}\frac{1}{\overline{V}} & \frac{\partial \dot{V}}{\partial \theta}\frac{1}{\overline{V}} & \frac{\partial \dot{V}}{\partial V} & \frac{\partial \dot{V}}{\partial P}\frac{1}{\overline{V}} & \frac{\partial \dot{V}}{\partial R}\frac{1}{\overline{V}} & \frac{\partial \dot{V}}{\partial \phi}\frac{1}{\overline{V}} \\ \frac{\partial \dot{P}}{\partial U} & \frac{\partial \dot{P}}{\partial W}\overline{V} & \frac{\partial \dot{P}}{\partial Q} & \frac{\partial \dot{P}}{\partial \theta} & \frac{\partial \dot{P}}{\partial V}\overline{V} & \frac{\partial \dot{P}}{\partial P} & \frac{\partial \dot{P}}{\partial R} & \frac{\partial \dot{P}}{\partial \phi} \\ \frac{\partial \dot{R}}{\partial U} & \frac{\partial \dot{R}}{\partial W}\overline{V} & \frac{\partial \dot{R}}{\partial Q} & \frac{\partial \dot{R}}{\partial \theta} & \frac{\partial \dot{R}}{\partial V}\overline{V} & \frac{\partial \dot{R}}{\partial P} & \frac{\partial \dot{R}}{\partial R} & \frac{\partial \dot{R}}{\partial \phi} \\ \frac{\partial \dot{\phi}}{\partial U} & \frac{\partial \dot{\phi}}{\partial W}\overline{V} & \frac{\partial \dot{\phi}}{\partial Q} & \frac{\partial \dot{\phi}}{\partial \theta} & \frac{\partial \dot{\phi}}{\partial V}\overline{V} & \frac{\partial \dot{\phi}}{\partial P} & \frac{\partial \dot{\phi}}{\partial R} & \frac{\partial \dot{\phi}}{\partial \phi} \end{bmatrix} \begin{bmatrix} \overline{v} \\ \alpha \\ q \\ \theta \\ \beta \\ p \\ r \\ \phi \end{bmatrix}$$

$$+ \begin{bmatrix} \frac{\partial \dot{U}}{\partial \delta_A} & \frac{\partial \dot{U}}{\partial \delta_E} & \frac{\partial \dot{U}}{\partial \delta_R} & \frac{\partial \dot{U}}{\partial \Delta T} \\ \frac{\partial \dot{W}}{\partial \delta_A}\frac{1}{\overline{V}} & \frac{\partial \dot{W}}{\partial \delta_E}\frac{1}{\overline{V}} & \frac{\partial \dot{W}}{\partial \delta_R}\frac{1}{\overline{V}} & \frac{\partial \dot{W}}{\partial \Delta T}\frac{1}{\overline{V}} \\ \frac{\partial \dot{Q}}{\partial \delta_A} & \frac{\partial \dot{Q}}{\partial \delta_E} & \frac{\partial \dot{Q}}{\partial \delta_R} & \frac{\partial \dot{Q}}{\partial \Delta T} \\ \frac{\partial \dot{\theta}}{\partial \delta_A} & \frac{\partial \dot{\theta}}{\partial \delta_E} & \frac{\partial \dot{\theta}}{\partial \delta_R} & \frac{\partial \dot{\theta}}{\partial \Delta T} \\ \frac{\partial \dot{V}}{\partial \delta_A}\frac{1}{\overline{V}} & \frac{\partial \dot{V}}{\partial \delta_E}\frac{1}{\overline{V}} & \frac{\partial \dot{V}}{\partial \delta_R}\frac{1}{\overline{V}} & \frac{\partial \dot{V}}{\partial \Delta T}\frac{1}{\overline{V}} \\ \frac{\partial \dot{P}}{\partial \delta_A} & \frac{\partial \dot{P}}{\partial \delta_E} & \frac{\partial \dot{P}}{\partial \delta_R} & \frac{\partial \dot{P}}{\partial \Delta T} \\ \frac{\partial \dot{R}}{\partial \delta_A} & \frac{\partial \dot{R}}{\partial \delta_E} & \frac{\partial \dot{R}}{\partial \delta_R} & \frac{\partial \dot{R}}{\partial \Delta T} \\ \frac{\partial \dot{\phi}}{\partial \delta_A} & \frac{\partial \dot{\phi}}{\partial \delta_E} & \frac{\partial \dot{\phi}}{\partial \delta_R} & \frac{\partial \dot{\phi}}{\partial \Delta T} \end{bmatrix} \begin{bmatrix} \delta_a \\ \delta_e \\ \delta_r \\ \Delta T \end{bmatrix} \tag{4.1.23}$$

The linear state space model represented by equation 4.1.23 could then be used to analyse the stability of the aircraft as a function of percentage partial horizontal and vertical stabiliser losses, and also served as the basis for the control system design.

4.2 Validity of Decoupling the Longitudinal and Lateral Dynamics

As noted in the previous section (see 4.1), it is common to decouple the longitudinal and lateral dynamics of the aircraft. However, for the asymmetric aircraft model, it may not be a good approximation to assume decoupling because the changes in the centre of gravity (CG) location, change of mass and the moment of inertia (MoI) and the change of aerodynamic coefficients may significantly increase the cross-coupling between the longitudinal and the lateral dynamics. In this section, the cross-coupling terms for the asymmetric damaged aircraft are compared to the cross-coupling terms of the healthy aircraft.

The linear coupled state space models for both the healthy and the asymmetric damaged aircraft, with parameters calculated for 70% left horizontal stabiliser and 20% vertical stabiliser loss, are shown in equations 4.2.1 and 4.2.2 respectively. The independent left horizontal stabiliser and vertical stabiliser linear state space models can be found in Appendix C.

The linear coupled state space model for the healthy aircraft is:

$$\begin{bmatrix} \dot{\overline{v}} \\ \dot{\alpha} \\ \dot{q} \\ \dot{\theta} \\ \dot{\beta} \\ \dot{p} \\ \dot{r} \\ \dot{\phi} \end{bmatrix} = \begin{bmatrix} -0.1729 & 14.6187 & -1.9720 & -9.7457 & 0.0000 & -0.0000 & 0.0004 & 0.0000 \\ -0.0280 & -5.0125 & 0.9068 & -0.0623 & 0.0000 & -0.0000 & -0.0000 & 0.0000 \\ 0.4313 & -68.0758 & -7.6577 & 0.0000 & 0.0000 & 0.0000 & 0.0000 & 0.0000 \\ 0.0000 & 0.0000 & 1.0000 & 0.0000 & 0.0000 & 0.0000 & 0.0000 & 0.0000 \\ 0.0000 & 0.0000 & 0.0000 & 0.0000 & -0.2870 & 0.1251 & -0.9851 & 0.5414 \\ 0.0000 & -0.0004 & -0.0000 & 0.0000 & -23.9906 & -7.8698 & 2.8058 & 0.0000 \\ -0.0000 & 0.0028 & 0.0000 & 0.0000 & 16.4925 & -1.5123 & -0.8682 & 0.0000 \\ 0.0000 & 0.0000 & 0.0000 & 0.0000 & 0.0000 & 1.0000 & 0.1150 & 0.0000 \end{bmatrix} \begin{bmatrix} \overline{v} \\ \alpha \\ q \\ \theta \\ \beta \\ p \\ r \\ \phi \end{bmatrix} + \begin{bmatrix} -0.0000 & 0.4818 & 0.0000 & 0.1408 \\ 0.0000 & -0.4898 & 0.0000 & 0.0000 \\ 0.0001 & -96.3550 & 0.0000 & 0.0000 \\ 0.0000 & 0.0000 & 0.0000 & 0.0000 \\ 0.0147 & 0.0000 & 0.1269 & 0.0000 \\ -98.4180 & 0.0000 & 2.1546 & 0.0000 \\ -7.9429 & 0.0000 & -14.3644 & 0.0000 \\ 0.0000 & 0.0000 & 0.0000 & 0.0000 \end{bmatrix} \begin{bmatrix} \delta_a \\ \delta_e \\ \delta_r \\ \Delta T \end{bmatrix} \tag{4.2.1}$$

The linear coupled state space model for the nominal damage configuration is:

$$\begin{bmatrix} \dot{\overline{v}} \\ \dot{\alpha} \\ \dot{q} \\ \dot{\theta} \\ \dot{\beta} \\ \dot{p} \\ \dot{r} \\ \dot{\phi} \end{bmatrix} = \begin{bmatrix} -0.1764 & 14.7141 & -1.9916 & -9.7451 & 0.0277 & -0.0032 & 0.0496 & 0.0000 \\ -0.0281 & -4.9744 & 0.9176 & -0.0626 & 0.0287 & -0.0022 & -0.0018 & 0.0000 \\ 0.4293 & -67.1664 & -5.9379 & 0.0000 & 5.6911 & 0.1766 & -0.3593 & 0.0000 \\ 0.0000 & 0.0000 & 1.0000 & 0.0000 & 0.0000 & 0.0000 & 0.0000 & 0.0000 \\ 0.0000 & 0.0069 & 0.0006 & 0.0000 & -0.2640 & 0.1225 & -0.9858 & 0.5414 \\ 0.0015 & 0.3624 & -0.1951 & 0.0000 & -24.1879 & -7.9450 & 2.8403 & 0.0000 \\ -0.0028 & -0.9128 & -0.0920 & 0.0000 & 14.2628 & -1.1775 & -0.8041 & 0.0000 \\ 0.0000 & 0.0000 & 0.0000 & 0.0000 & 0.0000 & 1.0000 & 0.1156 & 0.0000 \end{bmatrix} \begin{bmatrix} \overline{v} \\ \alpha \\ q \\ \theta \\ \beta \\ p \\ r \\ \phi \end{bmatrix} + \begin{bmatrix} -0.0224 & 0.3260 & -0.0167 & 0.1439 \\ 0.0231 & -0.3443 & -0.0257 & -0.0000 \\ 5.0018 & -69.9535 & -4.9957 & -0.0019 \\ 0.0000 & 0.0000 & 0.0000 & 0.0000 \\ -0.0039 & 0.0064 & 0.1009 & -0.0000 \\ -100.0991 & -3.0022 & 1.7193 & 0.0000 \\ -5.7422 & -1.3157 & -11.6057 & 0.0044 \\ 0.0000 & 0.0000 & 0.0000 & 0.0000 \end{bmatrix} \begin{bmatrix} \delta_a \\ \delta_e \\ \delta_r \\ \Delta T \end{bmatrix} \tag{4.2.2}$$

The linear state space models were calculated at the trim points for straight and level flight at an airspeed of $18m.s^{-1}$ and an altitude of $30m$. The asymmetric aircraft was trimmed for zero sideslip angle flight. The mass, MoI, CG location, and aerodynamic stability control

derivatives calculated for the nominal damage case of 70% left horizontal stabiliser damage and 20% vertical stabiliser damage were used for the combined damage case.

The following effects of the partial horizontal stabiliser loss was observed:

- The pitch accelerations due to angle of attack($\frac{\partial \dot{Q}}{\partial \alpha}$) and pitch rate($\frac{\partial \dot{Q}}{\partial Q}$) are smaller in magnitude due to the reduction in the surface area of the horizontal stabiliser.
- The pitch acceleration due to elevator deflection($\frac{\partial \dot{Q}}{\partial \delta_e}$) is smaller in magnitude due to the partial loss of the elevator control surface.

The following effects of the partial vertical stabiliser loss was observed:

- The pitch accelerations due to angle of attack($\frac{\partial \dot{Q}}{\partial \alpha}$) and pitch rate($\frac{\partial \dot{Q}}{\partial Q}$) are larger in magnitude due to the forward shift in CG resulting from the loss of mass of the vertical stabiliser.
- The pitch acceleration due to elevator deflection($\frac{\partial \dot{Q}}{\partial \delta_e}$) is larger in magnitude due to the forward shift in CG resulting from the loss of mass of the vertical stabiliser.
- The yaw accelerations due to sideslip angle($\frac{\partial \dot{R}}{\partial \beta}$) and yaw rate($\frac{\partial \dot{R}}{\partial R}$) decrease in magnitude due to the reduction in surface area of the vertical stabiliser.
- The yaw acceleration due to rudder deflection($\frac{\partial \dot{R}}{\partial \delta_r}$) is smaller in magnitude due to the partial loss of rudder control surface.

The following effects of the combined partial horizontal and vertical stabiliser losses were observed:

- The pitch accelerations due to angle of attack and pitch rate are smaller due to the reduction in the surface area of the horizontal stabiliser.
- The pitch acceleration due to elevator deflection is much smaller due to the partial loss of the elevator control surface.
- The yaw accelerations due to sideslip angle and yaw rate are smaller due to the reduction in the surface area of the vertical stabiliser.
- The yaw acceleration due to rudder deflection is smaller due to the partial loss of rudder control surface.
- The cross-coupling terms between the longitudinal and lateral dynamics change noticeably, but the change is not significant.
- All the other partial derivatives do not change much.

The pitch rate acceleration was affected by both the horizontal and vertical stabiliser loss. For the horizontal stabiliser damage, the acceleration became smaller in magnitude (due to the reduction in surface area of the horizontal stabiliser), and for the vertical stabiliser damage,

the acceleration became larger (due to the forward shift in CG). As a result, these two effects almost cancelled each other out in the nominal aircraft configuration. The other accelerations that were affected were only due to damage on either the horizontal or vertical stabiliser and affected the nominal damage case independently.

The effect of the damage on the cross-coupling terms was small enough that the decoupling between the longitudinal and lateral dynamics could be assumed.

4.3 Stability Analysis

In this section, an overview of the different modes of the aircraft is provided and the stability and transient response of the natural modes of motion of the aircraft are analysed as a function of the partial stabiliser losses. The stability analysis is performed by plotting the open-loop poles of the linearised aircraft dynamics as a function of percentage partial horizontal and vertical stabiliser losses. The stability, damping ratio, and natural frequencies of the open-loop poles over the range of damage cases are then interpreted and evaluated.

4.3.1 Modes of Motion Overview

The modes of motion for a symmetric aircraft can be decoupled into longitudinal and lateral modes. These modes of motion describe the natural longitudinal and lateral behaviour of an aircraft. Sections 4.3.1.1 and 4.3.1.2 describe these modes of motion.

4.3.1.1 Longitudinal Modes

Figure 4.1 depicts the longitudinal modes of motion of an aircraft. There are typically two modes associated with the longitudinal nature of the aircraft. These two modes are identified as:

Short Period mode The higher frequency pole pair in Figure 4.1 is referred to as the short period mode. This mode describes the tendency of the aircraft to naturally realign itself with the velocity vector when disturbed.

Phugoid mode The lower frequency pole pair in Figure 4.1 is referred to as the phugoid mode. This mode describes the exchange of potential and kinetic energy in the aircraft. This is an exchange of altitude and airspeed. As the aircraft loses altitude, it gains airspeed. As airspeed is gained, more lift is generated, resulting in the aircraft gaining altitude.

4.3.1.2 Lateral Modes

Figure 4.2 depicts the lateral modes of motion of an aircraft. There are typically three modes associated with the lateral nature of the aircraft. These three modes are identified as:

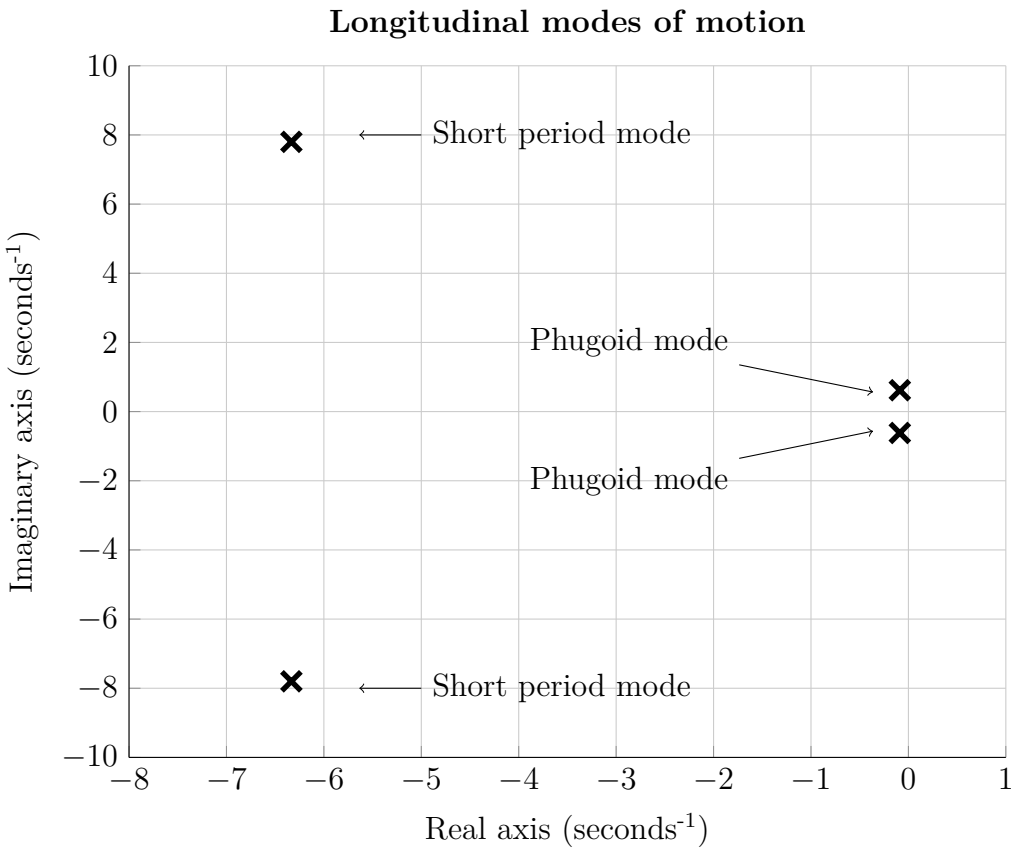

Figure 4.1: Longitudinal modes of motion

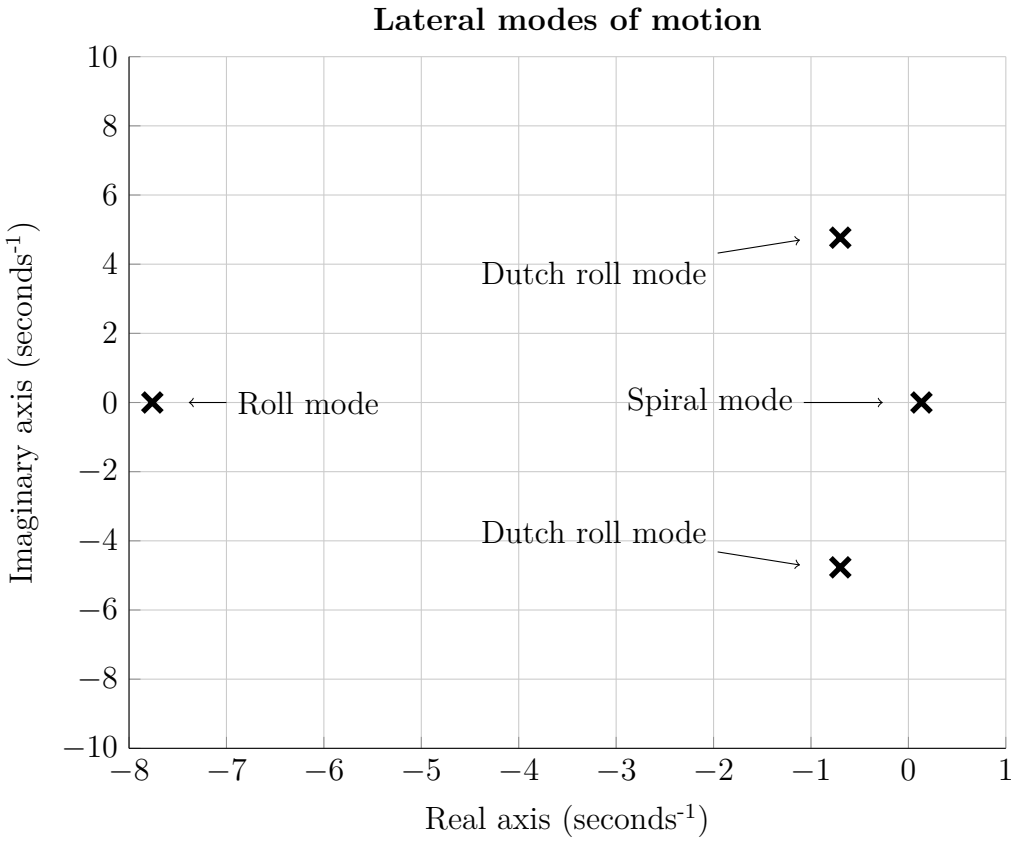

Figure 4.2: Lateral modes of motion

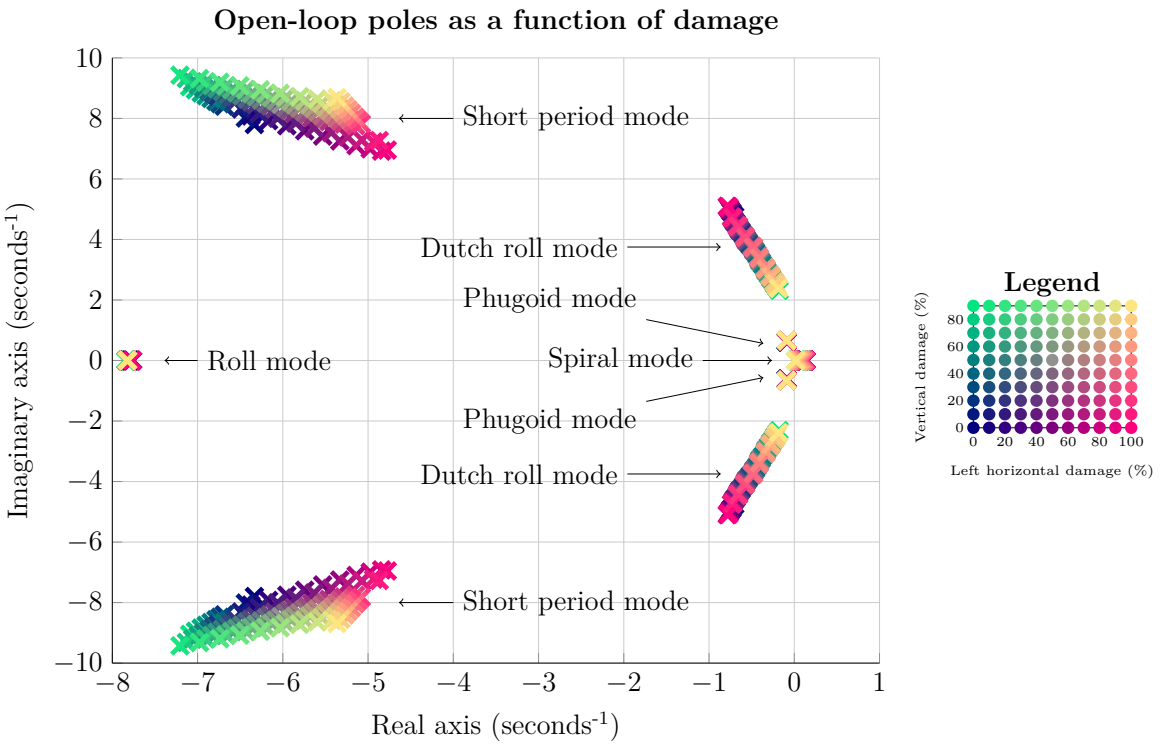

Figure 4.3: Open-loop pole cloud of different damage cases

Roll mode The high frequency real pole in Figure 4.2 is the roll mode pole. This describes the roll rate dynamics of the aircraft. When an aircraft experiences a roll moment disturbance, the roll rate will initially start to grow. The wing provides a natural roll damping. This damping roll moment will eventually build up to counter the roll moment disturbance and result in a constant roll rate.

Dutch roll mode The complex pole pair in Figure 4.2 is referred to as the dutch roll mode. The dutch roll mode is almost the lateral equivalent of the short period mode. It describes the tendency of the aircraft to align itself with the oncoming airflow when disturbed laterally. During the lateral oscillation, differential lift and drag is experienced due to the differential velocity on the aircraft wings. This causes small roll rate perturbations, which in turn cause differential lift and drag perturbations. The differential drag experienced by the aircraft damp the yaw rate motions further. The net effect is that the aircraft oscillates both in yaw and roll.

Spiral mode The lower frequency pole in Figure 4.2 is the spiral mode pole. The spiral mode describes the tendency of the aircraft to return itself to or divert from wings level when laterally disturbed. For this aircraft, this mode is unstable but very slow.

4.3.2 Discussion

The loci of the open-loop poles for the full aircraft dynamics, as a function of percentage stabiliser loss is shown in Figure 4.3. The open-loop poles were obtained by calculating the eigenvalues of the 8x8 full system matrix over all damage cases.

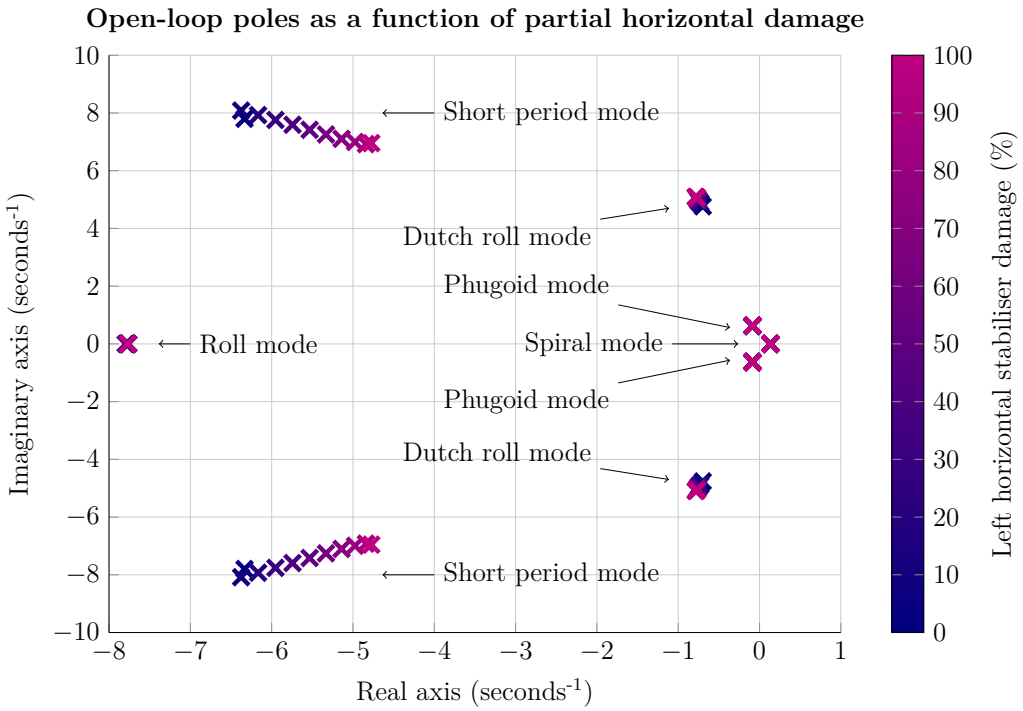

Figure 4.4: Open-loop pole cloud of longitudinal dynamics

The loci of the open-loop poles for the longitudinal and lateral dynamics for the independent horizontal and vertical stabiliser loss percentages are shown in Figures 4.4 and 4.5 respectively. Figure 4.4 shows the loci of the open-loop longitudinal dynamics as a function of partial horizontal stabiliser loss, and Figure 4.5 shows the loci of the open-loop lateral dynamics as a function of percentage partial vertical stabiliser loss.

By comparing Figure 4.3 with Figures 4.4 and 4.5, it can be seen that the open-loop poles of the full coupled dynamics are simply the combination of the longitudinal and lateral dynamics for the independent horizontal and vertical stabiliser loss percentages. This indicated that the locations of the longitudinal and lateral poles were not significantly affected by the cross-coupling, and that decoupling could be assumed when designing the flight control laws.

To determine the change in dynamics of the aircraft, the following factors were looked at:

stability the poles had to be in the left-half plane to be stable;

damping ratio the angle of the pole relative to the imaginary axis (indicates how the oscillations decay); and

natural frequency the radial distance from the origin (indicates the frequency of oscillations).

Figure 4.4 shows that the partial horizontal stabiliser loss mainly affected the short period mode of the aircraft. As the damage increased, the frequency of the mode decreased and became less damped. This lower frequency and damping ratio was expected as the physical surface area of the horizontal stabiliser is reduced due to the damage. This reduced the effectiveness of the aircraft to realign itself with the oncoming wind when the aircraft was disturbed. The short period mode thus took longer to settle, with larger oscillations. The other modes of the aircraft were not significantly affected by the horizontal stabiliser damage.

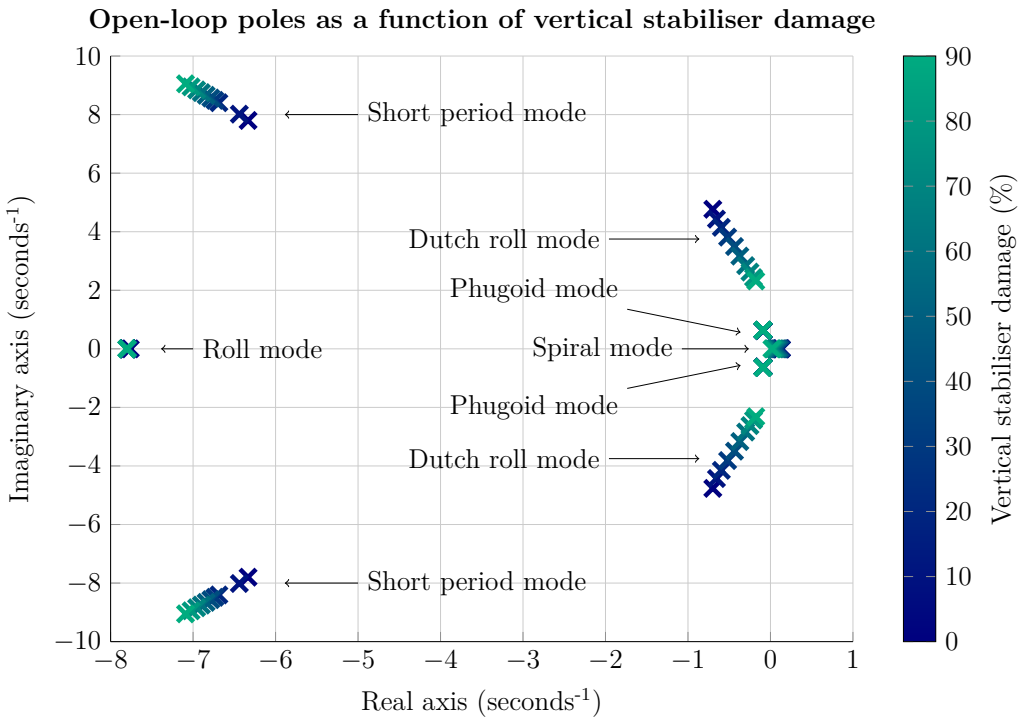

Figure 4.5: Open-loop pole cloud of lateral dynamics

Figure 4.5 shows the effects that the vertical stabiliser damage had on the open-loop modes of the aircraft. The vertical stabiliser loss affected the short period mode and the dutch roll modes of the aircraft. The short period mode frequency increased and the damping ratio decreased. This change was due to the CG that shifted forward as more of the vertical stabiliser was removed. This forward shift increased the stability of the aircraft by increasing the moment generated by the CG around the centre of lift. The dutch roll mode poles decreased in frequency and damping as a function of vertical stabiliser loss. This was due to the reduced physical surface area of the vertical stabiliser due to damage. This reduced the effectiveness of the aircraft to realign itself with the oncoming wind vector when the aircraft was laterally disturbed. The other modes of the aircraft were not significantly affected by the vertical stabiliser damage.

Figure 4.3 depicts a pole "cloud" of open-loop pole locations to determine the worst-case stability, worst-case damping ratio and worst-case natural frequency over all the damage cases. The cloud of open-loop pole locations is plotted over the entire range of partial horizontal and vertical stabiliser losses to check the worst-case stability and transient response characteristics that can be expected over all damage cases.

From the cloud of open-loop pole locations it can be seen that all of the open-loop poles remain in the left half-plane which means that the natural dynamics of the aircraft will remain stable over all expected damage cases (except the spiral mode which is easily controlled).

For the short period mode, the lowest damping ratio (most oscillatory response) was 0.566 and the lowest natural frequency (slowest response) was $8.44\,\text{rad.s}^{-1}$. For the nominal case, the damping ratio was 0.569 and the natural frequency was $9.6\,\text{rad.s}^{-1}$.

For the dutch roll mode, the lowest damping ratio (most oscillatory response) was 0.077 and the lowest natural frequency (slowest response) was $2.33\,\text{rad.s}^{-1}$. For the nominal case, the

damping ratio was 0.148 and the natural frequency was 4.46 rad.s^{-1}

For the roll mode, the longest time constant (slowest response) was 0.129 s. For the nominal case, the time constant was 0.128 s.

The effect of the damage on the phugoid mode and spiral mode were not really of importance, since these two natural motions operate over much longer time scales, and they were easily stabilised my middle and outer-loop controllers.

The next chapter (see 5) makes use of this linear model to present the design and implementation of the control architecture and gain design for the flight control system of the aircraft.

§ 5

Controller Design

This chapter presents the design and implementation of the flight control system for the aircraft. The controllers were designed to be robust and unaware of any damage that occurs. A combination of classic and acceleration-based control theory from [1, 19, 20] was used. Previous projects showed that both classic and acceleration-based control techniques have robust properties, which were investigated, in this study, for this specific damage case of partial horizontal and vertical stabiliser loss.

First, the control architecture is discussed. The longitudinal and lateral controllers that were used in this project are presented. The aircraft model was decoupled to simplify the control design process. The controllers were required to be robust and unaware of the damage, so the control system was designed for the healthy configuration and assuming symmetry. With the controller architecture chosen, the controller specifications and gain design is presented.

Next, the controllers were verified on the linear system for which they were designed. The linear system was the full, coupled system representing both the longitudinal and lateral aircraft dynamics. These results were evaluated against their controller specifications, and were evaluated for both the healthy and damaged configurations to show the level of robustness in the controller. The controllers are verified on the nonlinear aircraft model in Chapter 6.

A closed-loop pole analysis depicted the resultant poles of the aircraft with the full controller implemented. This pole analysis shows the closed loop pole positions for the different aircraft damage configurations as an indication of the robustness of the control system.

5.1 Control Architecture

This section reports on the control design approach that was used for the control system that was implemented on this UAV. The longitudinal controllers that were used are listed below:

- airspeed controller — commands thrust to control airspeed;
- normal specific acceleration (NSA) controller — commands elevator to control NSA;
- climb rate controller — commands NSA to control climb rate; and

- altitude controller — commands climb rate to control altitude.

The lateral controllers that were used are listed below:

- lateral specific acceleration (LSA) controller — commands rudder to control LSA;
- roll angle controller — commands aileron to control roll angle; and
- cross track controller — commands roll angle to control cross track.

Most of the controllers were designed using the root locus method. This allows the root locus of the system to be altered by placing closed-loop poles to acquire the desired response. The specifications for the different controllers were selected and an appropriate controller architecture was used to modify the root locus to meet the specifications.

5.1.1 Decoupling

The control system was designed using the decoupling assumption and analysed using the full, coupled system. The decoupling of the system assumed symmetry in the aircraft, and that the cross-coupling terms, if any, were negligible. The resultant equations are shown in equations 5.1.1 and 5.1.2. When discussing the decoupled plants, reference is made to these equations.

$$\begin{bmatrix} \dot{\overline{V}} \\ \dot{\alpha} \\ \dot{Q} \\ \dot{\theta} \end{bmatrix} = \begin{bmatrix} \frac{\partial \dot{U}}{\partial U} & \frac{\partial \dot{U}}{\partial W}\overline{V} & \frac{\partial \dot{U}}{\partial Q} & \frac{\partial \dot{U}}{\partial \theta} \\ \frac{\partial \dot{W}}{\partial U}\frac{1}{\overline{V}} & \frac{\partial \dot{W}}{\partial W} & \frac{\partial \dot{W}}{\partial Q}\frac{1}{\overline{V}} & \frac{\partial \dot{W}}{\partial \theta}\frac{1}{\overline{V}} \\ \frac{\partial \dot{Q}}{\partial U} & \frac{\partial \dot{Q}}{\partial W}\overline{V} & \frac{\partial \dot{Q}}{\partial Q} & \frac{\partial \dot{Q}}{\partial \theta} \\ \frac{\partial \dot{\theta}}{\partial U} & \frac{\partial \dot{\theta}}{\partial W}\overline{V} & \frac{\partial \dot{\theta}}{\partial Q} & \frac{\partial \dot{\theta}}{\partial \theta} \end{bmatrix} \begin{bmatrix} \overline{V} \\ \alpha \\ Q \\ \theta \end{bmatrix} + \begin{bmatrix} \frac{\partial \dot{U}}{\partial \delta_E} & \frac{\partial \dot{U}}{\partial \Delta T} \\ \frac{\partial \dot{W}}{\partial \delta_E}\frac{1}{\overline{V}} & \frac{\partial \dot{W}}{\partial \Delta T}\frac{1}{\overline{V}} \\ \frac{\partial \dot{Q}}{\partial \delta_E} & \frac{\partial \dot{Q}}{\partial \Delta T} \\ \frac{\partial \dot{\theta}}{\partial \delta_E} & \frac{\partial \dot{\theta}}{\partial \Delta T} \end{bmatrix} \begin{bmatrix} \delta_E \\ \Delta T \end{bmatrix} \tag{5.1.1}$$

$$\begin{bmatrix} \dot{\beta} \\ \dot{P} \\ \dot{R} \\ \dot{\phi} \end{bmatrix} = \begin{bmatrix} \frac{\partial \dot{V}}{\partial V} & \frac{\partial \dot{V}}{\partial P}\frac{1}{\overline{V}} & \frac{\partial \dot{V}}{\partial R}\frac{1}{\overline{V}} & \frac{\partial \dot{V}}{\partial \phi}\frac{1}{\overline{V}} \\ \frac{\partial \dot{P}}{\partial V}\overline{V} & \frac{\partial \dot{P}}{\partial P} & \frac{\partial \dot{P}}{\partial R} & \frac{\partial \dot{P}}{\partial \phi} \\ \frac{\partial \dot{R}}{\partial V}\overline{V} & \frac{\partial \dot{R}}{\partial P} & \frac{\partial \dot{R}}{\partial R} & \frac{\partial \dot{R}}{\partial \phi} \\ \frac{\partial \dot{\phi}}{\partial V}\overline{V} & \frac{\partial \dot{\phi}}{\partial P} & \frac{\partial \dot{\phi}}{\partial R} & \frac{\partial \dot{\phi}}{\partial \phi} \end{bmatrix} \begin{bmatrix} \beta \\ P \\ R \\ \phi \end{bmatrix} + \begin{bmatrix} \frac{\partial \dot{V}}{\partial \delta_A}\frac{1}{\overline{V}} & \frac{\partial \dot{V}}{\partial \delta_R}\frac{1}{\overline{V}} \\ \frac{\partial \dot{P}}{\partial \delta_A} & \frac{\partial \dot{P}}{\partial \delta_R} \\ \frac{\partial \dot{R}}{\partial \delta_A} & \frac{\partial \dot{R}}{\partial \delta_R} \\ \frac{\partial \dot{\phi}}{\partial \delta_A} & \frac{\partial \dot{\phi}}{\partial \delta_R} \end{bmatrix} \begin{bmatrix} \delta_A \\ \delta_R \end{bmatrix} \tag{5.1.2}$$

The poles that were attributed to the lateral and longitudinal modes of the aircraft are as follows:

Longitudinal poles	Lateral poles
$s = -6.333 \pm 7.799j$	$s = -7.761$
$s = -0.088 \pm 0.618j$	$s = -0.699 \pm 4.767j$
	$s = 0.1339$

This information along with the decoupled state-space matrices in equations 5.1.1 and 5.1.2 were used as the open-loop model of the aircraft that serves as the basis for the design of the control system.

5.1.2 Longitudinal Controllers

This section describes the control architecture that was used for the longitudinal control of the aircraft, including design decisions and procedures.

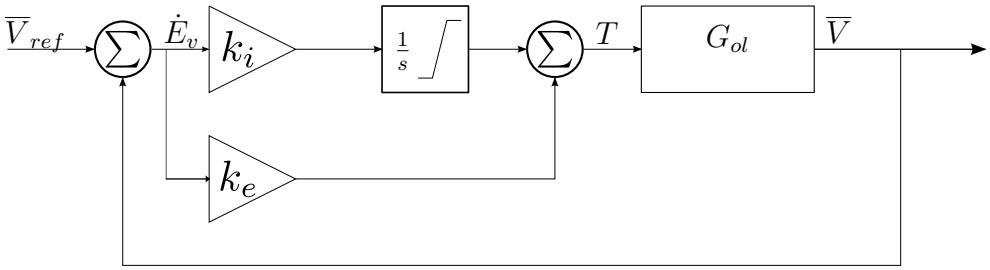

Figure 5.1: Airspeed controller architecture

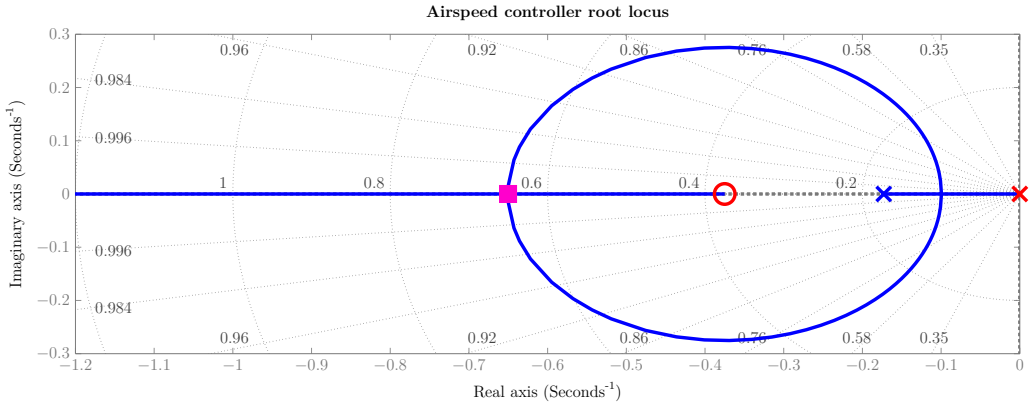

Figure 5.2: Airspeed controller root locus

5.1.2.1 Airspeed Controller

An airspeed controller was used to command the thrust of the aircraft to achieve the desired airspeed. A proportional integral (PI) controller was used to provide the airspeed control. This allowed the aircraft to maintain its airspeed without a steady state error in the tracking of the airspeed reference.

The controller used the measured airspeed of the aircraft as provided by the pitot tube and pressure sensor of the aircraft. The engine of the aircraft was modelled as a first-order lag model with a time constant of $\tau = 0.25$. The engine response is modelled by equation 2.2.38. The block diagram of the airspeed controller is shown in Figure 5.1.

The response of the airspeed controller was desired to be fast and have very little overshoot. The integrator from the PI control design introduces overshoot into the response. A compromise between significant overshoot and a long settling time was found which resulted in an overshoot of 7% and a settling time of 7 s. The `rltool` toolbox in `Matlab` is used to determine the necessary gains for the system. The root locus plot is shown in Figure 5.2. The design criteria resulted in the following values for k_i and k_e:

$$k_i = 3; \tag{5.1.3}$$

$$k_e = 8. \tag{5.1.4}$$

5.1.2.2 Normal Specific Acceleration Controller

The NSA controller commands the elevator of the aircraft to control the normal specific acceleration measured by the body z-axis acceleration sensor.

This controller, developed by Peddle [19], was used with an added feed-forward component to compensate for the slower response resulting from an integrator that was added by the controller to provide zero steady-state tracking error. The NSA controller is designed using a reduced-order model of the normal specific acceleration dynamics and it is assumed that the airspeed remains constant over the time scale of the NSA dynamics.

$$\begin{bmatrix}\dot{\alpha}\\ \dot{Q}\end{bmatrix} = \begin{bmatrix}-\frac{L_\alpha}{m\bar{V}} & 1\\ \frac{M_\alpha}{I_{yy}} & \frac{M_Q}{I_{yy}}\end{bmatrix}\begin{bmatrix}\alpha\\ Q\end{bmatrix} + \begin{bmatrix}0\\ \frac{M_{\delta_E}}{I_{yy}}\end{bmatrix}\delta_E + \begin{bmatrix}-\frac{L_0}{m\bar{V}}\\ \frac{M_0}{I_{yy}}\end{bmatrix} + \begin{bmatrix}\frac{g}{\bar{V}}\\ 0\end{bmatrix} e_{33}^{WI} \tag{5.1.5}$$

$$C_W = \begin{bmatrix}-\frac{L_\alpha}{m} & 0\end{bmatrix}\begin{bmatrix}\alpha\\ Q\end{bmatrix} + \begin{bmatrix}0\end{bmatrix}\delta_E + \begin{bmatrix}-\frac{L_0}{m}\end{bmatrix} \tag{5.1.6}$$

where M_{δ_E} was the pitching moment relative to the elevator deflection, M_Q the pitching moment relative to pitch rate, L_α the lift force due to α, and M_α the pitching moment relative to α.

Equation 5.1.6 is differentiated twice with respect to time to allow the elevator input to cancel the effect of the attitude angle coupling terms on the normal specific acceleration dynamics as

$$\begin{aligned}\ddot{C}_W = &\left[\frac{M_Q}{I_{yy}} - \frac{L_\alpha}{m\bar{V}}\right]\dot{C}_W + \left[\frac{M_\alpha}{I_{yy}} + \frac{L_\alpha M_Q}{mI_{yy}}\right]C_w + \left[-\frac{L_\alpha M_{\delta_E}}{mI_{yy}}\right]\delta_E + \left[\frac{L_0 M_\alpha}{mI_{yy}} - \frac{L_\alpha M_0}{mI_{yy}}\right]\\ &+ \left[\frac{L_\alpha g}{m\bar{V}}\left(\frac{M_Q}{I_{yy}}e_{33}^{WI} - \dot{e}_{ee}^{WI}\right)\right]\end{aligned} \tag{5.1.7}$$

A PI control law is defined as

$$\delta_E = -k_q Q - k_c C_W - k_e E_C + \delta_{E_G} \tag{5.1.8}$$

$$\dot{E}_C = C_W - C_{W_R} \tag{5.1.9}$$

where C_{W_R} is the reference NSA command. Offset disturbance terms, such as those due to static lift and pitching moments are ignored in the design due to the integral action of the control law. Substituting the control law (5.1.8 and 5.1.9) into equation 5.1.6 results in the following closed loop normal dynamics:

$$\begin{aligned}\ddot{C}_W = &\left[\frac{M_Q}{I_{yy}} - \frac{L_\alpha}{m\bar{V}} - \frac{M_{\delta_E}}{I_{yy}}k_q\right]\dot{C}_W + \left[\frac{M_\alpha}{I_{yy}} + \frac{L_\alpha M_Q}{m\bar{I}_{yy}} + \frac{L_\alpha M_{\delta_E}}{mI_{yy}}k_c - \frac{L_\alpha M_{\delta_E}}{mI_{yy}}k_q\right]C_W\\ &+ \left[\frac{L_\alpha M_{\delta_E}}{mI_{yy}}k_e\right]E_C\end{aligned} \tag{5.1.10}$$

$$\dot{E}_C = C_W - C_{W_R} \tag{5.1.11}$$

The closed loop normal dynamics can be matched to the desired closed loop characteristic equation for the normal dynamics:

$$\alpha_c(s) = s^3 + \alpha_0 s^2 + \alpha_1 s + \alpha_2$$

An upper bound for the natural frequency of the system is

$$\omega_n < \frac{1}{3}\left|\sqrt{\frac{L_\alpha}{I_{yy}}(l_T - l_N)}\right| \tag{5.1.12}$$

where

$$l_T = -\frac{M_\alpha}{L_\alpha} \tag{5.1.13}$$

$$l_N = -\frac{M_{\delta_E}}{L_{\delta_E}} \tag{5.1.14}$$

The upper bound for this aircraft model is $10.1\,\text{rad.s}^{-1}$. The natural frequency of the controller was therefore chosen to be at $\omega_n = 9\,\text{rad.s}^{-1}$ with a damping ratio of $\zeta = 0.9$ and the integrator pole at $\omega_i = 5.5\,\text{rad.s}^{-1}$. This criterion resulted in the following characteristic equation:

$$\alpha_c(s) = s^3 + 21.7s^2 + 170.1s + 445.5 \tag{5.1.15}$$

The following equations were then used to determine the necessary gains for the controller:

$$k_q = \frac{I_{yy}}{M_{\delta_E}}\left(\alpha_2 + \frac{M_Q}{I_{yy}} - \frac{L_\alpha}{m\overline{V}}\right) \tag{5.1.16}$$

$$k_c = -\frac{mI_{yy}}{L_\alpha M_{\delta_E}}\left(\alpha_1 + \frac{M_\alpha}{I_{yy}} - \frac{L_\alpha}{m\overline{V}}\left(\alpha_2 - \frac{L_\alpha}{m\overline{V}}\right)\right) \tag{5.1.17}$$

$$k_e = -\frac{mI_{yy}}{L_\alpha M_{\delta_E}}\alpha_0 \tag{5.1.18}$$

$$\overline{N} = \frac{k_e}{\omega_i} \tag{5.1.19}$$

Using equations 5.1.16 to 5.1.19 and the given design specifications the following gains were calculated:

$$k_q = -0.0921; \tag{5.1.20}$$

$$k_c = 0.0507; \tag{5.1.21}$$

$$k_e = 0.0021; \tag{5.1.22}$$

$$\overline{N} = 0.0092. \tag{5.1.23}$$

The architecture of the NSA controller is shown in Figure 5.3.

5.1.2.3 Climb Rate Controller

The climb rate controller commanded a normal specific acceleration in order to achieve a desired climb rate. This controller was designed using the transfer function from NSA reference to climb rate, which consists of the NSA controller transfer function augmented with the relationship between normal specific acceleration and climb rate. The climb rate of the aircraft could be

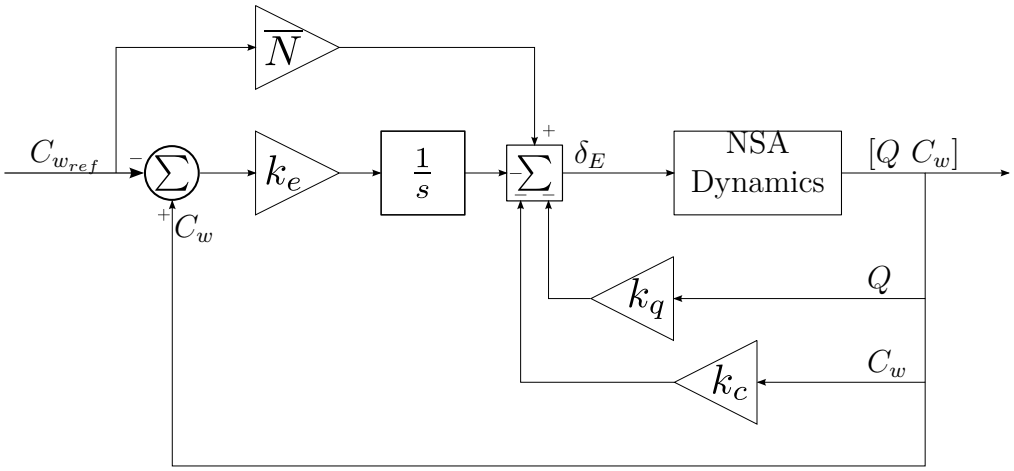

Figure 5.3: NSA controller architecture

estimated from the longitudinal dynamics of the aircraft as $\dot{h} = -\overline{V}_T\alpha + \overline{V}_T\theta$. The transfer function of the NSA ($C_{w_{ref}}$) input to climb rate output ($\dot{h}$) is:

$$G_{cr} = -0.08119\frac{(s-36.3)(s+25.63)(s+5.51)}{(s+4.878)(s-0.06194)(s^2+16.69s+84.36)} \tag{5.1.24}$$

The architecture for the climb rate controller is shown in Figure 5.4.

A simple proportional controller was designed to control the climb rate with a limited integrator added afterwards to help with disturbance rejection and to provide zero steady-state error. A limited integrator introduces the steady state tracking of integral control, but also limits the contribution of the integrator to the output command. This reduces the overall effect on the transients of the controller when an integrator is added. The controller gain needed to be multiplied by -1 because a negative elevator deflection produces a positive pitching moment. This multiplication resulted in a negative feedback loop.

The specifications for the climb rate controller were a settling time of $t_{s_{2\%}} = 1.5$ seconds with a damping ratio of 0.9. The settling time was chosen as three times larger than that of the NSA to ensure time scale separation. The limited integrator increased this settling time resulting in an even larger time scale separation. This resulted in almost no overshoot, while allowing the response of the controller to be sufficiently fast. The integrator that was added later introduced some overshoot, and also an increase in the settling time of the controller. The effects of adding the integrator are discussed in Section 5.2.

The proportional gain k_p is determined through root locus design. The `rltool` toolbox in `Matlab` was used to determine this gain. Figure 5.5 shows the root locus for the climb rate controller. The integrator gain is determined later through simulation. The gain is chosen to be small, and limits introduced to reduce the dominant effect of the integrator pole. This design criterion resulted in the following k_p as well as the chosen integrator gain of k_i and integrator

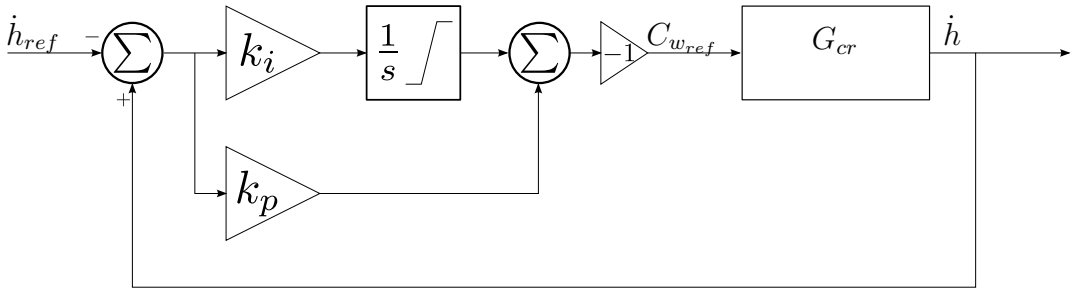

Figure 5.4: Climb rate controller architecture

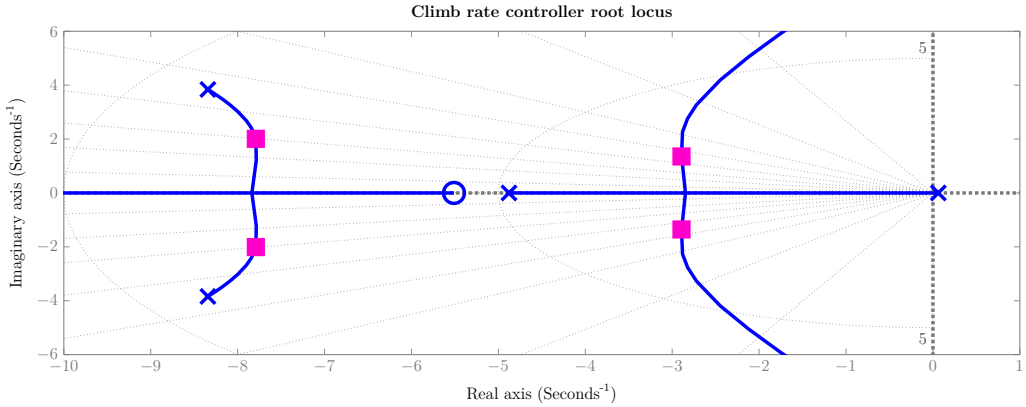

Figure 5.5: Climb rate controller root locus

limits $u_{i_{lim}}$:

$$k_p = -1.65; \tag{5.1.25}$$

$$k_i = -0.2; \tag{5.1.26}$$

$$u_{i_{lim}} = \pm 1m.s^{-2}. \tag{5.1.27}$$

The limits $u_{i_{lim}}$ is the minimum and maximum contribution of the integrator to the control law.

5.1.2.4 Altitude Controller

The altitude controller commanded a climb rate to control the altitude. In the present study, the altitude controller was designed using the augmented aircraft model after the climb rate controller had been implemented. The altitude could be approximated by using the integral of the climb rate used for the climb rate controller as $h = \int \dot{h} = \int (-\overline{V}_T \alpha + \overline{V}_T \theta)$. The transfer function of the climb rate input $(\dot{h}_{ref})$ to altitude output $(\dot{h})$ is:

$$G_{alt} = -0.13385 \frac{(s - 36.3)(s + 25.63)(s + 5.511)}{s(s^2 + 5.785s + 10.2)(s^2 + 15.58s + 64.75)} \tag{5.1.28}$$

The architecture of the altitude controller is shown in Figure 5.6

A proportional controller was used for the altitude control on this aircraft. The design specifications for this controller were no overshoot and a settling time of 13 seconds to ensure time scale separation from the climb rate controller. This settling time was also chosen more

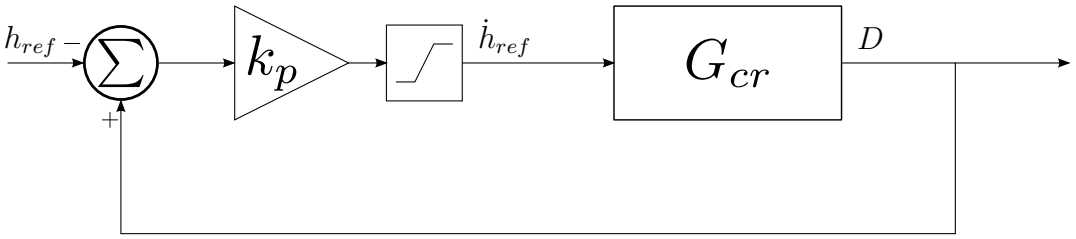

Figure 5.6: Altitude controller architecture

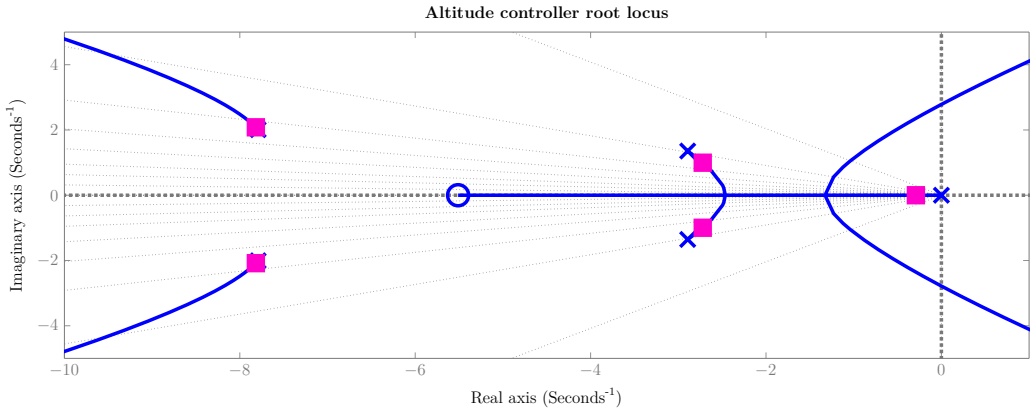

Figure 5.7: Altitude controller root locus

conservatively due to the integrator that was added later. A root locus design was used to determine the gain for this controller. The `rltool` toolbox in `Matlab` was used for this design. The root locus for the altitude controller design is shown in Figure 5.7. These specifications result in a proportional gain k_p as:

$$k_p = 0.233. \tag{5.1.29}$$

This concludes the discussion on the design of the longitudinal controllers. The performance of these controllers are discussed later in this chapter in Section 5.2.

5.1.3 Lateral Controllers

This section reports on the control architecture that was used for the lateral control of the aircraft, including design decisions and procedures.

5.1.3.1 Lateral Specific Acceleration Controller

The LSA controller was used to regulate the lateral specific acceleration in the body y-axis using the rudder of the aircraft. The LSA controller used was that developed by Peddle [19].

A reduced-order model of the lateral specific acceleration dynamics was used as:

$$\begin{bmatrix}\dot{\beta}\\ \dot{R}\end{bmatrix} = \begin{bmatrix}\frac{Y_\beta}{m\overline{V}} & -1\\ \frac{\overline{N}_\beta}{I_{zz}} & \frac{\overline{N}_R}{I_{zz}}\end{bmatrix}\begin{bmatrix}\beta\\ R\end{bmatrix} + \begin{bmatrix}\frac{Y_{\delta_R}}{m\overline{V}}\\ \frac{\overline{N}_{\delta_R}}{I_{zz}}\end{bmatrix}\delta_R + \begin{bmatrix}-\frac{Y_{\delta_R}}{m\overline{V}}\frac{\overline{N}_{\delta_A}}{\overline{N}_{\delta_R}}\\ 0\end{bmatrix}\delta_A \tag{5.1.30}$$

$$B_W = \begin{bmatrix}\frac{Y_\beta}{m} & \frac{Y_R}{m}\end{bmatrix}\begin{bmatrix}\beta\\ R\end{bmatrix} + \begin{bmatrix}\frac{Y_{\delta_R}}{m}\end{bmatrix}\delta_R + \begin{bmatrix}-\frac{Y_{\delta_R}}{m}\frac{\overline{N}_{\delta_A}}{\overline{N}_{\delta_R}}\end{bmatrix}\delta_A \tag{5.1.31}$$

where Y_β was the lateral force relative to the sideslip, Y_{δ_R} was the lateral force due to rudder deflection. N_R was the yaw moment relative to yaw rate, N_β the yaw moment due to sideslip and N_{δ_R} was the yawing moment due to rudder deflection.

The stability control law is defined as

$$\delta_R = -k_r R - k_b B_W + \delta_{R_R} \tag{5.1.32}$$

where δ_{R_R} was used as the input for the regulation control law.

It is further shown that the closed loop poles can be approximated with:

$$\alpha_c(s) = s^2 + \alpha_0 s + \alpha_2 \tag{5.1.33}$$

$$\alpha_c(s) = s^2 - \left(\frac{Y_\beta}{m\overline{V}} + \frac{\overline{N}_R}{I_{zz}} - \frac{\overline{N}_{\delta_R}}{I_{zz}}k_r\right)Xs + \left[\frac{Y_\beta}{m\overline{V}}\frac{\overline{N}_R}{I_{zz}} + \frac{\overline{N}_\beta}{I_{zz}} + \frac{Y_{\delta_R}}{m}\frac{Y_\beta}{I_{zz}}\left(\frac{\overline{N}_\beta}{Y_\beta} - \frac{\overline{N_{\delta_R}}}{Y_{\delta_R}}\right)k_b\right]X \tag{5.1.34}$$

where

$$X = \left(1 + k_b\frac{Y_{\delta_R}}{m}\right)^{-1} \tag{5.1.35}$$

It is necessary for time scale separation between the stability augmentation LSA controller and the outer regulating LSA controller. The upper bound for the regulating controller is defined as:

$$\omega_n < \frac{1}{3}\left|\sqrt{\frac{-Y_\beta(l_F - l_W)}{I_{zz}}}\right| \tag{5.1.36}$$

where

$$l_F = -\frac{\overline{N}_{\delta_R}}{Y_{\delta_R}} \tag{5.1.37}$$

$$l_W = -\frac{\overline{N}_\beta}{Y_\beta} \tag{5.1.38}$$

The regulating component of the LSA controller needs to smaller than the upper bound from equation 5.1.36. The upper bound for this aircraft model is $1.26 rad.s^{-1}$. The natural frequency of this controller was chosen to be $\omega_n = 4.6 rad.s^{-1}$ with a damping ratio of $\zeta = 1$ and an

integrator at $\omega_i = 0.6rad.s^{-1}$. These specifications were chosen to ensure time scale separation between the stability and regulating controllers. The integrator was added as a final step and did not contribute to the characteristic equation. As a result, the characteristic equation was defined as:

$$s = s^2 + 9.2s + 21.16 \tag{5.1.39}$$

The characteristic equation can then be matched with equation 5.1.34 to yield the following gain equations:

$$k_b = \frac{\frac{Y_\beta}{m\overline{V}}\frac{\overline{N}_R}{I_{zz}} + \frac{\overline{N}_\beta}{I_{zz}} - \alpha_0}{\frac{Y_{\delta_R}}{m}\left(\alpha_0 - \frac{Y_\beta}{I_{zz}}\left(\frac{\overline{N}_\beta}{Y_\beta} - \frac{\overline{N}_{\delta_R}}{Y_{\delta_R}}\right)\right)} \tag{5.1.40}$$

$$k_r = \frac{I_{zz}}{\overline{N}_{\delta_R}}\left(\frac{Y_\beta}{m\overline{V}} + \frac{\overline{N}_R}{I_{zz}} + \alpha_1\left(1 + \frac{k_b Y_{\delta_R}}{m}\right)\right) \tag{5.1.41}$$

The steady-state gain of the transfer function was calculated as K_{ss}, as shown in equation 5.1.42 and the integrator gain was determined using equation 5.1.47:

$$K_{ss} = \frac{Y_{\delta_R}}{m}\frac{Y_\beta}{I_{zz}}\left(\frac{\overline{N}_\beta}{Y_\beta} - \frac{\overline{N}_{\delta_R}}{Y_{\delta_R}}\right)\frac{1}{\alpha_0}\left(1 + k_b\frac{Y_{\delta_R}}{m}\right)^{-1} \tag{5.1.42}$$

For the regulating controller design, the control law was defined as:

$$\delta_{R_R} = -k_e E_B \tag{5.1.43}$$

$$\dot{E}_B = B_W - B_{W_R} \tag{5.1.44}$$

where B_{W_R} is the reference LSA command. The closed loop characteristic equation is given by:

$$s + K_{ss}k_e = 0 \tag{5.1.45}$$

The characteristic equation is then given by

$$\alpha_c(s) = s + \alpha_0 \tag{5.1.46}$$

where α_0 is the desired integrator pole location ω_i:

$$k_e = \frac{\omega_i}{K_{ss}} \tag{5.1.47}$$

Using the gain equations, the specific gains for the above characteristic equation and specifica-

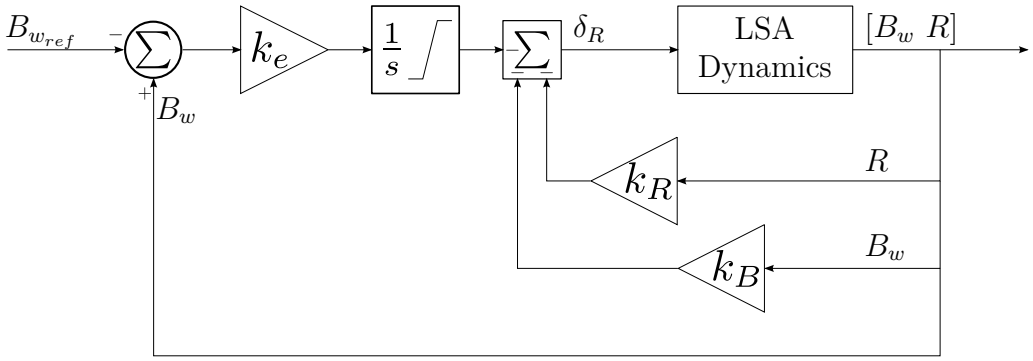

Figure 5.8: LSA controller architecture

tions were calculated as:

$$k_b = -0.0266; \tag{5.1.48}$$

$$k_r = -0.4930; \tag{5.1.49}$$

$$k_e = -0.3605. \tag{5.1.50}$$

The architecture of this controller is shown in Figure 5.8.

5.1.3.2 Roll Angle Controller

A roll angle controller was used to control the bank angle of the aircraft using the ailerons. A PI controller was used to provide the desired response. The architecture of this controller is shown in Figure 5.9. The specifications for this controller were set as a damping ratio of $\zeta = 0.9$ to reduce the overshoot of the system to prevent the aircraft from losing significant lift and a settling time of $t_{s_{2\%}} = 6\,\text{s}$ to provide a less aggressive rolling moment.

The controller gain needed to be multiplied by -1 as a positive aileron deflection produces a negative rolling moment. This multiplication resulted in a negative feedback loop. The gains for this controller were calculated using through root locus design. The `rltool` toolbox in `Matlab` was used to determine these gains. Figure 5.10 shows the root locus for the roll angle controller. The following proportional gain k_p and integral gain k_i were calculated to meet the given specifications.

$$k_p = 0.32; \tag{5.1.51}$$

$$k_i = 0.1867. \tag{5.1.52}$$

5.1.3.3 Cross track Controller

The cross track controller controls the cross track displacement of the aircraft relative to a given ground track by commanding the roll angle. This allows the aircraft to perform waypoint navigation. A proportional integral derivative (PID) controller was used to perform cross track control. The first step of the controller design was to determine the derivative gain K_d. The `rltool` toolbox in `Matlab` is used to move the open-loop integrator pole to become a real

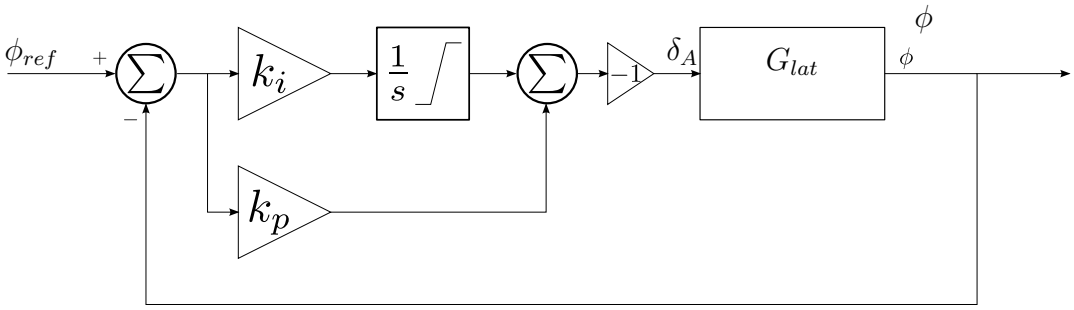

Figure 5.9: Roll angle controller architecture

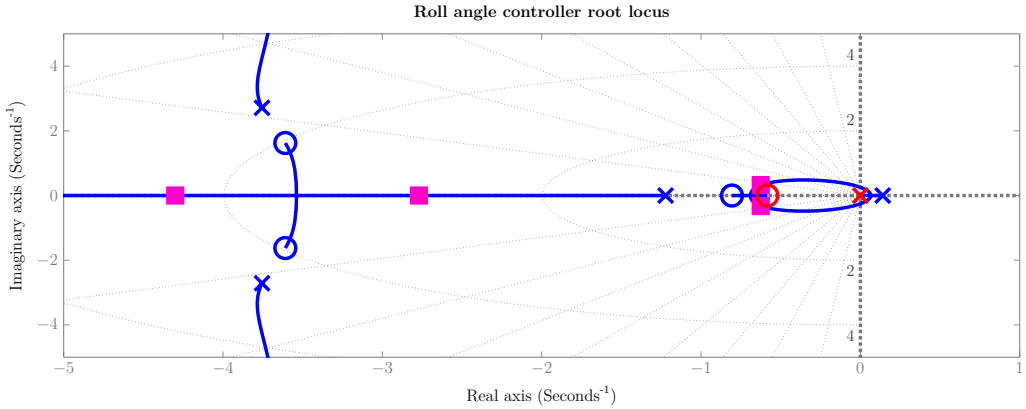

Figure 5.10: Roll angle controller root locus

negative pole with a desired time constant. This loop is then used with an integrator in series to represent the natural integration of $\dot{y}$ to y. This is then used as the open-loop transfer function that serves as the basis for the proportional gain K_p. The architecture for this controller is shown in Figure 5.11. The root locus for the different gain calculations are shown in Figures 5.12 and 5.13.

The design criteria were zero overshoot and a settling time of $t_{s_{2\%}} = 8\,\text{s}$ on the derivative component to ensure time scale separation. The proportional component was designed for $\zeta = 0.9$ and a settling time of $t_{s_{2\%}} = 12\,\text{s}$ to provide little overshoot and sufficient time scale separation from the roll angle controller. A limited integrator was added later which further increased the settling time of the system ensuring the time scale separation. The following proportional gain k_p, integral gain k_i and derivative gain k_d were calculated to meet the given specifications:

$$k_p = 0.27; \tag{5.1.53}$$

$$k_i = 0.175; \tag{5.1.54}$$

$$k_d = 0.108. \tag{5.1.55}$$

This concludes the discussion of the controller design for the aircraft. The next section reports on an investigation of the performance of these controllers to see how well they performed when all the aircraft dynamics were taken into account and whether the decoupling assumption held validity.

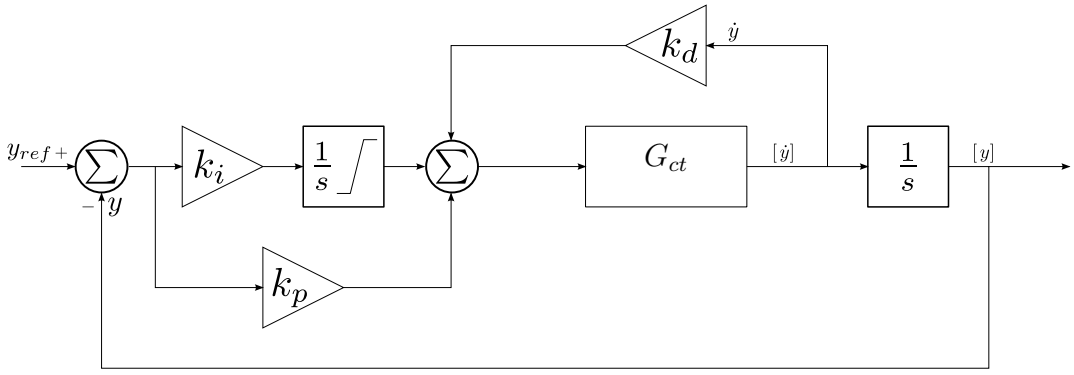

Figure 5.11: Cross track controller architecture

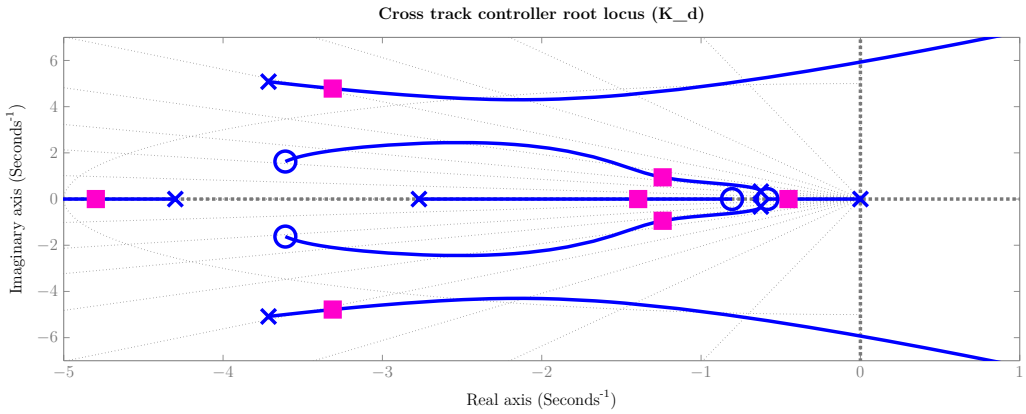

Figure 5.12: Cross track controller root locus (K_d)

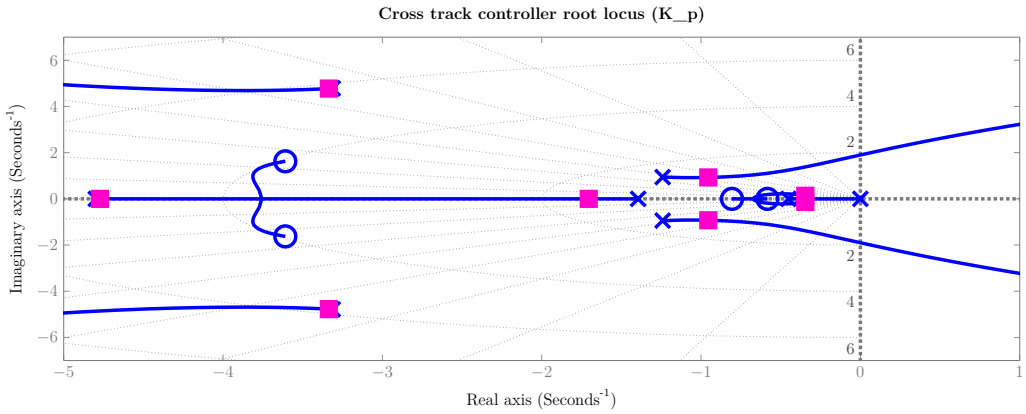

Figure 5.13: Cross track controller root locus (K_p)

5.2 Controller Verification

This section focuses on the verification of the controller design through linear simulation taking the full linear aircraft model into account. This allows the performance of the controller design to be verified while taking the cross-coupling into account. The simulation was run on the healthy and the nominal damage case (70% left horizontal stabiliser and 20% vertical stabiliser loss) of the aircraft to investigate the controller design and to provide insight into the effect of the damage on the aircraft and the performance of the controllers. The controllers responses for the healthy aircraft configuration are presented first. The responses are compared to the design specifications and any differences are discussed. The controller responses for the nominal damaged asymmetric configuration are presented next, and are compared to the responses for the healthy configuration to show how the responses change. The controller responses are analysed by considering their simulated step responses as well as the locations of their closed-loop poles.

5.2.1 Healthy Aircraft

The controller responses are investigated for the healthy aircraft first as the controllers were designed based on the healthy configuration.

5.2.1.1 Airspeed Controller

The design specifications for the airspeed controller are an overshoot of 7% and a settling time of 7 s. The step response of the airspeed controller is shown in Figure 5.14a and exhibits an overshoot of 7% with a settling time of 7.28 s. The thrust response depicted in Figure 5.14b indicates that the thrust remains within the minimum and maximum limits for the aircraft. The thrust was not the same as the expected trim thrust as the full nonlinear aircraft model was not used for this simulation.

Based on the design specifications for the airspeed controller, the dominant pole of the airspeed controller should be located at -0.65 on the real axis as shown in Figure 5.21c. The resultant pole for the airspeed controller using the full linear model of the aircraft was at -0.6498 on the real axis, as expected.

5.2.1.2 Normal Specific Acceleration Controller

The design specifications for the NSA controller are no overshoot and a settling time of 0.45 seconds. The step response of the NSA controller is shown in Figure 5.15a and exhibits no overshoot, and a settling time of 0.5 s. This difference in settling time could have been due to the integrator pole not being perfectly cancelled by the zero. The difference in settling time is not significant and was considered acceptable for the climb rate controller to be designed around. The actuator deflection depicted in Figure 5.15b shows how the elevator command

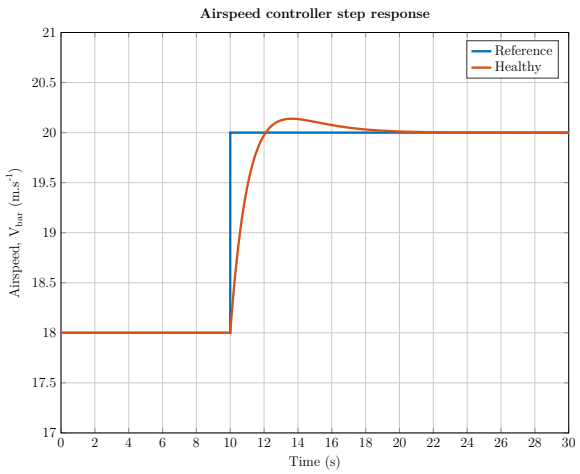

(a) Airspeed controller step

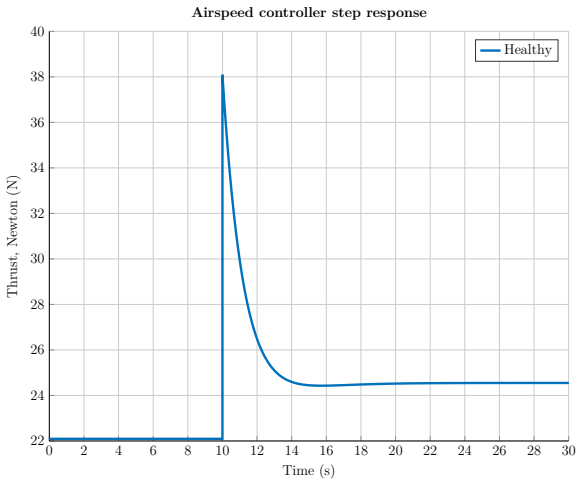

(b) Airspeed step actuator deflection

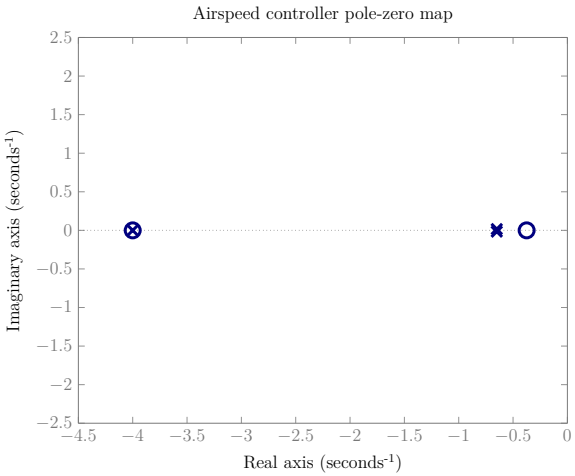

(c) Airspeed controller closed-loop poles

Figure 5.14: Airspeed controller plots

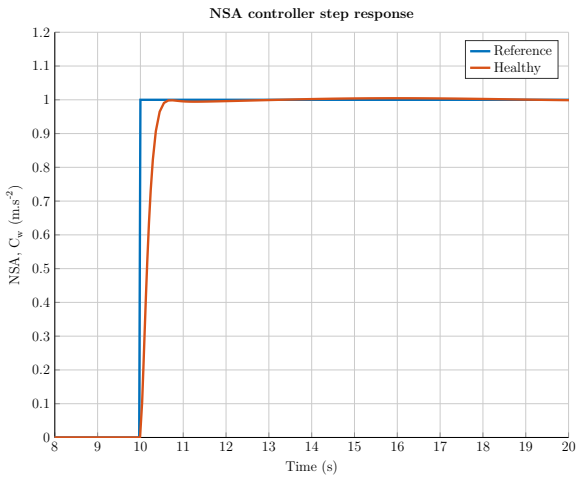

(a) NSA controller step

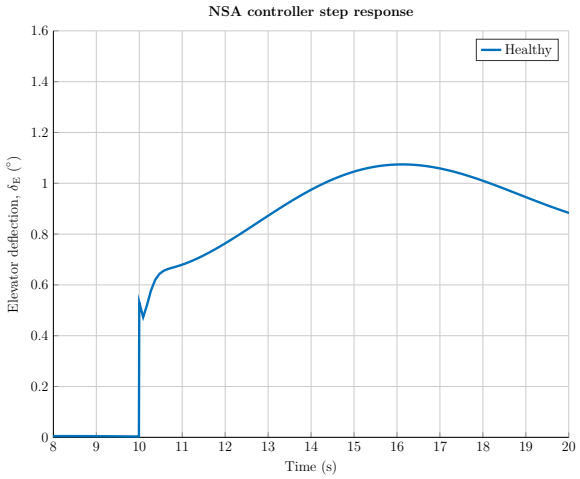

(b) NSA step actuator deflection

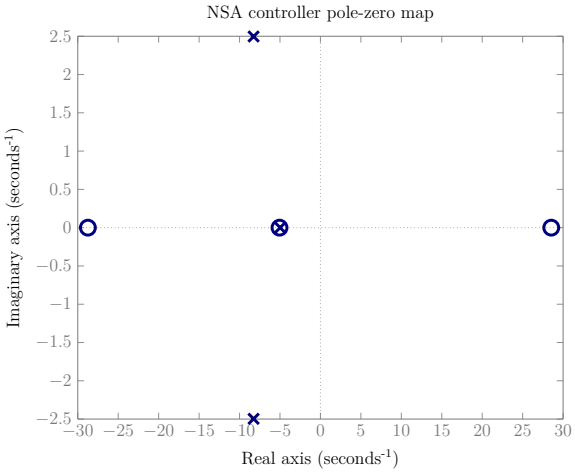

(c) NSA controller closed-loop poles

Figure 5.15: NSA controller plots

changed during the step response. This deflection was well within the range of the actuator limits.

Based on the design specifications for the NSA controller the closed-loop poles were expected to be a real pole located at -5.5 on the real axis, and a complex pole pair located at $-8.1 \pm 3.923j$. However, a number of approximations were made in the design of the NSA controller, such as the fact the reduced-order model was used that assumed that the airspeed remains constant. This resulted in the closed-loop poles not being in the location they were designed for when applied to the full linear model of the aircraft. The actual closed-loop poles are a real pole at -4.979, and a complex pole pair at $-8.261 \pm 2.495j$. This resulted in the real closed-loop pole having a larger effect on the transient response, since it is no longer completely cancelled by the zero which was placed at its expected location.

5.2.1.3 Climb Rate Controller

The design specifications for the closed-loop controller are an overshoot of 0.14% and a 2% settling time of 1.3 s. The step response for the climb rate controller is shown in Figure 5.16a

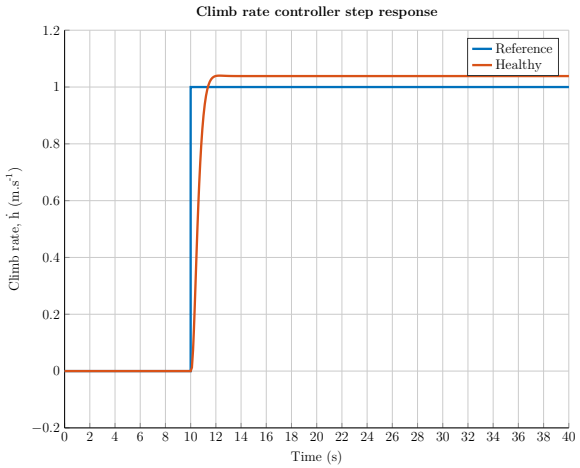

(a) Climb rate controller step

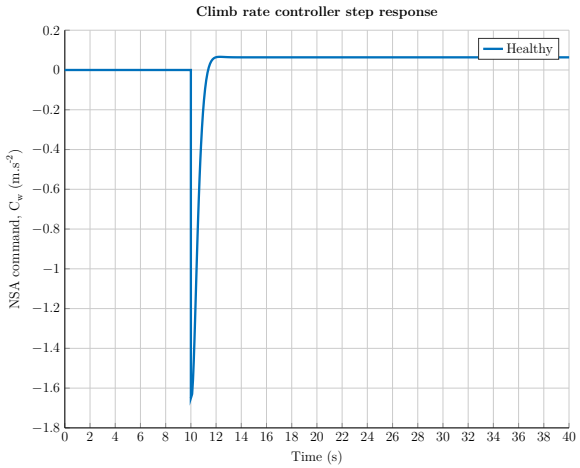

(b) Climb rate step actuator deflection

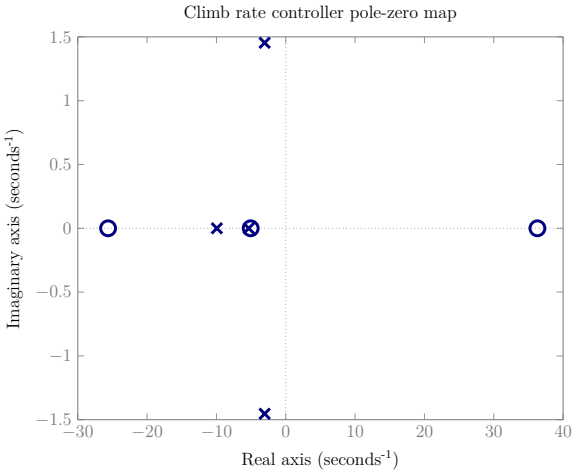

(c) Climb rate controller closed-loop poles

Figure 5.16: Climb rate controller plots

and exhibits a 0.1% overshoot and a 2% settling time of 1.52 s. Figure 5.16b shows the NSA command that was generated during the climb rate step response. This command was slightly larger than the step provided in the previous section (see 5.2.1.2), but would not saturate the elevator.

The response of the climb rate controller with the added integrator was desired to perform similarly to the proportional control. It was desired to keep the overshoot as small as possible while sacrificing the settling time. This allowed the altitude control to make use of the quick rise time and small overshoot to obtain the correct altitude. The step response of the aircraft with the included integrator will be discussed in Chapter 6.

Based on the design specifications for the climb rate controller, the closed-loop poles are expected at $-2.9 \pm 1.35j$, without taking the integrator that will be added later into account. The closed-loop poles of the climb rate controller for the healthy configuration as well as over all damage cases are plotted in Figure 5.16c. The plot shows that for the healthy configuration dominant poles were located slightly off from where they were expected at $-3.05 \pm 1.48j$.

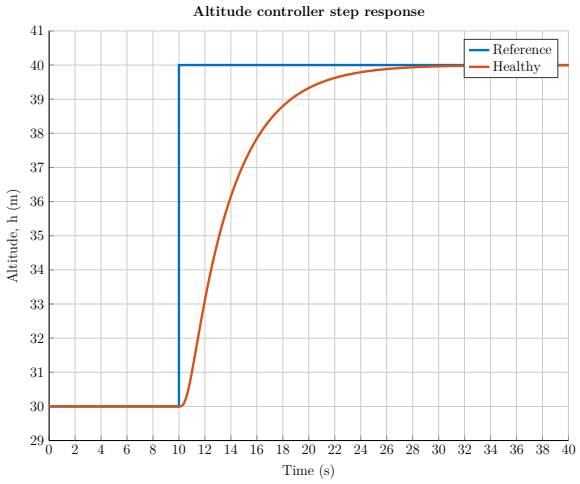

(a) Altitude controller step

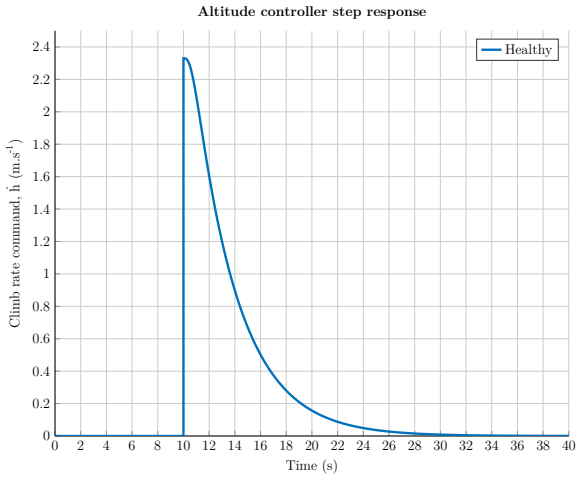

(b) Altitude step actuator deflection

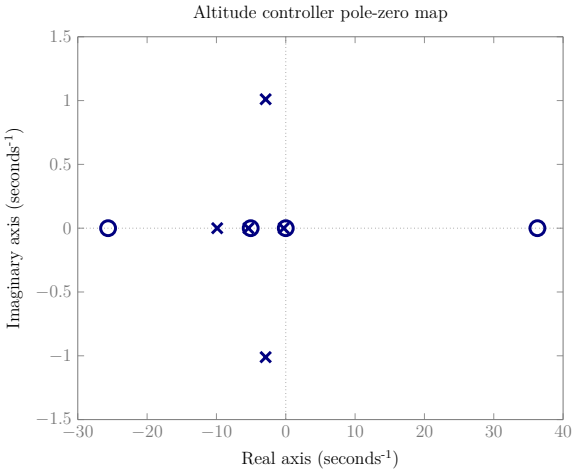

(c) Altitude controller closed-loop poles

Figure 5.17: Altitude controller plots

5.2.1.4 Altitude Controller

The design specifications for the altitude controller are a 2% settling time of 13.7 s and no overshoot. The step response for the altitude controller is shown in Figure 5.17a and exhibit no overshoot, and a 2% settling time of 14.17 s. The overshoot of the altitude controller is expected to increase when the integrator is added to the climb rate controller. The altitude controller is therefore designed very conservatively to have less overshoot before the integrator is added. The climb rate command generated by the altitude controller is shown in Figure 5.17b. This command had a relatively small peak, significantly less than the climb rate step that was previously discussed (see 5.2.1.3).

Based on the design specifications for the altitude controller, its dominant closed-loop pole is expected to be at -0.291 on the real axis. The closed-loop poles of the altitude controller for the healthy configuration as well as over all damage cases are plotted in Figure 5.17c. The plot shows that for the healthy configuration the dominant pole was located at -0.292.

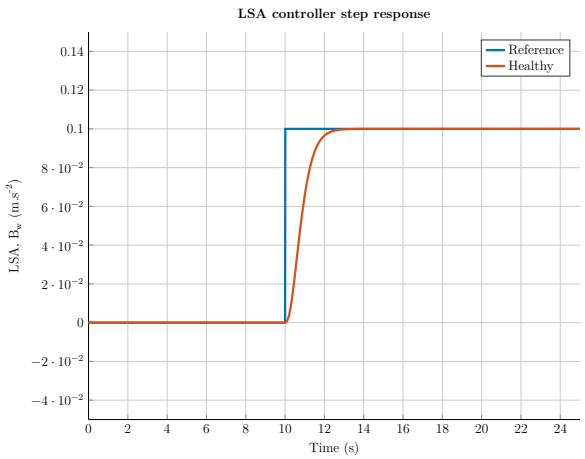

(a) LSA controller step

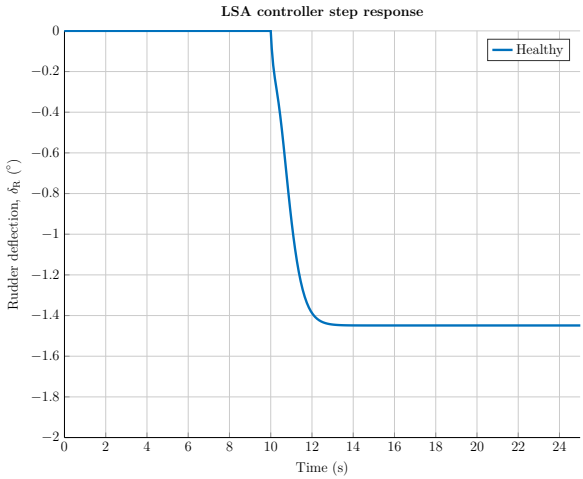

(b) LSA step actuator deflection

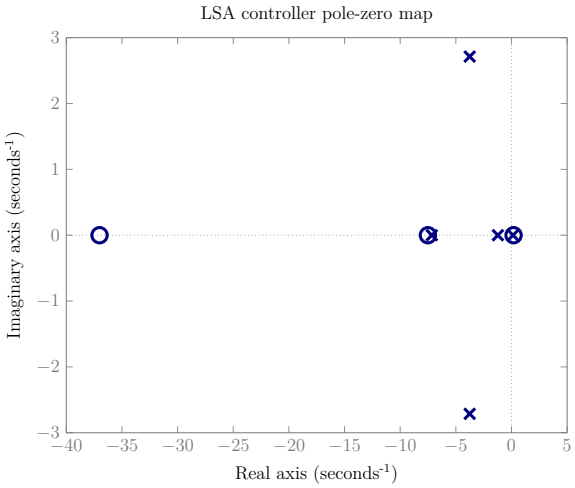

(c) LSA controller closed-loop poles

Figure 5.18: LSA controller plots

5.2.1.5 Lateral Specific Acceleration Controller

The design specifications for the LSA controller are no overshoot, and a 2% settling time of 3.3 s. The step response of the LSA controller is shown in Figure 5.18a an exhibits no overshoot, and a settling time quite a bit faster than the design specification at 2.2 s. The rudder deflection is shown in Figure 5.18b for the LSA step. This shows a fairly large actuator deflection for a fairly small lateral acceleration. This could prove problematic for damage cases where the vertical stabiliser is smaller in size. The LSA controller, like the NSA controller, made use of a reduced-order model. This resulted in the final pole locations not being as accurate as was designed. The design of the LSA resulted in poles at -4.6 and -0.6 on the real axis. The actual system after augmentation resulted in the poles at -7.16 and -1.22. The large difference was due to the reduced-order simplified model that was used to determine the controller gains. This also explains the faster settling time as the resultant system poles are located at a higher frequency. This is due to a significant difference in $\frac{\partial \dot{R}}{\partial \beta}$ (18.65 for the reduced-order model and 16.49 for the full linear model) and $\frac{\partial \dot{R}}{\partial R}$ (-1.12 for the reduced order model and -0.86 for the full linear model) between the reduced-order model and the full linear model.

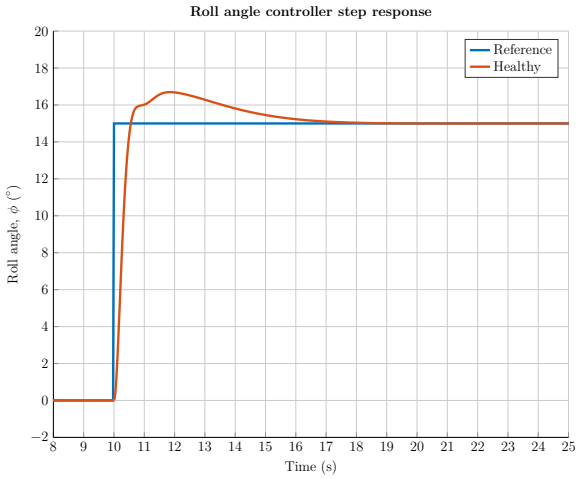

(a) Roll angle controller step

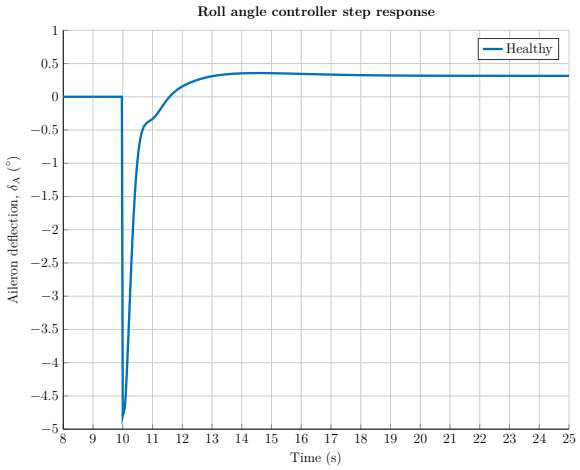

(b) Roll angle step actuator deflection

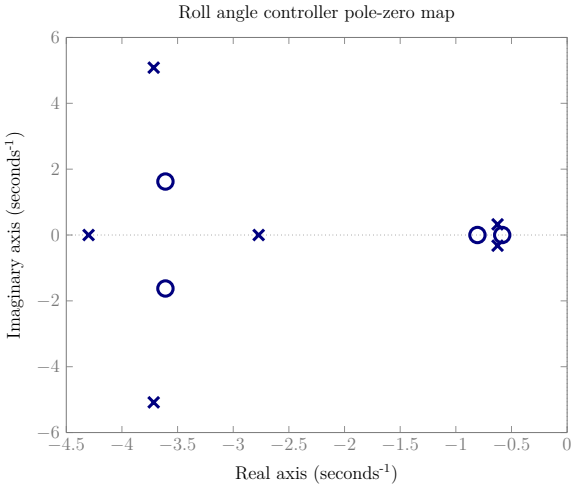

(c) Roll angle controller closed-loop poles

Figure 5.19: Roll angle controller plots

5.2.1.6 Roll Angle Controller

The design specifications for the roll angle controller are an overshoot of 0.23% and a settling time of 6.4 s. There was however a zero very close to this pole pair, which increased the overshoot of the system. The step response of the roll angle controller is shown in Figure 5.19a and exhibits an 11.3% overshoot and a settling time of 5.63 s. The overshoot was larger than expected but could not be avoided with this controller architecture. The PI control method introduced a zero to the system resulting in this increased overshoot. The settling time of the system was still within the desired specification. Figure 5.19b shows the aileron deflection during a roll angle command. This deflection was fairly large, as was expected, to generate the quick roll angle response. However, the deflection was still within the aileron actuator limits of the aircraft.

Based on the design specifications for the roll angle controller, the desired closed-loop poles were located at $-0.625 \pm 0.327j$. The actual poles on the full augmented system were located at $-0.6252 \pm 0.3239j$ as shown in Figure 5.19c.

5.2.1.7 Cross Track Controller

The design specifications for the cross track controller are no overshoot and a settling time of 9.26 s. The step response for the cross track controller is shown in Figure 5.20a and exhibits no overshoot and a settling time of 11.18 s. A limited integrator was later added to help remove any steady-state error that might have occurred due to external disturbances or biases on the sensors. This integrator was tested in the hardware simulations to have as little effect as possible on the response of the controller while still allowing the zero steady-state error. Figure 5.20b shows the roll angle command during a cross track step. This indicates a relatively small roll angle, which the roll angle controller is capable of commanding. The roll angle from the guidance controller was limited in firmware to not exceed safe roll angle commands. The complex pole pair from the design is located at $-0.346 \pm 0.132j$. The resultant poles after the plant augmentation are located at $-0.4318 \pm 0.09482j$. This shows a difference between the design specifications and the full linear pole positions. The damping ratio was designed to be 0.934 and ended up at 0.977, while the natural frequency was designed to be $0.37\,\text{rad.s}^{-1}$ and ended up at $0.44\,\text{rad.s}^{-1}$. This difference is not an issue as it results in a higher damping ratio and increased frequency response.

This shows that the controller design is valid even though it was designed using the decoupled system. The next part of this section will investigate the positions of the closed-loop poles and step responses for the nominal damage case.

5.2.2 Robustness of Controllers to Partial Stabiliser Loss

This section carries a report on the stability of the controlled damaged aircraft, which was investigated and evaluated relative to the healthy aircraft. The step responses of the nominal aircraft damage configuration are compared to the healthy responses from Section 5.2.1. Closed-loop pole clouds for all the damage cases are also presented to be compared to the closed-loop poles of the healthy aircraft configuration. All the damage cases are considered in the closed-loop pole plots under the assumption that the aircraft can be trimmed for each damage case.

5.2.2.1 Airspeed Controller

The step response, throttle command and closed-loop poles for the airspeed controller on the nominal damage configuration is shown in Figures 5.21a to 5.21c. The step response had no noticeable difference in transients from the healthy aircraft configuration. This was expected as damage to the aircraft stabilisers do not influence the airspeed dynamics of the aircraft. The dominant pole of the airspeed controller moved from -0.65 on the real axis to -0.569.

5.2.2.2 Normal Specific Acceleration Controller

The NSA controller was designed to be rather aggressive and not very robust; therefore, these poles were expected to move significantly more than from the other controllers as the NSA controller relies on very a specific model. The robustness of the NSA controller is shown in

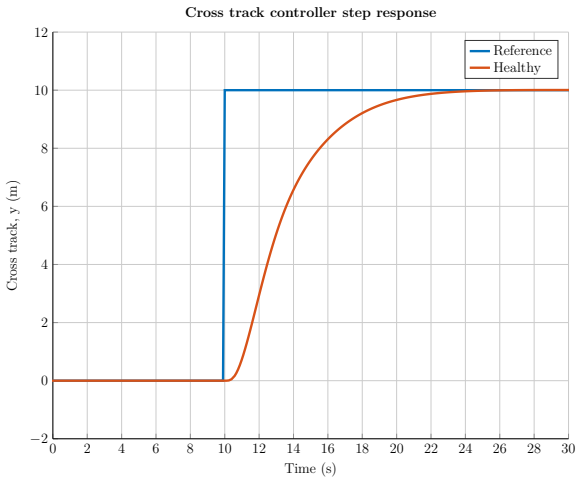

(a) Cross track controller step

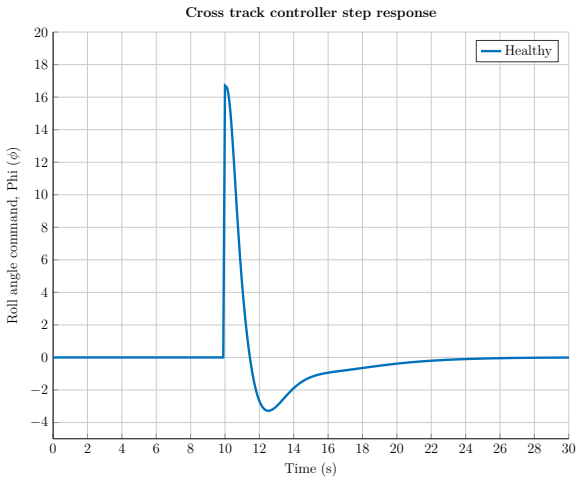

(b) Cross track step actuator deflection

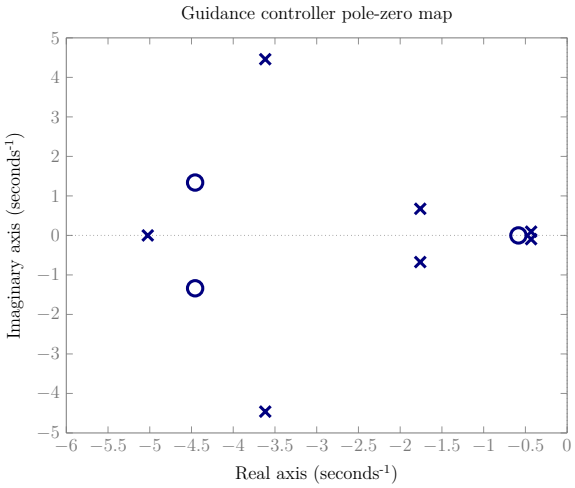

(c) Cross track controller closed-loop poles

Figure 5.20: Guidance controller plots

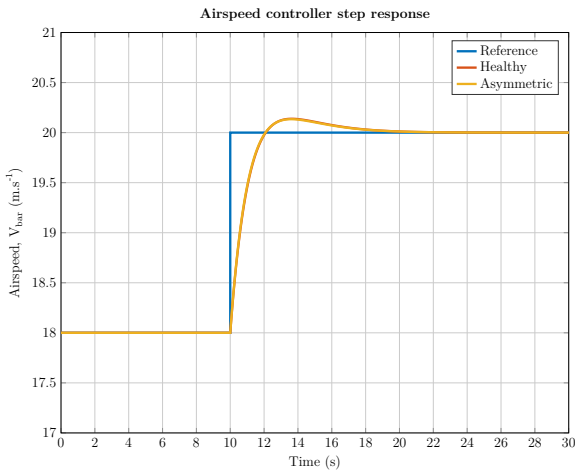

(a) Airspeed controller step

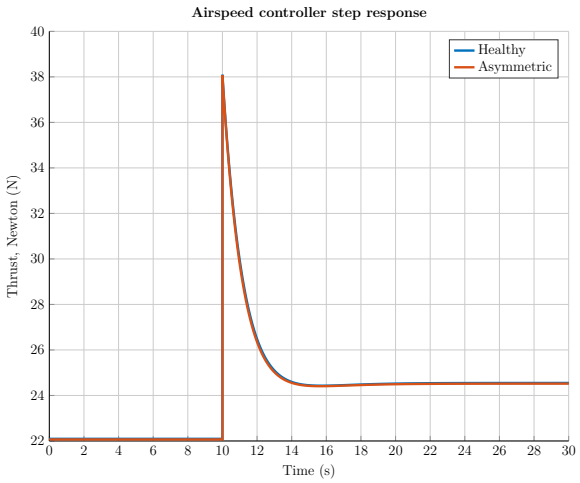

(b) Airspeed step actuator deflection

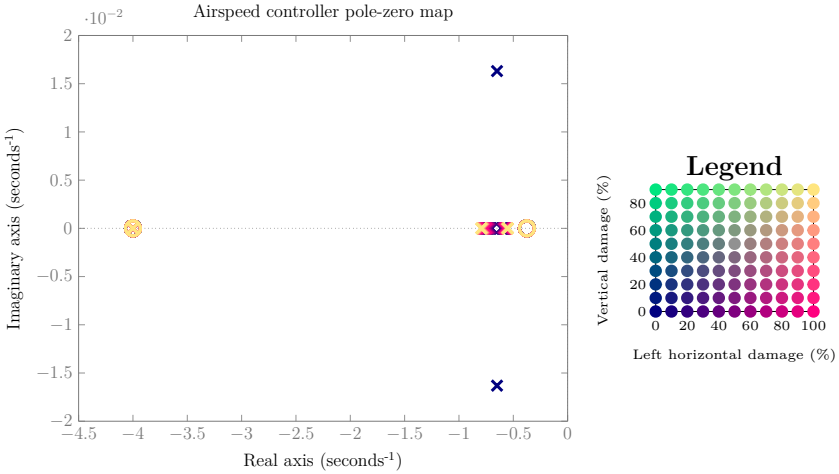

(c) Airspeed controller closed-loop poles

Figure 5.21: Airspeed controller plots

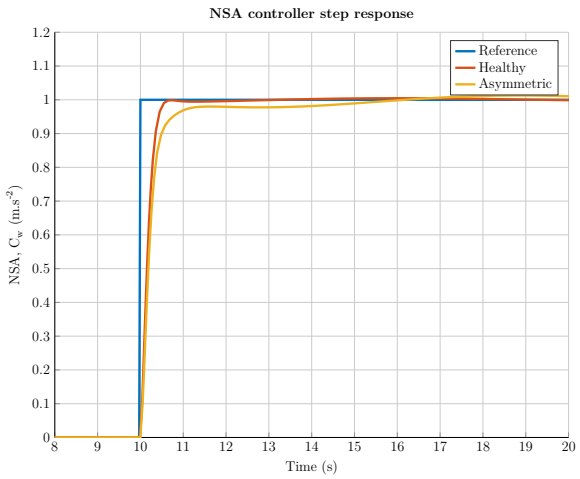

(a) NSA controller step

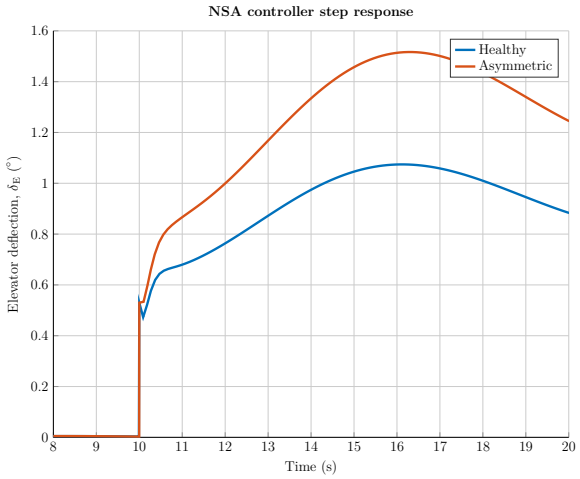

(b) NSA step actuator deflection

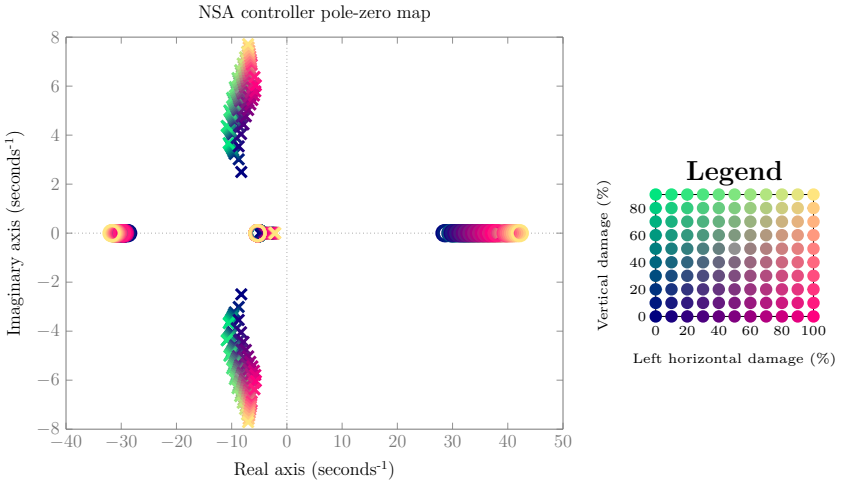

(c) NSA controller closed-loop poles

Figure 5.22: NSA controller plots

Figure 5.22a to 5.22c. The step response is shown in Figure 5.22a with the input signal (elevator deflection) shown in Figure 5.22b. In the case of the asymmetric aircraft, the NSA response was noticeably slower than that of the healthy one. The input signal to the system was also well within the operating regions of the aircraft actuator. While it was within the operating region, there was still significantly more deflection to achieve a similar NSA response. To avoid any issue regarding the actuator deflection, the maximum NSA command was limited in order not to saturate the actuator.

Figure 5.22c shows that the pole on the real axis moved from -8.465 to -3.056 and the complex pole pair moves from $-6.583 \pm 2.4j$ to $-7.148 \pm 6.182j$. This change was quite significant and explained the slower response seen in the step response of the system. The dominant pole became much slower than before, resulting in an overall slower response of the controller.

5.2.2.3 Climb Rate Controller

Figures 5.23a and 5.23b show the climb rate step and the input to the NSA controller for a step response of the climb rate controller. The asymmetric model had some overshoot introduced

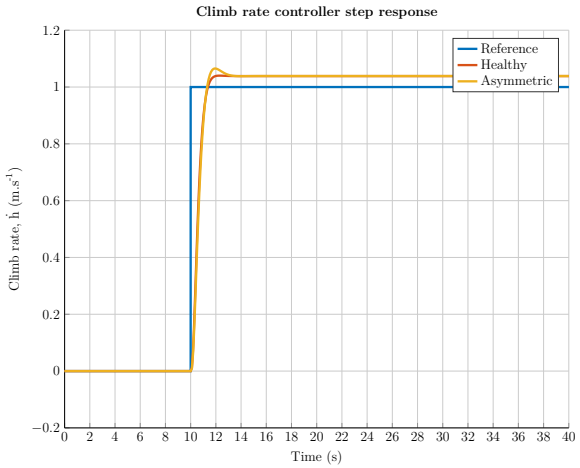

(a) Climb rate controller step

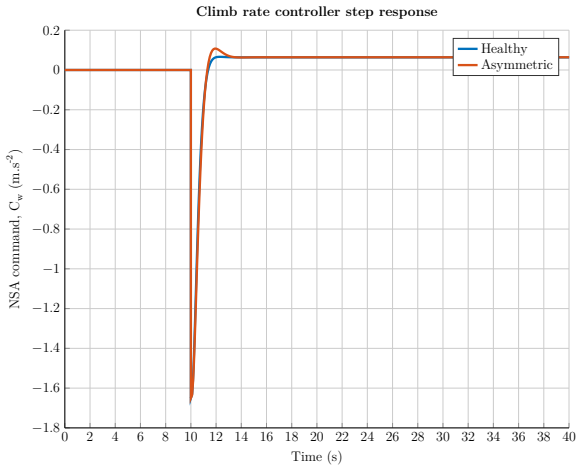

(b) Climb rate step actuator deflection

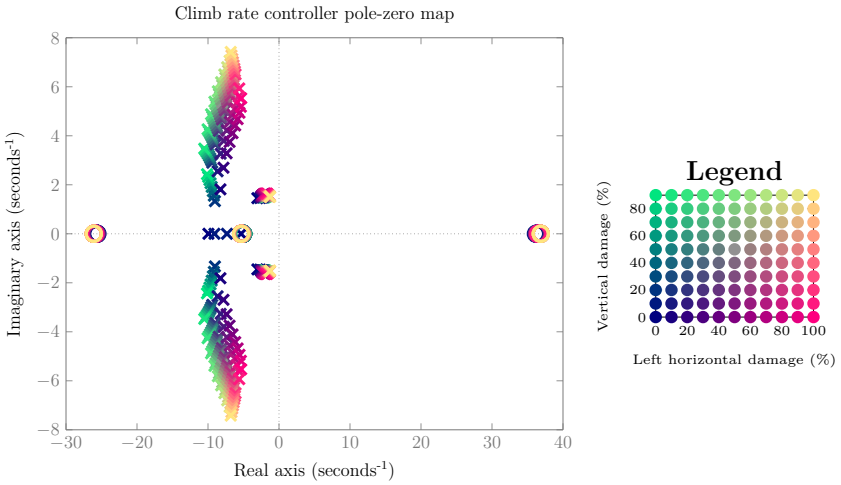

(c) Climb rate controller closed-loop poles

Figure 5.23: Climb rate controller plots

in the step response due to the reduced horizontal stabiliser resulting in the NSA controller not responding as the climb rate controller expected. While the NSA response of the aircraft changed, it was not significant enough to cause a problem with the aircraft control. It should be noted that the response in the hardware simulation will differ from this because of the integrator that was introduced and tuned from the simulation results to allow for zero steady-state error tracking.

The climb rate controller poles also changed quite significantly due to the inner-loop NSA poles having shifted as shown in Figure 5.23. The real pole that was located at -2.665 became a complex pole pair located at $1.995 \pm 1.515j$. This meant that more overshoot was expected as depicted in Figure 5.23a.

5.2.2.4 Altitude Controller

The altitude controller step response and plant input are shown in Figures 5.24a and 5.24b. The step response of the altitude controller was not noticeably affected due to the asymmetry of the aircraft. This was due to a small gain that was used.

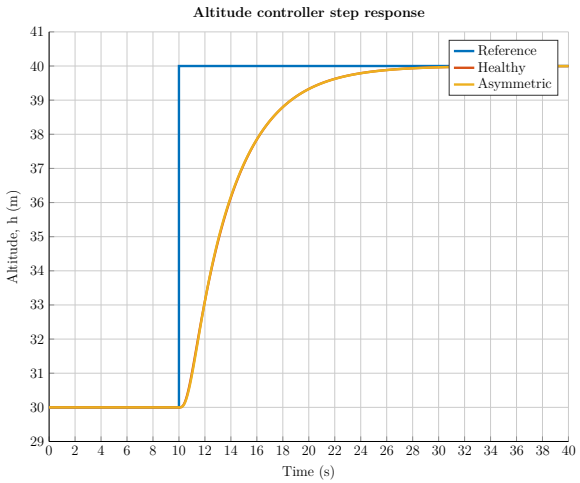

(a) Altitude controller step

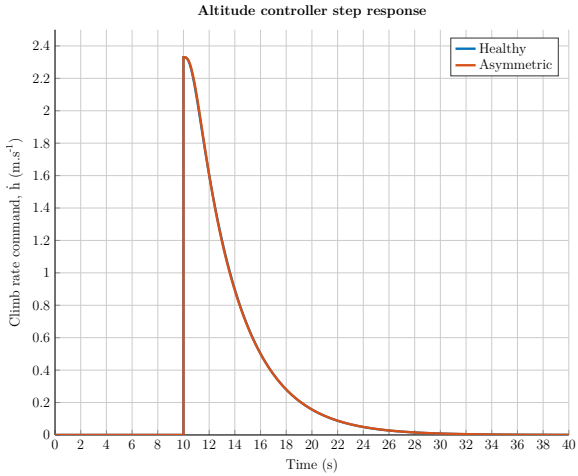

(b) Altitude step actuator deflection

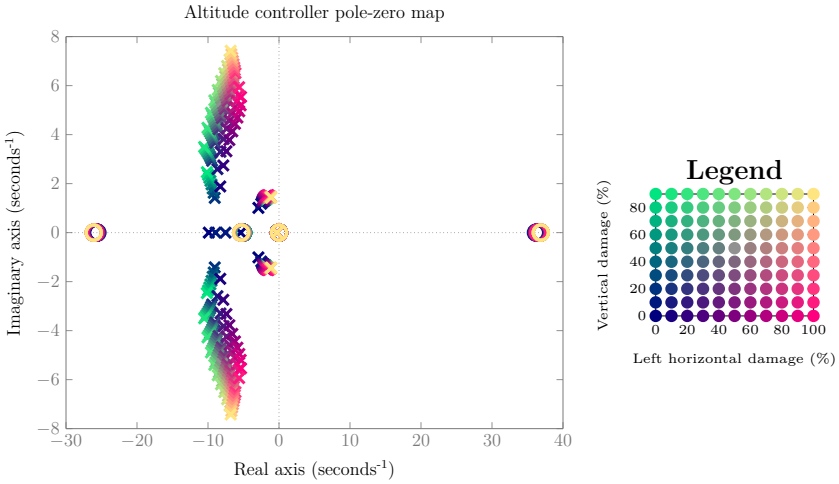

(c) Altitude controller closed-loop poles

Figure 5.24: Altitude controller plots

It is clear from the pole plot for the altitude controller in Figure 5.24c that this pole hardly moved as a function of percentage stabiliser damage on the aircraft, which agreed with what was seen in the step response. The altitude controller gain was chosen to be really small so as to improve the robustness of the altitude controller. This can be seen by the resulting pole only moving from -0.2944 to -0.2902. This change was not significant and resulted in the outer-loop altitude control performing as expected in both the healthy and nominal aircraft damage configurations.

5.2.2.5 Lateral Specific Acceleration Controller

Figures 5.25a and 5.25b depict the step response and the required actuator deflection for an LSA step. While the actual lateral acceleration step response did not differ much between the healthy and asymmetric case, there was a significant difference in the actuator deflection required to generate the same amount of lateral acceleration. This added to the limitation of the amount of vertical stabiliser loss that could be accommodated. The LSA was only in place to maintain the yaw of the aircraft and to damp the dutch roll motions of the aircraft. Under normal flying conditions, the LSA controller should be able to regulate zero lateral acceleration. In non-ideal weather, such as with wind or other external disturbances, the LSA controller might struggle more to regulate due to the large actuator deflection requirements.

For the nominal damage case, the dominant integrator pole of the LSA controller did not move much from -0.6 to -0.5592. The larger damage cases indicated a much larger change where this pole moved to around -0.13. This was due to the LSA controller being designed fairly slow to help with robustness as the rudder is the main yaw-inducing actuator and necessary to ensure lateral stability in yaw. The complex pole pair moved from $-4.14 \pm 2.52j$ to $-3.281 \pm 3.017j$ for the nominal case, and to $-0.196 \pm 2.32j$ for the worst-case tail damage. This clearly indicates the problem that arose as more of the vertical stabiliser was removed, indicating large oscillations and slow settling times. For larger damage cases, a more robust or alternative LSA controller should be implemented.

5.2.2.6 Roll Angle Controller

The roll mode of the aircraft was not expected to change drastically due to the inflicted damage and, as a result, the roll angle controller response was not expected to change significantly. Figures 5.26a and 5.26b show a roll angle step and the corresponding actuator command. There is no noticeable difference between the healthy and asymmetric model. This observation agrees with the fact that the dominant closed-loop pole for the roll angle controller hardly moved for the different damage configurations. The actuator deflection also had the same amount of travel in the different damage configurations, so the effect on performance was negligible.

Figure 5.26 shows the closed-loop poles for the roll angle controller. The roll angle controller was not affected significantly through loss of partial horizontal and vertical stabilisers. The dominant closed-loop poles — even after the inflicted damage — were very close to where they were designed to be. The poles moved from $-0.6249 \pm 0.327j$ to $-0.6293 \pm 0.3024j$. The higher

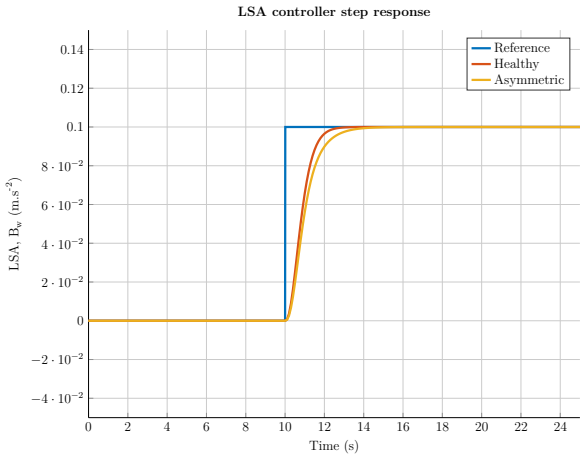

(a) LSA controller step

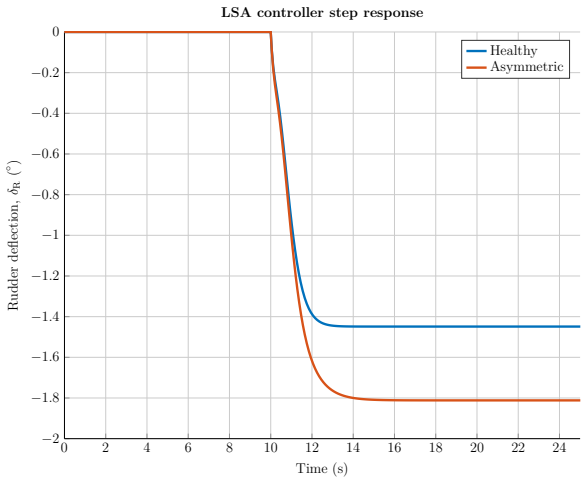

(b) LSA step actuator deflection

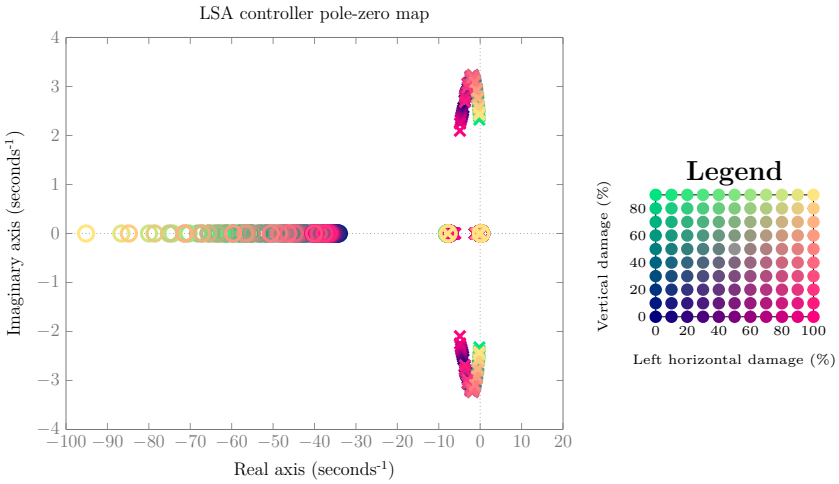

(c) LSA controller closed-loop poles

Figure 5.25: LSA controller plots

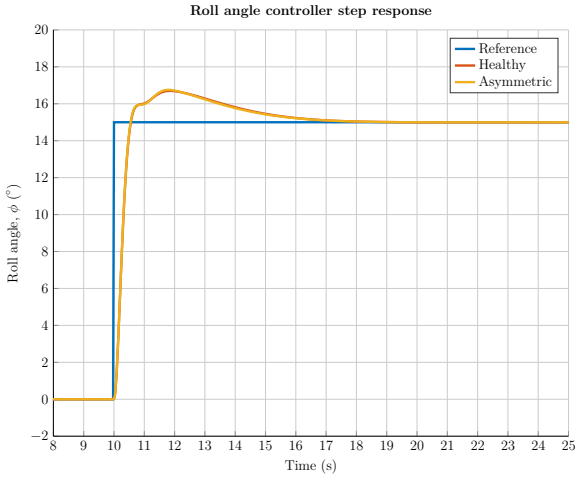

(a) Roll angle controller step

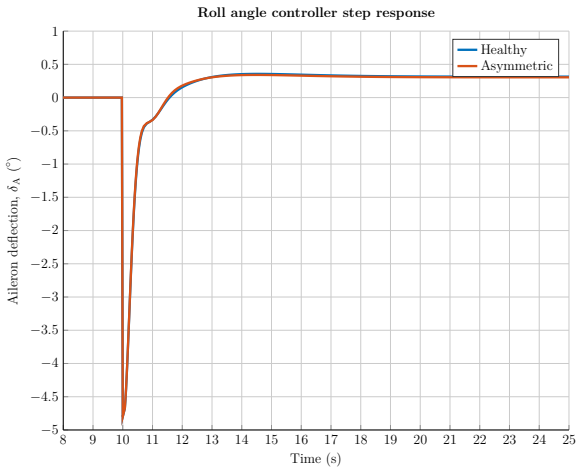

(b) Roll angle step actuator deflection

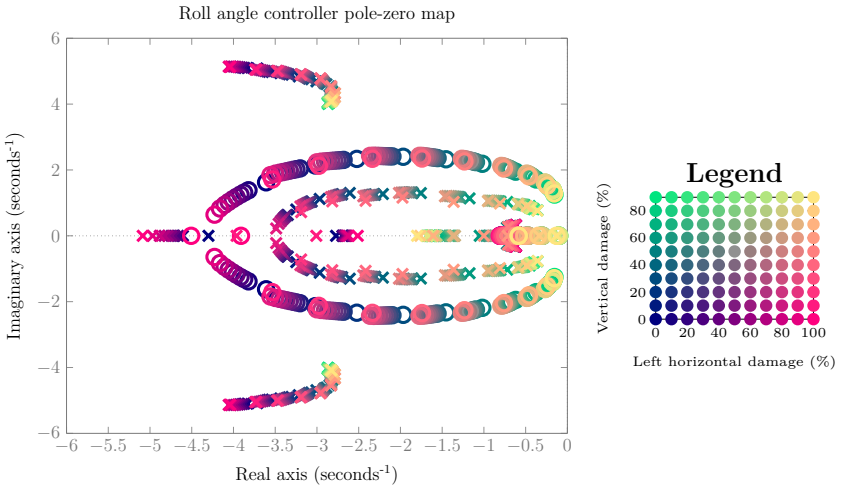

(c) Roll angle controller closed-loop poles

Figure 5.26: Roll angle controller plots

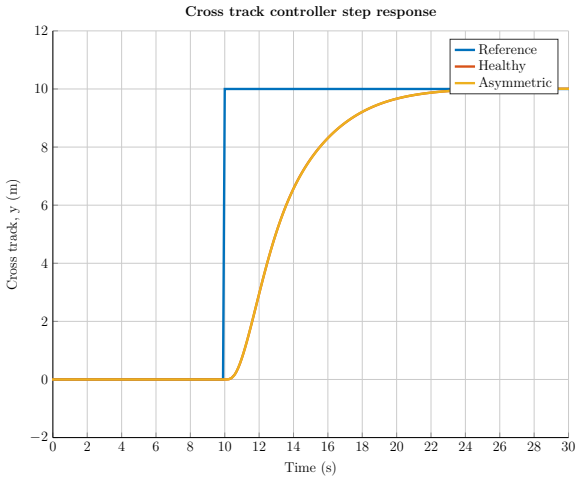

(a) Cross track controller step

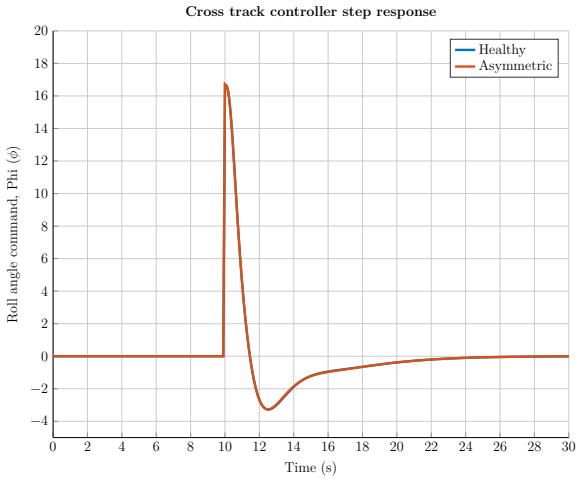

(b) Cross track step actuator deflection

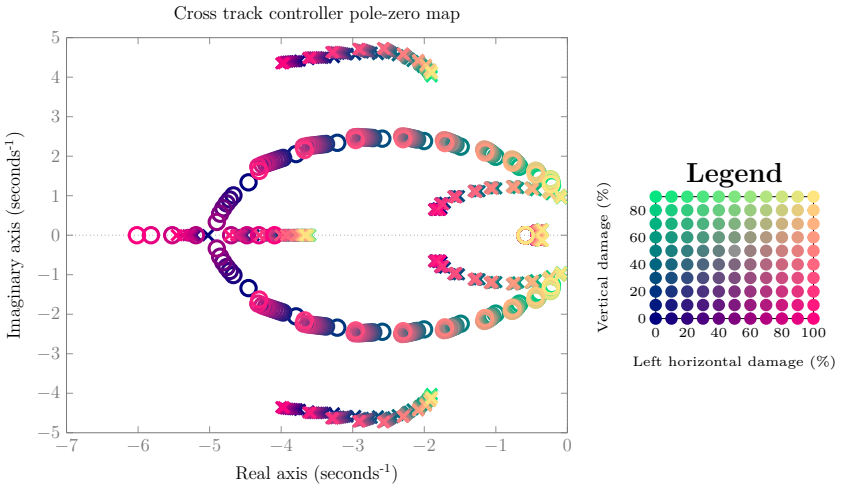

(c) Cross track controller closed-loop poles

Figure 5.27: Guidance controller plots

frequency poles of the aircraft moved around a bit more, but had very little influence on the performance of the controller.

5.2.2.7 Cross Track Controller

The step response for a cross track step command can be seen in Figure 5.27a and the input is shown in Figure 5.27b. With the roll angle controller being robust to the asymmetry of the aircraft, it was expected that the guidance controller would perform similarly to the healthy case, which it does. It should be noted that an integrator was be added during the hardware simulation. This introduced overshoot to the system and also slowed the system down.

The cross track controller poles also are located very close to where they were situated on the healthy aircraft. This was due to the small change on the inner roll angle controller that the cross track controller commanded. The dominant poles moved from $-0.4318 \pm 0.09482j$ to $-0.4287 \pm 0.0976j$.

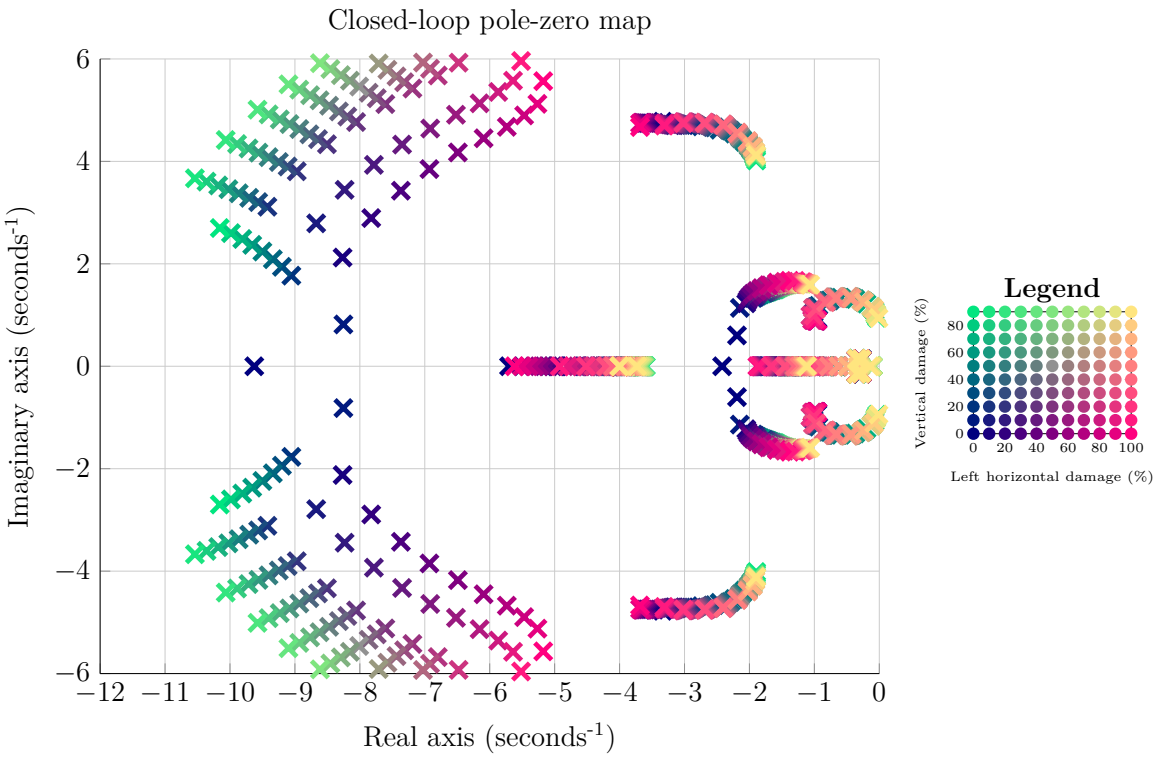

Figure 5.28: Closed-loop pole cloud

5.2.3 Closed-loop Pole Analysis

The closed-loop poles of the system were investigated to determine the robustness of the flight control system. Figure 5.28 shows a cloud of the closed-loop poles of the aircraft with all the longitudinal and lateral controllers added in. This agrees with Section 5.2.2 regarding the changes in the closed-loop poles due to the partial stabiliser loss. This also shows that as the horizontal and vertical stabiliser were partially removed, the closed-loop poles of the controllers of the system were still in the left-hand plane of the pole plot indicating that they were stable after the induced damage. The larger damage cases showed the plant poles nearing the right-hand plane and approaching instability. In these borderline cases, the aircraft might actually not have been stable due to the actuator limitations. Some of the inner-loop controllers on the damaged aircraft configurations had noticeable differences in their responses and pole locations when compared to the healthy one. However, the outer-loop controllers remained consistent in their response from the healthy to damaged configuration. This indicates that the control system is capable of controlling the nominal aircraft damage configuration.

The next chapter focuses on the implementation of these controllers on the hardware that was used for the practical flight testing, as well as full nonlinear simulation to provide insight into how the controllers performed with the full aircraft model.

§ 6

Hardware in the Loop Simulation

This section presents the hardware-in-the-loop (HIL) nonlinear simulation environment and results.

The HIL simulation allowed a full nonlinear simulation to be run to provide the OBC with simulated sensor information. This allows the real onboard computer hardware and software to be tested in a simulated flight. The HIL simulation also allowed the nonlinear aircraft model to be verified against the control system design specifications and linear model step responses.

A nonlinear aircraft model was set up in `Matlab Simulink` and connected to a HIL simulation board via a serial cable. This HIL simulation board in turn provided the OBC with all the simulated sensor data that the it would normally receive during practical operation (airspeed, attitude, GPS, heading, etc.) and also provided the simulation environment with the servo board and actuator outputs to run the simulation with the OBC-generated commands.

The HIL simulation environment allowed all the controllers that were to be used on the aircraft to be thoroughly tested and debugged before being implemented practically on the aircraft to reduce the risk in the practical flight testing.

First, the HIL simulations were performed on the different aircraft configurations, both healthy and damaged. These simulations included all the step responses for the different controllers to verify their performance before they were practically tested on a physical vehicle. These step responses were compared to the linear responses from Section 5.2, to identify whether there were any discrepancies in the performance of the controller.

Next, the transition from healthy to damaged configuration was simulated. This provided a baseline of the expected effects of the transition process on the aircraft. It allowed the control system to be tested with representative sensor noise, actuator lag and wind disturbances. The disturbances caused by wind and vibrations were disabled to prevent contamination of the results. This provided an indication of what could be expected in practical flight.

6.1 Nonlinear Simulation Results

This section reports on the implementation of the control system on the OBC as well as the HIL simulation results using the step commands that were also used in the practical flight tests for the assessment of the performance of the controllers. These step response results provided the expected responses under ideal conditions and also showed how the controllers would perform in a practical test. The HIL simulations allowed sensor noise to be simulated to show how the aircraft control system handled sensor noise. External disturbances, such as wind and vibrations, were not taken into account in these simulation results.

6.1.1 Controller Step Responses

This section presents the results obtained during the nonlinear simulation of the flight controller where step responses were carried out. This allows the effect of the nonlinearity on the flight controller to be investigated. These step responses are compared against the linear responses from Chapter 5 to identify any differences in the controller response.

6.1.1.1 Airspeed Controller

Figure 6.1 shows the step responses for the airspeed controller in the different damage configurations. As shown in Section 5.2 there was not much difference between the airspeed controller response for the healthy and damaged configurations. The step responses show a similar trend where the responses of the different configurations were very similar. Both the healthy and the asymmetric configurations had an overshoot of about 17% and a settling time of 7 s. This was more overshoot than expected from the full linear model but the settling time was around what it was expected to be. The larger overshoot could be attributed to the nonlinearity of the system. The linearisation assumptions also reduced the airspeed to $\overline{V} \approx U$, which was then used to design the control system. While there is a larger overshoot, the settling time is still within the design specifications.

6.1.1.2 Normal Specific Acceleration Controller

The NSA controller is not easy to test and it is risky to perform step response tests (in practice) as it controls an acceleration. Simply setting the NSA reference back to zero will not necessarily return the aircraft to straight and level flight. Figure 6.2 depicts the response of the NSA controller during a climb rate step to show the performance and ability of the NSA controller to track the reference command. The figure indicated almost no difference in the two responses as expected from the linear response shown in Section 5.2.

6.1.1.3 Climb Rate Controller

Figure 6.3 shows the step responses for the climb rate in the different damage configurations as well as their expected linear responses. Section 5.2 indicates that there was a slight difference

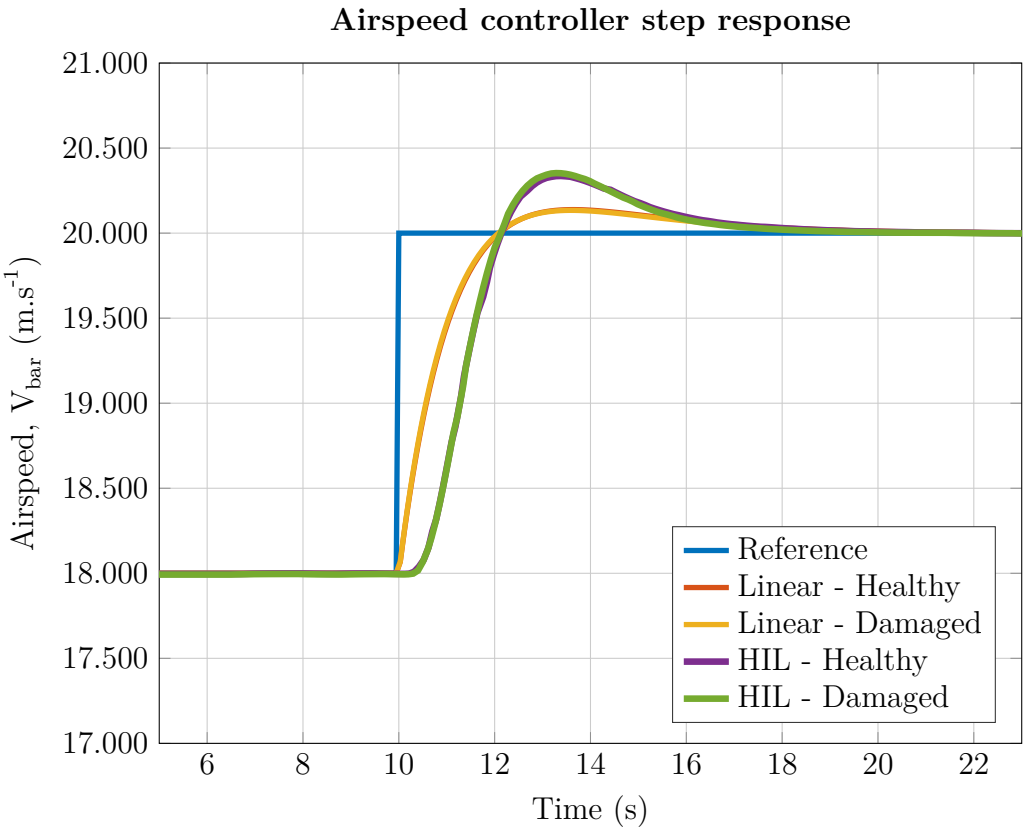

Figure 6.1: Airspeed controller step response

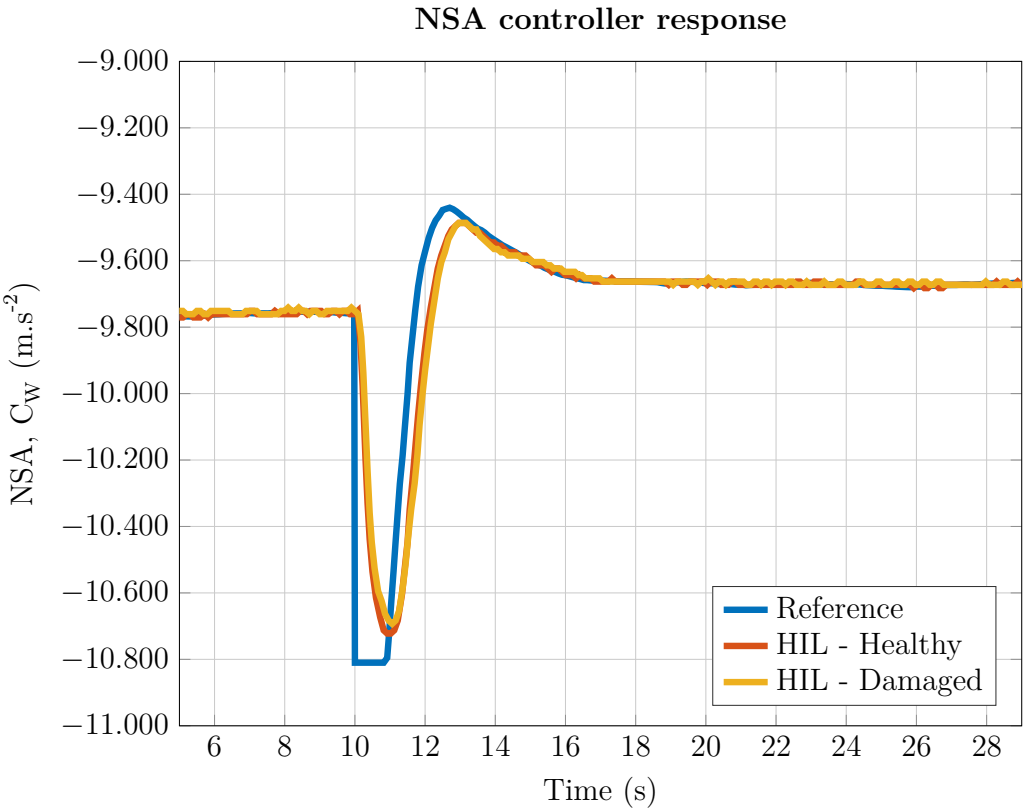

Figure 6.2: NSA controller response

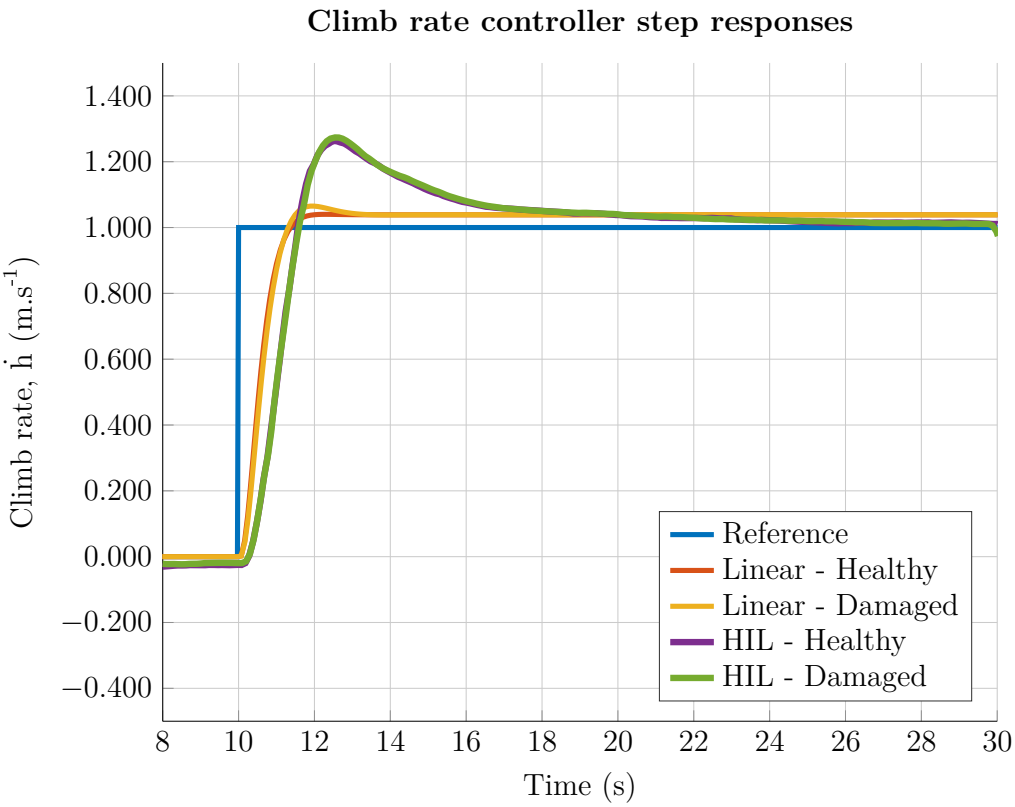

Figure 6.3: Climb rate controller step response

in performance between the healthy and asymmetric cases. In the present project there was a noticeable difference between the linear and HIL simulation results due to the added integrator in the system. The integrator was added to improve the steady-state tracking of the controller. This resulted in the controller being much slower than originally designed. A small integrator gain is used due to an initially slow and delayed measurement from the GPS providing the climb rate reading. The low gain was chosen to help with the robustness with the slow sensor and the damage case. This sensor was later upgraded, but there was insufficient time to redesign and test the climb rate controller to specification with the new sensor. Neglecting to add the integrator in the design process resulted in unexpected behaviour. The integrator was limited to reduce the effect it had on the transient response. However, the steady state tracking required these limits to be wider. If the integrator was included in the design process a more optimal controller could have been designed. This resulted in an overshoot of 26.3% and 27.7% and settling times of 14.5 s and 14.8 s for the different damage cases respectively. The overshoot was not too large, and the slow settling was not a problem in the end. The reference for the climb rate controller will be commanded by the altitude controller. The outer loop altitude controller made use of the quick rise time of the climb rate controller rather than the ability to settle quickly as is clear in Section 6.1.1.4. The damage however had a very small influence on the performance of the climb rate controller, allowing both cases to perform very closely to each other.

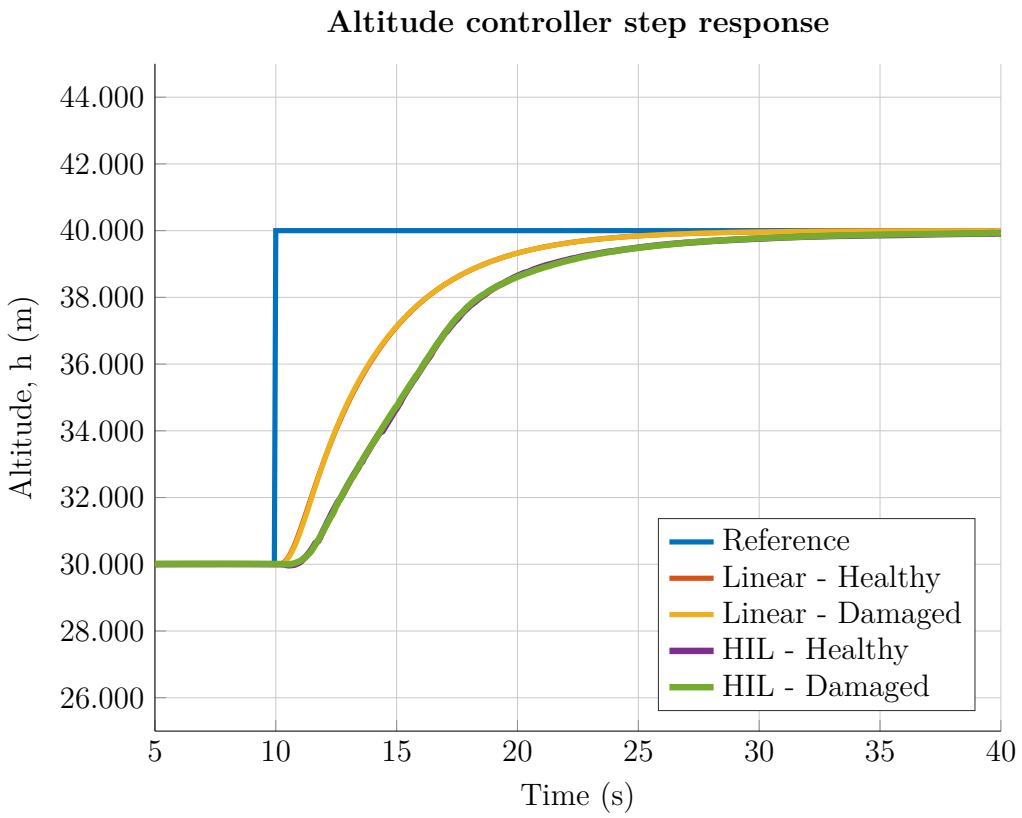

Figure 6.4: Altitude controller step response

6.1.1.4 Altitude Controller

Figure 6.4 shows the step responses for the altitude steps in the different damage configurations and the expected responses from the linear model. The linear responses in Section 5.2 reported almost no difference between the step responses of the healthy and damaged cases. The step responses agreed with this observation showing settling times of 18.6 s and 18.4 s for the healthy and damaged cases respectively. This settling time was slightly larger than what was originally designed for, but this was due to the added integrator on the climb rate controller resulting in a much slower response in the altitude controller as well. A climb rate limiter was implemented to prevent the aircraft from climbing too quickly and stalling, resulting in a slower rise time for large step commands. There was no overshoot in either of the configurations as expected from the linear simulation. While the larger settling time of the altitude controller was not ideal, it is clear that the longitudinal controllers were still stable when the aircraft was in both the healthy and damaged configurations.

6.1.1.5 Lateral Specific Acceleration Controller

The LSA controller acts as a regulator for the lateral acceleration experienced by the aircraft. As a result, the step response of the controller was not investigated. Figure 6.5 depicts the measured lateral specific acceleration after an induced rudder disturbance. With the LSA regulation enabled, the lateral specific acceleration transients settled faster than with no regulation. The exact transients cannot be measured from this signal as the inputs were not generated ex-

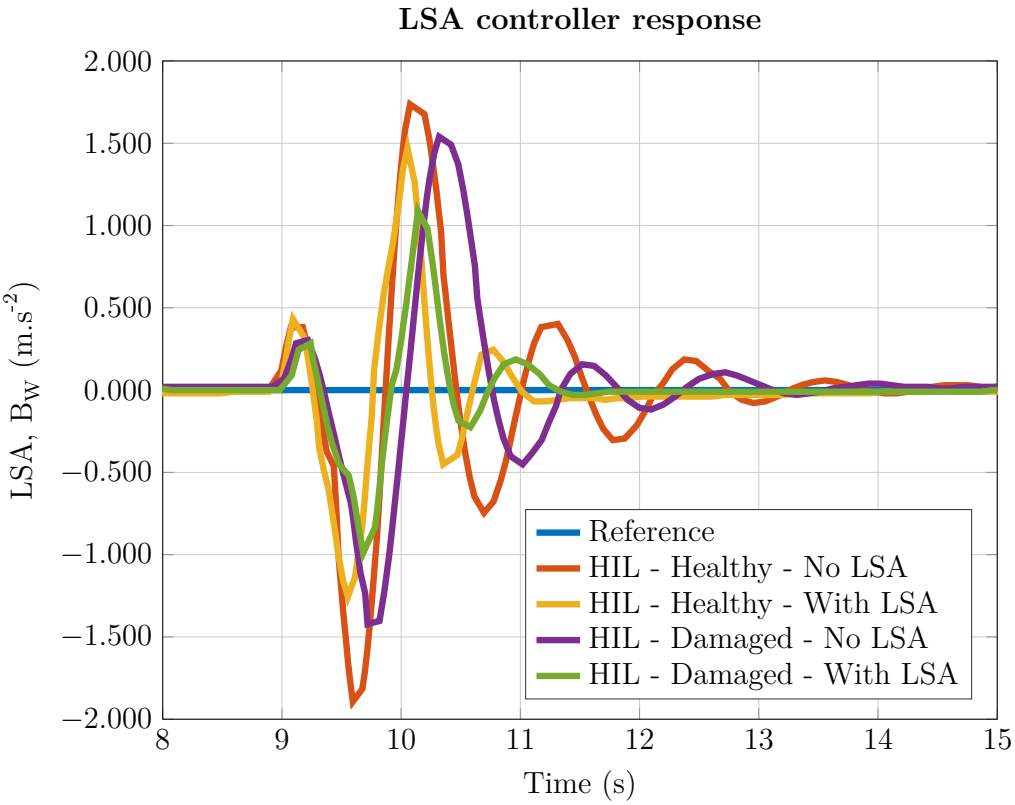

Figure 6.5: LSA controller response

actly the same for each test. When the LSA controller is enabled, the aircraft settles around 2.5 s faster than the open loop system. This shows that the LSA performs as expected when regulating a zero lateral acceleration.

6.1.1.6 Roll Angle Controller

Figure 6.6 depicts the different roll angle step responses. The linear step responses of Section 5.2 showed very little difference between the healthy and damaged cases, but this was not the case in the HIL simulation results. An overshoot of 18.8% and 26.5% and settling time of 5.4 s and 5.8 s were observed for the healthy and damaged nonlinear cases respectively. This was more overshoot than was expected from the linear model and was due to the usage of the full nonlinear aircraft model. This resulted in the elevator deflection coupling into it with the lateral dynamics when an NSA command is given during the roll. The LSA controller could also influence the roll of the aircraft because it tried to regulate the lateral acceleration of the aircraft to zero. These dynamics in turn affected the performance of the roll angle controller due to effects that were not modelled during the control system design and the verification on the full linear model. A limit was therefore put on the maximum roll angle command to prevent the aircraft from rolling too far and losing lift. The settling time was still around the expected value of 5.6 s, which allowed the controller to settle quickly enough and follow the bank angle commanded by the guidance controller.

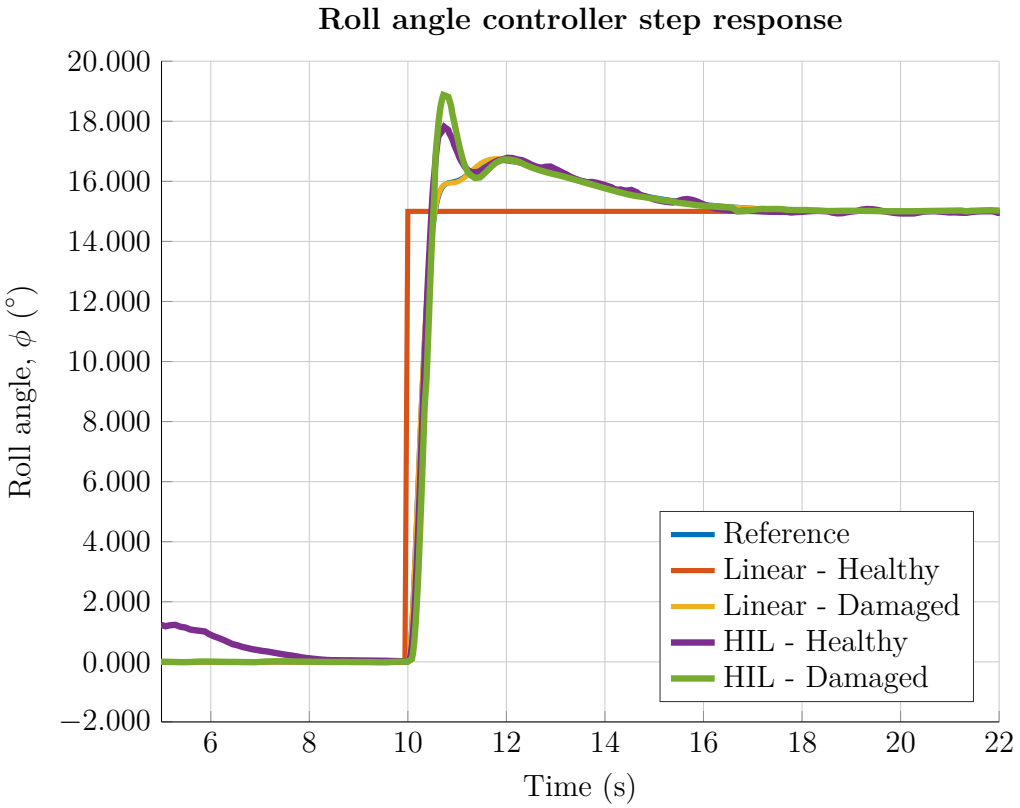

Figure 6.6: Roll angle controller step response

6.1.1.7 Guidance Controller

The guidance controller is mainly used for waypoint navigation and as a result, cross track step responses were not investigated. Figure 6.7 shows the a top down view of the path flown by the aircraft and the ability to follow waypoints. Figure 6.8 shows the NED path flown by the aircraft. This shows that the aircraft was able to follow waypoints successfully. This also showed that the waypoint navigation could be used in the practical flight test to test the transition. It would also ensure that all the aircraft controllers were active for the transition test.

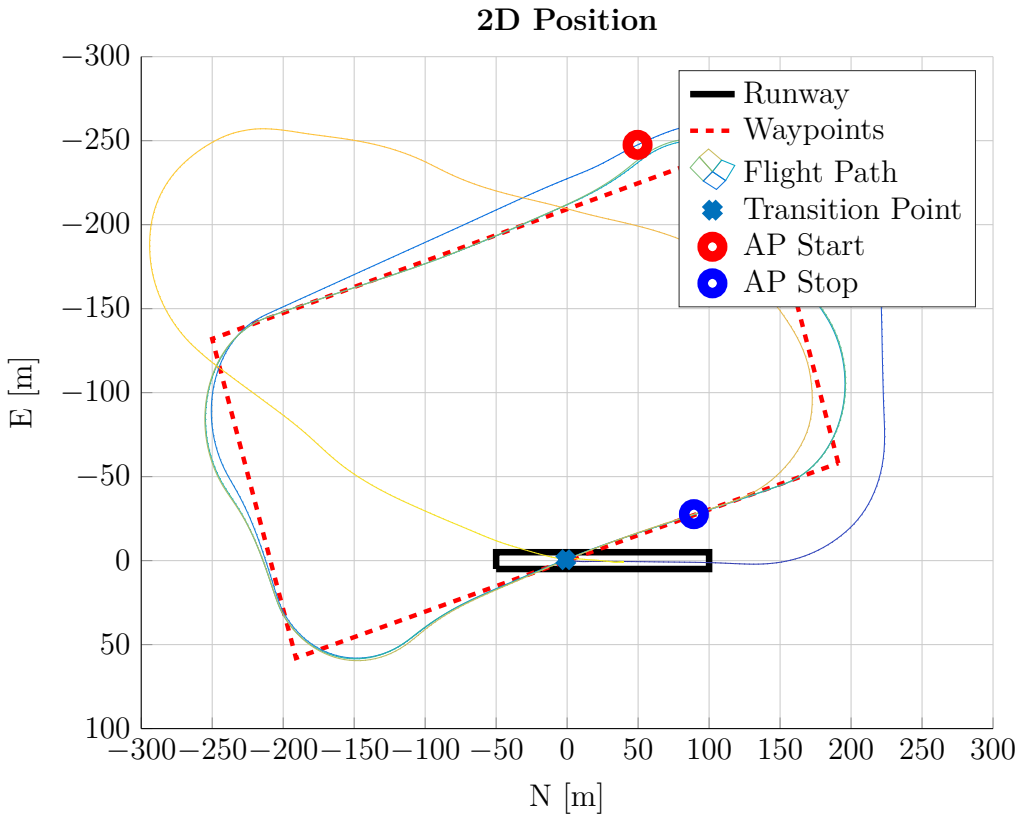

Figure 6.7: Guidance during damage transition — NE

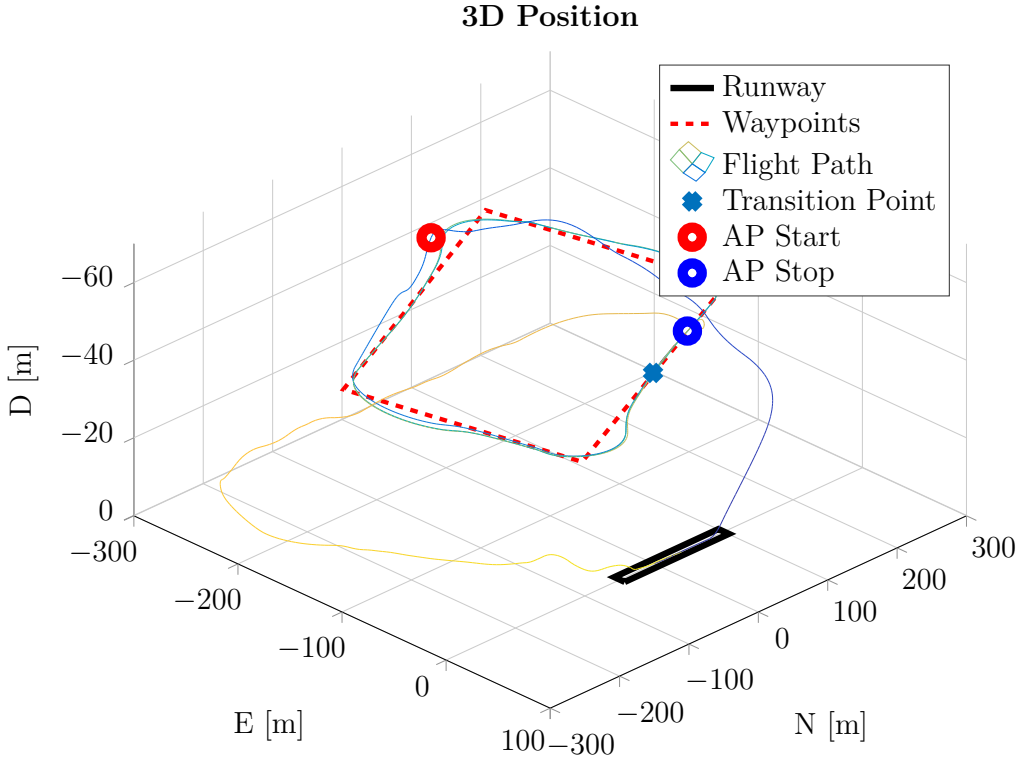

Figure 6.8: Guidance during damage transition — NED

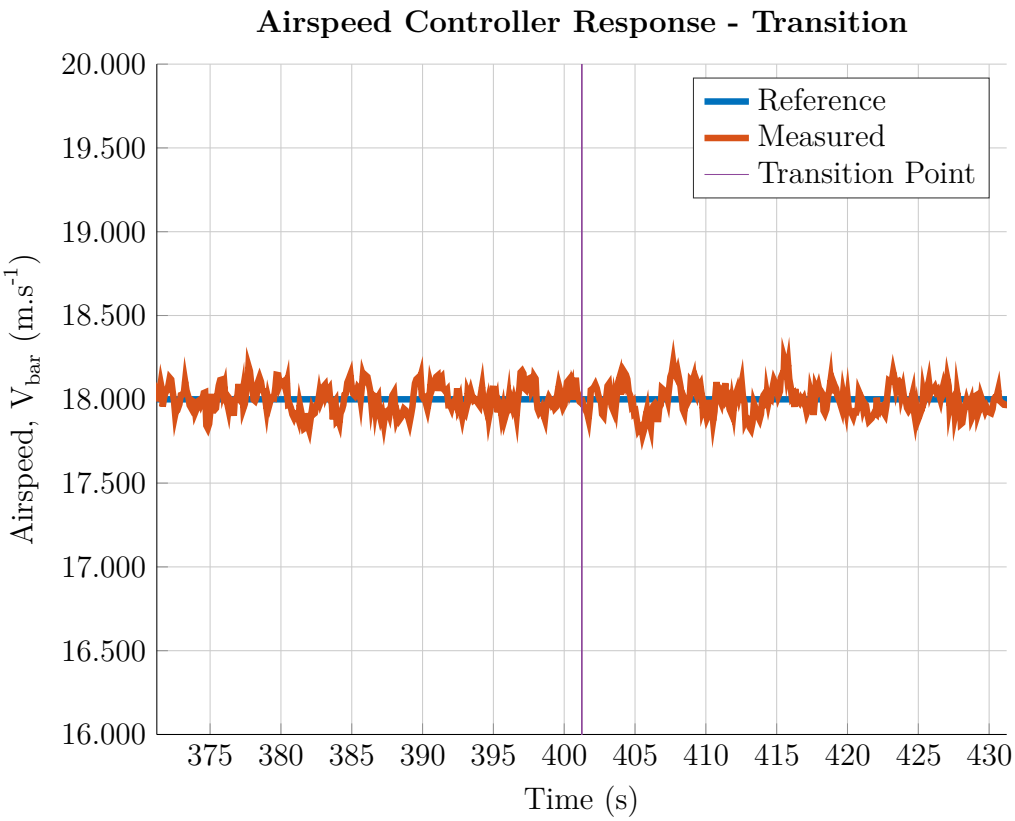

Figure 6.9: Airspeed during damage transition

6.1.2 In-Flight Transition for Healthy to Damaged Configuration

After the controllers were successfully tested on both the healthy and damaged aircraft configurations and provided satisfactory performance, the in-flight transition from the healthy configuration to the damaged configuration was tested. A simulation was performed where the horizontal and vertical stabiliser end-pieces were jettisoned from the aircraft in-flight to verify that the flight controller can find the new equilibrium point for the damaged aircraft, stabilise the aircraft about this new equilibrium point, and continue with the waypoint navigation. Figures 6.9 to 6.14b show the controller and actuator responses as well as the flight path when testing the transition from the healthy to the damaged configuration in HIL simulation.

6.1.2.1 Airspeed Response

Figure 6.9 shows the airspeed during the transition process. There was no noticeable effect of the transition on the airspeed of the aircraft. The behaviour of the airspeed controller was consistent before, during and after the transition. A change in airspeed was not really expected as the aircraft did not need to adjust airspeed to recover from the damage as indicated by the trim results (see 3.3.2).

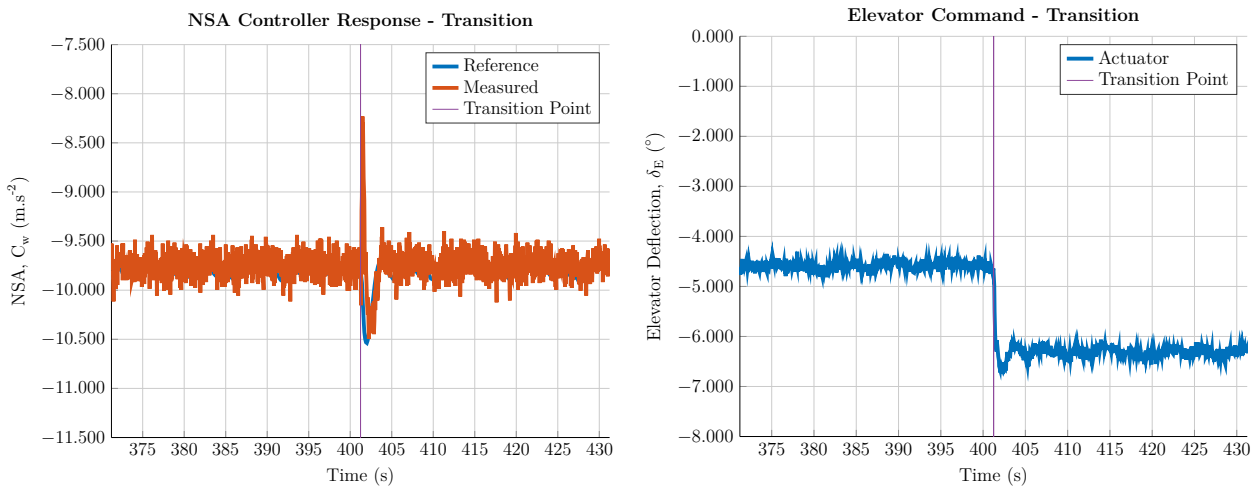

(a) NSA during damage transition

(b) Elevator during damage transition

Figure 6.10: NSA transients

6.1.2.2 Normal Specific Acceleration Response

The response of the NSA controller during the transition is shown in Figure 6.10a. As the transition occurred, there was a downward acceleration of the aircraft, as was expected due to the partial loss of horizontal stabiliser as well as the shift in CG. The NSA controller immediately commanded an upward acceleration to counter this behaviour. Figure 6.10b depicts the elevator deflection before, during and after the transition process. It can be clearly seen that the elevator commanded a larger deflection to generate the necessary angle of attack to maintain straight and level flight. This elevator deflection also agreed with the trim calculations shown in Section 3.3.2.

6.1.2.3 Climb Rate Response

The climb rate of the aircraft during the transition is shown in Figure 6.11 and further indicated that the aircraft started descending directly after the stabiliser are jettisoned. As a result, a positive climb rate was commanded in order to maintain the aircraft altitude. This agreed with the upward acceleration command given that the NSA controller received from the climb rate controller.

6.1.2.4 Altitude Response

The altitude controller response in figure 6.12 showed that, immediately after the transition, the aircraft lost some altitude. The aircraft then started to gain altitude again after the transition period and returned to to its original altitude. This altitude loss was very small and was not noticeable among the noise and disturbances of the practical flight test results.

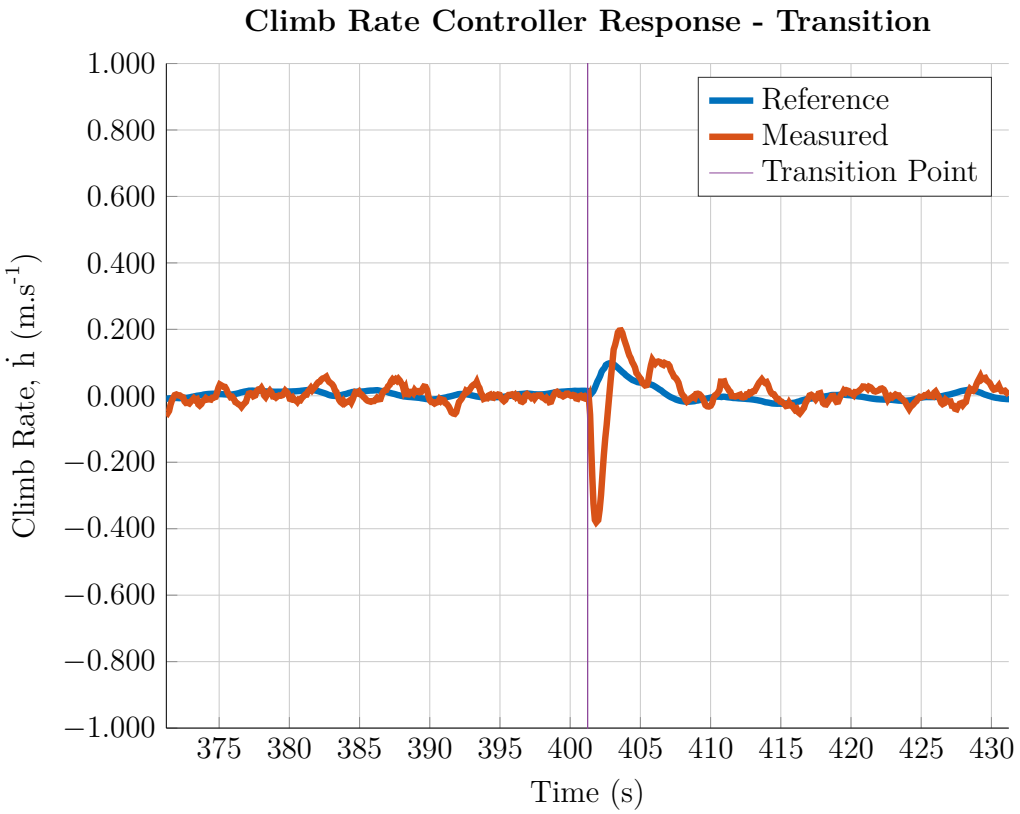

Figure 6.11: Climb rate during damage transition

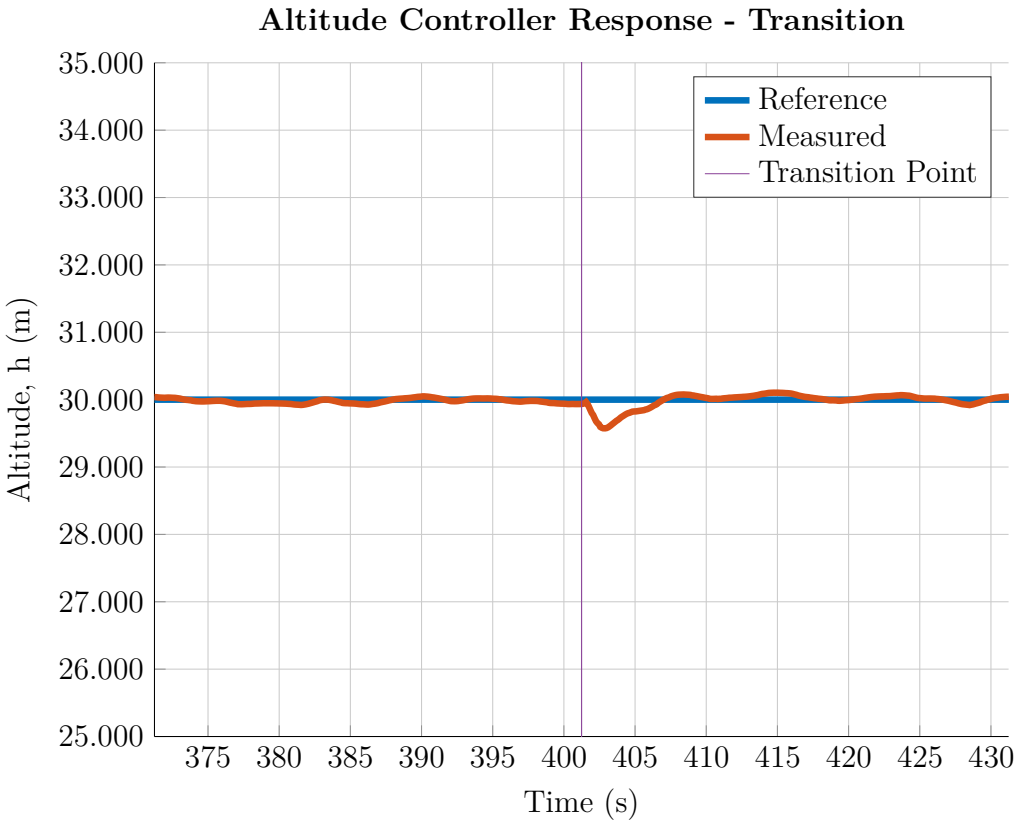

Figure 6.12: Altitude during damage transition

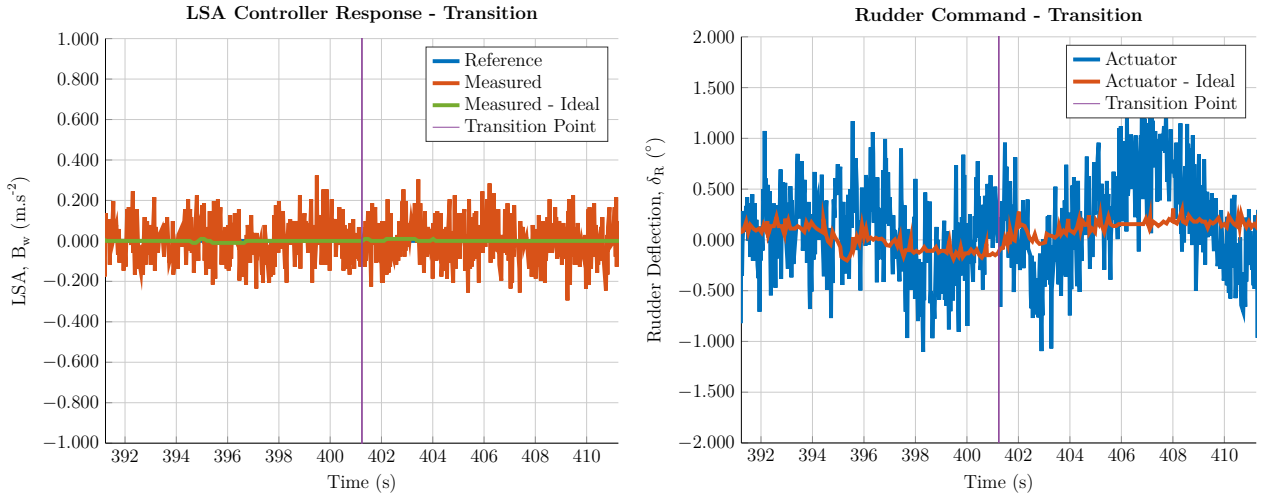

(a) LSA during damage transition

(b) Rudder during damage transition

Figure 6.13: LSA transients

6.1.2.5 Lateral Specific Acceleration Response

The LSA was not affected during the transition of the aircraft as shown in Figure 6.13a. This was expected as there was no direct effect on the lateral dynamics of the aircraft during the transition. The rudder response of the aircraft is depicted in Figure 6.13b. This figure shows that the trim changed slightly due to the asymmetry of the aircraft. From the trim calculation (see 3.3.2), it was expected that the rudder would have a slightly positive deflection in the damaged configuration. A separate HIL simulation was run to remove the sensor noise from the simulation. This shows that the rudder does move in the expected direction to approximately 0.25°.

6.1.2.6 Roll Angle Response

The aircraft experienced a small roll after the transition of the aircraft from healthy to damaged as shown in Figure 6.14a. This roll was caused by the shift in CG due to the partial horizontal stabiliser being removed. This moved the CG to the right of the aircraft resulting in a positive rolling moment. Figure 6.14b shows that the aileron trim changed from 0° to around 0.2°. This agreed with the trim of 0.215° for the nominal aircraft damage configuration shown in Table 3.8.

6.1.2.7 Guidance

Figure 6.8 shows the flight path of the aircraft for the HIL simulation of the transition response. The aircraft flew one circuit of the predefined track, triggered the release of the horizontal and vertical stabiliser end pieces and continued to fly another circuit before being landed under user control. This was a simulation of the final flight test investigation.

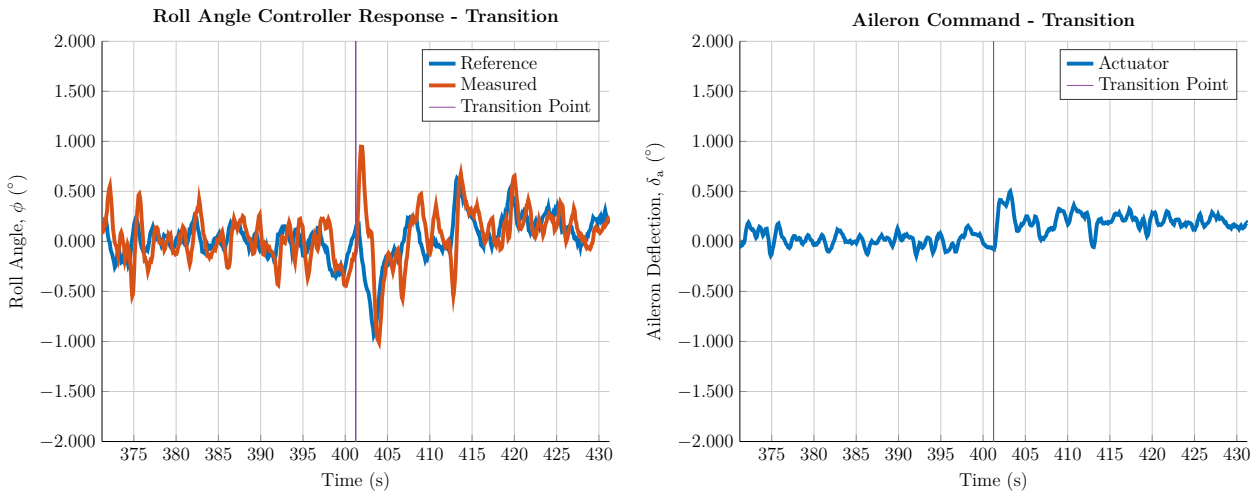

(a) Roll Angle during damage transition

(b) Aileron during damage transition

Figure 6.14: Roll angle transients

6.2 Conclusion

The HIL simulation results provided useful indications into how the aircraft should perform practically during a flight test and how well the different controllers should perform. It also allowed testing for bugs and identifying anomalous behaviour without the risk of actual flight testing. While some of the controllers did not perform to their design specifications, reasons for these performance discrepancies were identified, as was discussed in Section 6.1.1. Even though the performance was not as good as expected from the linear simulations, the aircraft does remain stable and matches a number of the linear transients even under the damage and asymmetry conditions which is the main focus of this project. The difference in transients between the linear results from Chapter 5 an the nonlinear results in this chapter are not very large. Where differences occurred, the reason for these differences was found. As a result the linear model provides a good approximation of the linear model to predict the performance of the model.

Chapter 7 reports on the performance of the controllers and the aircraft in real-world practical flight tests.

§ 7

Flight Tests

This chapter presents the flight tests that were performed to verify the performance of the control system practically on an actual healthy and damaged unmanned aerial vehicle (UAV).

First, an overview of the original UAV system that was used for the flight tests is given, and the modifications that were made to the aircraft to allow the testing of the partial horizontal and vertical stabiliser loss are discussed. The flight tests for the damaged aircraft were performed with 70% left horizontal and 20% vertical stabiliser loss, based on the trim and stability analysis results obtained and reported on in Chapters 3 and 4, as well as some initial investigative piloted flight tests. This nominal damage case was chosen as it was dramatic enough to present a reasonable challenge for the automatic flight control system, while remaining manageable enough for the safety pilot to be able to control the damaged aircraft manually to perform take-off, flight and landing and to recover in case of unexpected behaviour. A novel release mechanism was designed and implemented so that sections of the horizontal and vertical stabilisers could be ejected from the aircraft during a flight test.

Next, an overview of the flight test campaign is provided, and the detailed flight test results are presented and discussed. Incremental flight tests were performed to successively build up to and test the full longitudinal and lateral flight control loops on both the healthy and damaged aircraft. The flight tests culminated in full automatic flight control with airspeed control, altitude control and waypoint navigation for both the healthy and damaged aircraft configuration. For the final flight test, the aircraft started off in the healthy configuration, and then 70% of the left horizontal and 20% vertical stabiliser were jettisoned in flight to verify that the control system was able to handle dynamics present during the transition from the healthy to damaged aircraft configuration.

The practical flight test results showed that the flight control system was able to control the aircraft successfully in both the healthy and damaged configuration, as well as to accommodate the transition from the healthy to damaged configuration.

7.1 Research Vehicle Modifications

In order to achieve the outcomes of this project, modifications needed to be made to the aircraft to allow all the required testing. The aircraft and avionics system were discussed in section 1.5. The rest of this section presents the modifications that were necessary for this project.

7.1.1 Hardware Modifications to Represent Partial Stabiliser Losses

For this project, the horizontal and vertical stabilisers of the aircraft were modified to allow the transition from healthy to damaged aircraft configuration during flight. The necessary modifications added a significant amount of weight and, with the large moment arm due to the stabiliser position, a substantial counter-weight had to be added to ensure the aircraft was properly balanced. The increased mass of the aircraft necessitated the use of a larger battery to drive the main motor to increase the amount of thrust available for the aircraft. The release mechanism is discussed in more detail in section 7.1.2.

7.1.2 Release Mechanism

In order to get a complete representation of the performance of the controllers on the healthy and damaged state of the aircraft, it was necessary to be able to transition from a healthy state to a damaged one. It was possible for the aircraft controller to be able to control both the healthy and damaged configurations independently, which does not guarantee that it could handle a transition from the healthy to damaged configuration. In order to do this, portions of the horizontal and vertical stabilisers needed to be jettisoned off during flight. Beeton [7] made use of a servo locking mechanism to connect the main wing portion to the aircraft and allow mid-flight release. This solution requires a significant amount of space to house the mechanism allowing it to work in the aircraft wing. The profile of the aircraft stabilisers does not provide sufficient housing space or structural strength for this technique to be viable. A burn wire release mechanism used to deploy the solar panels in CubeSat projects was used to release the portions of horizontal and vertical stabilisers [21]. New horizontal and vertical stabilisers were manufactured and modified to provide the support and strength necessary to accommodate the release mechanism. The new horizontal stabiliser can be seen in the images in 7.1 showing the modifications that were necessary for a successful release.

The burn wire mechanism used a piece of nichrome (resistive) wire and nylon string. The nichrome was wrapped multiple times on a printed circuit board to make a coil. A voltage was applied to this coil, which caused the nichrome to heat up. The nylon string held the stabiliser pieces in place through connecting it to the body so that the nylon string lay over the nichrome. When the nichrome heated up, it melted the nylon string and released the stabiliser end pieces, allowing them to be jettisoned from the vehicle. Figure 7.2 shows the horizontal and vertical stabilisers and their connected release mechanism. The horizontal stabiliser image in Figure

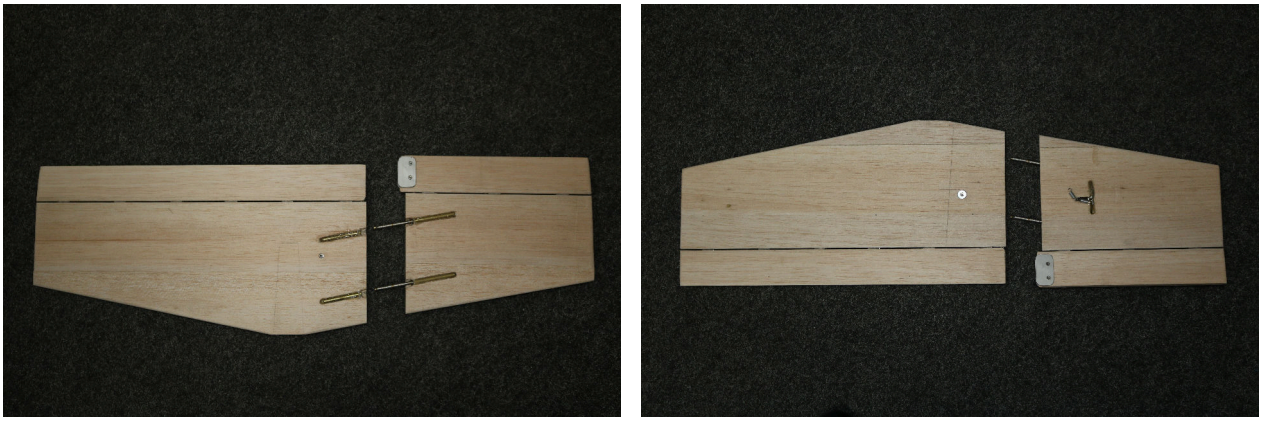

(a) Horizontal stabiliser — Top (b) Horizontal stabiliser — Bottom

Figure 7.1: Horizontal stabiliser modification

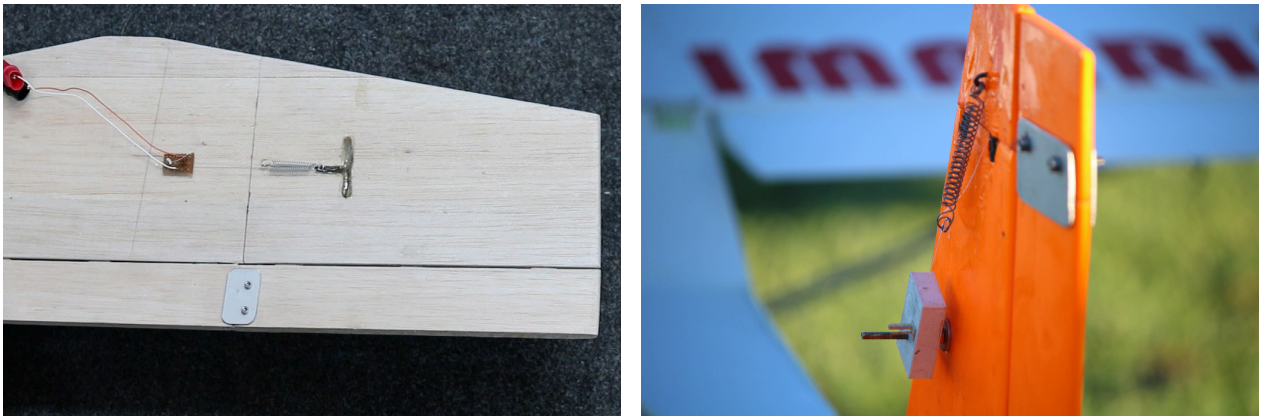

(a) Horizontal stabiliser connected (b) Vertical stabiliser connected

Figure 7.2: Partial stabiliser connections

7.2a shows the connection of the voltage source to the terminals of the nichrome for testing purposes.

There was a noticeable delay between triggering the release and when the release actually occurred. This was expected as the nichrome did not heat up instantly. The release mechanism was housed in a custom-made 3D printed box in order to concentrate the heat on the nichrome and not let the passing wind cool it down. On the ground with no wind, the release mechanism took around 1 s after the command had been given to release. In practical flight, the actual release occurred approximately 3 s to 4 s after being triggered. This delay was not ideal, but was still quick and predictable enough to ensure the aircraft was steady enough before releasing.

7.2 Flight Test Overview

This section presents an overview of the flight tests that were performed to verify the aircraft control system practically on an actual UAV, both in the healthy and damaged configuration. An overview of the flight test plan is presented followed by a chronological account of the execution of the flight test campaign.

7.2.1 Flight Test Plan

Testing a new controller architecture implementation practically is a complex task. The implemented controllers were tested separately in order to ensure that each successive controller performed as expected. Even though the system with all its components was tested in simulation, there were real-world effects that could not be taken into account fully, or the modelling might have had differences to the practical model. It was also possible that implementation errors were present that could not be revealed in simulation testing. In an attempt to minimise the risk, the control systems were tested incrementally with as little risk as possible in each iteration.

The first flight tests were for the safety pilot to determine whether the aircraft could be controlled under the specified damage condition. This test was conducted without any avionics on board, with just the 'bare-bones' RC system. This allowed the safety pilot to provide feedback on the performance of the aircraft under the different damage cases and reduce the risk of losing avionics should a problem arise. If the pilot was confident that they could take off, land and recover the aircraft if necessary under the damage condition, the release mechanism could be tested in flight. This was also tested incrementally (one surface at a time) in order to provide insight about the transition process. When the release mechanism was tested and working as desired, the avionics package was installed in the vehicle, and the controllers were tested on the healthy aircraft. The controllers were then tested on the separate damage configurations (partial horizontal and partial vertical stabiliser) independently and finally with the combined stabiliser loss. After a successful damaged configuration autonomous flight, the final in-flight transition from healthy to damaged aircraft was tested to investigate the performance of the controller during the transition.

The next subsection (7.2.2) looks at the flight tests that were conducted and discusses the observations and tests executed for each flight.

7.2.2 Flight Test Campaign

This subsection reports on the flight test campaign. The purpose of the different flight tests and observations that were made during the flight tests are presented here.

7.2.2.1 Flight Test: RC Flight

The purpose of the first few flight tests was to determine whether the release mechanism worked as expected and whether the safety pilot was comfortable with the manoeuvrability of the aircraft with the partial stabilisers. As previously mentioned (see 7.2.1), the aircraft was operated only in RC mode with most of the avionics removed and replaced with dummy weight to reduce the risk yet still providing an accurate representation of the complete aircraft.

The aircraft was first flown in its healthy configuration. The safety pilot took off with the aircraft in the healthy configuration, executed some common manoeuvres and landed the aircraft in the healthy configuration.

The safety pilot then took off in the different damage configurations (70% left horizontal, 40% vertical and the combined configuration) performed similar manoeuvres and landed the aircraft in the respective damaged configuration.

The transition from healthy to damaged configuration was then tested to check the release mechanism and observe the effect the transition had on the aircraft. The safety pilot took off with the aircraft in the healthy configuration. During the flight, the portions of the stabilisers were to test the release mechanism. Finally, the safety pilot landed the aircraft in the combined damage configuration. The safety pilot was capable of flying the aircraft with 40% vertical stabiliser loss, but was not comfortable that he could recover in the event of unexpected behaviour. The vertical stabiliser was then modified to 20% loss to allow for safe recovery if needed. According to the safety pilot, the difference from the damage configurations was noticeable. The aircraft had to be re-trimmed on the RC for each damage configuration to counter the effects of the change. The lower damping on the aircraft was also noticeable. The release mechanism worked as expected and allowed transition from healthy to damaged configuration during flight.

7.2.2.2 Flight Test: Estimator Flight

This flight test was used to obtain telemetry data for the aircraft under RC flight. This provided information that gave confidence in the sensors and also provided insight into how the different damage configurations affected the dynamics of the aircraft. After the first few flight tests, it was safe to say that the aircraft can be flown in the different damage configurations. The avionics were reinstalled on the aircraft and calibrated accordingly. The full estimator was enabled and the telemetry logged for investigation after the flight. The healthy aircraft was flown in its symmetric configuration to provide a baseline of the behaviour of the aircraft. The take-off and landing were both performed on the healthy configuration. The aircraft was then flown with partial horizontal and partial vertical stabiliser respectively and finally combined. For each of these flights, the aircraft took off, executed manoeuvres and landed in the respective damage configuration. A flight with a transition from healthy to damaged was also conducted to provide insight into the dynamics of the aircraft as its model changed. The transition flight had the safety pilot take off with the healthy aircraft. During flight, the transition was triggered. The safety pilot then landed the aircraft in the damage configuration. Under RC testing, the safety pilot was constantly making corrections to the aircraft to ensure that it stayed in the air. As a result of these constant corrections, small events, such as the transitions or doublets, were not observable from the sensor measurements.

7.2.2.3 Flight Test: Controller Tests on Healthy Aircraft Configuration

The control system was first implemented and tested on the healthy aircraft. As a safety measure, the different controllers were tested independently where possible and successively. This allowed somewhat independent testing of the different controllers while reducing the coupling that might be experienced. The safety of the vehicle was first priority, so tests were not executed that might have compromised the vehicle and avionics. The following strategy was used

to test the controllers:

- Airspeed, NSA and climb rate controllers were armed. Airspeed steps were executed. Climb rate steps were executed.
- Altitude controller was armed. Altitude steps were executed.
- LSA controller was armed. LSA regulation was observed.
- Roll angle controller was armed. Roll angle steps were executed.
- Cross track controller was armed. Autonomous following of predefined waypoints was observed.

A number of problems were encountered that delayed the flight tests. The original accelerometer would saturate, due to large vibrations in the aircraft, resulting in the estimator providing incorrect readings resulting in the climb rate controller not working correctly due to an incorrect climb rate estimate. The accelerometer was replaced with one with a larger range. The uBlox GPS unit had a very slow update rate as well as delayed measurements as mentioned in the hardware simulation section (see 6.1.1.3). This was replaced with a NovAtel GPS unit providing a more accurate reading and almost no delay on the measurement. After resolving these hardware complications, the controllers were tested successfully on the healthy aircraft. The airspeed and climb rate controllers regulated the airspeed and executed steps as expected. The altitude controller regulated the altitude accurately and executed altitude steps as expected. The LSA controller was armed and regulated the lateral acceleration of the aircraft without oscillation. The roll angle controller held a zero roll angle and rolled the aircraft to the given angle when commanded. Waypoint navigation was also tested and the aircraft followed the provided track. This was conducted with the uBlox GPS unit. The controller followed the waypoints, but with larger transients than expected. Time constraints prevented retesting of the waypoint navigation with the more accurate NovAtel GPS unit. Waypoint navigation was not a priority of the project and was simply included to allow full autonomous flight while keeping the aircraft in range.

7.2.2.4 Flight Test: Controller Tests with Partial Stabiliser Loss

When the performance of the aircraft controller on the healthy aircraft was satisfactory, the control system was tested on the different damage configurations. Having solved the hardware problems during the healthy flight tests, it was expected that the rest of the flight testing would not be subject to similar problems. The controllers were tested in the same manner and performed as expected with all the controllers regulating as expected as well as responding to the step responses. Due to the nature of the practical tests, the difference in controller performance could not be observed visually. The detailed results of the controller tests with partial stabiliser loss are presented and discussed in section 7.3.

7.2.2.5 Flight Test: In-Flight Transition from Healthy to Damaged Aircraft Configuration

After the controllers had been tested successfully on both the healthy and the damaged aircraft configurations separately and provided satisfactory performance, the in-flight transition from the healthy to the damaged aircraft configuration could be tested. The safety pilot took off with the aircraft in the healthy configuration. The safety pilot then armed the autopilot, which put the aircraft in full autonomous mode with waypoint navigation enabled. When the aircraft settled out of the turn over the runway the release switch was armed by the safety pilot. The horizontal and vertical stabiliser end-pieces were then jettisoned from the aircraft and the flight controller found the new equilibrium point for the damaged configuration, stabilised the aircraft about this new equilibrium condition, and continued the waypoint navigation. The safety pilot then landed the aircraft in its damaged configuration. These results indicate successful flight testing. A significant wind was experienced during the final transition flight. This wind caused significant disturbances on the aircraft and resulted in larger oscillations than expected on the control surfaces.

The next section reports the results from the practical flight tests with some relevant step responses included to show the change in performance of the aircraft.

7.3 Flight Test Results

This section presents the practical results from the flight tests discussed in the previous section. The relevant control system steps are shown and discussed and finally compared to that which was to be expected from the HIL simulation results in Chapter 6. The flight test step responses are seldom as ideal as those obtained from the linear and nonlinear simulations because the practical results are often contaminated with disturbance signals from wind, vibrations and coupling of the lateral and longitudinal dynamics. It is therefore difficult to read and verify transient response characteristics, such as the rise time, percentage overshoot and settling time of the closed-loop step responses obtained in flight tests accurately. This makes it difficult to compare the transient response characteristics for the flight test step responses with those of the simulated step responses accurately. For step responses that are significantly contaminated by disturbance signals, only an approximate correspondence between the practical transient responses and those predicted by analyses and simulations is possible.

7.3.1 Longitudinal Flight Control - Healthy and Damaged Aircraft Configurations

The longitudinal flight controllers were responsible for maintaining the airspeed and altitude of the aircraft. This set of tests was executed to ensure that the aircraft controller was capable of maintaining a reference airspeed and altitude during flight in the different damage configurations. The safety pilot conducted the take-off of the aircraft at the beginning of the

test. When the safety pilot was satisfied with the performance of the aircraft, he toggled the autopilot switch on the RC and the airspeed, NSA and climb rate controllers were armed. Airspeed and climb rate step commands were given to the aircraft controller via the GCS and the aircraft executed these steps. The altitude control was then armed via the GCS and the aircraft regulated the altitude. Altitude steps were given to the aircraft via the GCS and the aircraft executed the steps. These tests were done on both the healthy and damaged aircraft configurations. For these tests, the aircraft took off under safety pilot control, executed manoeuvres under autopilot control and landed again under safety pilot control in the respective damage configurations. The following subsections (7.3.1.1 - 7.3.1.4) present the telemetry for the practical results for the longitudinal controllers.

7.3.1.1 Airspeed Controller

Figure 7.3 shows the airspeed step response of the simulation and practical tests. There was very little difference in the airspeed between the response of the healthy and damaged aircraft from the practical tests. The most important thing to note is that the steady-state airspeed followed the reference it was provided. The rise time of the practical and simulated results were the same indicating a corresponding natural frequency between the simulation and practical results. The overshoot and settling time of the practical results were difficult to read and obtain any accurate measurements. The overshoot was approximated at 9% and 14% for the healthy and damaged configurations respectively. The settling times were also very difficult to read off due to the noise indicating approximate settling times of 3 s and 4 s for the healthy and damaged aircraft configurations respectively. It is known that AVL does not calculate the drag of the models accurately. The aircraft fuselage was also excluded from the AVL model contributing to the incorrect drag coefficient. As a result, the airspeed response differs between the HIL and the practical results. Increasing the drag coefficient in the simulations presents a lower overshoot more in line with what was seen in the practical results.

7.3.1.2 Normal Specific Acceleration Controller

The NSA controller could not be tested safely on its own in practice. The NSA controller controls the normal acceleration experienced by the aircraft [19]. The accelerometer on the aircraft measured a substantial amount noise due to vibrations and turbulence resulting in inaccurate acceleration measurements. In order to counter the gravitational acceleration, it was necessary to compensate for the pitch angle, which also had a noisy signal as it was provided by the estimator, which used the noisy accelerometer. As a result, if the reference provided was not exactly the same as the gravitational component acting on the normal of the aircraft, the aircraft would start accelerating in its normal and become unstable quickly. This instability would happen very quickly and the safety pilot may not be able to recover the aircraft quickly enough. The climb rate controller was capable of updating the reference command much faster and more dynamically than the operator. As a result, the climb rate controller was safe to test.

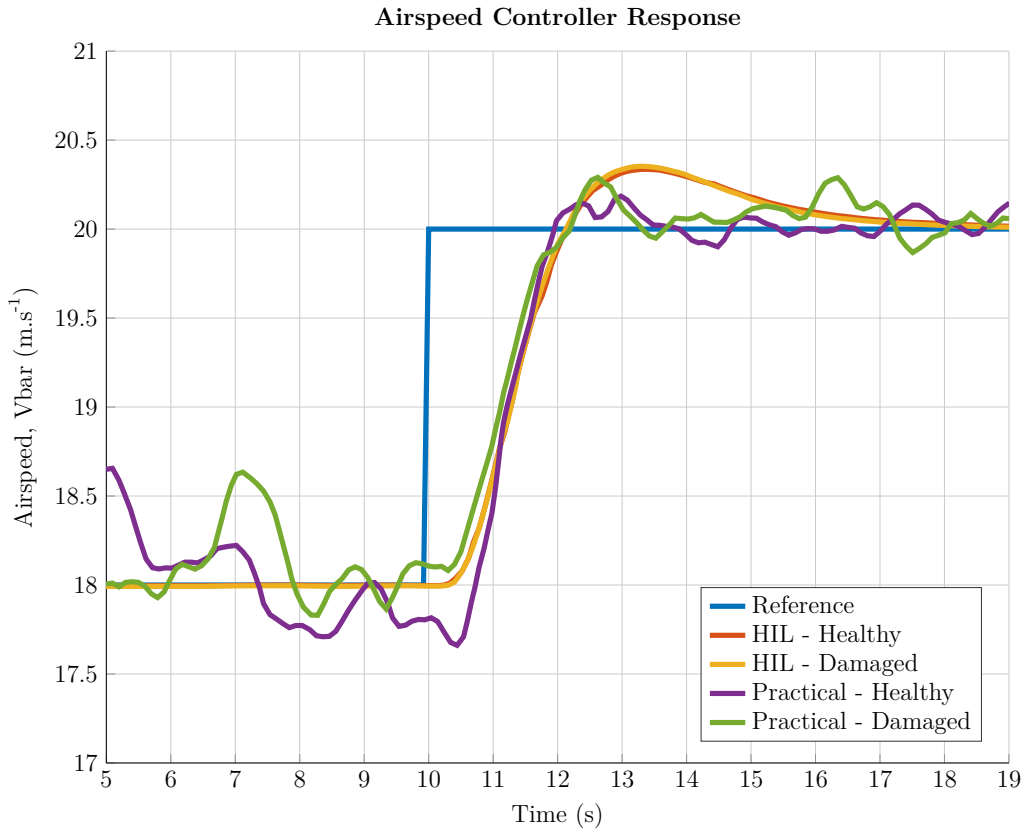

Figure 7.3: Airspeed controller step response

7.3.1.3 Climb Rate Controller

The climb rate controller was the lowest level control loop that could be tested safely for the vertical control of the aircraft. An integrator was added to help with the steady-state tracking of the climb rate, which introduced overshoot in the response. Figure 7.4 shows the climb rate response of the HIL simulation and practical results. Most importantly, the climb rate controller followed the reference signal in both the healthy and damaged configurations. This signal was highly contaminated with noise and no conclusions could really be drawn from it aside from showing that the climb rate vaguely followed the reference signal. The rise times between the HIL simulation and the practical results were also similar. The amount of noise on this signal was due to poor mounting of the IMU to the aircraft. This resulted in the IMU measuring the accelerations due to the vibration on the aircraft from the main motor. This noise then contaminated the estimator data resulting in a noisy climb rate measurement. Introducing this level of noise to the HIL simulation showed a similar behaviour where the transient characteristics could not be read.

7.3.1.4 Altitude Controller

Figure 7.5 shows the altitude step responses from the HIL simulations and the practical flight tests. These responses are very similar to each other and have similar properties. The steady-state altitude provided by the altitude controller followed the reference signal. The time constant of the practical step response and the HIL simulation response were the same. The noise

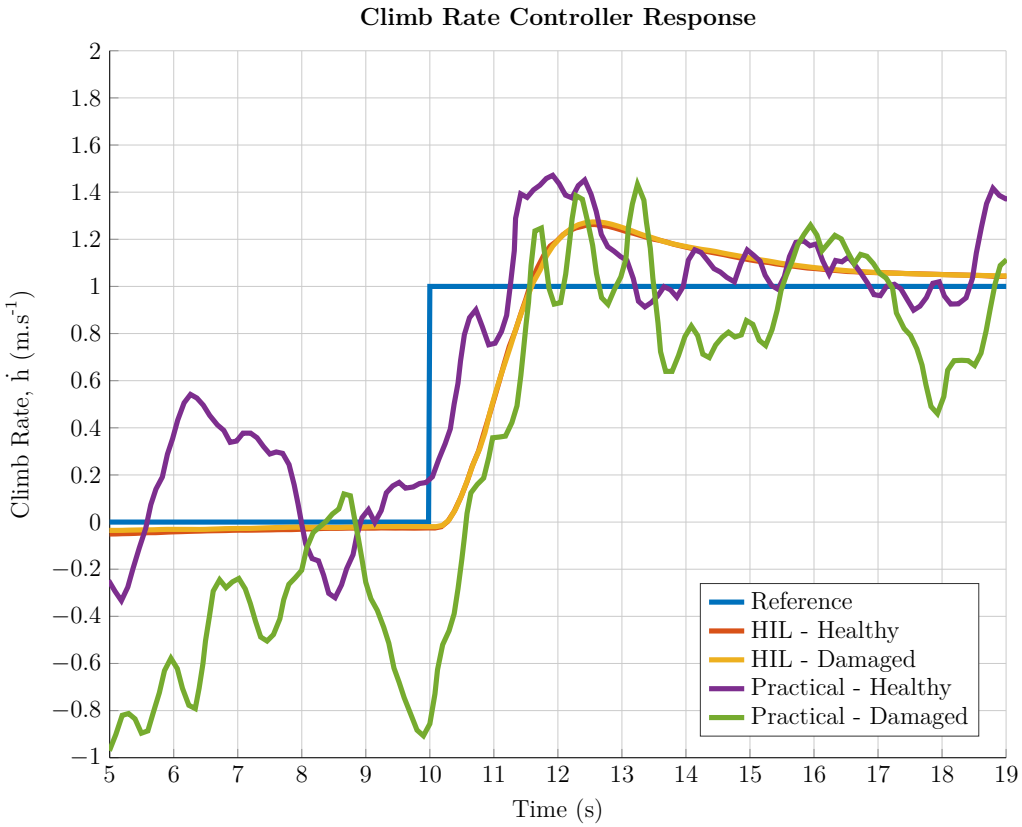

Figure 7.4: Climb rate controller step response

on the climb rate measurement resulted in poor accuracy for the climb rate controller. As a result when the altitude controller started commanding a smaller reference climb rate as it approached steady state, the noise on the climb rate controller prevented the climb rate from matching the necessary climb rate perfectly to achieve the commanded altitude. The figure shows that the altitude eventually settled at the reference. As a result, there was a longer settling time from the practical results when compared to the HIL simulation results. It can be noted that the difference in the healthy and damaged configuration response was negligible, indicating sufficient robustness in the altitude control of the system.

The results show that the healthy and damaged configurations diverge at around 38 seconds. This divergence was due to the next step response command being uploaded.

7.3.2 Lateral Flight Control - Healthy and Damaged Aircraft Configurations

The lateral flight controllers were responsible for maintaining the sideslip and roll angles of the aircraft. This set of tests was executed to ensure that the aircraft controller was capable of flying at a provided roll angle or with a specified sideslip angle. This allowed the aircraft to follow a predefined path in order to keep the aircraft within a usable range when under autopilot. The safety pilot conducted the take-off of the aircraft at the beginning of the test. When the safety pilot was satisfied with the performance of the aircraft, he toggled the autopilot switch on the RC and the aircraft armed into full longitudinal control. The LSA controller was then armed

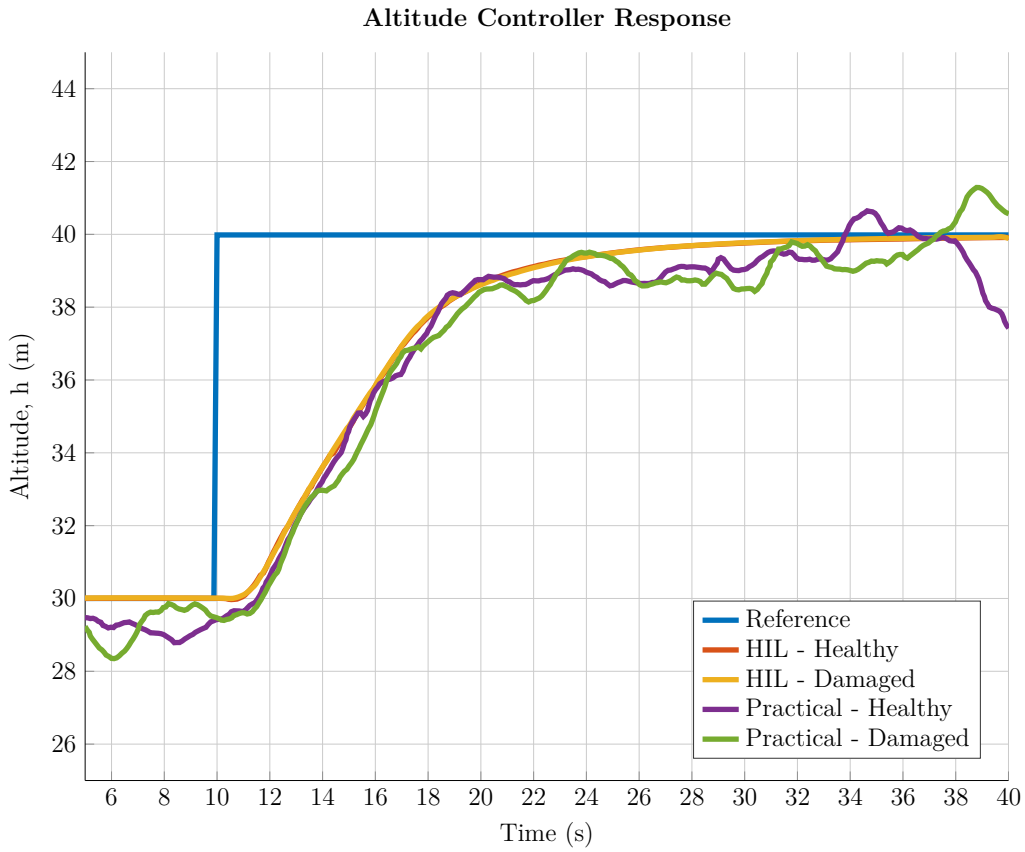

Figure 7.5: Altitude controller step response

from the GCS and observed for any oscillations. The roll angle controller was then armed from the GCS and the aircraft regulated zero roll angle. Roll angle steps were then given to the aircraft via the GCS and the aircraft executed the steps. These tests were done on both the healthy and damaged aircraft configurations. There were no transitions for these tests so the aircraft took off under safety pilot control, executed manoeuvres and steps under automated control and was landed under safety pilot control in the respective damage configuration. The following subsections (7.3.2.1 - 7.3.2.3) present the telemetry results for the practical results of the lateral controllers.

7.3.2.1 Lateral Specific Acceleration Regulation

The LSA controller of the aircraft was implemented to provide regulation of the lateral acceleration to zero. Step response tests were not performed for this controller. The lateral acceleration of the aircraft was observed with the LSA regulation armed in the healthy and damaged case. The plots in Figure 7.6 show the regulation for the healthy and damaged cases as well as the rudder actuator deflections for each respectively. In both cases, the lateral specification acceleration was regulated to zero as expected, but larger amplitude oscillations were observed in the damaged aircraft case. The oscillations occurred due to the disturbances constantly acting on the aircraft. This was due to the reduced vertical stabiliser which had a smaller effect on the aircraft and struggled more to bring the aircraft acceleration back to zero. The reduced vertical fin portion resulted in a smaller restoring moment in the aircraft and the reduced

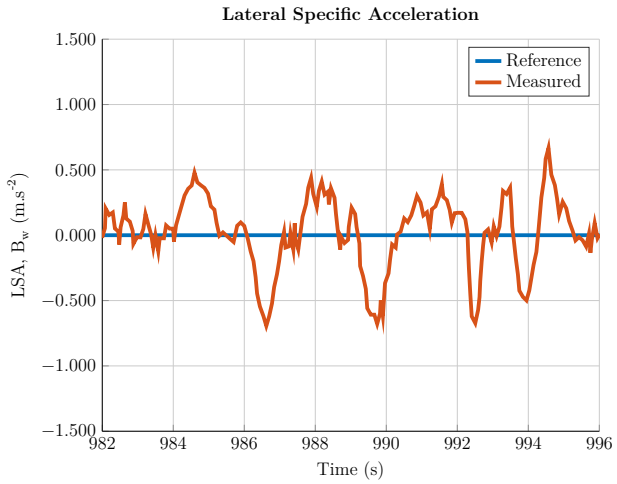

(a) Healthy practical LSA regulation

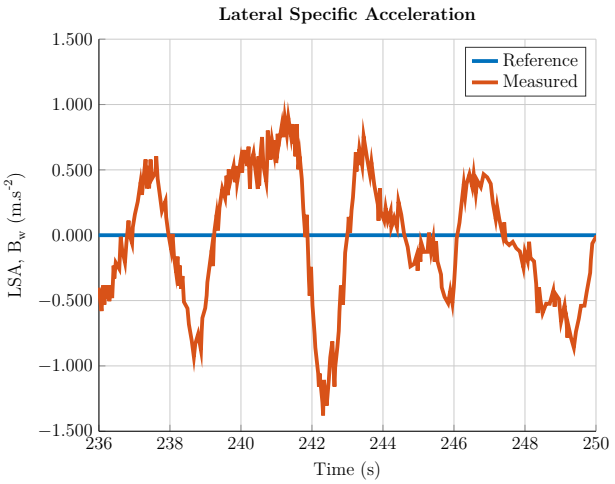

(b) Damaged practical LSA regulation

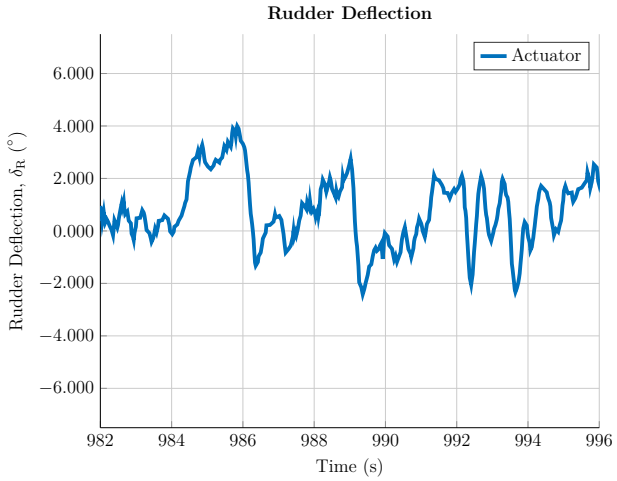

(c) Healthy practical LSA regulation — rudder deflection

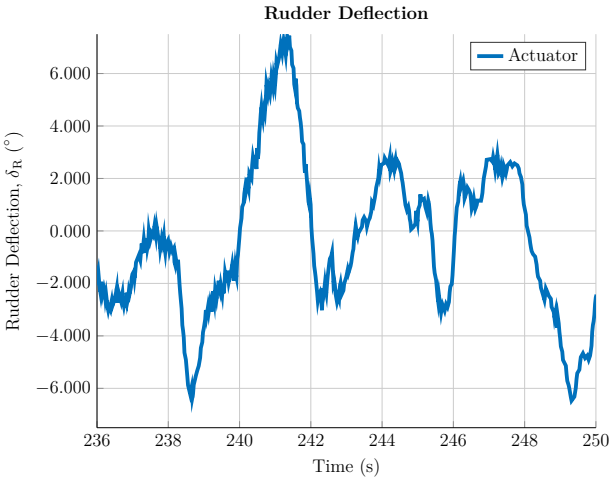

(d) Damaged practical LSA regulation — rudder deflection

Figure 7.6: LSA regulation

rudder portion resulted in the controller struggling more to regulate the zero lateral specific acceleration. This was clear from the larger rudder deflections in the damage configuration in Figure 7.6d compared to the healthy configuration in Figure 7.6c. The larger actuator deflections were expected due to the reduced size of the vertical stabiliser. In both configurations, the LSA controller regulated the lateral specific acceleration of the aircraft around zero without inducing oscillations or becoming unstable. This also indicates that, as more of the vertical stabiliser is removed, there will not be sufficient rudder actuation available to provide the zero lateral acceleration.

7.3.2.2 Roll Angle Controller

Figure 7.7 shows the roll angle controller step responses from the HIL simulation and during practical flights. The figure shows that the roll angle controller was capable of tracking the steady-state reference that was commanded. The rise time of the practical and simulated roll angle steps also match, showing correspondence in the natural frequency of the simulation and

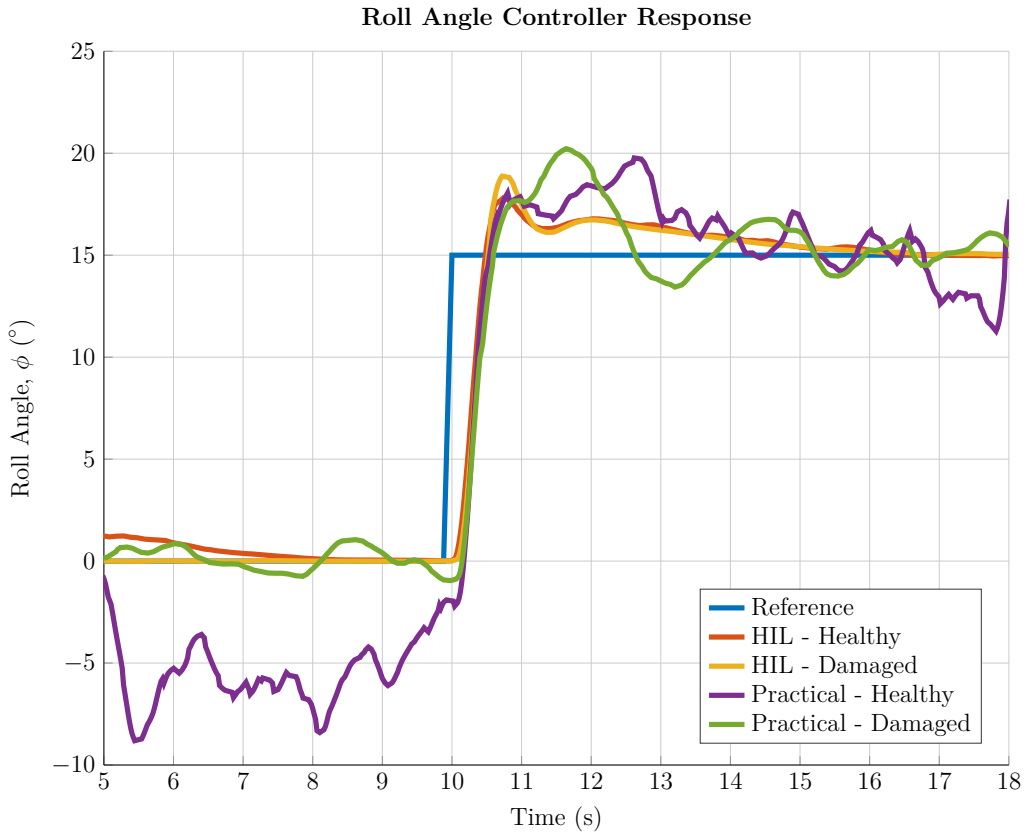

Figure 7.7: Roll angle controller step response

practical response. The other transient characteristics could not be read off accurately due to the noise and disturbances on the signal. There seemed to be more overshoot and a roughly similar settling time in the practical responses compared to the simulations.

At 18 s on the simulation the roll angle seems to diverge from the steady state reference, this divergence is due to the next command being uploaded.

7.3.2.3 Cross Track Controller

The cross track controller is responsible for the waypoint navigation during the autonomous aircraft flight. The waypoint navigation was tested on both the healthy and damaged aircraft configurations. The practical waypoint navigation for the healthy configuration was performed before the GPS unit was upgraded. The aircraft flew between the waypoints but had large overshoot due to the delayed and inaccurate measurements. The practical flight test for the damaged aircraft configuration had the GPS upgrade and performed significantly better. As a result the waypoint navigation for the healthy aircraft configuration had worse transients than the damaged aircraft configuration. Ultimately, the aircraft followed the waypoints accurately enough in both damage configurations to proceed to the practical flight test for the in-flight transition.

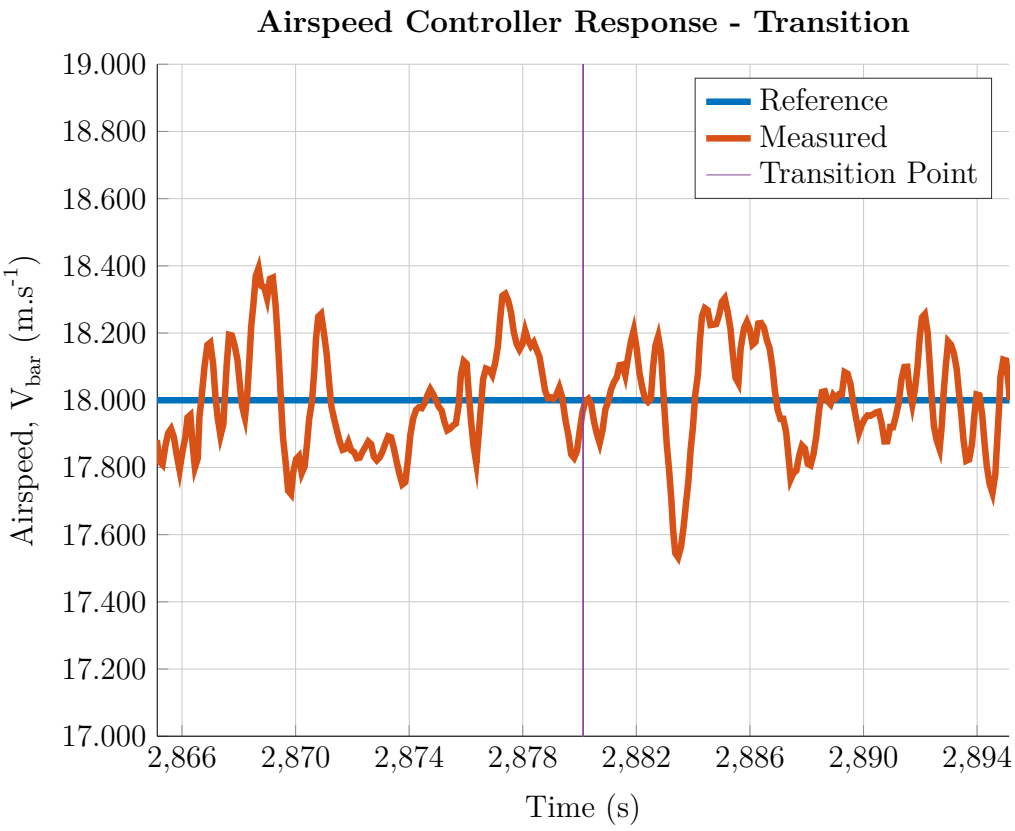

Figure 7.8: Airspeed during practical damage transition

7.3.3 In-Flight Transition from Healthy to Damaged Configuration

All the controllers were tested through regulating and maintaining straight and level flight and executing steps. The waypoint navigation allowed a predefined path to be flown by the UAV. This allowed the transition to be tested in a practical flight test. The transition between the configurations was tested to determine whether the aircraft was capable of determining the new trim for the new aircraft configuration. The safety pilot took off with the healthy aircraft. All the controllers were then armed causing the aircraft to follow the predefined path. During the flight, when the aircraft was over the runway, the release was toggled and the partial stabilisers were jettisoned from the aircraft. The aircraft continued flying the defined path autonomously. The safety pilot then took control and landed the damaged aircraft. The rest of this section discusses the observations that were made during the transition process of the aircraft.

Figure 7.8 shows the airspeed during the transition. The airspeed measurement had quite a bit of noise on the signal and the behaviour of the airspeed at the moment of transition could not be tied to the effect of the transition as the noisy behaviour was there throughout the airspeed regulation. This agreed with the behaviour expected from the HIL simulation where there was no direct effect on the airspeed of the aircraft during the transition.

The climb rate during the transition is shown in Figure 7.9a. The HIL simulation indicated that the climb rate of the aircraft quickly decreased and then returned to normal regulation. In the practical result, there is a dip but it was indiscernible from the oscillations the climb rate controller was already experiencing. As a result, it cannot be said that the transition resulted

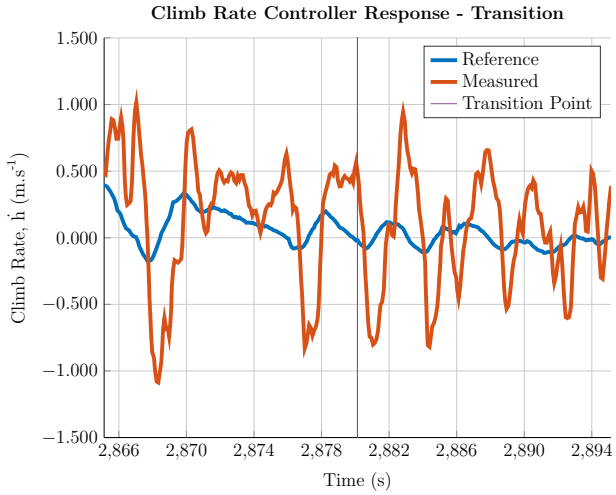

(a) Climb Rate during practical damage transition

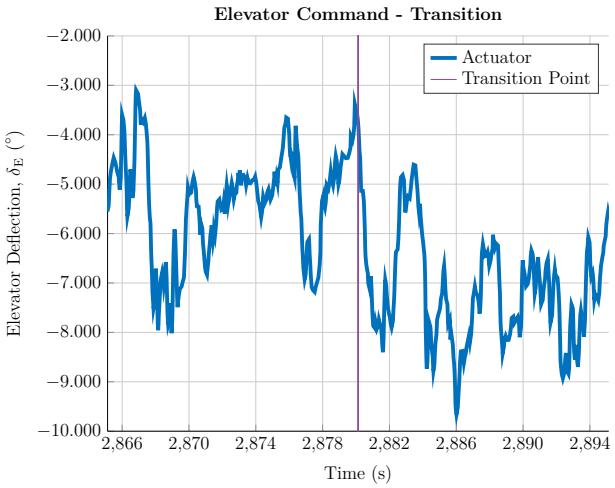

(b) Elevator deflection during practical damage transition

Figure 7.9: Climb rate transients

in a change in the climb rate, however, the aircraft was capable of regulating the climb rate after the damage had occurred.

Figure 7.9b shows the elevator deflection during this release event. It shows that the elevator was around 5° for the level section of flight before the transition. After the transition, the elevator setting was closer to 7°, which is where the new trim of the aircraft was expected to be. The exact values could not be used as they were too noisy, but the trend of the actuator setting could be used to provide an idea of what the trim value might be. These values are close to those calculated in section 3.3.2 and observed in the HIL simulations in section 6.1.2.

The altitude of the aircraft did not change much and followed on from what was observed from the climb rate as shown in Figure 7.10. The HIL simulation indicated a slight loss in altitude immediately after the transition. The simulation was an ideal case and indicated a minimal loss in altitude. It was therefore expected that, for the practical test, the loss in altitude would not be observed amongst the disturbances.

The LSA controller regulated the lateral acceleration of the aircraft around zero both before and after the damage of the aircraft as shown in Figure 7.11a. The rudder deflections are shown in Figure 7.11b. This figure shows that the rudder seemed to oscillate at around 0° before the damage, and after the damage it seemed to oscillate around 0.5° to 1.0°. This deflection was slightly larger than the expected trim of 0.181°, but was in the same direction as the expected deflection from those calculated in Section 3.3.2 and shown in the HIL simulation results in Section 6.1.2.

The roll angle of the aircraft during transition is shown in Figure 7.12a. The track the aircraft flew was not long enough for the roll angle controller to settle, resulting in small rolling oscillations during the transition. As a result, no effect of the transition on the roll angle of the aircraft could be seen. Figure 7.12b shows the aileron deflection during the transition. The expected trim values that were calculated and reported in section 3.3.2 and observed from the HIL simulations in 6.1.2 were very small at 0.2° and cannot be seen in the practical results due

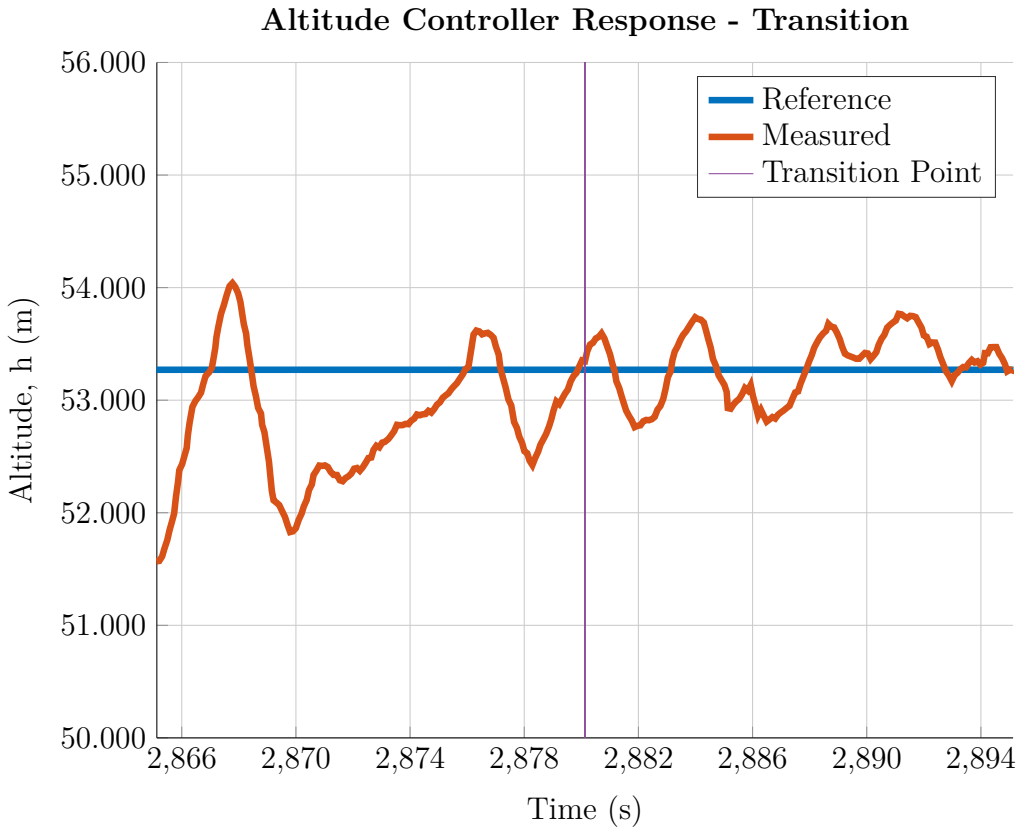

Figure 7.10: Altitude during practical damage transition

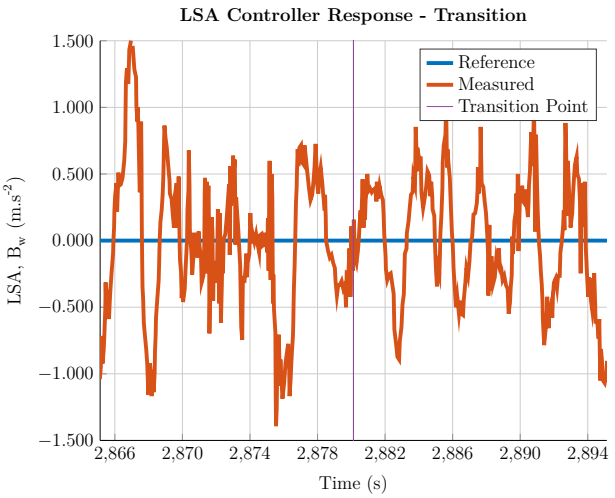

(a) LSA during practical damage transition

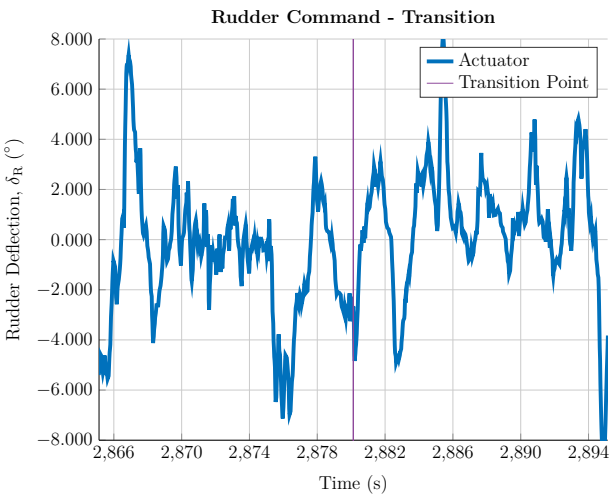

(b) Rudder deflection during practical damage transition

Figure 7.11: LSA transients

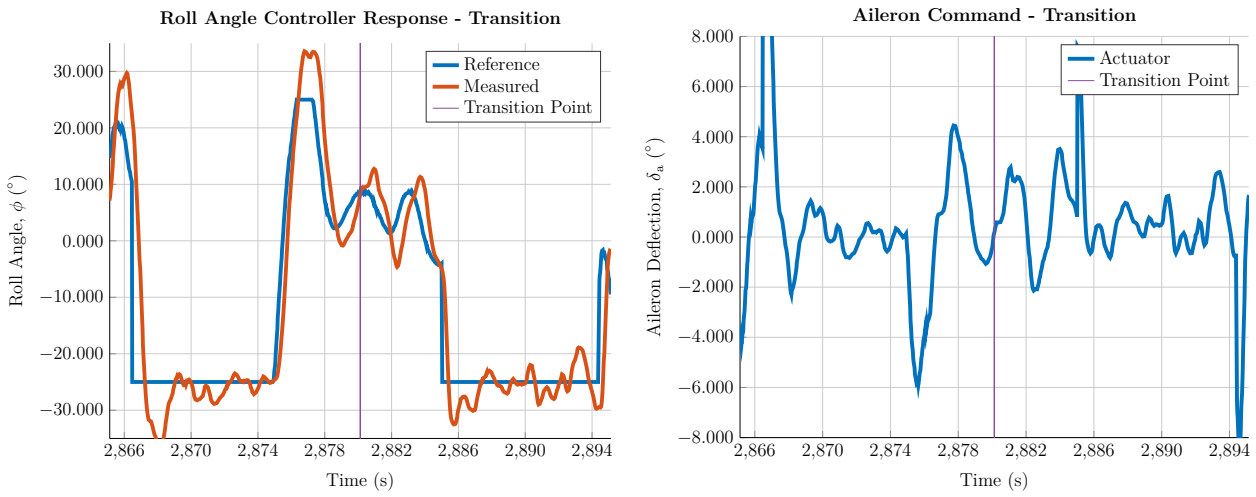

(a) Roll Angle during practical damage transition

(b) Aileron deflection during practical damage transition

Figure 7.12: Roll angle transients

to the roll angle not settling. Figures 7.13 and 7.14 show the flight path of the aircraft while the autopilot (AP) was active for the practical transition flight. The transition happened shortly after exiting a turn, resulting in not all the transients dying out before the release. The aircraft flew the predefined flight path after the safety pilot had enabled the AP. When the aircraft was over the runway, the transition was toggled by the safety pilot. The stabiliser portions were jettisoned off and the aircraft continued flying the path after the transition. After the down leg of the autonomous flight, the safety pilot took control of the aircraft again and landed the aircraft safely.

This concludes the practical flight test results and evidence that the control system was capable of handling the damage inflicted with acceptable performance. The controllers were designed with a high level of robustness with the knowledge that the aircraft would be damaged in order to increase the safety of the aircraft.

7.4 Summary

The flight test results showed that the flight controllers were stable in both healthy and damaged aircraft configurations. The airspeed, climb rate, altitude and roll angle controllers were all capable of tracking a reference command successfully in both the healthy and damaged configurations. The LSA controller was stable in both the healthy and damaged configurations and regulated the LSA to zero in both configurations. The rise times of the airspeed, climb rate and roll angle controllers agreed with the rise time of the simulated response. The altitude controller time constant agreed with that of the simulated step response. The flight controller was able to handle the transition from the healthy to damaged aircraft configuration. The aircraft remained stable, maintained altitude and continued with the waypoint navigation during and after the transition. The LSA controller was able to continue regulating the LSA

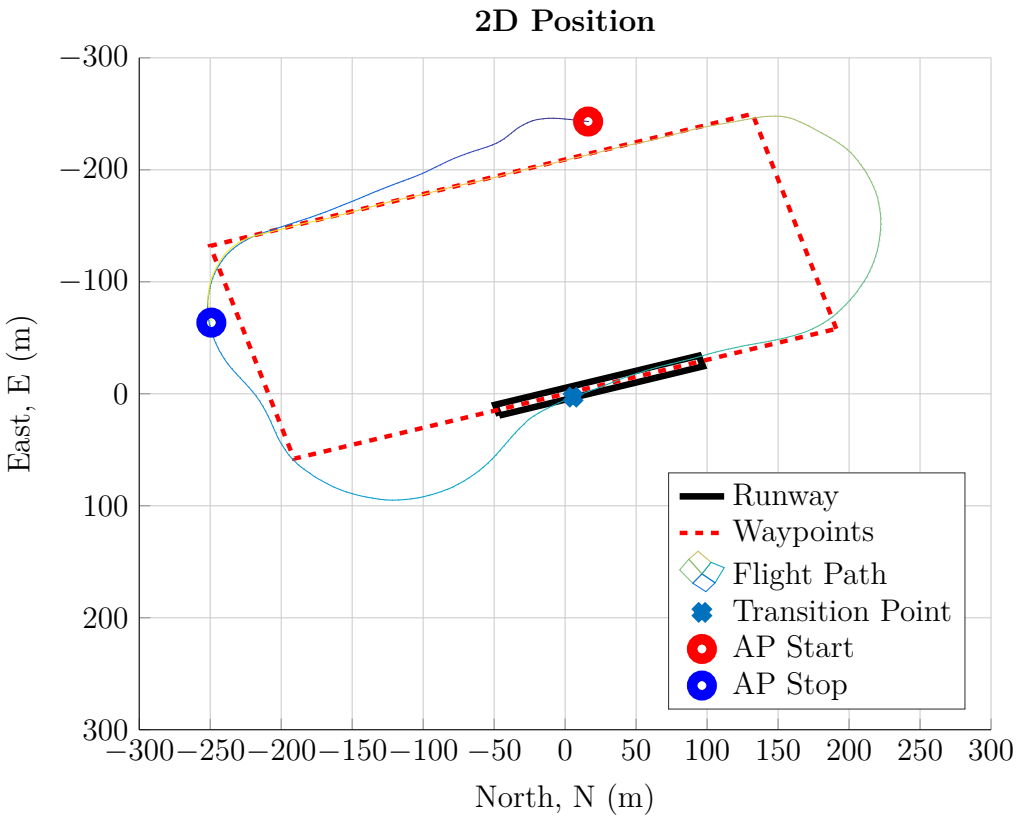

Figure 7.13: Flight path during practical damage transition — NE

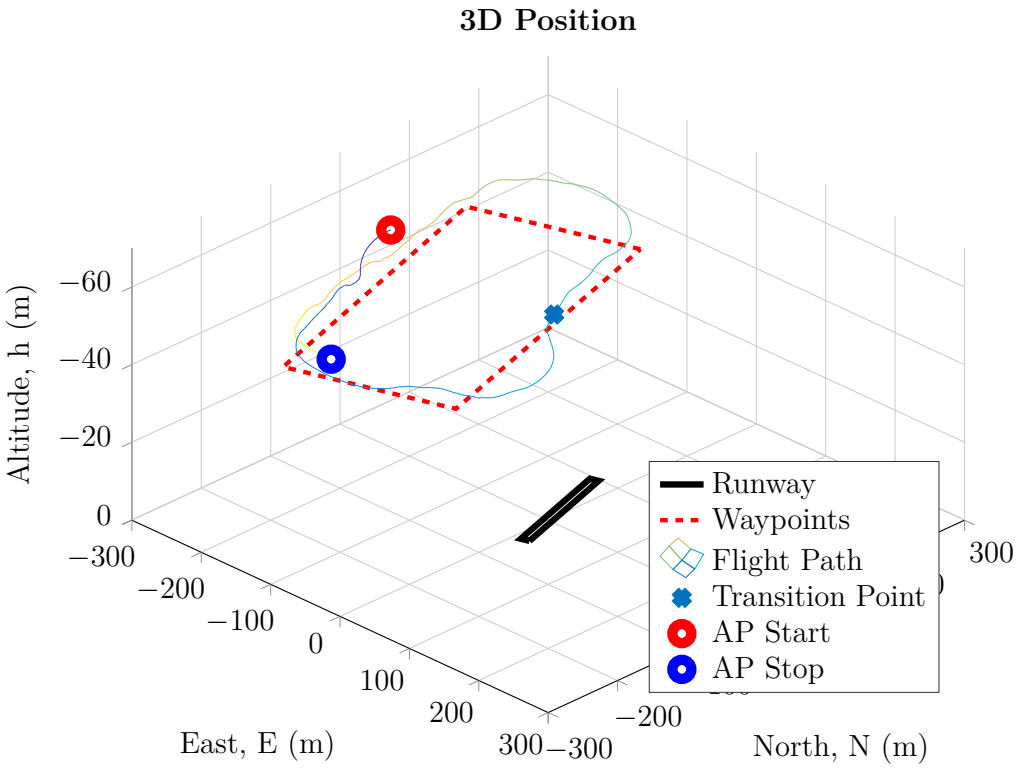

Figure 7.14: Flight path during practical damage transition — NED

of the aircraft after the transition. All the effects of the transition were not discernible on the telemetry data. The elevator setting changed significantly after the transition while there was a very small change on the rudder setting as the control system found the new trim.

The aircraft controllers followed their steady-state references and maintained aircraft stability before, during and after the transition from the healthy to damaged configuration. This indicated a successful flight test campaign.

§ 8

Conclusions

This chapter presents a summary of the results obtained in this study as well as a list of the most important observations made regarding the partial stabiliser damage and a list of recommendations for further research.

8.1 Summary

This thesis presented the investigation, design, implementation and verification of a fault-tolerant flight control system for a fixed-wing unmanned aerial vehicle that has suffered partial horizontal and partial vertical stabiliser loss. An asymmetric flight dynamics model was derived that models the effects of of the partial stabiliser losses. The maximum percentages of partial horizontal and vertical stabiliser losses that can realistically be accommodated were then determined through a trim analysis. The aircraft model was then linearised and the stability of the natural dynamics were analysed as a function of the percentage loss. A robust, non-adaptive flight control system was then designed to provide acceptable closed-loop dynamics over all feasible damage cases. The flight control system was verified through simulation and practical flight testing.

Chapter 1 introduced the research problem and motivated its importance for the unmanned aircraft industry. A literature study provided an overview of previous research on the topic and provided a basis that was used for the modelling and control strategies for the damaged aircraft. The research objective was discussed and the main contributions of the research were outlined. An overview of the thesis was given and the goal of each chapter was discussed.

Chapter 2 presented the mathematical modelling of the aircraft that includes the effects of partial horizontal and vertical stabiliser loss. The reference frames and conventions used in the present study were discussed as well as the notation associated with these conventions. The flight dynamics were presented for the healthy and damaged aircraft configurations with their respective 6DoF EoM models. An extended flight mechanics model was defined to include the effects of partial stabiliser loss. A non-CM-centric method was used to determine the forces and moments model for the asymmetric aircraft by taking the change in CG and MoI into account.

Chapter 3 presents the trim analysis for the aircraft in both the healthy and the damaged configurations. An analytic trim-solving technique was first used to determine the aircraft trim. This method used a number of simplifications that did not take the full aircraft model into account when calculating the trim settings for the aircraft. A multivariate Newton–Raphson technique was implemented, which used the full 6DoF and forces and moments model of the aircraft to determine an equilibrium. The Newton–Raphson technique provided a trim condition that resulted in equilibrium flight for all the damage configurations. For some damage cases, the required actuator trim settings are close to, or exceed, the actuator limits, which implies that a flight equilibrium cannot be achieved for the specific damage cases. The trim analysis therefore reveals the maximum percentage horizontal and vertical stabiliser loss that can realistically be accommodated. A notable change in trim was experienced for the different damage cases due to the change in the aerodynamic surfaces and the shift in CG and MoI.

Chapter 4 presented a stability analysis for the different damage configurations of the aircraft. The aircraft was linearised about the respective trim conditions for each of the different damage configurations allowing the open-loop dynamics to be investigated. The aircraft model was not decoupled into longitudinal and lateral dynamics due to cross-coupling as a result of the asymmetry of the aircraft. The short period and dutch roll modes of the aircraft were affected most by the partial horizontal and vertical stabiliser losses, where they both reduced in frequency and became less damped. The open-loop dynamics showed that all the damage configurations resulted in a stable aircraft model. There were, however, trim conditions that were out of the range of the actuators or very close to their limits, which could prove impossible to control due to insufficient range on the actuators.

Chapter 5 presented the controller architecture and design. The control system was designed without awareness of the damage inflicted. As a result, the aircraft model was assumed to be decoupled and the control system was designed for the healthy aircraft configuration with more of a focus on robustness rather than on performance. A combination of classical and acceleration-based control techniques was used in this study. The controller specifications were relaxed slightly to provide robustness to model changes caused by the different damage configurations. The linear controller verification showed that the designed controllers performed to specification on the fully coupled aircraft model. The closed-loop pole analysis showed that the controllers remained stable for all the damage configurations; assuming that it is possible to trim the aircraft in the first place.

Chapter 6 described the hardware in the loop simulation process. This process allowed the testing of the aircraft control system running on the OBC within a simulation environment. This simulation method used the full nonlinear aircraft model to simulate the aircraft behaviour. The different controller step responses were executed and compared to the ideal linear simulations. A transition simulation was performed to show that the aircraft was capable of handling the transition from the healthy to damaged configuration. The HIL simulation results showed that the aircraft controller was capable of performing the step responses and determined the new trim after a transition from the healthy to damaged aircraft configuration.

Chapter 7 presented the practical flight test results. An overview of the hardware modifications made to the aircraft to enable flight testing with partial horizontal and vertical stabiliser loss is provided. A flight test plan was discussed, explaining the different tests that were performed and the motivation for those tests. The flight test results were discussed and compared to those expected from the nonlinear simulation. All the controllers tracked their respective reference signal in steady state and their response times between the practical flight tests and the simulations agreed. Sensor noise made it difficult to read the rest of the transient characteristics accurately. The aircraft control system was able to keep the aircraft stable during the transition, found the new trim actuator settings and continued the waypoint navigation.

In conclusion, damage to the horizontal and vertical stabiliser had a large effect on the stability of the aircraft by reducing the frequency and damping of the system. Existing control systems designed with a focus on robustness for model changes are capable of providing sufficient control to maintain flight and execute manoeuvres in both the healthy and damaged configuration with small differences in response. The existing control system is also capable of handling the transition from the healthy to damaged configuration through finding the new trim and keeping the vehicle in the air.

8.2 Observations

The following are significant observations that were made during the project and highlight important aspects of this study.

- Partial horizontal stabiliser damage resulted in large changes in the lift and pitch, describing aerodynamic coefficients.
- Partial vertical stabiliser damage resulted in large changes in the lateral force and yaw, describing aerodynamic coefficients.
- Certain trim conditions had significant actuator deflections which would result in the control surfaces saturating and the aircraft becoming unstable (see Table 3.10).
- Partial horizontal stabiliser damage resulted in a large change in the short period mode frequency and damping.
- Partial vertical stabiliser damage resulted in a large change in the dutch roll mode frequency and damping.
- All the damage configurations that had a trim condition within the actuator range were stable.
- The aircraft controllers were capable of tracking the steady-state reference signals with similar rise times and time constants as those expected from simulation.

- The aircraft controllers were capable of handling the transition from healthy to damaged configuration and of determining the required trim to maintain flight and waypoint navigation.

8.3 Recommendations

The following recommendations suggest possible future work as a continuation of the existing research as well as improvements that could have been made to this project.

8.3.1 Future Work

Combined aircraft damage investigation Previous research at the ESL investigated the design of a flight control system that is able to accommodate partial wing loss. This previous research could be combined with the research on partial stabiliser damage presented in this thesis to design a flight control system that can accommodate combined wing, horizontal stabiliser and vertical stabiliser damage.

Autonomous landing of a damaged aircraft If a piloted aircraft were to be damaged during flight, it is possible that the pilot may lose consciousness or he/she may be disoriented and unable to land the aircraft safely. In such a case, an automated flight system would be able to return home and perform an autonomous landing with the pilot knowing that the aircraft is capable of withstanding certain damage configurations.

Full robust or adaptive control design for damaged aircraft If the aircraft control system were designed with certain damage configurations in mind, the aircraft would be able to perform significantly better under damage cases. Gain scheduling or an adaptive control system would be able to compensate for the model changes and adjust the gains as necessary to provide the optimal flight control autonomously or via a fly-by-wire system to the pilot.

8.3.2 Improvements

IMU mounting Sensor noise made it difficult to read the transient characteristics of the practical results accurately. Proper vibration isolation mounting on the IMU would significantly reduce this noise. The IMU measurements are vital in this avionics package as the acceleration and rate measurements are heavily weighted in the aircraft estimator.

Weight reduction The stabiliser modifications resulted in a large mass being added far away from the CG. To counter this effect, a large mass was added to the front of the aircraft. As a result, the aircraft was significantly heavier than the original unmodified aircraft. Remanufacturing the stabiliser with lightweight materials would result in better performance, longer battery life and more agility from the aircraft.

Appendix A

Asymmetric Forces and Moment Equation Derivation

This derivation was adapted from Bacon [9] and makes use of figure 2.9 and the conventions defined in subsection 2.3.2.

A.1 Force Equations

From Newton's Second Law, the translational motion of the body is governed by

$$\sum \mathbf{F} = \sum m_i \boldsymbol{a}_i \tag{A.1.1}$$

where a_i can also be described as $\boldsymbol{a}_i = \ddot{\boldsymbol{r}}_i = (\ddot{\boldsymbol{r}})_O$ where $\sum \boldsymbol{F}$ is the sum of all the external forces on m and $\boldsymbol{a}_i$ is the acceleration of the centre of mass as observed from the fixed inertial reference frame. It is necessary to define equation A.1.1 in the body-fixed reference axis around A. This is done by taking the derivative of equation 2.3.1 with respect to the inertial reference frame.

$$\begin{aligned}\left(\frac{[\,]}{dt}\right)_O &= \left(\frac{[\,]}{dt}\right)_i + \boldsymbol{\omega} \times [\,] \text{ so } (\dot{\boldsymbol{r}}_i)_O = (\dot{\boldsymbol{r}}_A)_O + (\dot{\boldsymbol{\rho}}_i)_O \text{ becomes} \\ &\qquad (\dot{\boldsymbol{r}}_i)_O = \boldsymbol{v}_A + \dot{\boldsymbol{\rho}}_i + \boldsymbol{\omega} \times \boldsymbol{\rho}_i\end{aligned} \tag{A.1.2}$$

where $\boldsymbol{v}_A$ is $(\dot{\boldsymbol{r}}_A)_O$ expressed in the body coordinates. Here, $\boldsymbol{\rho}_i$ and $\boldsymbol{\omega}$ are expressed in the body coordinates. The velocity of m_i in body coordinates is referenced as $\dot{\boldsymbol{\rho}}_i$. Taking the derivative of equation A.1.2 with respect to the inertial axis system results in the acceleration

$$\begin{aligned}(\ddot{\boldsymbol{r}}_i)_O &= \left(\frac{d}{dt}(\boldsymbol{v}_A + \dot{\boldsymbol{\rho}}_i + \boldsymbol{\omega} \times \boldsymbol{\rho}_i)\right)_i + \boldsymbol{\omega} \times (\boldsymbol{v}_A + \dot{\boldsymbol{\rho}}_i + \boldsymbol{\omega} \times \boldsymbol{\rho}_i) \\ &= \dot{\boldsymbol{v}}_A + \boldsymbol{\omega} \times \boldsymbol{v}_A + \ddot{\boldsymbol{\rho}}_i + \dot{\boldsymbol{\omega}} \times \boldsymbol{\rho}_i + 2(\boldsymbol{\omega} \times \dot{\boldsymbol{\rho}}_i) + \boldsymbol{\omega} \times (\boldsymbol{\omega} \times \boldsymbol{\rho}_i)\end{aligned} \tag{A.1.3}$$

Equation A.1.3 gives the acceleration term of the object. This acceleration is used in Newton's second law, equation A.1.1 resulting in

$$\begin{aligned}\sum \boldsymbol{F} &= m_i(\dot{\boldsymbol{v}}_A + \boldsymbol{\omega} \times \boldsymbol{v}_A + \ddot{\boldsymbol{\rho}}_i + \dot{\boldsymbol{\omega}} \times \boldsymbol{\rho}_i) + \boldsymbol{\omega} \times (\boldsymbol{\omega} \times \boldsymbol{\rho}_i) \\ &= m(\dot{\boldsymbol{v}}_A + \boldsymbol{\omega} \times \boldsymbol{v}_A) + \sum m_i \ddot{\boldsymbol{\rho}}_i + 2(\boldsymbol{\omega} \times \sum m_i \dot{\boldsymbol{\rho}}_i) + \dot{\boldsymbol{\omega}} \times \sum m_i \boldsymbol{\rho}_i + \boldsymbol{\omega} \times (\boldsymbol{\omega} \times \sum m_i \boldsymbol{\rho}_i) \\ &= m(\dot{\boldsymbol{v}}_A + \boldsymbol{\omega} \times \boldsymbol{v}_A) + m\ddot{\overline{\boldsymbol{\rho}}} + 2(\boldsymbol{\omega} \times m\dot{\overline{\boldsymbol{\rho}}}) + \dot{\boldsymbol{\omega}} \times m\overline{\boldsymbol{\rho}} + \boldsymbol{\omega} \times (\boldsymbol{\omega} \times m\overline{\boldsymbol{\rho}}) \qquad \text{(A.1.4)}\end{aligned}$$

The body is assumed to be rigid, that is, $\overline{\boldsymbol{\rho}}$ is a constant. There may be a CG shift as the UAV enters the partial stabiliser loss state, but this change is regarded as an instantaneous shift and not something that changes over time. $\overline{\boldsymbol{\rho}}$ can therefore be treated as having a constant value i.e. $\ddot{\overline{\boldsymbol{\rho}}} = \dot{\overline{\boldsymbol{\rho}}} = 0$. Equation A.1.4 then becomes

$$\sum \boldsymbol{F} = m(\dot{\boldsymbol{v}}_A + \boldsymbol{\omega} \times \boldsymbol{v}_A) + \dot{\boldsymbol{\omega}} \times m\overline{\boldsymbol{\rho}} + \boldsymbol{\omega} \times (\boldsymbol{\omega} \times m\overline{\boldsymbol{\rho}}) \qquad \text{(A.1.5)}$$

Equation A.1.5 is used with the following vector representations for the angular rates, CG position and body velocity,

$$\begin{aligned}\boldsymbol{\omega} &= P\boldsymbol{i} + Q\boldsymbol{j} + R\boldsymbol{k} \\ \overline{\boldsymbol{\rho}} &= \Delta x\boldsymbol{i} + \Delta y\boldsymbol{j} + \Delta z\boldsymbol{k} \\ \boldsymbol{v}_A &= U_A\boldsymbol{i} + V_A\boldsymbol{j} + W_A\boldsymbol{k}\end{aligned}$$

The x, y and z components of $\Sigma\boldsymbol{F}$ can then be represented as

$$\sum \boldsymbol{F}_x = m(\dot{U}_A + QW_A - RV_A - (Q^2 + R^2)\Delta x + (QP - \dot{R})\Delta y + (RP + \dot{Q})\Delta z \qquad \text{(A.1.6)}$$

$$\sum \boldsymbol{F}_y = m(\dot{V}_A + RU_A - PW_A + (PQ + \dot{R})\Delta x - (P^2 + R^2)\Delta y + (QR - \dot{P})\Delta z \qquad \text{(A.1.7)}$$

$$\sum \boldsymbol{F}_z = m(\dot{W}_A + PV_A - QU_A + (PR - \dot{Q})\Delta x + (QR + \dot{P})\Delta y + (P^2 + Q^2)\Delta z \qquad \text{(A.1.8)}$$

A.2 Moment Equations

Figure 2.9 is used again to discuss the moment equations of the asymmetric aircraft model. The same axis system that is mentioned at the beginning of this subsection applies for the derivation of the moment equations for the damaged aircraft. The rest of this section uses the momentum principle, relating the rate of change of angular momentum to the external moments, as formulated for the linear moment taken about A.

$$\boldsymbol{H}_A = \sum(\boldsymbol{\rho}_i \times m_i\boldsymbol{v}_i) \qquad \text{(A.2.1)}$$

where $\boldsymbol{v}_i = (\dot{\boldsymbol{r}}_i)_O$ is the velocity of m_i in the inertial reference frame. The derivative of $\boldsymbol{H}_A$ of equation A.2.1 is taken with respect to the inertial reference frame.

$$(\dot{\boldsymbol{H}}_A)_O = \sum((\dot{\boldsymbol{\rho}}_i)_O \times m_i\boldsymbol{v}_i) + \sum(\boldsymbol{\rho}_i \times m_i(\dot{\boldsymbol{v}}_i)_O) \qquad \text{(A.2.2)}$$

Figure 2.9 shows that $(\dot{\boldsymbol{\rho}}_i)_O = (\dot{\boldsymbol{r}}_i - \dot{\boldsymbol{r}}_A)_O$ and $(\dot{\boldsymbol{v}}_i)_O = (\ddot{\boldsymbol{r}}_i)_O$. The cross-product $(\dot{\boldsymbol{r}}_i)_O \times \boldsymbol{v}_i = 0$ and the sum of external moments about A is defined by $\sum(\boldsymbol{\rho}_i \times m_i(\ddot{\boldsymbol{r}}_i)_O)$. Using this, equation A.2.2 can be rewritten as

$$\sum \boldsymbol{M}_A = (\dot{\boldsymbol{H}}_A)_O + (\dot{\boldsymbol{r}}_A)_O \times \sum m_i \boldsymbol{v}_i \tag{A.2.3}$$

The velocity of the centre of mass with respect to the inertial reference fram $(\boldsymbol{v})$ satisfies $m\boldsymbol{v} = \sum m_i \boldsymbol{v}_i$. Additionally, $\boldsymbol{v}$ can be defined as $\boldsymbol{v}_A + (\dot{\boldsymbol{\rho}})_O$ with regard to figure 2.9. This simplifies equation A.2.3 to

$$\sum \boldsymbol{M}_A = (\dot{\boldsymbol{H}}_A)_O + \boldsymbol{v}_A \times m(\dot{\boldsymbol{\rho}})_O \tag{A.2.4}$$

If the centre of mass is at A, $\boldsymbol{v} = \boldsymbol{v}_A$ and $\sum \boldsymbol{M}_A = (\dot{\boldsymbol{H}}_A)_O$. Equation A.2.4 can be expressed in terms of its components coordinated in the body reference frame. To do this, equation A.2.2 is rewritten as

$$\boldsymbol{H}_A = \sum(\boldsymbol{\rho}_i \times m_i(\boldsymbol{v}_A + \dot{\boldsymbol{\rho}}_i + \boldsymbol{\omega} \times \boldsymbol{\rho}_i)) \tag{A.2.5}$$

The assumption that the body is rigid (as discussed in section A.1) is made, resulting in $\dot{\boldsymbol{\rho}}_i = 0$ so

$$\boldsymbol{H}_A = \sum m_i \boldsymbol{\rho}_i \times \boldsymbol{v}_A + \sum \boldsymbol{\rho}_i \times m_i(\boldsymbol{\omega} \times \boldsymbol{\rho}_i) \text{ or} \tag{A.2.6}$$

$$\boldsymbol{H}_A = m\overline{\boldsymbol{\rho}} \times \boldsymbol{v}_A + \boldsymbol{I}\boldsymbol{\omega} \tag{A.2.7}$$

The derivatives as observed in the inertial reference frame can be derived through the use of equation A.1.2 with the results shown below

$$(\dot{\boldsymbol{H}}_A)_O = (\dot{\boldsymbol{H}}_A)_i + \boldsymbol{\omega} \times \boldsymbol{H}_A \tag{A.2.8}$$

$$(\dot{\overline{\boldsymbol{\rho}}}_O) = (\dot{\overline{\boldsymbol{\rho}}}_i) + \boldsymbol{\omega} \times \overline{\boldsymbol{\rho}} \tag{A.2.9}$$

Equation A.2.7 is then substituted into A.2.8 resulting in

$$(\dot{\boldsymbol{H}}_A)_O = \left(\frac{d}{dt}(m\overline{\boldsymbol{\rho}} \times \boldsymbol{v}_A + \boldsymbol{I}\boldsymbol{\omega})\right)_i + \boldsymbol{\omega} \times (m\overline{\boldsymbol{\rho}} \times \boldsymbol{v}_A + \boldsymbol{I}\boldsymbol{\omega}) \tag{A.2.10}$$

$$= m\dot{\overline{\boldsymbol{\rho}}} \times \boldsymbol{v}_A + m\overline{\boldsymbol{\rho}} \times \dot{\boldsymbol{v}}_A + \boldsymbol{I}\dot{\boldsymbol{\omega}} + \boldsymbol{\omega} \times (m\overline{\boldsymbol{\rho}} \times \boldsymbol{v}_A) + \boldsymbol{\omega} \times \boldsymbol{I}\boldsymbol{\omega} \tag{A.2.11}$$

$$= \boldsymbol{I}\dot{\boldsymbol{\omega}} + \boldsymbol{\omega} \times \boldsymbol{I}\boldsymbol{\omega} + m\overline{\boldsymbol{\rho}} \times \dot{\boldsymbol{v}}_A + \boldsymbol{\omega} \times (m\overline{\boldsymbol{\rho}} \times \boldsymbol{v}_A) \tag{A.2.12}$$

As previously discussed, derivatives without subscripts are assumed to be with respect to the body reference axis, i.e. $(\,)_i$. It is still assumed that the body is rigid, i.e. $\dot{\overline{\boldsymbol{\rho}}} = 0$ and $(\dot{\overline{\boldsymbol{\rho}}})_O = \boldsymbol{\omega} \times \overline{\boldsymbol{\rho}}$. Substituting this result and A.2.12 into A.2.4 yields

$$\sum \boldsymbol{M}_A = \boldsymbol{I}\dot{\boldsymbol{\omega}} + \boldsymbol{\omega} \times \boldsymbol{I}\boldsymbol{\omega} + m\overline{\boldsymbol{\rho}} \times \dot{\boldsymbol{v}}_A + m\boldsymbol{\omega} \times (\overline{\boldsymbol{\rho}} \times \boldsymbol{v}_A) + m\boldsymbol{v}_A \times (\boldsymbol{\omega} \times \overline{\boldsymbol{\rho}}). \tag{A.2.13}$$

It is important to note that $\boldsymbol{I\omega}$ is shorthand for

$$\boldsymbol{I\omega} = (I_{xx}P - I_{xy}Q - I_{xz}R)\boldsymbol{i} + (-I_{xy}P + I_{yy}Q - I_{yz}R)\boldsymbol{j} + (-I_{xz}P - I_{yz}Q + I_{zz}R)\boldsymbol{k} \tag{A.2.14}$$

With no assumptions of symmetry in any of the planes (i.e. $I_{xy} \neq 0$, $I_{xz} \neq 0$, $I_{yz} \neq 0$), equation A.2.13 expands to equations 2.3.5 to

$$\begin{aligned}
\sum \boldsymbol{L} =& I_{xx}\dot{P} - I_{xy}\dot{Q} - I_{xz}\dot{R} + I_{xy}PR - I_{xz}PQ + (I_{zz} - I_{yy})QR + (R^2 - Q^2)I_{yz} \\
&+ m((PV_A - QU_A + \dot{W}_A)\Delta y + (PW_A - RU_A - \dot{(V)}_A)\Delta z) \qquad \text{(A.2.15)} \\
\sum \boldsymbol{M} =& - I_{xy}\dot{P} + I_{yy}\dot{Q} - I_{yz}\dot{R} + I_{yz}PQ - I_{xy}QR + (I_{xx} - I_{zz})PR + (P^2 - R^2)I_{xz} \\
&+ m((QU_A - PV_A - \dot{W}_A)\Delta x + QW_A - RV_A + \dot{U}_A)\Delta z) \qquad \text{(A.2.16)} \\
\sum \boldsymbol{N} =& - I_{xz}\dot{P} + I_{yz}\dot{Q} + I_{zz}\dot{R} + I_{xz}QR - I_{yz}PR + (I_{yy} - I_{xx})PQ + (Q^2 - P^2)I_{xy} \\
&+ m((RU_A - PW_A + \dot{V}_A)\Delta x + (RV_A - QW_A - \dot{U}_A)\Delta y) \qquad \text{(A.2.17)}
\end{aligned}$$

Appendix B

Analytic asymmetric trim

B.1 Analytic solution: Zero roll angle

This section reports on an analytic trim technique based on zero bank angle with sideslip. With reference to Figure 3.1, forces $\boldsymbol{C}$, $\boldsymbol{D}$ and $\boldsymbol{L}$ acted on the body, but were referenced in the wind axis. Force $\boldsymbol{G}$ acted on the body, referenced in the inertial axis, and $\boldsymbol{T}$ acted on the body, referenced in the body axis. These forces needed to be transformed into the body axis in order to determine an equilibrium/trim state for the aircraft. Equation 2.1.1 and 2.1.5 were used to translate these forces from inertial axis and wind axis to body axis respectively as:

$$\begin{bmatrix} X_{BI} \\ Y_{BI} \\ Z_{BI} \end{bmatrix} = DCM_{I\to B} \begin{bmatrix} 0 \\ 0 \\ G \end{bmatrix} = \begin{bmatrix} -S_\Theta G \\ C_\Theta S_\Phi G \\ C_\Theta C_\Phi G \end{bmatrix} \tag{B.1.1}$$

$$\begin{bmatrix} X_{BW} \\ Y_{BW} \\ Z_{BW} \end{bmatrix} = DCM_{W\to B} \begin{bmatrix} -D \\ -C \\ -L \end{bmatrix} = \begin{bmatrix} -C_\alpha C_\beta D + C_\alpha S_\beta C + S_\alpha L \\ -S_\beta D - C_\beta C \\ -S_\alpha C_\beta D + S_\alpha S_\beta C - C_\alpha L \end{bmatrix} \tag{B.1.2}$$

The total force acting on the body of the aircraft was determined by summing the forces in equations B.1.1 and B.1.2 as well as the thrust to get:

$$\begin{bmatrix} X_B \\ Y_B \\ Z_B \end{bmatrix} = \begin{bmatrix} X_{BW} \\ Y_{BW} \\ Z_{BW} \end{bmatrix} + \begin{bmatrix} X_{BI} \\ Y_{BI} \\ Z_{BI} \end{bmatrix} + \begin{bmatrix} T \\ 0 \\ 0 \end{bmatrix} = \begin{bmatrix} -S_\Theta G - C_\alpha C_\beta D + C_\alpha S_\beta C + S_\alpha L + T \\ C_\Theta S_\Phi G - S_\beta D - C_\beta C \\ C_\Theta C_\Phi G - S_\alpha C_\beta D + S_\alpha S_\beta C - C_\alpha L \end{bmatrix} \tag{B.1.3}$$

Due to the shift in CG, there were new moments acting on the aircraft due to gravity. It was necessary to translate gravity from the inertial reference frame to body reference frame, and to

determine the moments it generated. These moments are

$$\begin{bmatrix} L_G \\ M_G \\ N_G \end{bmatrix} = \begin{bmatrix} 0 & -\Delta_z & \Delta_y \\ \Delta_z & 0 & -\Delta_x \\ -\Delta_y & \Delta_x & 0 \end{bmatrix} \begin{bmatrix} -S_\Theta G \\ C_\Theta S_\Phi G \\ C_\Theta C_\Phi G \end{bmatrix} = \begin{bmatrix} \Delta_y C_\Theta C_\Phi G - \Delta_z C_\Theta S_\Phi G \\ -\Delta_x C_\Theta C_\Phi G - \Delta_z S_\Theta G \\ \Delta_x C_\Theta S_\Phi G + \Delta_y S_\Theta G \end{bmatrix} \tag{B.1.4}$$

The moments were then defined as $L = L_A + L_G, M = M_A + M_G, N = N_A + N_G$. In straight trim, it is assumed that the attitude of the aircraft should represent the orientation of the wind axis. This allowed the following assumptions to be made: $\theta = \alpha, \psi = \beta$ and $\phi = 0$. These assumptions were made on account of the relationship of the known angles between the attitude of the aircraft and the wind axis. The small angle assumption was then used to get

$$\begin{bmatrix} X_B \\ Y_B \\ Z_B \end{bmatrix} = \begin{bmatrix} -\alpha G - D + \beta C + \alpha L + T \\ -\beta D - C \\ G - \alpha D + \alpha\beta C - L \end{bmatrix} \tag{B.1.5}$$

$$\begin{bmatrix} L_G \\ M_G \\ N_G \end{bmatrix} = \begin{bmatrix} \Delta_y G \\ -\Delta_x G - \Delta_z \alpha G \\ \Delta_y \alpha G \end{bmatrix} \tag{B.1.6}$$

It was assumed that the drag was an order of magnitude less than lift and that it could be ignored in the force and moment equations. The incident angles were also assumed to be small and were neglected in the following force and moment equations:

$$C_{Y_\beta}\beta + C_{Y_{\delta_A}}\delta_A + C_{Y_{\delta_R}}\delta_R = 0 \tag{B.1.7}$$

$$C_{L_\alpha}\alpha + C_{L_{\delta_E}}\delta_E = \frac{G}{qS} \tag{B.1.8}$$

$$C_{l_\beta}\beta + C_{l_{\delta_A}}\delta_A + C_{l_{\delta_E}}\delta_E = -\frac{\Delta_y G}{qSb} \tag{B.1.9}$$

$$\left(-\frac{\Delta_z G}{qS\overline{c}} + C_{m_\alpha}\right)\alpha + C_{m_{\delta_E}}\delta_E = \frac{\Delta_x G}{qS\overline{c}} \tag{B.1.10}$$

$$\frac{\Delta_y G}{qSb}\alpha + C_{n_\beta}\beta + C_{n_{\delta_A}}\delta_A + C_{n_{\delta_R}}\delta_R = 0 \tag{B.1.11}$$

Equations B.1.7 to B.1.11 were solved for $\begin{bmatrix} \alpha & \beta & \delta_A & \delta_E & \delta_R \end{bmatrix}$. This provided an equation that allowed the calculation of thrust using:

$$T = C_\alpha C_\beta D - C_\alpha S_\beta C - S_\alpha L + S_\theta G \tag{B.1.12}$$

This resulted in an analytic solution of the trim settings required for straight flight with zero roll angle. The force equations were still of a reduced form and did not take the full dynamics of the aircraft into account.

Tables B.1 and B.2 show the necessary trim setting for the different amounts of stabiliser

Table B.1: Analytic trim calculation with partial left horizontal stabiliser — Zero Roll

(Perc)	Thrust (N)	α (°)	β (°)	δ_A (°)	δ_E (°)	δ_R (°)
0%	13.039	6.707	−0.000	−0.000	−4.707	−0.000
10%	13.014	6.713	0.084	0.070	−5.007	0.206
20%	13.008	6.716	0.098	0.079	−5.061	0.270
30%	13.003	6.719	0.109	0.087	−5.121	0.337
40%	12.997	6.722	0.121	0.098	−5.201	0.411
50%	12.991	6.726	0.130	0.110	−5.299	0.491
60%	12.984	6.729	0.138	0.125	−5.438	0.579
70%	12.978	6.731	0.145	0.141	−5.621	0.669
80%	12.972	6.734	0.152	0.161	−5.897	0.754
90%	12.966	6.736	0.156	0.182	−6.276	0.805
100%	12.957	6.739	0.166	0.215	−6.935	0.751

Table B.2: Analytic trim calculation with partial vertical stabiliser — Zero Roll

(Perc)	Thrust (N)	α (°)	β (°)	δ_A (°)	δ_E (°)	δ_R (°)
0%	13.039	6.707	−0.000	−0.000	−4.707	−0.000
10%	13.017	6.691	−0.000	−0.000	−4.869	−0.000
20%	13.013	6.711	−0.000	−0.000	−5.128	−0.000
30%	13.009	6.712	−0.000	−0.000	−5.185	−0.000
40%	13.006	6.712	−0.000	−0.000	−5.241	−0.000
50%	13.002	6.712	−0.000	−0.000	−5.305	−0.000
60%	12.998	6.712	−0.000	−0.000	−5.369	−0.000
70%	12.993	6.712	−0.000	−0.000	−5.433	−0.001
80%	12.989	6.713	−0.000	−0.000	−5.505	−0.001
90%	12.984	6.713	−0.000	−0.000	−5.576	−0.005

damage to maintain straight flight with zero roll angle. The actuator deflections all change quite significantly for the partial horizontal stabiliser damage configuration. The elevator deflection changes significantly to accommodate the shift in CG and the reduced horizontal stabiliser size. The aileron and rudder deflects to ensure the zero roll angle. For the partial vertical stabiliser damage cases, the shift in CG causes the elevator deflection to increase in size. The aircraft remains symmetric and as a result there are no deflections on the aileron and negligible deflections on the rudder.

Tables B.3 to B.5 show the residual forces acting on the aircraft for the respective trim conditions. The forces for the partial horizontal stabiliser loss are all nonzero and cause the aircraft to become unstable quickly. The partial vertical stabiliser configuration still has a significant force in the z-axis and a slight pitching moment. This causes the aircraft to become unstable, albeit slower.

Figure B.1 shows the flight paths of all the different damage cases of the aircraft with the trim calculated using this technique. These figures show that the trim was capable of maintaining straight and level flight for about $50m$ before veering off to the side and losing

Table B.3: Asymmetric analytic trim residual forces and moments — Partial left horizontal stabiliser

(Perc)	X (N)	Y (N)	Z (N)	L (Nm)	M (Nm)	N (Nm)
0%	−0.000	0.000	−1.533	−0.000	0.000	0.000
10%	0.000	0.011	−1.531	0.002	0.002	−0.017
20%	0.000	0.024	−1.531	0.003	0.002	−0.024
30%	0.000	0.040	−1.530	0.004	0.001	−0.034
40%	0.000	0.060	−1.529	0.006	−0.001	−0.048
50%	0.001	0.083	−1.528	0.008	−0.004	−0.066
60%	0.001	0.111	−1.526	0.010	−0.010	−0.087
70%	0.002	0.139	−1.524	0.013	−0.017	−0.110
80%	0.002	0.162	−1.522	0.015	−0.027	−0.130
90%	0.003	0.163	−1.521	0.016	−0.037	−0.133
100%	0.003	0.088	−1.524	0.009	−0.034	−0.079

Table B.4: Asymmetric analytic trim residual forces and moments — Partial vertical stabiliser

(Perc)	X (N)	Y (N)	Z (N)	L (Nm)	M (Nm)	N (Nm)
0%	−0.000	0.000	−1.533	−0.000	0.000	0.000
10%	−0.000	0.000	−1.527	−0.000	0.001	0.000
20%	−0.000	0.000	−1.531	−0.000	0.002	0.000
30%	−0.000	0.000	−1.531	−0.000	0.003	0.000
40%	0.000	0.000	−1.531	−0.000	0.003	0.000
50%	−0.000	0.000	−1.530	−0.000	0.003	0.000
60%	−0.000	0.000	−1.530	−0.000	0.004	0.000
70%	−0.000	0.000	−1.529	−0.000	0.004	0.000
80%	−0.000	0.000	−1.529	−0.000	0.005	0.000
90%	−0.000	0.000	−1.528	−0.000	0.005	0.000

Table B.5: Asymmetric analytic trim residual forces and moments — Nominal damage case

(Perc)	X (N)	Y (N)	Z (N)	L (Nm)	M (Nm)	N (Nm)
0% − 0%	−0.000	0.000	−1.533	−0.000	0.000	0.000
70% − 20%	0.002	0.087	−1.523	0.008	−0.014	−0.069

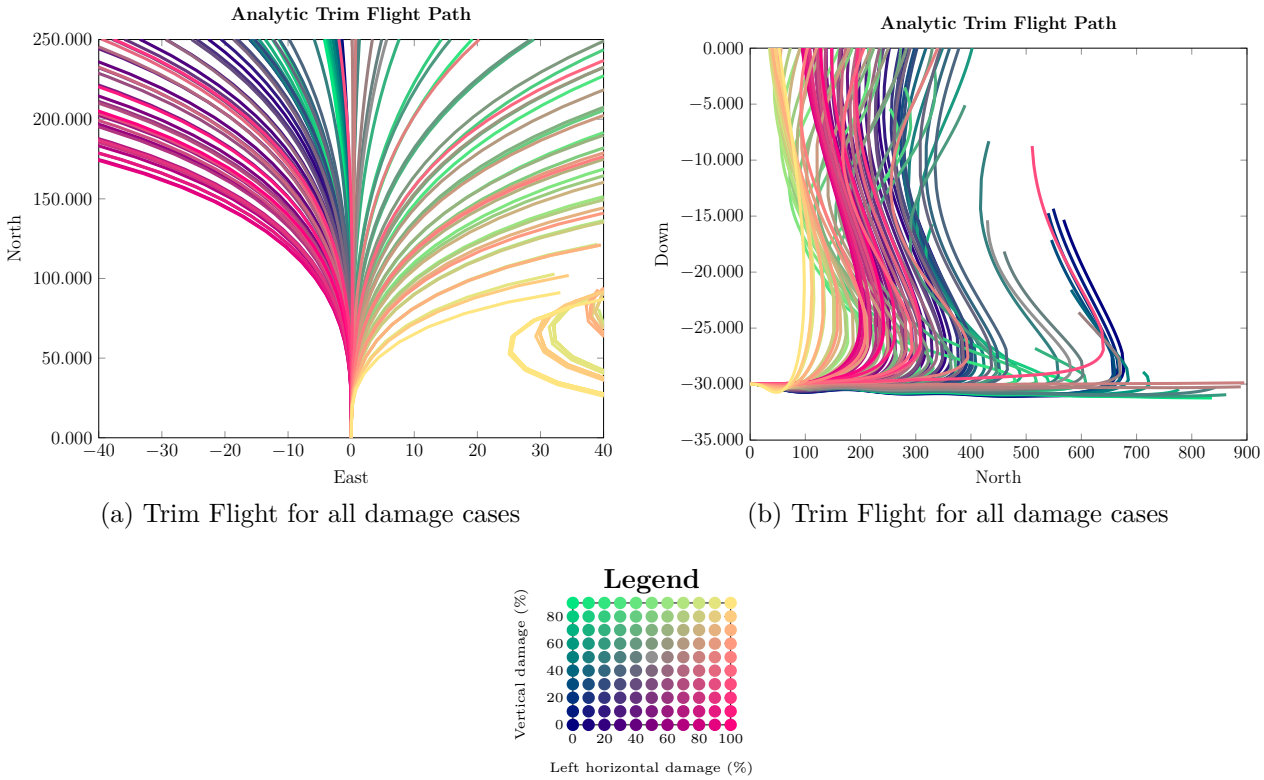

(a) Trim Flight for all damage cases

(b) Trim Flight for all damage cases

Figure B.1: Analytic trim flight path — zero roll angle

altitude.

B.2 Analytic solution: Zero sideslip angle

The aircraft could also be trimmed with zero sideslip angle and a nonzero bank angle. A similar approach was followed as shown in section B.1. The main difference here was that $\beta = 0$ and the trim calculated a roll angle ϕ. The wind to body DCM was modified to show this simplification as:

$$DCM_{W\to B} = \begin{bmatrix} C_\alpha & 0 & -S_\alpha \\ S_\alpha S_\phi & C_\phi & C_\alpha S_\phi \\ S_\alpha C_\phi & -S_\theta & C_\alpha C_\phi \end{bmatrix} \tag{B.2.1}$$

This equation was used to determine the forces acting on the body of the aircraft by multiplying it with the forces acting in the wind axis resulting in the following equation:

$$\begin{bmatrix} X_{BW} \\ Y_{BW} \\ Z_{BW} \end{bmatrix} = DCM_{W\to B} \begin{bmatrix} -D \\ -C \\ -L \end{bmatrix} = \begin{bmatrix} -DC_\alpha + LS_\alpha \\ -DS_\alpha S_\phi - CC_\phi - LC_\alpha S_\phi \\ -DS_\alpha C_\phi + CS_\phi - LC_\alpha C_\phi \end{bmatrix} \tag{B.2.2}$$

Equation B.1.4 was used for the moment equations as roll or sideslip angles had no effect on it. The small angle assumption was used on equations B.1.4 and B.2.2 resulting in:

$$\begin{bmatrix} X_B \\ Y_B \\ Z_B \end{bmatrix} = \begin{bmatrix} -D + L\alpha - G\alpha + T \\ -D\alpha\phi - C - L\phi + G\phi \\ -D\alpha + C\phi - L + G \end{bmatrix} \tag{B.2.3}$$

$$\begin{bmatrix} L_G \\ M_G \\ N_G \end{bmatrix} = \begin{bmatrix} \Delta_y G - \Delta_z \phi G \\ -\Delta_x G - \Delta_z \alpha G \\ \Delta_x \phi G + \Delta_y \alpha G \end{bmatrix} \tag{B.2.4}$$

It was assumed that the drag on the aircraft was an order of magnitude smaller than the lift generated and that it could be ignored in the forces and moment equations. This resulted in the following:

$$\frac{G}{qS}\phi - C_{Y_{\delta_A}}\delta_A - C_{Y_{\delta_R}}\delta_R = 0 \tag{B.2.5}$$

$$C_{L_\alpha}\alpha + C_{L_{\delta_E}}\delta_E = \frac{G}{qS} \tag{B.2.6}$$

$$-\frac{\Delta_z G}{qSb}\phi + C_{l_{\delta_A}}\delta_A + C_{l_{\delta_R}}\delta_R = -\frac{\Delta_y G}{qSb} \tag{B.2.7}$$

$$\left(-\frac{\Delta_z G}{qS\bar{c}} + C_{m_\alpha}\right)\alpha + C_{m_{\delta_E}}\delta_E = \frac{\Delta_x}{qS\bar{c}} \tag{B.2.8}$$

$$\frac{\Delta_y G}{qSb}\alpha + \frac{\Delta_x G}{qSb}\phi + C_{n_{\delta_A}}\delta_A + C_{n_{\delta_R}}\delta_R = 0 \tag{B.2.9}$$

Equations B.2.5 to B.2.9 were solved simultaneously to determine the actuator trim settings. The required thrust of the aircraft at this trim setting was then be determined with:

$$T = C_\alpha D - S_\alpha (L - mg) \tag{B.2.10}$$

Tables B.6 and B.7 show the different trim settings that were calculated for the different damage cases to provide straight flight with no sideslip and a nonzero roll angle. There is a significant change in actuator deflections for the partial horizontal stabiliser damage case. The elevator deflects significantly to accommodate the shift in CG and change in physical size of the horizontal stabiliser. The aileron and rudder deflections are necessary to maintain straight flight due to the aircraft asymmetry. The partial vertical damage configuration maintains aircraft symmetry, and only the elevator had a change in deflection to accommodate the shift in CG.

Tables B.8 to B.10 show the residual forces and moments acting on the aircraft for the different damage configurations and their trim settings. For the partial horizontal stabiliser loss configuration there are forces and moments in all directions which resulted in the aircraft becoming unstable quickly. For the partial vertical stabiliser case, the residual forces were zero in all directions except the longitudinal. The force in the z-axis as well the pitching moment resulted in a change in altitude.

Table B.6: Analytic trim calculation with partial left horizontal stabiliser — Zero Sideslip

(Perc)	Thrust (N)	α (°)	ϕ (°)	δ_A (°)	δ_E (°)	δ_R (°)
0%	13.039	6.707	0.000	−0.000	−4.707	−0.000
10%	13.020	6.703	−0.020	0.088	−5.001	0.099
20%	13.016	6.703	−0.023	0.100	−5.054	0.146
30%	13.013	6.703	−0.026	0.111	−5.114	0.197
40%	13.009	6.704	−0.029	0.125	−5.197	0.258
50%	13.004	6.705	−0.031	0.139	−5.301	0.326
60%	12.999	6.706	−0.033	0.156	−5.451	0.403
70%	12.994	6.709	−0.035	0.175	−5.654	0.485
80%	12.987	6.713	−0.036	0.198	−5.958	0.564
90%	12.980	6.718	−0.037	0.221	−6.370	0.611
100%	12.968	6.726	−0.040	0.256	−7.031	0.547

Table B.7: Analytic trim calculation with partial vertical stabiliser — Zero Sideslip

(Perc)	Thrust (N)	α (°)	ϕ (°)	δ_A (°)	δ_E (°)	δ_R (°)
0%	13.039	6.707	0.000	−0.000	−4.707	−0.000
10%	13.017	6.691	0.000	−0.000	−4.869	−0.000
20%	13.013	6.711	0.000	−0.000	−5.128	−0.000
30%	13.009	6.712	0.000	−0.000	−5.185	−0.000
40%	13.006	6.712	0.000	−0.000	−5.241	−0.000
50%	13.002	6.712	0.000	−0.000	−5.305	−0.000
60%	12.998	6.712	0.000	−0.000	−5.369	−0.000
70%	12.993	6.712	0.000	−0.000	−5.433	−0.001
80%	12.989	6.713	0.000	−0.000	−5.505	−0.001
90%	12.984	6.713	0.000	−0.000	−5.576	−0.005

Table B.8: Asymmetric analytic trim residual forces and moments — Partial left horizontal stabiliser

(Perc)	X (N)	Y (N)	Z (N)	L (Nm)	M (Nm)	N (Nm)
0%	−0.000	0.000	−1.533	−0.000	0.000	0.000
10%	0.000	0.011	−1.427	0.002	0.002	−0.017
20%	0.000	0.024	−1.390	0.003	0.003	−0.024
30%	0.000	0.040	−1.356	0.004	0.004	−0.034
40%	0.000	0.060	−1.324	0.006	0.004	−0.048
50%	0.001	0.083	−1.296	0.008	0.005	−0.066
60%	0.001	0.111	−1.274	0.010	0.006	−0.087
70%	0.002	0.139	−1.261	0.013	0.006	−0.110
80%	0.002	0.162	−1.261	0.015	0.007	−0.129
90%	0.003	0.163	−1.281	0.016	0.008	−0.133
100%	0.003	0.088	−1.336	0.009	0.008	−0.079

Table B.9: Asymmetric analytic trim residual forces and moments — Partial vertical stabiliser

(Perc)	X (N)	Y (N)	Z (N)	L (Nm)	M (Nm)	N (Nm)
0%	−0.000	0.000	−1.533	−0.000	0.000	0.000
10%	−0.000	0.000	−1.527	−0.000	0.001	0.000
20%	−0.000	0.000	−1.531	−0.000	0.002	0.000
30%	−0.000	0.000	−1.531	−0.000	0.003	0.000
40%	0.000	0.000	−1.531	−0.000	0.003	0.000
50%	−0.000	0.000	−1.530	−0.000	0.003	0.000
60%	−0.000	0.000	−1.530	−0.000	0.004	0.000
70%	−0.000	0.000	−1.529	−0.000	0.004	0.000
80%	−0.000	0.000	−1.529	−0.000	0.005	0.000
90%	−0.000	0.000	−1.528	−0.000	0.005	0.000

Table B.10: Asymmetric analytic trim residual forces and moments — Nominal damage case

(Perc)	X (N)	Y (N)	Z (N)	L (Nm)	M (Nm)	N (Nm)
0% − 0%	−0.000	0.000	−1.533	−0.000	0.000	0.000
70% − 20%	0.002	0.087	−1.183	0.008	0.009	−0.068

Figure B.2 shows the flight paths for all the different calculated trim settings using this technique. The trim settings took the shift in CG as well as the change in aerodynamic coefficients into account as can be seen by the change in elevator setting. These trim settings seemed to maintain straight flight for around $50m$ as well, but the aircraft veered off to the side shortly after that. The altitude also was not stable at $30m$, at which the aircraft was initialised. While these trim settings provided a good point around which to linearise the aircraft, an iterative technique was investigated in an order to provide a more accurate trim setting.

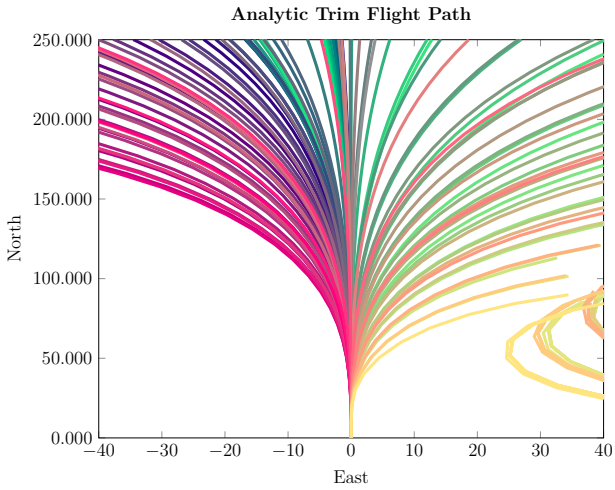

(a) Trim Flight for all damage cases

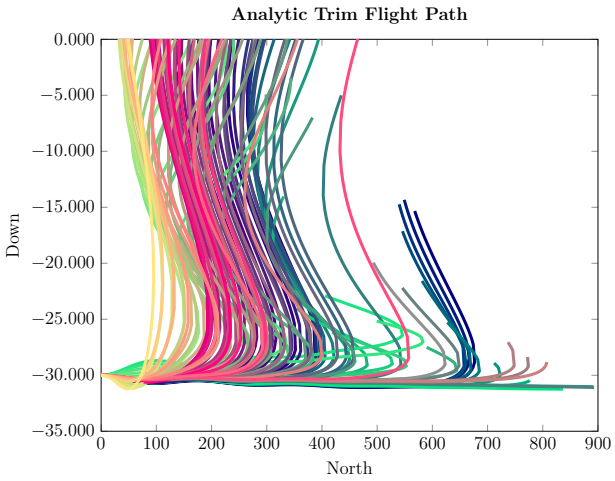

(b) Trim Flight for all damage cases

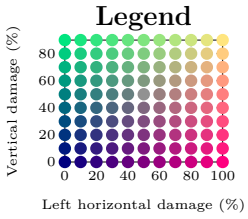

Figure B.2: Analytic trim flight path — zero sideslip angle

Appendix C

Linearised state equation values

C.1 0% left horizontal 0% vertical stabiliser loss

$$\begin{bmatrix} \dot{\overline{v}} \\ \dot{\alpha} \\ \dot{q} \\ \dot{\theta} \\ \dot{\beta} \\ \dot{p} \\ \dot{r} \\ \dot{\phi} \end{bmatrix} = \begin{bmatrix} -0.1729 & 14.6187 & -1.9720 & -9.7457 & 0.0000 & -0.0000 & 0.0004 & 0.0000 \\ -0.0280 & -5.0125 & 0.9068 & -0.0623 & 0.0000 & -0.0000 & -0.0000 & 0.0000 \\ 0.4313 & -68.0758 & -7.6577 & 0.0000 & 0.0000 & 0.0000 & 0.0000 & 0.0000 \\ 0.0000 & 0.0000 & 1.0000 & 0.0000 & 0.0000 & 0.0000 & 0.0000 & 0.0000 \\ 0.0000 & 0.0000 & 0.0000 & 0.0000 & -0.2870 & 0.1251 & -0.9851 & 0.5414 \\ 0.0000 & -0.0004 & -0.0000 & 0.0000 & -23.9906 & -7.8698 & 2.8058 & 0.0000 \\ -0.0000 & 0.0028 & 0.0000 & 0.0000 & 16.4925 & -1.5123 & -0.8682 & 0.0000 \\ 0.0000 & 0.0000 & 0.0000 & 0.0000 & 0.0000 & 1.0000 & 0.1150 & 0.0000 \end{bmatrix} \begin{bmatrix} \overline{v} \\ \alpha \\ q \\ \theta \\ \beta \\ p \\ r \\ \phi \end{bmatrix}$$
$$+ \begin{bmatrix} -0.0000 & 0.4818 & 0.0000 & 0.1408 \\ 0.0000 & -0.4898 & 0.0000 & 0.0000 \\ 0.0001 & -96.3550 & 0.0000 & 0.0000 \\ 0.0000 & 0.0000 & 0.0000 & 0.0000 \\ 0.0147 & 0.0000 & 0.1269 & 0.0000 \\ -98.4180 & 0.0000 & 2.1546 & 0.0000 \\ -7.9429 & 0.0000 & -14.3644 & 0.0000 \\ 0.0000 & 0.0000 & 0.0000 & 0.0000 \end{bmatrix} \begin{bmatrix} \delta_a \\ \delta_e \\ \delta_r \\ \Delta T \end{bmatrix} \tag{C.1.1}$$

C.2 70% left horizontal 0% vertical stabiliser loss

$$\begin{bmatrix} \dot{\overline{v}} \\ \dot{\alpha} \\ \dot{q} \\ \dot{\theta} \\ \dot{\beta} \\ \dot{p} \\ \dot{r} \\ \dot{\phi} \end{bmatrix} = \begin{bmatrix} -0.1745 & 14.5439 & -2.0011 & -9.7452 & 0.0483 & -0.0037 & 0.0467 & 0.0000 \\ -0.0285 & -4.9155 & 0.9202 & -0.0625 & 0.0334 & -0.0033 & -0.0019 & 0.0000 \\ 0.3396 & -54.0381 & -5.3653 & 0.0000 & 6.5136 & -0.0625 & -0.3756 & 0.0000 \\ 0.0000 & 0.0000 & 1.0000 & 0.0000 & 0.0000 & 0.0000 & 0.0000 & 0.0000 \\ -0.0000 & 0.0103 & 0.0009 & 0.0000 & -0.3023 & 0.1272 & -0.9844 & 0.5414 \\ 0.0040 & -0.0008 & -0.2070 & 0.0000 & -25.0510 & -7.8762 & 2.8737 & 0.0000 \\ -0.0008 & -1.2787 & -0.1238 & 0.0000 & 18.7938 & -1.6121 & -0.9902 & 0.0000 \\ 0.0000 & 0.0000 & 0.0000 & 0.0000 & 0.0000 & 1.0000 & 0.1155 & 0.0000 \end{bmatrix} \begin{bmatrix} \overline{v} \\ \alpha \\ q \\ \theta \\ \beta \\ p \\ r \\ \phi \end{bmatrix}$$
$$+ \begin{bmatrix} -0.0181 & 0.2088 & -0.0356 & 0.1430 \\ 0.0155 & -0.3183 & -0.0304 & 0.0000 \\ 3.4803 & -64.0372 & -5.8440 & 0.0022 \\ 0.0000 & 0.0000 & 0.0000 & 0.0000 \\ 0.0255 & 0.0094 & 0.1388 & -0.0000 \\ -99.2272 & -3.0924 & 3.0013 & -0.0001 \\ -7.9268 & -1.6068 & -15.9093 & 0.0042 \\ 0.0000 & 0.0000 & 0.0000 & 0.0000 \end{bmatrix} \begin{bmatrix} \delta_a \\ \delta_e \\ \delta_r \\ \Delta T \end{bmatrix} \tag{C.2.1}$$

C.3 100% left horizontal 0% vertical stabiliser loss

$$\begin{bmatrix} \dot{\overline{v}} \\ \dot{\alpha} \\ \dot{q} \\ \dot{\theta} \\ \dot{\beta} \\ \dot{p} \\ \dot{r} \\ \dot{\phi} \end{bmatrix} = \begin{bmatrix} -0.1752 & 14.5377 & -2.0093 & -9.7450 & 0.0561 & -0.0038 & 0.0390 & 0.0000 \\ -0.0286 & -4.8947 & 0.9243 & -0.0626 & 0.0293 & -0.0033 & -0.0017 & 0.0000 \\ 0.3232 & -51.5740 & -4.6539 & 0.0000 & 5.9064 & -0.1352 & -0.3437 & 0.0000 \\ 0.0000 & 0.0000 & 1.0000 & 0.0000 & 0.0000 & 0.0000 & 0.0000 & 0.0000 \\ 0.0000 & 0.0069 & 0.0006 & 0.0000 & -0.3021 & 0.1280 & -0.9845 & 0.5414 \\ 0.0025 & 0.1508 & -0.2129 & 0.0000 & -25.0504 & -7.8745 & 2.8729 & 0.0000 \\ -0.0027 & -0.9604 & -0.0967 & 0.0000 & 18.8603 & -1.6881 & -0.9883 & 0.0000 \\ 0.0000 & 0.0000 & 0.0000 & 0.0000 & 0.0000 & 1.0000 & 0.1157 & 0.0000 \end{bmatrix} \begin{bmatrix} \overline{v} \\ \alpha \\ q \\ \theta \\ \beta \\ p \\ r \\ \phi \end{bmatrix}$$
$$+ \begin{bmatrix} -0.0169 & 0.1305 & -0.0319 & 0.1438 \\ 0.0137 & -0.2446 & -0.0469 & 0.0000 \\ 3.1517 & -49.5270 & -9.0513 & 0.0032 \\ 0.0000 & 0.0000 & 0.0000 & 0.0000 \\ 0.0302 & 0.0091 & 0.1421 & -0.0000 \\ -99.1969 & -3.4192 & 3.0429 & -0.0001 \\ -8.4432 & -1.5449 & -16.3142 & 0.0044 \\ 0.0000 & 0.0000 & 0.0000 & 0.0000 \end{bmatrix} \begin{bmatrix} \delta_a \\ \delta_e \\ \delta_r \\ \Delta T \end{bmatrix} \tag{C.3.1}$$

C.4 0% left horizontal 20% vertical stabiliser loss

$$\begin{bmatrix} \dot{\overline{v}} \\ \dot{\alpha} \\ \dot{q} \\ \dot{\theta} \\ \dot{\beta} \\ \dot{p} \\ \dot{r} \\ \dot{\phi} \end{bmatrix} = \begin{bmatrix} -0.1750 & 14.8217 & -1.9581 & -9.7456 & 0.0000 & -0.0000 & 0.0005 & 0.0000 \\ -0.0277 & -5.0656 & 0.9039 & -0.0623 & 0.0000 & -0.0000 & -0.0000 & 0.0000 \\ 0.5121 & -79.9906 & -8.3125 & 0.0000 & 0.0000 & 0.0000 & -0.0000 & 0.0000 \\ 0.0000 & 0.0000 & 1.0000 & 0.0000 & 0.0000 & 0.0000 & 0.0000 & 0.0000 \\ 0.0000 & 0.0000 & 0.0000 & 0.0000 & -0.2512 & 0.1207 & -0.9864 & 0.5414 \\ 0.0000 & -0.0001 & -0.0000 & 0.0000 & -23.3135 & -7.9078 & 2.7789 & 0.0000 \\ -0.0000 & 0.0032 & 0.0000 & 0.0000 & 12.3081 & -1.1159 & -0.6950 & 0.0000 \\ 0.0000 & 0.0000 & 0.0000 & 0.0000 & 0.0000 & 1.0000 & 0.1151 & 0.0000 \end{bmatrix} \begin{bmatrix} \overline{v} \\ \alpha \\ q \\ \theta \\ \beta \\ p \\ r \\ \phi \end{bmatrix} + \begin{bmatrix} -0.0000 & 0.6621 & 0.0000 & 0.1417 \\ 0.0000 & -0.5222 & 0.0000 & -0.0000 \\ 0.0001 & -103.7658 & 0.0000 & -0.0035 \\ 0.0000 & 0.0000 & 0.0000 & 0.0000 \\ -0.0130 & 0.0000 & 0.0915 & 0.0000 \\ -99.1261 & 0.0000 & 1.0467 & 0.0000 \\ -5.9840 & 0.0000 & -10.4110 & 0.0000 \\ 0.0000 & 0.0000 & 0.0000 & 0.0000 \end{bmatrix} \begin{bmatrix} \delta_a \\ \delta_e \\ \delta_r \\ \Delta T \end{bmatrix} \tag{C.4.1}$$

C.5 0% left horizontal 90% vertical stabiliser loss

$$\begin{bmatrix} \dot{\overline{v}} \\ \dot{\alpha} \\ \dot{q} \\ \dot{\theta} \\ \dot{\beta} \\ \dot{p} \\ \dot{r} \\ \dot{\phi} \end{bmatrix} = \begin{bmatrix} -0.1770 & 14.9825 & -1.9500 & -9.7456 & 0.0000 & -0.0000 & 0.0005 & 0.0000 \\ -0.0272 & -5.1342 & 0.9003 & -0.0623 & 0.0000 & -0.0000 & -0.0000 & 0.0000 \\ 0.6035 & -93.9938 & -9.0535 & 0.0000 & 0.0000 & 0.0000 & -0.0000 & 0.0000 \\ 0.0000 & 0.0000 & 1.0000 & 0.0000 & 0.0000 & 0.0000 & 0.0000 & 0.0000 \\ 0.0000 & 0.0000 & 0.0000 & 0.0000 & -0.1367 & 0.1213 & -0.9920 & 0.5414 \\ 0.0000 & -0.0001 & -0.0000 & 0.0000 & -23.5203 & -7.9191 & 2.7880 & 0.0000 \\ -0.0000 & 0.0033 & 0.0000 & 0.0000 & 0.0364 & -1.2121 & -0.0864 & 0.0000 \\ 0.0000 & 0.0000 & 0.0000 & 0.0000 & 0.0000 & 1.0000 & 0.1151 & 0.0000 \end{bmatrix} \begin{bmatrix} \overline{v} \\ \alpha \\ q \\ \theta \\ \beta \\ p \\ r \\ \phi \end{bmatrix} + \begin{bmatrix} -0.0000 & 0.7578 & 0.0000 & 0.1427 \\ 0.0000 & -0.5631 & 0.0000 & -0.0000 \\ 0.0001 & -112.0567 & 0.0000 & -0.0052 \\ 0.0000 & 0.0000 & 0.0000 & 0.0000 \\ -0.0117 & 0.0000 & 0.0019 & 0.0000 \\ -99.1813 & 0.0000 & -0.0151 & 0.0000 \\ -6.4923 & 0.0000 & -0.2235 & 0.0000 \\ 0.0000 & 0.0000 & 0.0000 & 0.0000 \end{bmatrix} \begin{bmatrix} \delta_a \\ \delta_e \\ \delta_r \\ \Delta T \end{bmatrix} \tag{C.5.1}$$

C.6 70% left horizontal 20% vertical stabiliser loss

$$\begin{bmatrix} \dot{\overline{v}} \\ \dot{\alpha} \\ \dot{q} \\ \dot{\theta} \\ \dot{\beta} \\ \dot{p} \\ \dot{r} \\ \dot{\phi} \end{bmatrix} = \begin{bmatrix} -0.1764 & 14.7141 & -1.9916 & -9.7451 & 0.0277 & -0.0032 & 0.0496 & 0.0000 \\ -0.0281 & -4.9744 & 0.9176 & -0.0626 & 0.0287 & -0.0022 & -0.0018 & 0.0000 \\ 0.4293 & -67.1664 & -5.9379 & 0.0000 & 5.6911 & 0.1766 & -0.3593 & 0.0000 \\ 0.0000 & 0.0000 & 1.0000 & 0.0000 & 0.0000 & 0.0000 & 0.0000 & 0.0000 \\ 0.0000 & 0.0069 & 0.0006 & 0.0000 & -0.2640 & 0.1225 & -0.9858 & 0.5414 \\ 0.0015 & 0.3624 & -0.1951 & 0.0000 & -24.1879 & -7.9450 & 2.8403 & 0.0000 \\ -0.0028 & -0.9128 & -0.0920 & 0.0000 & 14.2628 & -1.1775 & -0.8041 & 0.0000 \\ 0.0000 & 0.0000 & 0.0000 & 0.0000 & 0.0000 & 1.0000 & 0.1156 & 0.0000 \end{bmatrix} \begin{bmatrix} \overline{v} \\ \alpha \\ q \\ \theta \\ \beta \\ p \\ r \\ \phi \end{bmatrix}$$

$$+ \begin{bmatrix} -0.0224 & 0.3260 & -0.0167 & 0.1439 \\ 0.0231 & -0.3443 & -0.0257 & -0.0000 \\ 5.0018 & -69.9535 & -4.9957 & -0.0019 \\ 0.0000 & 0.0000 & 0.0000 & 0.0000 \\ -0.0039 & 0.0064 & 0.1009 & -0.0000 \\ -100.0991 & -3.0022 & 1.7193 & 0.0000 \\ -5.7422 & -1.3157 & -11.6057 & 0.0044 \\ 0.0000 & 0.0000 & 0.0000 & 0.0000 \end{bmatrix} \begin{bmatrix} \delta_a \\ \delta_e \\ \delta_r \\ \Delta T \end{bmatrix} \tag{C.6.1}$$

References

[1] I. K. Peddle, "Autonomous Flight of a Model Aircraft," *Dissertation*, no. April, pp. 1–190, 2005.

[2] D. Blaauw, *Flight Control System for a Variable Stability Blended-Wing-Body Unmanned Aerial Vehicle*. PhD thesis, 2009.

[3] W. H. Pietersen, "System identification for fault tolerant control of unmanned aerial vehicles," mar 2010.

[4] W. A. Basson, *Fault tolerant adaptive control of an unmanned aerial vehicle*. PhD thesis, Stellenbosch : University of Stellenbosch, 2011.

[5] L. Basson, *Control allocation as part of a fault-tolerant control architecture for UAVs*. PhD thesis, mar 2011.

[6] H. M. Odendaal, *An Analysis and Comparison of Two Methods for UAV Actuator Fault Detection and Isolation*. PhD thesis, 2012.

[7] W. Beeton, "Fault Tolerant Flight Control of a UAV with Asymmetric Damage to its Primary Lifting Surface," no. December, 2013.

[8] G. Shah, "Aerodynamic effects and modeling of damage to transport aircraft," *AIAA Paper*, 2008.

[9] B. J. Bacon and I. M. Gregory, "General Equations of Motion for a Damaged Asymmetric Aircraft," aug 2007.

[10] J. Ahn, K. Kim, and J. Suk, "Dynamic analysis of an asymmetric UAV with partial wing damage," in *11th International Conference on Control, Automation and Systems*, no. 1, pp. 112–116, 2011.

[11] P. Cheng, C. Wu, X. Duan, Y. Guo, Pengfei Cheng, Chengfu Wu, Xiaojun Duan, and Yue Guo, "An approach of flight trim for wing-damaged asymmetric aircraft," *Control Conference (CCC), ...*, pp. 6071–6076, 2013.

[12] D. B. Jourdan, M. D. Piedmonte, V. Gavrilets, and D. W. Vos, "Enhancing UAV Survivability Through Damage Tolerant Control," in *Proceedings of the AIAA Guidnace, Navigation, and Control Conference*, pp. 1–26, 2010.

[13] NASA, "SP-367 Introduction to the Aerodynamics of Flight," 2015.

[14] J. H. Blakelock, *Automatic Control of Aircraft and Missiles, 2nd Edition*. 1991.

[15] M. V. Cook, *Flight dynamics principles*. Arnold, 1997.

[16] R. S. Shevel, *Fundamentals of flight*. Prentice-Hall, 1983.

[17] M. Drela and H. Youngren, "AVL," 2014.

[18] B. Etkin and L. D. Reid, *Dynamics of flight, stability and control*. J. Wiley and Sons, 1996.

[19] I. K. Peddle, "Acceleration based manoeuvre flight control system for unmanned aerial vehicles," dec 2008.

[20] G. F. Franklin, J. D. Powel, and A. Emami-Naeini, *Feedback Control of Dynamic Systems*. Pearson, sixth ed., 2010.

[21] A. Thurn, S. Huynh, S. Koss, P. Oppenheimer, S. Butcher, J. Schlater, and P. Hagan, "A Nichrome Burn Wire Release Mechanism for CubeSats,"

[22] S. Boyd, L. E. Ghaoui, E. Feron, and V. Balakrishnan, *Linear matrix inequalities in system and control theory*. 1994.

[23] J. L. Meriam and L. G. Kraige, *Engineering Mechanics Dynamics*. 2008.

[24] D. L. Donoho, "For Most Large Underdetermined Systems of Equations, the Minimal ' 1 -norm Near-Solution Approximates the Sparsest Near-Solution," tech. rep., 2004.

[25] Y. Wu, X. Wang, and Y. Wu, "Dynamic Flight Envelope Estimation for Damaged Asymmetric Aircraft," *Research Notes in Information Science (RNIS)*, vol. 12, 2013.

[26] Y. Huang, T. Pe, A. P. Popov, H. Werner, and F. Thielecke, "Control of a two-load-path Trimmable Horizontal Stabilizer Actuator of an aircraft - Comparison of H-infinity design approaches," in *49th IEEE Conference on Decision and Control (CDC)*, pp. 4863–4868, IEEE, dec 2010.

[27] D. Donoho, H. Kakavand, and J. Mammen, "The Simplest Solution to an Underdetermined System of Linear Equations," in *2006 IEEE International Symposium on Information Theory*, pp. 1924–1928, IEEE, jul 2006.

[28] W. H. Pietersen, "System identification for fault tolerant control of unmanned aerial vehicles," mar 2010.

[29] J. Grasmeyer, "Stability and control derivative estimation and engine-out analysis," 1998.

[30] M. Gopal, *Control Systems - Principles and Design*. Mc Graw Hill, 2002.

[31] Y. Hitachi, "Damage-Tolerant Flight Control System Design for Propulsion-Controlled Aircraft," 2009.

[32] M. Gopal, *Digital Control and State Variable Methods*. Mc Graw Hill, second edi ed., 2004.

[33] J. A. A. Engelbrecht, "Advance Automation 833 Introductory course to aircraft dynamics," no. April, 2013.

[34] R. D. De Hart, "Advanced take-off and flight control algorithms for fixed wing unmanned aerial vehicles," mar 2010.

[35] T. S. Richardson, C. McFarlane, A. Isikveren, K. Badcock, and A. Da Ronch, "Analysis of conventional and asymmetric aircraft configurations using CEASIOM," *Progress in Aerospace Sciences*, vol. 47, pp. 647–659, nov 2011.

[36] X. Li and H. H. T. Liu, "A Passive Fault Tolerant Flight Control for Maximum Allowable Vertical Tail Damaged Aircraft," *Journal of Dynamic Systems, Measurement, and Control*, vol. 134, p. 031006, may 2012.

[37] I. D. Landau and A. Karimi, "Adaptive Control," pp. 1–81, 2009.

[38] S. Park, J. Deyst, and J. P. How, "A New Nonlinear Guidance Logic for Trajectory Tracking," 2004.

[39] N. T. Nguyen, K. S. Krishnakumar, J. T. Kaneshige, and P. P. Nespeca, "Flight Dynamics and Hybrid Adaptive Control of Damaged Aircraft," *Journal of Guidance, Control, and Dynamics*, vol. 31, pp. 751–764, may 2008.

[40] J. Fisher and S. C. Smith, "Adaptive Robust Control of an F15 Aircraft," pp. 3191–3196, 2004.

[41] F. N. Alberts, "Accurate autonomous landing of a fixed-wing unmanned aerial vehicle," dec 2012.

[42] G. Feng and R. Lozano, *Adaptive control systems*. 1999.

[43] G. Chowdhary, "Autonomous guidance and control of airplanes under actuator failures and severe structural damage," 2012.

[44] J. Cieslak, A. Zolghadri, and D. Henry, "Fault tolerant flight control: from theory to piloted flight simulator experiments," *IET Control Theory & Applications*, vol. 4, pp. 1451–1464, aug 2010.

[45] L. Tong and H. Ji, "Multi-body dynamic modelling and roll control of asymmetric variable sweep morphing aircrafts," in *2013 10th IEEE International Conference on Control and Automation (ICCA)*, pp. 1567–1572, IEEE, jun 2013.

[46] Y. Liu, G. Tao, and S. S. M. Joshi, "Modeling and Model Reference Adaptive Control of Aircraft with Asymmetric Damage," *Journal of Guidance, Control, and Dynamics*, vol. 33, pp. 1500–1517, sep 2010.

[47] G. R. Drozeski, "A Fault-Tolerant Control Architecture for Unmanned Aerial Vehicles A Fault-Tolerant Control Architecture for Unmanned Aerial Vehicles," no. December, 2005.

[48] N. Nguyen and K. Krishnakumar, "Dynamics and adaptive control for stability recovery of damaged asymmetric aircraft," *... Navigation, and Control ...*, pp. 1–24, 2006.